



GE Nuclear Energy

NEDO-32176

Class 1

March 1996

Licensing Topical Report

TRACG Model Description

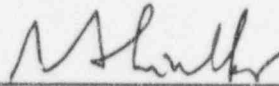
J.G.M. Andersen
Y.K. Cheung
C.L. Heck
L.A. Klebanov
J.C. Shaug
B.S. Shiralkar
W.R. Usry

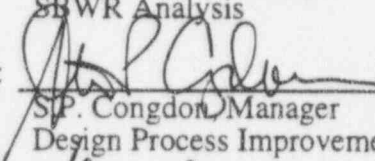
9604220047 960329
PDR ADDCK 05200004
A PDR

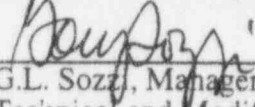


Licensing Topical Report
TRACG Model Description

J.G.M. Andersen
Y.K. Cheung
C.L. Heck
L.A. Klebanov
J.C. Shaug
B.S. Shiralkar
W.R. Usry

Approved: 
B.S. Shiralkar, Manager
SBWR Analysis

Approved: 
S.P. Congdon, Manager
Design Process Improvement

Approved: 
G.L. Sozzi, Manager
Technical and Modifications Services

Legal Notice

This document was prepared by the General Electric Company (GE). No other use, direct or indirect, of the document or the information it contains is authorized; and with respect to any unauthorized use, neither GE nor any of the contributors to this document makes any representation or warranty (express or implied) as to the completeness, accuracy, or usefulness of the information contained in this document or that such use of such information may not infringe privately owned rights; nor do they assume any responsibility for liability or damage of any kind which may result from such use of such information. Furnishing this document does not convey any license, express or implied, to use any patented invention or any information of GE disclosed herein, or any rights to publish or make copies of the document without prior written permission of GE.

Bars in left-hand margin denote substantive changes to this version from the previous revision; for example, where the only change is the number of an equation, that change has not been highlighted.

Acknowledgments

TRACG is the result of the technical contributions from many individuals and organizations. At the General Electric Company (GE), significant contributions to the development of TRACG have been made by M. M. Aburomia, Md. Alamgir, K. H. Chu, J. R. Fitch, and V. Parameswaran. The advice and careful review from G.E. Dix is highly appreciated. Also, J. E. Wood has provided valuable counsel.

The contributions to the TRACG development from H. Uematsu of Toshiba and Y. Fukasawa of Hitachi are acknowledged.

Earlier versions of this code were developed as a result of a technical collaboration between Idaho National Engineering Laboratory (INEL) and GE. Substantial contributions to the models have been made by M. M. Giles, S. Z. Rouhani, R. W. Shumway, G. L. Singer, J. W. Spore, D. A. Taylor and W. L. Weaver of INEL. The joint development was sponsored by GE, the Nuclear Regulatory Commission (NRC) and the Electric Power Research Institute (EPRI). The project leadership of W. D. Beckner of the NRC and M. Merilo and P. Kalra of EPRI is also acknowledged.

TRACG, like earlier BWR versions of TRAC, has inherited many features from TRAC-PIA developed at the Los Alamos National Laboratory. The contribution of the basic TRAC framework, as well as useful consultations obtained from members of the Safety Code Development Group at LANL, are gratefully appreciated.

Contents

Section

1.0 Introduction

- 1.1 Scope and Capabilities
- 1.2 Background
- 1.3 Enhancements in Revision 1
- 1.4 References

2.0 Modular Structure

- 2.1 Component Modules
- 2.2 Component Interfaces
 - 2.2.1 Flow Connections
 - 2.2.2 Heat Transfer Connections
- 2.3 Control System

3.0 Thermal-Hydraulic Model

- 3.1 Field Equations
 - 3.1.1 Nomenclature
 - 3.1.2 Model Formulation and Assumptions
 - 3.1.3 Noncondensable Gas
 - 3.1.4 Liquid Solute
 - 3.1.5 One-Dimensional Field Equations
- 3.2 Finite Difference Formulation
 - 3.2.1 One-Dimensional Finite Difference Formulation
 - 3.2.2 Three-Dimensional Finite Difference Formulation
- 3.3 Modifications to Momentum Equations
 - 3.3.1 Critical Flow
 - 3.3.2 Counter-Current Flow Limitation
 - 3.3.3 Stratified Horizontal Flow
- 3.4 References

4.0 Heat Conduction Model

- 4.1 Governing Equation for Heat Conduction in Solid Materials
 - 4.1.1 Lumped Slab Formulation of the Heat Conduction Model
 - 4.1.2 One-Dimensional Formulation of the Heat Conduction Model
- 4.2 Finite Difference Formulation of Heat Conduction Equation
 - 4.2.1 Lumped Slab Heat Conduction
 - 4.2.2 One-Dimensional Heat Conduction in Cartesian Coordinates
 - 4.2.3 One-Dimensional Heat Conduction in Cylindrical Coordinates

Contents (Continued)

Section

- 4.3 References
- 5.0 Flow Regime Map**
 - 5.1 Basis for Flow Regime Map in TRACG
 - 5.1.1 Churn to Annular Transition
 - 5.1.2 Entrainment
 - 5.1.3 Horizontal Flow
 - 5.2 Assessment and BWR Applicability
 - 5.3 References
- 6.0 Models and Correlations**
 - 6.1 Interfacial Shear
 - 6.1.1 Background
 - 6.1.2 Relation to Drift Flux Parameters
 - 6.1.3 Bubbly/Churn Flow
 - 6.1.4 Annular Flow
 - 6.1.5 Droplet Flow
 - 6.1.6 Annular/Droplet Flow
 - 6.1.7 Modifications to Interfacial Shear
 - 6.1.8 Assessment and Applicability to BWR
 - 6.1.9 References
 - 6.2 Wall Friction and Form Losses
 - 6.2.1 Wall Friction
 - 6.2.2 Form Losses at Abrupt Expansions and Contractions
 - 6.2.3 Assessment and Applicability to BWR
 - 6.2.4 References
 - 6.3 Critical Flow
 - 6.3.1 Technical Basis and Assumptions
 - 6.3.2 Implementation Details
 - 6.3.3 Calculation of Local Sonic Velocity
 - 6.3.4 Determination of Choked Flow Phasic Velocities
 - 6.3.5 Applicability
 - 6.3.6 Assessment and Applicability to BWR
 - 6.3.7 References
 - 6.4 Two-Phase Level Model
 - 6.4.1 Level Detection
 - 6.4.2 Calculation of Level Parameters

Contents (Continued)

Section

- 6.4.3 Model As Coded
- 6.4.4 Applicability
- 6.4.5 Assessment
- 6.4.6 References
- 6.5 Interfacial Heat Transfer
 - 6.5.1 Background
 - 6.5.2 Interfacial Area
 - 6.5.3 Bubbly/Churn Flow
 - 6.5.4 Annular Flow
 - 6.5.5 Droplet Flow
 - 6.5.6 Annular/Droplet Flow
 - 6.5.7 Transition to Annular Flow
 - 6.5.8 Free Surface in Vertical Pipes or 3D Cells
 - 6.5.9 Horizontal Stratified Flow in a Pipe
 - 6.5.10 Upper and Lower Limits for the Interfacial Heat Transfer
 - 6.5.11 Assessment and Application to BWR
 - 6.5.12 References
- 6.6 Wall Heat Transfer
 - 6.6.1 Background
 - 6.6.2 Heat Transfer Selection Logic
 - 6.6.3 Single-Phase Convection to Liquid
 - 6.6.4 Subcooled and Nucleate Boiling
 - 6.6.5 Single-Phase Convection to Vapor
 - 6.6.6 Boiling Transition Criteria
 - 6.6.7 Minimum Stable Film Boiling Temperature
 - 6.6.8 Transition Boiling
 - 6.6.9 Film Boiling - Low Void Fraction
 - 6.6.10 Film Boiling - High Void Fraction
 - 6.6.11 Condensation Heat Transfer in the Presence of Noncondensable Gases
 - 6.6.12 Thermal Radiation
 - 6.6.13 Quenching Heat Transfer
 - 6.6.14 Metal-Water Reaction
 - 6.6.15 Assessment and Application to BWR
 - 6.6.16 References
- 6.7 Turbulent and Molecular Mixing Models
 - 6.7.1 Technical Basis and Assumptions
 - 6.7.2 Applicability
 - 6.7.3 References

Contents (Continued)

Section

- 7.0 Component Models**
- 7.1 Pipe
- 7.2 Pump
 - 7.2.1 Pump Governing Equations
 - 7.2.2 Pump Head and Torque Homologous Curves
 - 7.2.3 References
- 7.3 Valve
- 7.4 Tee
- 7.5 Fuel Channel
 - 7.5.1 Leakage Flows
 - 7.5.2 Fuel Pellet Gap Conductance
 - 7.5.3 Cladding Perforation
 - 7.5.4 Thermal Radiation Heat Transfer
 - 7.5.5 Critical Power
 - 7.5.6 Upper Bound Temperature Estimate
 - 7.5.7 Water Rod Model
 - 7.5.8 References
- 7.6 Jet Pump
 - 7.6.1 Jet Pump Momentum Source
 - 7.6.2 Jet Pump Form Loss Coefficients
 - 7.6.3 Applicability
 - 7.6.4 Assessment
 - 7.6.5 References
- 7.7 Steam Separator
 - 7.7.1 Technical Basis and Assumptions
 - 7.7.2 Model Formulations
 - 7.7.3 Carryunder and Carryover
 - 7.7.4 Assessment
 - 7.7.5 References
- 7.8. Vessel
 - 7.8.1 Steam Dryer
 - 7.8.2 Upper Plenum Model
 - 7.8.3 References
- 7.9 Heat Exchanger
 - 7.9.1 Model Assumptions
 - 7.9.2 Heat Transfer Correlations
 - 7.9.3 References

Contents (Continued)

Section

- 7.10 Boundary Conditions
 - 7.10.1 Velocity Specified Boundary Conditions
 - 7.10.2 Pressure Specified Boundary Conditions
- 7.11 Containment Components
 - 7.11.1 Drywell
 - 7.11.2 Wetwell
 - 7.11.3 GDCS Pools
 - 7.11.4 Isolation Condenser (IC)/Passive Containment Condenser (PCC) Pools
 - 7.11.5 PCC/IC Units
 - 7.11.6 Depressurization Valves
 - 7.11.7 Safety/Relief Valves (SRVs) and Quenchers
 - 7.11.8 Horizontal Vent System
 - 7.11.9 GDCS Equalizing Lines
 - 7.11.10 Vacuum Breakers
 - 7.11.11 Break
- 8.0 Numerical Method**
 - 8.1 Finite Difference Formulation of Heat Conduction Equation
 - 8.1.1 Lumped Slab Heat Conduction
 - 8.1.2 One-Dimensional Heat Conduction in Cartesian Coordinates
 - 8.1.3 One-Dimensional Heat Conduction in Cylindrical Coordinates
 - 8.2 Discretization of Hydraulic Equations
 - 8.2.1 Predictor Step
 - 8.2.2 Network Solution
 - 8.2.3 Corrector Step
 - 8.2.4 Time Step Control
 - 8.3 References
- 9.0 Three-Dimensional Neutron Kinetics Model**
 - 9.1 Model Formulation and Assumptions
 - 9.2 Nuclear Parameters
 - 9.3 Decay Heat Model
 - 9.4 Thermal-Hydraulic Interface and Implementation
 - 9.5 Solution Procedure
 - 9.6 References

Contents (Continued)

Section

- 10.0 Control System
- 10.1 Control Blocks
- 10.2 Control System Interfaces
- 10.3 Control System Solution Procedure

Appendices

- A Differences Between TRACG and TRAC-BF1
- B Thermodynamic and Transport Fluid Properties
- C Material Properties
- D Derivation of the Isentropic Sound Speed as a Function of Pressure and Temperature for a Single-Component, Single-Phase Substance
- E Derivation of the Two-Phase, Two-Component HEM Sonic Velocity

Illustrations

Figure

- 2.0-1 Simulation of a BWR/6
- 3.2-1 Staggered Grid Variables
- 3.2-2 Cylindrical Coordinate System with Staggered Grid
- 3.3-1 Void Gradient Gravity Head
- 4.2-1 One-Dimensional Wall Geometry in Cartesian Coordinates
- 4.2-2 One-Dimensional Wall Geometry in Cylindrical Coordinates
- 4.2-3 One-Dimensional Fuel Rod Geometry
- 5.1-1 Flow Regime Map
- 5.1-2 Flow Regime Map
- 6.1-1 Right-Hand Side of Vapor Momentum Equation
- 6.1-2 Drift Flux Correlation and CCFL
- 6.3-1 Choking Cell Configuration
- 6.4-1 Two-Phase Level with Normal Void Profile
- 6.5-1 Sparrow-Uchida Degradation Factor
- 6.6-1 Boiling Curve
- 6.6-2 Selection Logic for Wall Heat Transfer Coefficient
- 6.6-3 Dittus-Boelter Correlation Plotted Along with Data for Forced, Turbulent Convection in Tubes
- 6.6-4 Fishenden and Saunders Correlation (Equation. 6.6-4) Plotted Against Natural Convection Data for Vertical Surfaces
- 6.6-5 Heat Transfer Coefficients Predicted by Three Pool Boiling Correlations vs. Wall Superheat
- 6.6-12 Comparison of Modified Bromley with Data During Reflood Test
- 6.6-13 Peak Cladding Temperature for a BWR Fuel Element
- 6.6-14 "Radiation Only" Experiment
- 6.6-16 Heat Transfer Coefficients Predicted by K-S-P and Vierow-Schlrock Correlations versus Vierow's Experimental Data
- 6.6-17 Comparison of the V-S and K-S-P Predictions of Heat Transfer Degradation Due to the Presence of Air
- 6.6-20 Radiation Heat Transfer at a Surface
- 7.1-1 PIPE Noding Diagram
- 7.2-1 PUMP Noding
- 7.2-2 Single-Phase Homologous Head
- 7.2-3 Fully Degraded Homologous Head Curves
- 7.2-4 Head Degradation Multiplier
- 7.2-5 Single-Phase Homologous Torque Curves
- 7.2-6 Fully Degraded Homologous Torque Curves
- 7.2-7 Torque Degradation Multiplier

Illustrations (Continued)

Figure

- 7.3-1 VLVE Noding Diagram
- 7.4-1 TEE Noding Diagram
- 7.4-2 Sample Noding Scheme for Tee Component
- 7.5-1 Channel Noding Diagram
- 7.5-2 Simplified Reactor Nodalization Showing CHAN Components
- 7.5-3 Leakage Flow Paths
- 7.6-1 Jet Pump Nodalization
- 7.6-2 Simple Noding Scheme for Jet Pump Component
- 7.6-3 Jet Pump Flow Regimes
- 7.7-1 Typical Types of Steam Separators
- 7.7-2 Schematic of the Separator Model
- 7.8-1 Boundaries of a Three-Dimensional Mesh Cell
- 7.8-4 Sample Geometry for Double-Sided Heat Slab
- 7.8-5 Dryer Efficiency Summary
- 7.9-1 Model of Feedwater Heater Using a HEAT Component (modified TEE) and PIPE Component for the Tube Bank
- 7.10-1 FILL Noding Diagram
- 7.10-2 BREK Noding Diagram
- 7.11-1 SBWR Containment
- 7.11-4 Horizontal Vent Component
- 7.11-5 Pressure Suppression Test Facility
- 8.2-1 Junction of 1-D Components
- 8.2-2 Junction of 1-D and 3-D Components
- 9.0-1 X-Y-Z View of the Core
- 9.0-2 Node and Mesh Arrangement for a Given Bundle
- 9.4-1 Data Transfer Between TRACG Models
- 10.1-1 Schematic Control Block Diagram
- 10.2-1 Simplified BWR Pressure Control System

Tables

Table

- 1.3-1 NUREG-1230 Requirements
- 6.3-1 Equilibrium Critical Flow Regimes
- 6.3-2 Input Call Parameters to CHOKER Subroutine
- 6.3-3 Outputs from Subroutine CHOKER
- 6.3-4 Summary of TRACG Choking Correlations and Throat Conditions
- 6.6-1 Selection Logic for Wall Heat Transfer
- 6.6-2 Range of Conditions for Data Used in Testing Correlations
- 6.6-3 Comparison of Correlations
- 6.6-5 Biasi Correlation Compared to Chalk River Data Bank
- 7.2-1 Definitions of the Four Curve Segments that Describe the Homologous Pump Curves
- 7.3-1 Control Options for VLVE
- 7.6-1 Mixing Losses
- 7.6-2 Nozzle Losses
- 7.7-1 Summary of Parameters Used in the Separator Model
- 8.2-1 Energy Error for PSTF Vessel Blowdown 5801-15
- 10.1-1 Description of Control Block Operations
- 10.2-1 Control System Input/Output Variables

Abstract

This document provides a description of the models in TRACG. TRACG is a computer code for the prediction of boiling water reactor transients ranging from simple operational transients to design basis loss-of-coolant accidents, stability and anticipated transients without scram. TRACG incorporates a two-fluid thermal-hydraulic model for the reactor vessel, the primary coolant system and the containment and a three-dimensional kinetics model for the reactor core. The physical models and the numerical scheme are described in this report. The basic conservation equations and their solution are detailed, and the models needed for the closure relationships are developed.

Revision 1 is also intended to serve as a Models and Correlations Report for TRACG. It expands the description of the individual models and correlations utilized in the code. The technical basis and assumptions, implementation details and range of applicability are discussed for each correlation.

1.0 Introduction

TRACG is a General Electric (GE) proprietary version of the Transient Reactor Analysis Code (TRAC) [1-1,1-2]. It is a best-estimate code for analysis of boiling water reactor (BWR) transients ranging from simple operational transients to design basis loss-of-coolant accidents (LOCAs), stability and anticipated transients without scram (ATWS).

1.1 Scope and Capabilities

TRACG is based on a multi-dimensional two-fluid model for the reactor and containment thermal hydraulics and a three-dimensional neutron kinetics model for the reactor core.

The two-fluid model used for the thermal hydraulics in TRACG is fundamentally the same as the basic two-fluid model in TRAC-PF1 [1-2] and TRAC-BF1 [1-1]. The two-fluid model solves the conservation equations for mass, momentum and energy for the gas and the liquid phases. TRACG does not include any assumptions about thermal or mechanical equilibrium between the phases. The gas phase may consist of a mixture of steam and noncondensable gases, and the liquid phase may contain dissolved boron. The thermal-hydraulic model is a multi-dimensional formulation for the vessel component and a one-dimensional formulation for all other components.

The conservation equations for mass, momentum and energy are closed through an extensive set of basic models consisting of constitutive correlations for shear and heat transfer at the gas/liquid interface as well as at the wall. The constitutive correlations are flow regime dependent, and are determined based on a single flow regime map, which is used consistently throughout the code.

In addition to the basic thermal-hydraulic models, TRACG also contains a set of component models for BWR components, such as recirculation pumps, jet pumps, fuel channels, steam separators and dryers. TRACG, furthermore, contains a control system model capable of simulating the major BWR control systems such as the pressure, level and recirculation flow control systems.

The three-dimensional kinetics model is consistent with the GE BWR core simulator PANACEA [1-3]. It solves a modified one-group diffusion model with six delayed neutron precursor groups. Feedback is provided from the thermal-hydraulic model for moderator density, fuel temperature, boron concentration and control rod position.

The TRACG structure is based on a modular approach. The TRACG thermal-hydraulic model contains a set of basic components, such as pipe, pump, valve, tee, channel, jet pump, steam separator, heat exchanger and vessel components. System simulations are constructed using these components as building blocks. Any number of these components may be combined. The number of components, their interaction, as well as the detail in each component, are

specified through code input. TRACG consequently has the capability to simulate a wide range of facilities, ranging from simple separate effects tests to complete BWR plants.

TRACG has been extensively qualified against separate effects tests, component performance data, integral system effects tests and full-scale BWR plant data. Separate qualification for the basic models against separate effects tests and component qualification against BWR component performance data are included in this report. The purpose of this qualification is to demonstrate the applicability of the basic models in TRACG and to quantify the model uncertainty.

1.2 Background

TRAC was originally developed for pressurized water reactor (PWR) analysis by Los Alamos National Laboratory (LANL), the first PWR version of TRAC being TRAC-PIA [1-4]. The development of a BWR version of TRAC started in 1979 in close cooperation between GE and Idaho National Engineering Laboratory. The objective of this cooperation was the development of a version of TRAC capable of simulating BWR LOCAs. The main tasks consisted of improving the basic models in TRAC for BWR applications and in developing models for the specific BWR components. This work culminated in the mid eighties with the development of TRACB04 at GE [1-6-1-12] and TRAC-BD1/MOD1 at INEL [1-5], which were the first major versions of TRAC having BWR LOCA capability. Due to the joint development effort, these versions were very similar, having virtually identical basic and component models. The GE contributions were jointly funded by GE, the Nuclear Regulatory Commission (NRC) and Electric Power Research Institute (EPRI) under the REFILL/REFLOOD and FIST programs.

The development of the BWR version has continued at GE since 1985. The objective of this development was to upgrade the capabilities of the code to include transient, stability and ATWS applications. During this phase, major developments included the implementation of the three-dimensional kinetics model and an implicit integration scheme into TRAC. The containment simulation was included for simplified boiling water reactor (SBWR) applications, and the simulation of the BWR fuel bundle was also improved. TRACG was the end result of this development.

This document is intended to be a complete, stand-alone description of TRACG. Because of their common ancestry, a number of sections are similar to those for other versions of TRAC, notably TRAC-BF1. Major differences between TRACG and TRAC-BF1 are discussed in Appendix A.

1.3 Enhancements in Revision 1

Revision 1 of this report has been expanded to provide additional details on the models and correlations. It is also intended to serve the purpose of a Models and Correlations Report as defined in the Compendium of ECCS Research for Realistic LOCA Analysis, NUREG-1230 [1-15]. This documentation supports the Code Scaling, Applicability and Uncertainty

Methodology [1-16] used for the application of best-estimate computer codes. According to NUREG-1230, the objectives of the documentation on the models and correlations are to:

- Provide detailed information on (the quality of) the closure equations (i.e., on correlation models and/or criteria used in the code).
- Describe how these closure equations are coded in the program and (to) assure that what is coded is indeed what the code uses.
- Provide a technical rationale and justification for using these closure relations in the range of interest to nuclear power plant (NPP) safety evaluations.

These objectives are to be met by providing the following information on each model/correlation:

- (1) The original correlation:
 - (a) Source or reference
 - (b) Database
 - (c) Accuracy
 - (d) Applicability to NPP conditions
- (2) Assessment of effects if the model/correlation is applied outside its database.
- (3) Implementation of the model/correlation in the code.
- (4) Description of modifications required to overcome computational difficulties.
- (5) Assessment of effects of implementation and/or modification on code overall applicability and accuracy.

Table 1.3-1 shows where these requirements have been addressed in the subsections of Sections 6 and 7. It is not practical to address the assessment of the code in detail in the Model Report. For this purpose, the TRACG Qualification Report has been frequently referenced.

Revision 1 also includes new models that have been added. These are:

- Capability for multiple noncondensable gas species (Section 3.1). Previously only one gas could be treated in addition to steam.
- A correlation (Forster-Zuber) for pool boiling (Section 6.6.4).
- The Kuhn-Schrock-Peterson correlation for condensation in the presence of noncondensibles (Section 6.6.11).

- The Uchida correlation as an option for condensation heat transfer from walls in the presence of noncondensibles (Section 6.6.11).
- An interpolation method for the calculation of the degradation factor for heat transfer to different species of noncondensable gases (Section 6.6.11).

These models were implemented after the release of the TRACG Qualification Report [1-13]. However, these models only affect the calculation of condensation heat transfer in the presence of noncondensibles, the distribution of noncondensable species in the drywell and the heat transfer in the condenser pools. Thus, none of the results, with the possible exception of the GIRAFFE test facility analysis, should be affected.

1.4 References

- 1-1 J.A. Borkowski, et. al., *TRAC-BF1/MOD1: An Advanced Best-Estimate Program for BWR Accident Analysis*, NUREG/CR-4356, Idaho National Engineering Laboratory, August 1992.
- 1-2 *TRAC-PF1/MOD2*, NUREG/CR-5673, Los Alamos National Laboratory.
- 1-3 *Steady-State Nuclear Methods*, NEDE-30130PA, April 1985.
- 1-4 R.J. Pryor, et. al., *TRAC-PIA, An Advanced Best-Estimate Computer Program for PWR LOCA Analysis*, Los Alamos Scientific Laboratory, NUREG/CRA-0665, May 1979.
- 1-5 D.D. Taylor, et. al., *TRAC-BD1/MOD1: An Advanced Best-Estimate Program for Boiling Water Reactor Transient Analysis*, Volumes 1-4, NUREG/CR-3633, Idaho National Engineering Laboratory, April 1984.
- 1-6 J.G.M. Andersen, K.H. Chu, and J.C. Shaug, *BWR REFILL/REFLOOD Program Task 4.7 - Model Development, Basic Models for the BWR Version of TRAC*, GEAP-22051, NUREG/CR-2573, EPRI NP-2375, April 1983.
- 1-7 Y.K. Cheung, V. Parameswaran, and J.C. Shaug, *BWR REFILL/REFLOOD Program Task 4.7 - Model Development, TRAC-BWR Component Models*, GEAP-22052, NUREG/CR-2574, EPRI NP-2376, April 1983.
- 1-8 Md. Alamgir, et. al., *BWR REFILL/REFLOOD Program Task 4.8 - TRAC-BWR Model Qualification for BWR Safety Analysis, Final Report*, GEAP-30157, NUREG/CR-2571, EPRI NP-2377, October 1983.
- 1-9 J.G.M. Andersen, and C.L. Heck, *BWR Full Integral Simulation Test (FIST) Program, TRAC-BWR Model Development, Volume 1 - Numerical Methods*, GEAP-30875-1, NUREG/CR-4127-1, EPRI NP-3987-1, November 1985.

- 1-10 K.H. Chu, J.G.M. Andersen, Y.K. Cheung, and J.C. Shaug, *BWR Full Integral Simulation Test (FIST) Program, TRAC-BWR Model Development, Volume 2 - Models*, GEAP-30875-2, NUREG/CR-4127-2, EPRI NP-3987-2, October 1985.
- 1-11 Y.K. Cheung, J.G.M. Andersen, K.H. Chu, and J.C. Shaug, *BWR Full Integral Simulation Test (FIST) Program, TRAC-BWR Model Development Volume 3 - Developmental Assessment for Plant Application*, GEAP-30875-3, NUREG/CR-4127-3, EPRI NP-3987-3, October 1985.
- 1-12 W.A. Sutherland, Md. Alamgir, J.A. Findlay, and W.S. Hwang, *BWR Full Integral Simulation Test (FIST) Program, Phase II Test Results and TRAC-BWR Model Qualification*, GEAP-30876, NUREG/CR-4128, EPRI NP-3988, October 1985.
- 1-15 *Compendium of ECCS Research for Realistic LOCA Analysis*, NUREG-1230, August 1988.
- 1-16 *Quantifying Reactor Safety Margins*, NUREG/CR/5249, December 1989.

Table 1.3-1
NUREG-1230 Requirements

Requirement	TRACG Section
1. The original correlation: a. Source or reference b. Database c. Accuracy	Technical Basis and Assumptions
d. Applicability to NPP conditions	Applicability
3. Implementation of the model/correlation in the code. 4. Description of modifications required to overcome computational difficulties.	Implementation
2. Assessment of effects if the model/correlation is applied outside its database. 5. Assessment of effects of implementation and/or modification on code overall applicability and accuracy.	Assessment

2.0 Modular Structure

TRACG has a modular structure and flexible geometry capability. It contains a set of basic thermal-hydraulic components, such as vessel, channel, pipe and tee components. These components are then used as building blocks to construct the system simulation. An example is shown in Figure 2.0-1, where a BWR/6 reactor vessel is simulated with the TRACG components. The components can be connected through flow paths or heat transfer paths. The components are described in detail in Section 7.

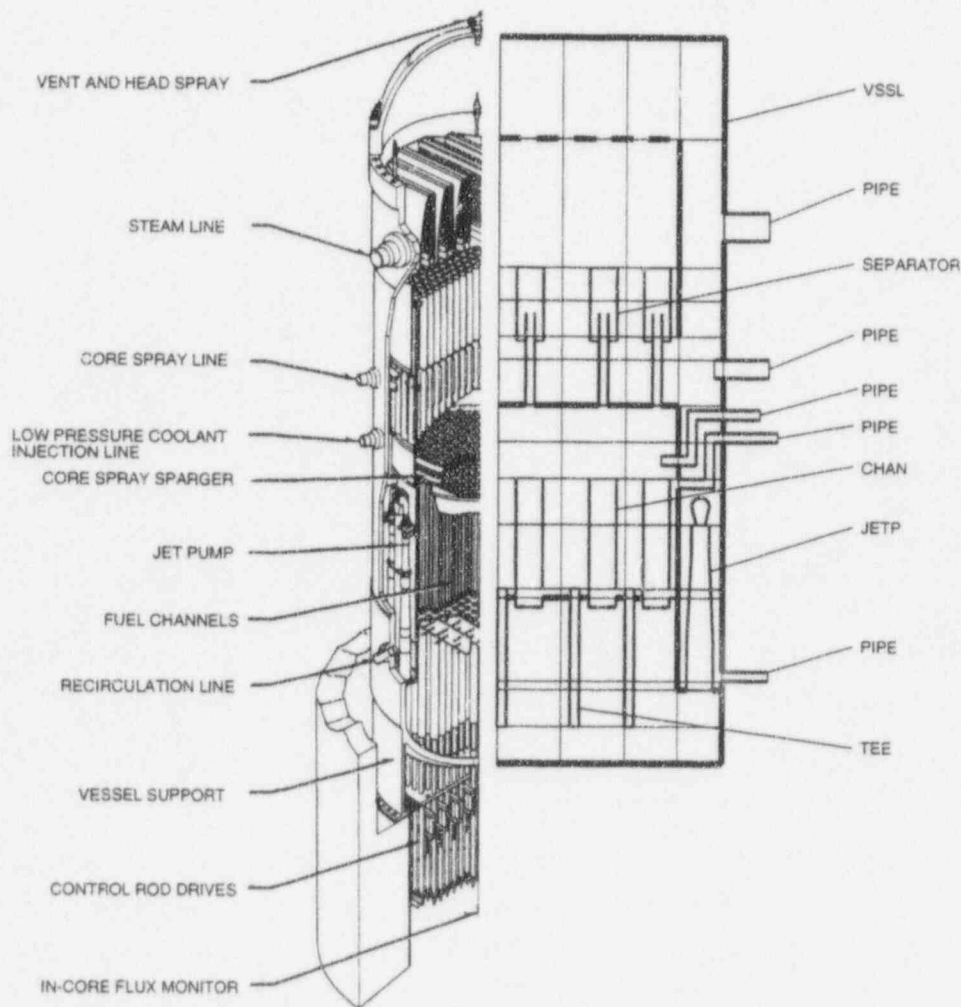


Figure 2.0-1. Simulation of a BWR/6

TRACG also contains a modular control system consisting of a set of control blocks. These control blocks can be connected either to each other or to thermal-hydraulic components to form complex control systems such as a BWR water level control system. The control system is described in detail in Section 10.

2.1 Component Modules

TRACG contains the following thermal-hydraulic components:

PIPE The pipe (PIPE) component is the simplest component in TRACG. It contains a one-dimensional hydraulic model for the fluid flow in the pipe and a one-dimensional model for the radial heat conduction in the pipe wall. The number of hydraulic cells for the fluid flow and radial nodes for the wall heat transfer are specified through input.

PUMP The pump (PUMP) component is similar to the pipe component, except that a model for a pump is included at one of the cell boundaries in the component. The pump model calculates the pump speed and the hydraulic head imposed by the pump on the fluid.

VLVE The valve (VLVE) component is similar to the pipe component, except that the flow area of one of the cell boundaries can be varied to simulate the opening and closing of a valve.

TEE The tee (TEE) component consists of two pipe components that are connected together to form a TEE or a WYE.

The separator is an option to the tee component. The primary branch simulates the standpipe and the separating barrel in a BWR steam separator, and the secondary branch simulates the liquid discharge path. When the separator option is activated, special models are included to simulate the separation of the steam and liquid in the component.

JETP The jet pump (JETP) component is similar to the tee component, except that special models for the interaction and mixing of the drive and suction flows are included.

CHAN The channel (CHAN) component is based on a tee component and includes simulation of the fuel rods. The primary branch represents the active channel, and the fuel rods are included there. The secondary branch simulates the leakage flow path from the bottom of a BWR fuel channel. An optional internal branch can be specified to simulate water rods within the channel. A one-dimensional model is included for the radial heat transfer in the fuel rods. Special models are included for the power generation and the heat transfer in the channel component.

HEAT The heat exchanger (HEAT) is a composite component. It is based on a tee component, which represents the primary side of a heat exchanger. The secondary

side of the heat exchanger is simulated by a pipe component. Special models are included for the heat transfer between the primary and secondary sides of the heat exchanger. The heat exchanger component is provided to simplify input generation. A heat exchanger can be constructed using the heat transfer connection between cells of an input defined primary and secondary side simulation.

VSSL. The vessel (VSSL) component is the only multi-dimensional component in TRACG. It can be nodalized in two dimensions using cartesian coordinates and in two or three dimensions using cylindrical coordinates. A multi-dimensional version of the hydraulic model is used for the fluid flow in the vessel component. Heat slabs simulating the structures can be included at several locations in the vessel component. A lumped heat slab can be included in every vessel cell and a one-dimensional heat slab can be included at the boundary between two vessel cells either in the axial or radial direction.

All the components in TRACG utilize the same basic models. There is a common one-dimensional hydraulic model used by all the one-dimensional components. The multi-dimensional hydraulic model is used by the vessel component only, and it is identical to the one-dimensional model, when reduced to one dimension. One common heat conduction model is used by all the one-dimensional components for the wall heat transfer and by the vessel component for the radial heat slabs. The one-dimensional heat conduction model used by the vessel component for the axial heat slabs is similar except for the discretization. Finally, there is only one set of constitutive correlations for shear and heat transfer in TRACG, and it is used by all the components.

2.2 Component Interfaces

TRACG components can interface with each other either through fluid flow or through heat transfer between components.

2.2.1 Flow Connections

One-dimensional components can be connected to each other at their junctions by specifying the same junction number for two components. A typical example of this is the recirculation line for a BWR, which can be simulated by combining pipe, pump, valve and jet pump components.

One-dimensional components can be connected to any cell in the three-dimensional vessel component by specifying a corresponding junction number for the one-dimensional component and source number for the vessel component. A typical example is the channel component in Figure 2.0-1, which is connected to the lower and upper plena in the vessel through the channel inlet and outlet junctions, and to the bypass region of the vessel through the leakage junction. Multiple source connections can be made to a single vessel cell.

2.2.2 Heat Transfer Connections

The walls of a one-dimensional component can communicate with the fluid in any other component through heat transfer. A typical example of this feature is the channel component in Figure 2.0-1, where there is heat transfer from the outside of the channel wall to the fluid in the bypass region of the vessel component. Another example is a heat exchanger, where the primary and secondary sides can be modelled by tee and pipe components which are connected through heat transfer.

2.3 Control System

TRACG has a modular control system in addition to the modular components. TRACG has a large number of control blocks, which perform elementary functions such as adding two signals. A control block has up to three inputs and one output signal. The input to a control block can be an output from another control block or a parameter from one of the TRACG components. An example of the latter is the water level position in a BWR vessel, which is an input to the water level control system. The output from a control block can go to another control block or to a TRACG component. An example of the latter is the control of the flow control valve position in a BWR/6.

3.0 Thermal-Hydraulic Model

The main purpose of the TRACG code is to solve a coupled set of field equations describing the thermal-hydraulic behavior of the fluid coolants in the BWR system, the flow of energy in the fuel and the structural components of the reactor, and the generation of the nuclear power in the reactor core.

The following subsections describe the fluid field equations. The field equations for structures are described in Section 4 and for the neutron kinetics in Section 9.

3.1 Field Equations

TRACG, like TRAC-PF1/MOD1 [3-1] and TRAC-BF1/MOD1 [3-2], uses a two-phase two-fluid model for fluid flow in both the one-dimensional (1-D) and three-dimensional (3-D) components. Kocamustafaogullari [3-3], Ishii [3-4], and Delhayé [3-5] have provided detailed derivations of the equations similar to those used in TRAC, and a more concise derivation related to the TRAC equations is available in a report by Addessio [3-6]. The fact that this model is formally ill-posed was the subject of considerable debate several years ago and is discussed by Stewart and Wendroff [3-7]. However, our experience has always been that this is a moot point, since the numerical solution procedures effectively introduce minor modifications to the field equations, making them well-posed. A paper by Stewart [3-8] confirms these observations and demonstrates clearly that, with normal models for interfacial drag and reasonable finite-difference nodalizations, the problem solved numerically is well-posed.

3.1.1 Nomenclature

Before presenting the fluid field equations, we need to define certain terminology. In our nomenclature, the term *gas* implies a general mixture of steam and noncondensable gases. The subscript *v* will denote a property or parameter applying to the gas mixture; the subscript *s* indicates a quantity applying specifically to steam and the subscript *a* formerly used for air now signifies the summation of all noncondensable gases. The term *liquid* implies pure liquid water, and the subscript *ℓ* denotes a quantity applying specifically to liquid water. For convenience, we define the following terms that will be used in the subsequent equations and list them alphabetically with the Greek symbols at the end:

Nomenclature

A	flow area between mesh cells
A_i	interfacial area
B_{mix}	shear term due to turbulence
B_s	source term in momentum equation
c	concentration (boron)
e	internal energy

E_{mix}	mixing term in energy equation
E_s	source term in energy equation
F_w	wall shear
f	interfacial shear
g	acceleration of gravity
h	heat transfer coefficient
h	internal enthalpy
h_{fg}	$h_g - h_f$
j	volumetric flux
K	Kutateladze constant in CCFL correlation
k	constant in virtual mass term in momentum equation
m	constant in CCFL correlation
M_{mix}	mixing term in continuity equation
M_s	source term in mass equation
P	pressure
q	heat transfer rate
R	gas constant
R	radial dimension for 3-D components
T	temperature
t	time
V	cell volume
v	velocity
x	dimension for 1-D component
z	axial dimension for 3-D components

Greek Symbols

α	gas volume fraction
Γ_g	interfacial mass transfer rate ($\Gamma_g = \Gamma_{vi}$)
ρ	microscopic density
σ	surface tension
τ	shear tensor
θ	azimuthal dimension for 3-D components

Subscript

a	all noncondensable gases
b	boron

c	continuous phase
crit	critical velocity
d	dispersed phase
f	saturated liquid
g	saturated steam
i	interface
ℓ	liquid phase
n	noncondensable gas
r	relative (vapor-liquid)
s	steam
sat	saturation
v	gas phase (mixture)
w	wall

Superscript

d	donor celled
n	time step number

In the discussion of the finite-difference equations, all quantities except for the velocities are centered in the hydrodynamic cell (cell-centered), and the velocities are cell-edge quantities.

3.1.2 Model Formulation and Assumptions

The basic two-phase, two-fluid model consists of the volume and time averaged conservation equations for mass, momentum and energy for each phase as given by Stuhmiller [3-9]:

Gas Mass:

$$\frac{\partial}{\partial t} (\alpha \rho_v) = -\nabla \cdot (\alpha \rho_v \bar{v}_v) + \Gamma_{vi} \quad (3.1-1)$$

Liquid Mass:

$$\frac{\partial}{\partial t} ((1 - \alpha) \rho_\ell) = -\nabla \cdot ((1 - \alpha) \rho_\ell \bar{v}_\ell) + \Gamma_{\ell i} \quad (3.1-2)$$

Conservation of mass at the interface require:

$$\Gamma_{vi} + \Gamma_{\ell i} = 0 \quad (3.1-3)$$

Gas Momentum:

$$\frac{\partial}{\partial t} (\alpha \rho_v \bar{v}_v) + \nabla \cdot (\alpha \rho_v \bar{v}_v \bar{v}_v) = -\nabla (\alpha P_v) + \nabla \cdot (\alpha \bar{\tau}_v) + \alpha \rho_v \bar{g} + \bar{M}_v \quad (3.1-4)$$

where the interphase momentum transfer term is given by:

$$\bar{M}_v = \Gamma_{vi} \bar{v}_{vi} + P_{vi} \nabla \alpha - \nabla \alpha \cdot \bar{\tau}_{vi} \quad (3.1-5)$$

Liquid Momentum:

$$\frac{\partial}{\partial t} ((1-\alpha) \rho_\ell \bar{v}_\ell) + \nabla \cdot ((1-\alpha) \rho_\ell \bar{v}_\ell \bar{v}_\ell) = -\nabla ((1-\alpha) P_\ell) + \nabla \cdot ((1-\alpha) \bar{\tau}_\ell) \quad (3.1-6)$$

$$+ (1-\alpha) \rho_\ell \bar{g} + \bar{M}_\ell$$

where:

$$\bar{M}_\ell = \Gamma_{\ell i} \bar{v}_{\ell i} + P_{\ell i} \nabla (1-\alpha) - \nabla (1-\alpha) \cdot \bar{\tau}_{\ell i} \quad (3.1-7)$$

Conservation of momentum at the interface requires:

$$\sum_k \left(\left(P_{ki} + \frac{\Gamma_{ki}^2}{\rho_{ki}} \right) \nabla \alpha_k - \nabla \alpha_k \cdot \bar{\tau}_{ki} \right) = f_\sigma \quad (3.1-8)$$

where k represents the liquid and gas phases, and f_σ is the pressure drop caused by the curvature of the interface.

In TRACG a number of simplifying assumptions have been made for the momentum equations:

- The mass transfer terms have been neglected. This is justifiable as these terms are small compared to the other interfacial forces like the interfacial drag. (For nucleate boiling in a BWR at a power density of 50 kW/l the interfacial force due to mass transfer is $\Gamma_g v_r = \frac{5 \cdot 10^7}{h_{fg}} v_r \approx 10 \text{ kg/m}^2\text{-sec}^2$ using $h_{fg} = 1.5 \cdot 10^6 \text{ J/kg}$ and $v_r = 0.3 \text{ m/sec}$, whereas the interfacial drag balancing the buoyancy is given by $\alpha (1-\alpha) \Delta \rho g \approx 1.6 \cdot 10^3 \text{ kg/m}^2\text{-sec}^2$, using $\alpha = 0.4$ and $P = 7 \text{ MPa}$).
- Uniform pressure has been assumed i.e., $P_v = P_{vi} = P_{\ell i} = P_\ell = P$. This assumption simplifies the equations in the sense that only one pressure needs to be calculated.

The effect of local pressure variations at the interface, however, is lost and must be accounted for in some other way. For dispersed flow e.g., droplet flow, the pressure variation around a droplet is directly related to the relative velocity of the droplet [3-10]. The interfacial force due to the local pressure variations around the droplet can thus be correlated with the relative velocity.

In TRACG two terms have been included; a term that is a function of the relative velocity:

$$\bar{f}_{\ell v} = \bar{f}_{\ell v}(\bar{v}_r)$$

which is the drag term; and a term that is a function of the derivative of the relative velocity:

$$\bar{f}_{VM} = \bar{f}_{VM} \left(\frac{d\bar{v}_r}{dt} \right)$$

which is the virtual mass term.

- The shear tensor is neglected except for shear at the boundaries against solid structures and shear at the interface for separated flow. The shear against the solid boundaries can be accounted for through wall friction terms F_{wv} and $F_{w\ell}$, which can be correlated against the fluid velocity and properties. The shear at the interface for separated flow $f_{\ell v}$ can be correlated against the fluid properties and the relative velocity.
- The pressure difference between the phases due to interphase curvature is neglected. This term has little impact on the fluid properties and does not impact the relative motion of the phases. (For particles with a radius of 10^{-4} m the pressure change across the interface is less than 10^3 Pa for typical BWR conditions.)

With these simplifications, the momentum equations reduce to:

Gas Momentum:

$$\frac{\partial}{\partial t} (\alpha \rho_v \bar{v}_v) + \nabla \cdot (\alpha \rho_v \bar{v}_v \bar{v}_v) = -\alpha \nabla P - \bar{F}_{wv} + \alpha \rho_v \bar{g} - \bar{f}_{\ell v} - \bar{f}_{VM} \quad (3.1-9)$$

This equation can be further simplified by subtracting the gas continuity equation (3.1-1) multiplied by \bar{v}_v . This gives:

$$\alpha \rho_v \frac{\partial \bar{v}_v}{\partial t} + \alpha \rho_v \bar{v}_v \cdot \nabla \bar{v}_v = -\alpha \nabla P - \bar{F}_{wv} + \alpha \rho_v \bar{g} - \bar{f}_{\ell v} - \bar{f}_{VM} \quad (3.1-10)$$

Similarly, the liquid momentum equation can be simplified.

Liquid Momentum:

$$(1 - \alpha)\rho_\ell \frac{\partial \bar{v}_\ell}{\partial t} + (1 - \alpha)\rho_\ell \bar{v}_\ell \cdot \nabla \bar{v}_\ell = -(1 - \alpha)\nabla P - F_{w\ell} + (1 - \alpha)\rho_\ell \bar{g} + f_{\ell v} + f_{VM} \quad (3.1-11)$$

Gas Energy:

$$\frac{\partial}{\partial t} \left(\alpha \rho_v \left(e_v + \frac{v_v^2}{2} \right) \right) + P \frac{\partial \alpha}{\partial t} = -\nabla \cdot \left(\alpha \rho_v \bar{v}_v \left(e_v + \frac{v_v^2}{2} \right) \right) \quad (3.1-12)$$

$$-\nabla \cdot (P\alpha \bar{v}_v) + q_{wv}'' + q_{iv}'' + \Gamma_g h_g$$

Liquid Energy:

$$\frac{\partial}{\partial t} \left((1 - \alpha)\rho_\ell \left(e_\ell + \frac{v_\ell^2}{2} \right) \right) - P \frac{\partial \alpha}{\partial t} = -\nabla \cdot \left((1 - \alpha)\rho_\ell \bar{v}_\ell \left(e_\ell + \frac{v_\ell^2}{2} \right) \right) \quad (3.1-13)$$

$$-\nabla \cdot (P(1 - \alpha)\bar{v}_\ell) + q_{w\ell}'' + q_{i\ell}'' - \Gamma_g h_f$$

In the energy equations similar assumptions have been made:

- Uniform pressure has been assumed i.e., $P_v = P_{vi} = P_{li} = P_\ell = P$.
- The terms associated with the shear tensor have been neglected.
- Conductive heat transfer in the fluid has been neglected except for heat transfer to solid structures which is included as the wall heat transfer terms q_{wv} and $q_{w\ell}$, and heat transfer at the interface q_{iv} and $q_{i\ell}$. Neglecting conductive energy transfer within the fluid is justified as it is much smaller than the convective heat transfer for steam water mixtures.
- Potential energy has been neglected as it is much smaller than the internal and mechanical energies.
- The mechanical energy or kinetic energy has been kept in the equations except for the terms associated with the interfacial mass and energy transfer. The omission of the kinetic energy for the latter term is justified as the relative velocity is much smaller than the fluid velocity for conditions where the kinetic energy is important (Note that except for critical flow, the kinetic energy is insignificant).
- The fluctuating energy term arising from the averaging of the fluctuating velocity has been neglected. Similar to the kinetic energy, this term is small.

An alternative to solving both the phasic mass equations is to solve one phasic mass equation and the total mass equation. The total mass equation is obtained by adding Equation 3.1-1 and Equation 3.1-2:

Total Mass:

$$\frac{\partial}{\partial t} [(1 - \alpha)\rho_\ell + \alpha\rho_v] = -\nabla \cdot [(1 - \alpha)\rho_\ell \bar{v}_\ell + \alpha\rho_v \bar{v}_v] \quad (3.1-14)$$

Solving either Equation 3.1-1 or 3.1-2 together with Equation 3.1-14 is completely equivalent to solving both Equations 3.1-1 and 3.1-2.

Similarly, the total energy equation is obtained by adding Equations 3.1-12 and 3.1-13:

$$\begin{aligned} \frac{\partial}{\partial t} \left(\alpha\rho_v \left(e_v + \frac{v_v^2}{2} \right) + (1 - \alpha)\rho_\ell \left(e_\ell + \frac{v_\ell^2}{2} \right) \right) = & \quad (3.1-15) \\ -\nabla \cdot \left(\alpha\rho_v \bar{v}_v \left(e_v + \frac{v_v^2}{2} \right) + (1 - \alpha)\rho_\ell \bar{v}_\ell \left(e_\ell + \frac{v_\ell^2}{2} \right) \right) \\ -\nabla \cdot (P(\alpha\bar{v}_v + (1 - \alpha)\bar{v}_\ell)) + q_{w\ell}'' + q_{wv}'' \end{aligned}$$

Solving either Equation 3.1-12 or 3.1-13 together with Equation 3.1-15 is completely equivalent to solving both Equations 3.1-12 and 3.1-13.

Closure is obtained for these equations with normal thermodynamic relations, which for water are described in Appendix B, and specifications for the interfacial-drag (f_{iv}), the interfacial heat transfer (q_{iv}'' and $q_{i\ell}''$), the phase-change rate (Γ_g), the wall shear (F_{wv} and $F_{w\ell}$) and the wall heat flows (q_{wv}'' and $q_{w\ell}''$). These equations do not require directly the quasi-steady assumption as long as the correct closure relations for the given transient exist. A real difficulty arises because, depending on how the closure relations were developed, a different set of closure relations may be required for each transient, and each set must comply with the assumptions associated with the definition of the time and volume averaging used in the field equations. However, if a steady- or quasi-steady-state database or a relationship derived from such a database is used to represent a closure relation, the code necessarily applies the quasi-steady assumption. This latter case applies for the closure relations within TRACG. Assessment shows that this is not a major limitation for BWR applications.

The phase-change rate required by the equation set is evaluated from a simple thermal-energy jump relation:

$$\Gamma_g = -\frac{q_{iv}'' + q_{i\ell}''}{h_{fg}} \quad (3.1-16)$$

where

$$q_{iv}'' = \frac{A_i h_{iv} (T_{sat} - T_v)}{V} \quad (3.1-17)$$

and

$$q_{i\ell}'' = \frac{A_i h_{i\ell} (T_{sat} - T_\ell)}{V} \quad (3.1-18)$$

Here, A_i and the h_i terms are the interfacial area and heat transfer coefficients and T_{sat} is the saturation temperature corresponding to the partial steam pressure. Section 6 discusses the closure relationships used to define A_i and h_i .

The wall heat flux is given by Newton's law:

$$q_{wv}'' = \frac{A_w h_{wv} (T_w - T_v)}{V} \quad (3.1-19)$$

and

$$q_{w\ell}'' = \frac{A_w h_{w\ell} (T_w - T_\ell)}{V} \quad (3.1-20)$$

where A_w is the actual heated surface area.

The h_{wv} and $h_{w\ell}$ of the cell include the information regarding the portion of the wall having gas and liquid contact. Section 6.6 discusses the closure relationships used to define h_{wv} and $h_{w\ell}$.

The mass and energy equations are written in fully conservative form to permit the construction of a numerical scheme that rigorously conserves some measure of the system fluid mass and energy. In previous TRAC versions, the kinetic energy was eliminated using the momentum equation. This simplified the energy equation; however, at the same time, the flow work was reduced to a nonconserving form. Consequently, energy was not perfectly conserved and energy balance errors would occur, particularly for high velocity flow as in critical gas flow. In TRACG, this simplification is not made, and the kinetic energy is implemented into the energy equations in a conserving form.

The nonconservative form of the momentum equations permits simpler numerical solution strategies and can generally be justified because the pressure and shear terms preclude a fully conserving form of the momentum equation. The shear tensor was neglected in the momentum and energy equations and shear is only accounted for through the wall and interfacial shear terms in the momentum equations. This is reasonable for most BWR applications as the wall shear is the dominant term due to the large wall surface area and corresponding small hydraulic diameter. The solution to the momentum equations will approximate a porous medium solution for these

regions. Large nodes, where not all cells are in contact with the wall can only exist in the upper plenum and the containment volumes. In these regions viscous shear is insignificant, but turbulent shear will affect the bulk motion and mixing of the fluid. In the TRACG nodalization an average velocity is used for each node boundary. Variations in the velocity and fluid properties, however, will exist across the node boundary either due to velocity profile or turbulent fluctuations. When fluid properties are averaged over the node boundary e.g., the $\alpha\rho v v$ term in the momentum equation, two terms result: $\bar{\alpha} \bar{\rho} \bar{v} \bar{v}$ where \bar{v} is the average velocity and $\overline{\alpha \rho v' v'}$ where v' represents the velocity fluctuations. For one-dimensional flow this latter term is usually accounted for through the wall friction. For multi-dimensional flow the term can be included as a simple mixing term.

Such mixing terms, which are based on Prandtl's mixing length model, have been very successful in modeling the flow and phase distribution with subchannel codes using relatively large computational cells [3-11].

In TRACG a mixing term has been included in the 3-dimensional finite difference equations (Section 3.2.2). The mixing term is described in Section 6.7.

3.1.3 Noncondensable Gas

Multiple noncondensable gases may be included. All noncondensable gases are assumed to be in thermal equilibrium with any steam that is present and to move with the same velocity as the steam (mechanical equilibrium). Hence, only a single field equation is needed to track the noncondensable gas. The noncondensable gas mass equations are solved individually for each gas; however, it is convenient to sum the individual equations to define a single equation that represents the total for all noncondensable gases.

Total Noncondensable Gas Mass:

$$\frac{\partial}{\partial t} (\alpha \rho_a) = - \nabla \cdot (\alpha \rho_a \bar{v}_v) \quad (3.1-21)$$

With this field present, the total gas density and energy are sums of the steam and the noncondensable components.

$$\rho_v = \rho_s + \rho_a = \rho_s + \sum \rho_n \quad (3.1-22)$$

and

$$\rho_v e_v = \rho_s e_s + \rho_a e_a = \rho_s e_s + \sum \rho_n e_n \quad (3.1-23)$$

We assume Dalton's law applies; therefore,

$$P_v = P_s + P_a = P_s + \sum P_n \quad (3.1-24)$$

We assume that the noncondensable gases are ideal gases, so that locally the gas constant for all noncondensibles is given by:

$$R_a = \frac{1}{\rho_a} \sum \rho_n R_n$$

The subscripts *s* and *a* indicate, respectively, the steam and total noncondensable properties. By default, the code applies the thermodynamic properties for air to a single noncondensable gas. However, the code user may select any single noncondensable gas or a combination of multiple noncondensable gases as an alternative.

3.1.4 Liquid Solute

TRACG includes a mass-continuity equation for a solute moving with the liquid field.

Liquid Solute Mass:

$$\frac{\partial}{\partial t} (c_b) = -\nabla \cdot (c_b \vec{v}_\ell) \tag{3.1-25}$$

where c_b is the solute concentration (mass of solute/unit volume) in the liquid phase.

The solute does not affect the hydrodynamics directly. If we assume that the solute represents boron, the amount of the dissolved and the plated-out boron in the core may affect the hydrodynamics indirectly through reactivity feedback. If the solute concentration exceeds the solubility at the liquid temperature in a specific hydrodynamic cell, we assume that the excess solute in that cell plates out. Plating can occur if the cell fluid flashes or boils and increases the concentration beyond the solubility limit. We also assume that any plated-out solute instantaneously redissolves to the maximum allowable concentration if more liquid enters the cell. Because the solute does not affect the hydrodynamics directly, the solute variable may be used as a tag to track the movement of fluid from a specific source through the system.

3.1.5 One-Dimensional Field Equations

In one dimension, the conservation equations reduce to:

Gas Mass:

$$\frac{\partial}{\partial t} (\alpha \rho_v) = -\frac{\partial}{\partial x} (\alpha \rho_v v_v) + \Gamma_g \tag{3.1-26}$$

Liquid Mass:

$$\frac{\partial}{\partial t} [(1 - \alpha) \rho_\ell] = -\frac{\partial}{\partial x} [(1 - \alpha) \rho_\ell v_\ell] - \Gamma_g \tag{3.1-27}$$

Total Noncondensable Gas Mass:

$$\frac{\partial}{\partial t} (\alpha \rho_a) = -\frac{\partial}{\partial x} (\alpha \rho_a v_v) \quad (3.1-28)$$

Liquid Solute Mass:

$$\frac{\partial}{\partial t} (c_b) = -\frac{\partial}{\partial x} (c_b v_\ell) \quad (3.1-29)$$

Gas Momentum:

$$\frac{\partial}{\partial t} v_v = -v_v \frac{\partial v_v}{\partial x} - \frac{1}{\rho_v} \frac{\partial P}{\partial x} - \frac{F_{wv}}{\alpha \rho_v} - \frac{f_{\ell v}}{\alpha \rho_v} + g - \frac{f_{VM}}{\alpha \rho_v} \quad (3.1-30)$$

Liquid Momentum:

$$\frac{\partial}{\partial t} v_\ell = -v_\ell \frac{\partial v_\ell}{\partial x} - \frac{1}{\rho_\ell} \frac{\partial P}{\partial x} - \frac{F_{w\ell}}{(1-\alpha)\rho_\ell} + \frac{f_{\ell v}}{(1-\alpha)\rho_\ell} + g + \frac{f_{VM}}{(1-\alpha)\rho_\ell} \quad (3.1-31)$$

Gas Energy:

$$\frac{\partial}{\partial t} \left(\alpha \rho_v \left(e_v + \frac{v_v^2}{2} \right) \right) + P \frac{\partial \alpha}{\partial t} = -\frac{\partial}{\partial x} \left(\alpha \rho_v v_v \left(e_v + \frac{v_v^2}{2} \right) \right) \quad (3.1-32)$$

$$-\frac{\partial}{\partial x} (\alpha P v_v) + q_{wv}'' + q_{iv}'' + \Gamma_g h_g$$

Liquid Energy:

$$\frac{\partial}{\partial t} \left((1-\alpha) \rho_\ell \left(e_\ell + \frac{v_\ell^2}{2} \right) \right) - P \frac{\partial \alpha}{\partial t} = -\frac{\partial}{\partial x} \left((1-\alpha) \rho_\ell v_\ell \left(e_\ell + \frac{v_\ell^2}{2} \right) \right) \quad (3.1-33)$$

$$-\frac{\partial}{\partial x} ((1-\alpha) P v_\ell) + q_{w\ell}'' + q_{i\ell}'' - \Gamma_g h_f$$

3.2 Finite Difference Formulation

3.2.1 One-Dimensional Finite Difference Formulation

For the 1-D components, the code solves Equations 3.1-26 through 3.1-33 to provide a complete description of the fluid field, although Equation 3.1-28 and/or 3.1-29 can be turned off through input. The spatial mesh used for the difference equations is staggered (Figure 3.2-1) with thermodynamic properties evaluated at the cell centers and velocities evaluated at the cell edges.

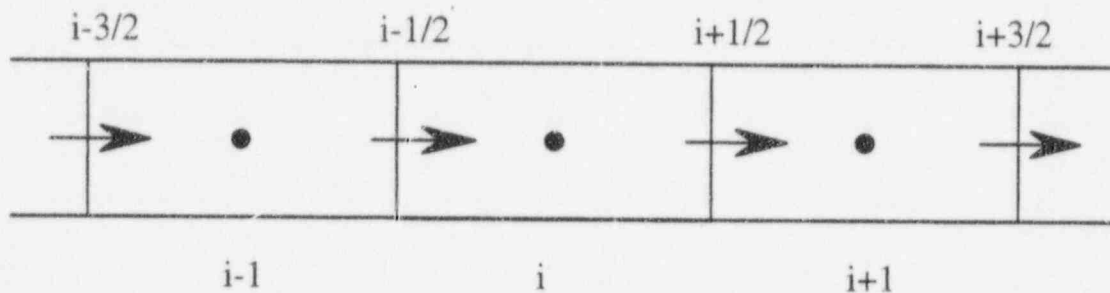


Figure 3.2-1 Staggered Grid Variables

Donor cell differencing is used everywhere, and the flux across an interface between two cells is given by:

$$(v\phi)_{i+1/2}^d = v_{i+1/2} \begin{cases} \phi_i & \text{if } v_{i+1/2} > 0 \\ \phi_{i+1} & \text{if } v_{i+1/2} < 0 \end{cases} \quad (3.2-1)$$

where ϕ can be any cell-center state variable or a combination of such variables, and v is either the liquid or vapor velocity, as appropriate. The subscript $i+1/2$ points to a cell interface, and the subscripts i and $i+1$ indicate the hydrodynamic cells on each side of the cell interface.

For the momentum equation, the donor-cell form of $v \frac{\partial v}{\partial x}$ at the interface between two cells is given by:

$$v_{i+1/2} \left(\frac{\partial v}{\partial x} \right)_{i+1/2}^d = Dv_{i+1/2} \begin{cases} \frac{Ev_{i+1/2} - Fv_{i-1/2}}{\Delta x_{i+1/2}} & \text{if } v_{i+1/2} > 0 \\ \frac{Ev_{i+3/2} - Fv_{i+1/2}}{\Delta x_{i+1/2}} & \text{if } v_{i+1/2} < 0 \end{cases} \quad (3.2-2)$$

where $\Delta x_{i+1/2}$ is the average of Δx_i and Δx_{i+1} , respectively, the cell lengths of cells i and $i+1$,

$$\Delta x_{i+1/2} = \frac{\Delta x_i + \Delta x_{i+1}}{2} \quad \text{and} \quad \phi_{i+1/2} = \frac{\Delta x_i \phi_i + \Delta x_{i+1} \phi_{i+1}}{\Delta x_i + \Delta x_{i+1}} \quad (3.2-3)$$

The factors D , E , and F are used to obtain the correct Bernoulli (or reversible) pressure loss (gain) through area reductions (expansions). The formulations for D , E , and F yield exact results for single-phase flow and approximately correct results if the change in the void fraction through the area change is small:

$$D = \frac{1}{2} \left(\frac{A_{i+1/2}}{A_i} + \frac{A_{i+1/2}}{A_{i+1}} \right) \quad (3.2-4)$$

where A_i is the average flow area in the cell:

$$A_i = \frac{V_i}{\Delta x_i} \quad (3.2-5)$$

and

$$E = \begin{cases} \frac{A_{i+1/2}}{A_{i+1}} & \text{for } v_{i+1/2} \geq 0 \\ \frac{A_{i+3/2}}{A_{i+1}} & \text{for } v_{i+1/2} < 0 \end{cases} \quad (3.2-6)$$

$$F = \begin{cases} \frac{A_{i-1/2}}{A_i} & \text{for } v_{i+1/2} \geq 0 \\ \frac{A_{i+1/2}}{A_i} & \text{for } v_{i+1/2} < 0 \end{cases} \quad (3.2-7)$$

3.2.1.1 Momentum Equations

The finite difference form of the 1-D momentum equations is given by:

Gas Momentum:

$$\frac{v_v^{n+1} - v_v^n}{\Delta t} + k \frac{\rho_{c,i+1/2}^n}{(\alpha \rho_v)_i^n} \frac{v_v^{n+1} - v_\ell^{n+1} - v_v^n + v_\ell^n}{\Delta t} = \quad (3.2-8)$$

$$-Dv_{v,i+1/2}^n \begin{cases} \frac{Ev_{v,i+1/2}^{n+1} - Fv_{v,i-1/2}^n}{\Delta x_{i+1/2}} & \text{for } v_{v,i+1/2} \geq 0 \\ \frac{Ev_{v,i+3/2}^n - Fv_{v,i+1/2}^{n+1}}{\Delta x_{i+1/2}} & \text{for } v_{v,i+1/2} < 0 \end{cases}$$

$$-k \frac{\rho_{c,i+1/2}^n}{(\alpha \rho_v)_i^n} v_{d,i+1/2}^n \begin{cases} \frac{v_{r,i+1/2}^{n+1} - v_{r,i-1/2}^n}{\Delta x_{i+1/2}} & \text{for } v_{d,i+1/2} \geq 0 \\ \frac{v_{r,i+3/2}^n - v_{r,i+1/2}^{n+1}}{\Delta x_{i+1/2}} & \text{for } v_{d,i+1/2} < 0 \end{cases}$$

$$- \frac{1}{\rho_{v,i+1/2}^n} \frac{P_{i+1}^{n+1} - P_i^{n+1}}{\Delta x_{i+1/2}} + g_{i+1/2} + B_{sv,i+1/2}$$

$$- \frac{1}{(\alpha \rho_v)_i^n} \left(F_{wv}^n + \frac{\partial F_{wv}^n}{\partial v_v} (v_v^{n+1} - v_v^n) + \frac{\partial F_{wv}^n}{\partial v_\ell} (v_\ell^{n+1} - v_\ell^n) \right)_{i+1/2}$$

$$- \frac{1}{(\alpha \rho_v)_i^n} \left(f_{\ell v}^n + \frac{\partial f_{\ell v}^n}{\partial v_v} (v_v^{n+1} - v_v^n) + \frac{\partial f_{\ell v}^n}{\partial v_\ell} (v_\ell^{n+1} - v_\ell^n) \right)_{i+1/2}$$

Here for convenience the virtual mass term has been introduced as

$$f_{VM} = f_{VM} \left(\frac{dv_r}{dt} \right) = k \rho_c \left\{ \frac{\partial v_r}{\partial t} + v_d \frac{\partial v_r}{\partial x} \right\} \quad (3.2-9)$$

and a source term has been introduced to account for connections to other components.

Liquid Momentum:

$$\frac{v_{\ell}^{n+1} - v_{\ell}^n}{\Delta t} - k \frac{\rho_{c,i+1/2}^n}{((1-\alpha)\rho_{\ell})_{i+1/2}^n} \frac{v_v^{n+1} - v_{\ell}^{n+1} - v_v^n + v_{\ell}^n}{\Delta t} = \tag{3.2-10}$$

$$-Dv_{\ell,i+1/2}^n \begin{cases} \frac{Ev_{\ell,i+1/2}^{n+1} - Fv_{\ell,i-1/2}^n}{\Delta x_{i+1/2}} & \text{for } v_{\ell,i+1/2} \geq 0 \\ \frac{Ev_{\ell,i+3/2}^n - Fv_{\ell,i+1/2}^{n+1}}{\Delta x_{i+1/2}} & \text{for } v_{\ell,i+1/2} < 0 \end{cases}$$

$$+k \frac{\rho_{c,i+1/2}^n}{((1-\alpha)\rho_{\ell})_{i+1/2}^n} v_{d,i+1/2}^n \begin{cases} \frac{v_{r,i+1/2}^{n-1} - v_{r,i-1/2}^n}{\Delta x_{i+1/2}} & \text{for } v_{d,i+1/2} \geq 0 \\ \frac{v_{r,i+3/2}^n - v_{r,i+1/2}^{n+1}}{\Delta x_{i+1/2}} & \text{for } v_{d,i+1/2} < 0 \end{cases}$$

$$- \frac{1}{\rho_{\ell,i+1/2}^n} \frac{p_{i+1}^{n+1} - p_i^{n+1}}{\Delta x_{i+1/2}} + g_{i+1/2} + B_{s\ell,i+1/2}$$

$$- \frac{1}{((1-\alpha)\rho_{\ell})_{i+1/2}^n} \left(F_{w\ell}^n + \frac{\partial F_{w\ell}^n}{\partial v_v} (v_v^{n+1} - v_v^n) + \frac{\partial F_{w\ell}^n}{\partial v_{\ell}} (v_{\ell}^{n+1} - v_{\ell}^n) \right)_{i+1/2}$$

$$+ \frac{1}{((1-\alpha)\rho_{\ell})_{i+1/2}^n} \left(f_{\ell v}^n + \frac{\partial f_{\ell v}^n}{\partial v_v} (v_v^{n+1} - v_v^n) + \frac{\partial f_{\ell v}^n}{\partial v_{\ell}} (v_{\ell}^{n+1} - v_{\ell}^n) \right)_{i+1/2}$$

3.2.1.2 Mass and Energy Equations

The 1-D mass and energy equations are integrated over the cell volume. The conserving finite difference formulation is given by:

Gas Mass:

$$V_i (\alpha_i^{n+1} \rho_{v,i}^{n+1} - \alpha_i^n \rho_{v,i}^n) = \tag{3.2-11}$$

$$+ \Delta t A_{i-1/2} v_{v,i-1/2}^{n+1} \begin{cases} (\alpha \rho_v)_{i-1}^{n+1} & \text{for } v_{v,i-1/2}^{n+1} \geq 0 \\ (\alpha \rho_v)_i^{n+1} & \text{for } v_{v,i-1/2}^{n+1} < 0 \end{cases}$$

$$- \Delta t A_{i+1/2} v_{v,i+1/2}^{n+1} \begin{cases} (\alpha \rho_v)_i^{n+1} & \text{for } v_{v,i+1/2}^{n+1} \geq 0 \\ (\alpha \rho_v)_{i+1}^{n+1} & \text{for } v_{v,i+1/2}^{n+1} < 0 \end{cases}$$

$$+ \Delta t V_i \Gamma_{g,i}^{n+1} + \Delta t V_i M_{sv,i}$$

Mixture Mass:

$$V_i (\alpha_i^{n+1} \rho_{v,i}^{n+1} + (1 - \alpha_i^{n+1}) \rho_{\ell,i}^{n+1} - \alpha_i^n \rho_{v,i}^n - (1 - \alpha_i^n) \rho_{\ell,i}^n) = \tag{3.2-12}$$

$$+ \Delta t A_{i-1/2} v_{v,i-1/2}^{n+1} \begin{cases} (\alpha \rho_v)_{i-1}^{n+1} & \text{for } v_{v,i-1/2}^{n+1} \geq 0 \\ (\alpha \rho_v)_i^{n+1} & \text{for } v_{v,i-1/2}^{n+1} < 0 \end{cases}$$

$$+ \Delta t A_{i-1/2} v_{\ell,i-1/2}^{n+1} \begin{cases} ((1 - \alpha) \rho_\ell)_{i-1}^{n+1} & \text{for } v_{\ell,i-1/2}^{n+1} \geq 0 \\ ((1 - \alpha) \rho_\ell)_i^{n+1} & \text{for } v_{\ell,i-1/2}^{n+1} < 0 \end{cases}$$

$$-\Delta t A_{i+1/2} v_{v,i+1/2}^{n+1} \begin{cases} (\alpha \rho_v)_i^{n+1} & \text{for } v_{v,i+1/2}^{n+1} \geq 0 \\ (\alpha \rho_v)_{i+1}^{n+1} & \text{for } v_{v,i+1/2}^{n+1} < 0 \end{cases}$$

$$-\Delta t A_{i+1/2} v_{\ell,i+1/2}^{n+1} \begin{cases} ((1-\alpha)\rho_\ell)_i^{n+1} & \text{for } v_{\ell,i+1/2}^{n+1} \geq 0 \\ ((1-\alpha)\rho_\ell)_{i+1}^{n+1} & \text{for } v_{\ell,i+1/2}^{n+1} < 0 \end{cases}$$

$$+\Delta t V_i (M_{sv,i} + M_{s\ell,i})$$

Total Noncondensable Gas Mass:

$$V_i (\alpha_i^{n+1} \rho_{a,i}^{n+1} - \alpha_i^n \rho_{a,i}^n) = \tag{3.2-13}$$

$$+\Delta t A_{i-1/2} v_{v,i-1/2}^{n+1} \begin{cases} (\alpha \rho_a)_{i-1}^{n+1} & \text{for } v_{v,i-1/2}^{n+1} \geq 0 \\ (\alpha \rho_a)_i^{n+1} & \text{for } v_{v,i-1/2}^{n+1} < 0 \end{cases}$$

$$-\Delta t A_{i+1/2} v_{v,i+1/2}^{n+1} \begin{cases} (\alpha \rho_a)_i^{n+1} & \text{for } v_{v,i+1/2}^{n+1} \geq 0 \\ (\alpha \rho_a)_{i+1}^{n+1} & \text{for } v_{v,i+1/2}^{n+1} < 0 \end{cases}$$

$$+\Delta t V_i M_{sa,i}$$

For a particular noncondensable gas n , the subscript a in Equation 3.2-13 is replaced by the subscript n .

Liquid Solute Mass:

$$\begin{aligned}
 &V_i(c_{b,i}^{n+1} - c_{b,i}^n) = \tag{3.2-14} \\
 &+ \Delta t A_{i-1/2} v_{\ell,i-1/2}^{n+1} \begin{cases} c_{b,i-1}^{n+1} & \text{for } v_{\ell,i-1/2}^{n+1} \geq 0 \\ c_{b,i}^{n+1} & \text{for } v_{\ell,i-1/2}^{n+1} < 0 \end{cases} \\
 &- \Delta t A_{i+1/2} v_{\ell,i+1/2}^{n+1} \begin{cases} c_{b,i}^{n+1} & \text{for } v_{\ell,i+1/2}^{n+1} \geq 0 \\ c_{b,i+1}^{n+1} & \text{for } v_{\ell,i+1/2}^{n+1} < 0 \end{cases}
 \end{aligned}$$

$$+ \Delta t V_i M_{sb,i}$$

Gas Energy:

$$\begin{aligned}
 &V_i \left((\alpha \rho_v (e_v + \frac{v_v^2}{2}))_i^{n+1} - (\alpha \rho_v (e_v + \frac{v_v^2}{2}))_i^n + P_i^n (\alpha_i^{n+1} - \alpha_i^n) \right) = \tag{3.2-15} \\
 &+ \Delta t A_{i-1/2} v_{v,i-1/2}^{n+1} \begin{cases} (\alpha \rho_v (h_v + \frac{v_v^2}{2}))_{i-1}^{n+1} & \text{for } v_{v,i-1/2}^{n+1} \geq 0 \\ (\alpha \rho_v (h_v + \frac{v_v^2}{2}))_i^{n+1} & \text{for } v_{v,i-1/2}^{n+1} < 0 \end{cases} \\
 &- \Delta t A_{i+1/2} v_{v,i+1/2}^{n+1} \begin{cases} (\alpha \rho_v (h_v + \frac{v_v^2}{2}))_i^{n+1} & \text{for } v_{v,i+1/2}^{n+1} \geq 0 \\ (\alpha \rho_v (h_v + \frac{v_v^2}{2}))_{i+1}^{n+1} & \text{for } v_{v,i+1/2}^{n+1} < 0 \end{cases} \\
 &+ \Delta t (V_i \Gamma_{g,i}^{n+1} h_{g,i}^{n+1} + V_i q_{wv,i}^{n+1} + V_i q_{iv,i}^{n+1} + V_i E_{sv,i})
 \end{aligned}$$

Liquid Energy:

$$V_i \left(\left((1 - \alpha) \rho_\ell \left(e_\ell + \frac{v_\ell^2}{2} \right) \right)_i^{n+1} - \left((1 - \alpha) \rho_\ell \left(e_\ell + \frac{v_\ell^2}{2} \right) \right)_i^n \right) - V_i P_i^n (\alpha_i^{n+1} - \alpha_i^n) = \quad (3.2-16)$$

$$+ \Delta t A_{i-1/2} v_{\ell,i-1/2}^{n+1} \begin{cases} \left((1 - \alpha) \rho_\ell \left(h_\ell + \frac{v_\ell^2}{2} \right) \right)_{i-1}^{n+1} & \text{for } v_{\ell,i-1/2}^{n+1} \geq 0 \\ \left((1 - \alpha) \rho_\ell \left(h_\ell + \frac{v_\ell^2}{2} \right) \right)_i^{n+1} & \text{for } v_{\ell,i-1/2}^{n+1} < 0 \end{cases}$$

$$- \Delta t A_{i+1/2} v_{\ell,i+1/2}^{n+1} \begin{cases} \left((1 - \alpha) \rho_\ell \left(h_\ell + \frac{v_\ell^2}{2} \right) \right)_i^{n+1} & \text{for } v_{\ell,i+1/2}^{n+1} \geq 0 \\ \left((1 - \alpha) \rho_\ell \left(h_\ell + \frac{v_\ell^2}{2} \right) \right)_{i+1}^{n+1} & \text{for } v_{\ell,i+1/2}^{n+1} < 0 \end{cases}$$

$$+ \Delta t (- V_i \Gamma_{g,i}^{n+1} h_{f,i}^{n+1} + V_i q_{w\ell,i}^{n+1} + V_i q_{i\ell,i}^{n+1} + V_i E_{s\ell,i})$$

As in the momentum equations, a source term has been introduced in these equations to account for connections to other components.

In these equations the heat flux terms are linearized with respect to void fraction and temperature as:

$$q_{iv}^{n+1} = \frac{A_i}{V_i} \left(h_{iv}^n (T_{sat}^{n+1} - T_v^{n+1}) + \frac{\partial h_{iv}^n}{\partial \alpha} (\alpha^{n+1} - \alpha^n) (T_{sat}^n - T_v^n) \right) \quad (3.2-17)$$

$$q_{i\ell}^{n+1} = \frac{A_i}{V_i} \left(h_{i\ell}^n (T_{sat}^{n+1} - T_\ell^{n+1}) + \frac{\partial h_{i\ell}^n}{\partial \alpha} (\alpha^{n+1} - \alpha^n) (T_{sat}^n - T_\ell^n) \right) \quad (3.2-18)$$

$$q_{wv}^{n+1} = \frac{A_w}{V_i} h_{wv}^n (T_w^{n+1} - T_v^{n+1}) \quad (3.2-19)$$

and

$$q_{i\ell}^{n+1} = \frac{A_w}{V_i} h_{w\ell}^n (T_w^{n+1} - T_\ell^{n+1}) \quad (3.2-20)$$

The interfacial heat transfer terms are linearized with respect to temperature and void fraction in order to assure numerical stability and to assure that the heat flux terms approach zero in case of thermal equilibrium and in the limit of α approaching 0 or 1. The wall heat transfer is linearized with respect to temperature to assure numerical stability and energy conservation in connection with the solution of the conduction equation for the wall.

3.2.2 Three-Dimensional Finite Difference Formulation

The 3-D vessel component in TRACG uses a cylindrical coordinate system, as shown in Figure 3.2-2.

The grid is staggered with the velocities specified at the boundary of each cell and the remaining properties such as α , P , ρ , e specified at the cell center.

Donor cell differencing is used everywhere (Section 3.2.1).

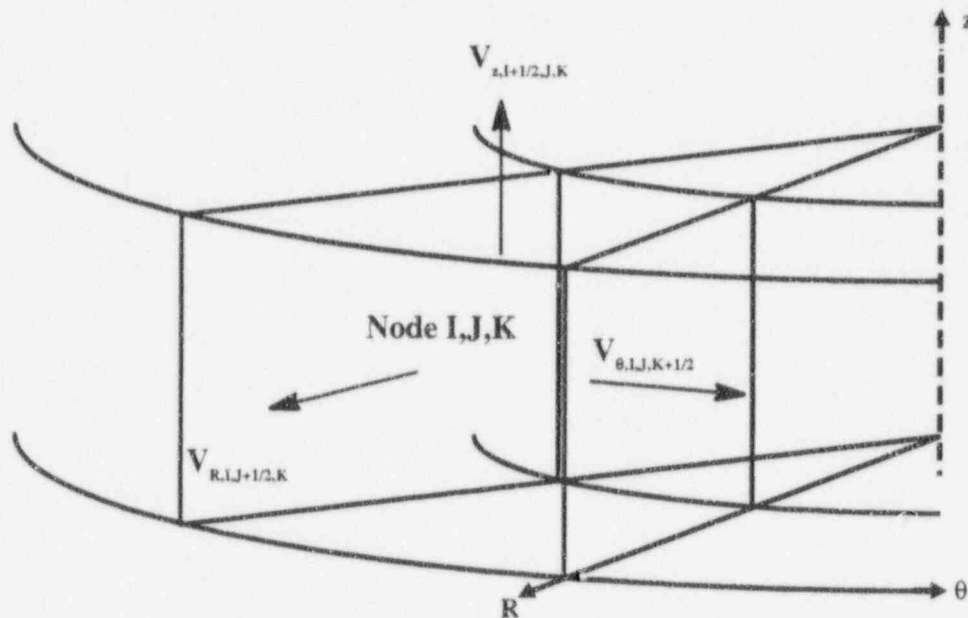


Figure 3.2-2. Cylindrical Coordinate System with Staggered Grid

3.2.2.1 Momentum Equations

In the 3-D formulation, when the shear tensor and the interfacial shear are integrated over the node and when the effect of local pressure variations is accounted for, terms for interaction with the walls $\bar{F}_{w\ell}$ and \bar{F}_{wg} and terms for interaction between the phases will arise. As in the 1-D formulation, the interfacial drag and the virtual mass are accounted for separately. In a 3-D formulation there will be other forces like the Bassett force and forces associated with the spatial distribution of phase, velocity and turbulent kinetic energy. TRACG, however, like the other versions of TRAC or RELAP5, uses relatively large nodes and a simulation of these terms is not meaningful. Consequently, these terms have been neglected in the 3-D finite difference formulation.

However, when the flow terms are integrated over the boundary for the node, a term will arise from the fluctuating component of the velocity. Again, with the relatively large nodes typically used in TRACG, standard turbulence models will not accurately model this term. Instead, using an equivalence to Prandtl's mixing length theory, a simple mixing term has been incorporated in the momentum equations. This way the effect of turbulent shear and mixing is included and sensitivity studies can be performed on the importance of the mixing.

The momentum equations are discretized directly for each face of the cell. Neglecting the off-diagonal terms in the virtual mass, the spatially discretized equations become:

Axial Gas Momentum:

$$\begin{aligned} & \left. \frac{\partial v_{vz,I+1/2,J,K}}{\partial t} + \left[v_{vz} \left(\frac{\partial v_{vz}}{\partial z} \right)^d + v_{vR} \left(\frac{\partial v_{vz}}{\partial R} \right)^d + \frac{v_{v\theta}}{R} \left(\frac{\partial v_{vz}}{\partial \theta} \right)^d \right] \right|_{I+1/2,J,K} \\ & + \left(\frac{k\rho_c}{\alpha\rho_v} \right)_{I+1/2,J,K} \left[\frac{\partial v_{rz}}{\partial t} + v_{dz} \left(\frac{\partial v_{rz}}{\partial z} \right)^d \right]_{I+1/2,J,K} = \\ & - \frac{1}{\rho_{v,I+1/2,J,K}} \frac{P_{I+1,J,K} - P_{I,J,K}}{\Delta z_{I+1/2}} - \left[g + \frac{1}{\alpha\rho_v} f_{lv} + \frac{1}{\alpha\rho_v} F_{wv} \right]_{z,I+1/2,J,K} \\ & + B_{svz,I+1/2,J,K} + B_{mixvz,I+1/2,J,K} \end{aligned} \quad (3.2-21)$$

Here, if a property is not defined at the face, linear averaging is used; e.g.:

$$\begin{aligned} \alpha_{I+1/2,J,K} &= \frac{\Delta z_I \alpha_{I,J,K} + \Delta z_{I+1} \alpha_{I+1,J,K}}{\Delta z_I + \Delta z_{I+1}} \\ v_{v\theta,I+1/2,J,K} &= \frac{\Delta z_I (v_{v\theta,I,J,K-1/2} + v_{v\theta,I,J,K+1/2}) + \Delta z_{I+1} (v_{v\theta,I+1,J,K-1/2} + v_{v\theta,I+1,J,K+1/2})}{2(\Delta z_I + \Delta z_{I+1})} \end{aligned}$$

The discretization with respect to time is identical to the discretization of the 1-D equations described in Section 3.2.1.1. The superscript *d* on the convective term indicates that the convective term is calculated using donor cell differencing, as described in Section 3.2.1 (Equation 3.2-2). (For the off-diagonal terms, a value of unity is used for D, E and F.)

Radial Gas Momentum:

$$\begin{aligned} & \frac{\partial v_{vR,I,J+1/2,K}}{\partial t} + \left[v_{vz} \left(\frac{\partial v_{vR}}{\partial z} \right)^d + v_{vR} \left(\frac{\partial v_{vR}}{\partial R} \right)^d + \frac{v_{v\theta}}{R} \left(\frac{\partial v_{vR}}{\partial \theta} \right)^d - \frac{v_{v\theta}^2}{R} \right] \\ & + \left(\frac{k\rho_c}{\alpha\rho_v} \right)_{I,J+1/2,K} \left[\frac{\partial}{\partial t} v_{rR} + v_{dR} \left(\frac{\partial v_{rR}}{\partial R} \right)^d \right]_{I,J+1/2,K} = \\ & - \frac{1}{\rho_{v,I,J+1/2,K}} \frac{P_{I,J+1,K} - P_{I,J,K}}{\Delta R_{J+1/2}} - \left[\frac{1}{\alpha\rho_v} f_{\ell v} + \frac{1}{\alpha\rho_v} F_{wv} \right]_{R,I,J+1/2,K} \\ & + B_{svR,I,J+1/2,K} + B_{mixvR,I,J+1/2,K} \end{aligned} \tag{3.2-22}$$

Azimuthal Gas Momentum:

$$\begin{aligned} & \frac{\partial v_{v\theta,I,J,K+1/2}}{\partial t} + \left[v_{vz} \left(\frac{\partial v_{v\theta}}{\partial z} \right)^d + v_{vR} \left(\frac{\partial v_{v\theta}}{\partial R} \right)^d + \frac{v_{v\theta}}{R} \left(\frac{\partial v_{v\theta}}{\partial \theta} \right)^d + \frac{v_{v\theta} v_{vR}}{R} \right]_{I,J,K+1/2} \\ & + \left(\frac{k\rho_c}{\alpha\rho_v} \right)_{I,J,K+1/2} \left[\frac{\partial}{\partial t} v_{r\theta} + \frac{v_{d\theta}}{R} \left(\frac{\partial v_{r\theta}}{\partial \theta} \right)^d \right]_{I,J,K+1/2} = \\ & - \frac{1}{\rho_{v,I,J,K+1/2}} \frac{P_{I,J,K+1} - P_{I,J,K}}{R_{J+1/2} \Delta \theta_{K+1/2}} - \left[\frac{1}{\alpha\rho_v} f_{\ell v} + \frac{1}{\alpha\rho_v} F_{wv} \right]_{\theta,I,J,K+1/2} \\ & + B_{sv\theta,I,J,K+1/2} + B_{mixv\theta,I,J,K+1/2} \end{aligned} \tag{3.2-23}$$

Similar expressions exist for the liquid phase.

Axial Liquid Momentum:

$$\frac{\partial v_{\ell z, I+1/2, J, K}}{\partial t} + \left[v_{\ell z} \left(\frac{\partial v_{\ell z}}{\partial z} \right)^d + v_{\ell R} \left(\frac{\partial v_{\ell z}}{\partial R} \right)^d + \frac{v_{\ell \theta}}{R} \left(\frac{\partial v_{\ell z}}{\partial \theta} \right)^d \right]_{I+1/2, J, K} \quad (3.2-24)$$

$$- \left(\frac{k p_c}{(1-\alpha)\rho_\ell} \right)_{I+1/2, J, K} \left[\frac{\partial v_{rz}}{\partial t} + v_{dz} \left(\frac{\partial v_{rz}}{\partial z} \right)^d \right]_{I+1/2, J, K} =$$

$$- \frac{1}{\rho_{\ell, I+1/2, J, K}} \frac{P_{I+1, J, K} - P_{I, J, K}}{\Delta z_{I+1/2}} - \left[g - \frac{1}{(1-\alpha)\rho_\ell} f_{\ell v} + \frac{1}{(1-\alpha)\rho_\ell} F_{w\ell} \right]_{z, I+1/2, J, K}$$

$$+ B_{s\ell z, I+1/2, J, K} + B_{mix\ell z, I+1/2, J, K}$$

Radial Liquid Momentum:

$$\frac{\partial v_{\ell R, I, J+1/2, K}}{\partial t} + \left[v_{\ell z} \left(\frac{\partial v_{\ell R}}{\partial z} \right)^d + v_{\ell R} \left(\frac{\partial v_{\ell R}}{\partial R} \right)^d + \frac{v_{\ell \theta}}{R} \left(\frac{\partial v_{\ell R}}{\partial \theta} \right)^d - \frac{v_{\ell \theta}^2}{R} \right] \quad (3.2-25)$$

$$- \left(\frac{k p_c}{(1-\alpha)\rho_\ell} \right)_{I, J+1/2, K} \left[\frac{\partial}{\partial t} v_{rR} + v_{dR} \left(\frac{\partial v_{rR}}{\partial R} \right)^d \right]_{I, J+1/2, K} =$$

$$- \frac{1}{\rho_{\ell, I, J+1/2, K}} \frac{P_{I, J+1, K} - P_{I, J, K}}{\Delta R_{J+1/2}} - \left[\frac{-1}{(1-\alpha)\rho_\ell} f_{\ell v} + \frac{1}{(1-\alpha)\rho_\ell} F_{w\ell} \right]_{R, I, J+1/2, K}$$

$$+ B_{s\ell R, I, J+1/2, K} + B_{mix\ell R, I, J+1/2, K}$$

Azimuthal Liquid Momentum:

$$\frac{\partial v_{\ell\theta, I, J, K+1/2}}{\partial t} + \left[v_z \left(\frac{\partial v_{v\theta}}{\partial z} \right)^d + v_{\ell R} \left(\frac{\partial v_{\ell\theta}}{\partial R} \right)^d + \frac{v_{\ell\theta}}{R} \left(\frac{\partial v_{\ell\theta}}{\partial \theta} \right)^d + \frac{v_{\ell\theta} v_{\ell R}}{R} \right]_{I, J, K+1/2} \quad (3.2-26)$$

$$\left(\frac{k\rho_c}{(1-\alpha)\rho_\ell} \right)_{I, J, K+1/2} \left[\frac{\partial}{\partial t} v_{r\theta} + \frac{v_{d\theta}}{R} \left(\frac{\partial v_{r\theta}}{\partial \theta} \right)^d \right]_{I, J, K+1/2} =$$

$$- \frac{1}{\rho_{\ell, I, J, K+1/2}} \frac{P_{I, J, K+1} - P_{I, J, K}}{R_{J+1/2} \Delta\theta_{K+1/2}} - \left[\frac{-1}{(1-\alpha)\rho_\ell} f_{\ell v} + \frac{1}{(1-\alpha)\rho_\ell} F_{w\ell} \right]_{\theta, I, J, K+1/2}$$

$$+ B_{s\ell\theta, I, J, K+1/2} + B_{mix\ell\theta, I, J, K+1/2}$$

3.2.2.2 Mass and Energy Equations

The mass and energy equations are integrated over the volume of the cell to give the total change in mass and energy for the cell.

Gas Mass:

$$V_{IJK} \frac{\partial}{\partial t} (\alpha\rho_v)_{IJK} + \sum_{j=1}^{N_f} (A\alpha\rho_v v_v)^d_{j, IJK} = V_{IJK} (\Gamma_g + M_{sv})_{IJK} \quad (3.2-27)$$

$$+ \sum_{j=1}^{N_f} (AM_{mixv})_{j, IJK}$$

In these equations the discretization with respect to time is identical to the discretization of the 1-D equations described in Section 3.2.1.2. The superscript *d* on the convective term indicates that the convective term is calculated using donor cell differencing, as described in Section 3.2.1 (Equation 3.2-1). In these equations, the summation over *j* indicates the summation over all the faces of the cell with the convention that flows out of the cell are positive.

Mixture Mass:

$$V_{IJK} \frac{\partial}{\partial t} [(1 - \alpha)\rho_\ell + \alpha\rho_v]_{IJK} + \sum_{j=1}^{N_f} (A(1 - \alpha)\rho_\ell v_\ell)^d_{j,IJK} \quad (3.2-28)$$

$$+ \sum_{j=1}^{N_f} (A\alpha\rho_v v_v)^d_{j,IJK} = V_{IJK}(M_{s\ell} + M_{sv})_{IJK} + \sum_{j=1}^{N_f} (A(M_{mixv} + M_{mix\ell}))_{j,IJK}$$

Total Noncondensable Mass:

$$V_{IJK} \frac{\partial}{\partial t} (\alpha\rho_a)_{IJK} + \sum_{j=1}^{N_f} (A\alpha\rho_a v_v)^d_{j,IJK} = V_{IJK}(M_{sa})_{IJK} + \sum_{j=1}^{N_f} (AM_{mixa})_{j,IJK} \quad (3.2-29)$$

Liquid Solute Mass:

$$V_{IJK} \frac{\partial}{\partial t} (c_b)_{IJK} + \sum_{j=1}^{N_f} (Ac_b v_\ell)^d_{j,IJK} = V_{IJK}(M_{sb})_{IJK} + \sum_{j=1}^{N_f} (AM_{mixb})_{j,IJK} \quad (3.2-30)$$

Vapor Energy:

$$V_{IJK} \frac{\partial}{\partial t} \left[\alpha\rho_v \left(e_v + \frac{v_v^2}{2} \right) \right]_{IJK} + \sum_{j=1}^{N_f} \left[A\alpha\rho_v v_v \left(h_v + \frac{v_v^2}{2} \right) \right]^d_{j,IJK} \quad (3.2-31)$$

$$+ V_{IJK} \left(P \frac{\partial \alpha}{\partial t} \right)_{IJK} = V_{IJK} (q_{iv}^{\sigma} + \Gamma_g h_g + q_{wv}^{\sigma} + E_{sv})_{IJK} + \sum_{j=1}^{N_f} (AE_{mixv})_{j,IJK}$$

Mixture Energy:

$$V_{IJK} \frac{\partial}{\partial t} \left[(1 - \alpha)\rho_\ell \left(e_\ell + \frac{v_\ell^2}{2} \right) + \alpha\rho_v \left(e_v + \frac{v_v^2}{2} \right) \right]_{IJK} \quad (3.2-32)$$

$$+ \sum_{j=1}^{N_f} \left[A(1 - \alpha)\rho_\ell v_\ell \left(h_\ell + \frac{v_\ell^2}{2} \right) \right]^d_{j,IJK} + \sum_{j=1}^{N_f} \left[A\alpha\rho_v v_v \left(h_v + \frac{v_v^2}{2} \right) \right]^d_{j,IJK} =$$

$$V_{IJK} (q_{w\ell}^{\sigma} + q_{wv}^{\sigma} + E_{sv} + E_{s\ell})_{IJK} + \sum_{j=1}^{N_f} (A(E_{mixv} + E_{mix\ell}))_{j,IJK}$$

3.3 Modifications to Momentum Equations

There are several situations and places in the code where the regular momentum equations, as discussed in the previous sections, are modified or are not used. These situations and places are:

- Critical flow or choking
- Counter-current flow limitation (CCFL)
- Stratified flow with void fraction gradients
- Pump component at the location of the pump impeller
- Steam separator component at the separating face entering the side branch
- Jet pump at the mixing region
- TEE component joining cell

The last four cases will be discussed in Section 7 of this report. The first three cases will be discussed here, since these modifications to the momentum equations may occur for all components.

3.3.1 Critical Flow

In previous versions of TRAC, the criteria for choked flow were determined by a characteristic analysis of the partial differential equations governing the flow. However, it has been found empirically [3-12] that a simplified, approximate criterion may be used in place of the detailed characteristic analysis and still obtain good code/data comparisons. Accordingly, the following criterion is used in TRACG to determine whether the flow is choked:

$$\frac{\alpha \rho_\ell v_v + (1 - \alpha) \rho_v v_\ell}{\alpha \rho_\ell + (1 - \alpha) \rho_v} = v_{\text{crit}} \quad (3.3-1)$$

If the velocity as calculated by Equation 3.3-1 exceeds the acoustic propagation speed, the velocity is limited to the critical velocity.

When the velocities are limited, an additional requirement is needed to determine the individual velocities. Conservation of the slip ratio is chosen as the additional criterion.

3.3.2 Counter-Current Flow Limitation

Counter-current flow limitation (CCFL), also called flooding, determines the amount of liquid that can penetrate flow restrictions. If limitation occurs (e.g., at the upper tie plate of a BWR fuel bundle), the amount of liquid that can penetrate into the bundle is reduced.

CCFL is a complicated hydrodynamic phenomenon and is thought to arise as a result of the interfacial friction between the liquid and the vapor phases [3-13]. CCFL in a BWR has been found to be described by a Kutateladze-type correlation of the form [3-14, 3-15]:

$$\sqrt{K_v} + m\sqrt{K_\ell} = \sqrt{K} \quad (3.3-2)$$

where:

$$K_v = \frac{j_v \sqrt{\rho_v}}{(\Delta\rho g \sigma)^{1/4}} \quad (3.3-3)$$

$$K_\ell = \frac{j_\ell \sqrt{\rho_\ell}}{(\Delta\rho g \sigma)^{1/4}} \quad (3.3-4)$$

This correlation specifies the maximum downflow liquid velocity in counter-current flow through flow restrictions that can be obtained for a given upward vapor velocity. Thus, CCFL represents an upper limit to the liquid penetration in counter-current flow. That is analogous to critical flow, which determines the upper limit of the discharge flow rate in co-current flow from a source of fluid at high pressure. A detailed description of the CCFL model is given in Section 6.1.7.2. If the calculated liquid velocity exceeds that allowed by the CCFL correlating it is limited such that the CCFL correlation is satisfied.

3.3.3 Stratified Horizontal Flow

In a horizontal flow path at low flow rates, a horizontally stratified flow will develop with a force resulting from the difference in the hydrostatic heads in adjacent computational cells (Figure 3.3-1). This force term is given by:

$$\Delta P_{\text{strat},i+1/2} = (P_i - P_{i+1})_{\text{strat}} = (\rho_\ell - \rho_v)_{i+1/2} g_{i+1/2} (\alpha_{i+1} - \alpha_i) \Delta z \quad (3.3-5)$$

This force is added to the liquid phase momentum equation. The main effect of this term is to equalize the liquid levels between the two cells. The term added to the momentum equation represents information lost in the derivation of the 1-D momentum equations by the integration over the cross-sectional area perpendicular to the flow direction.

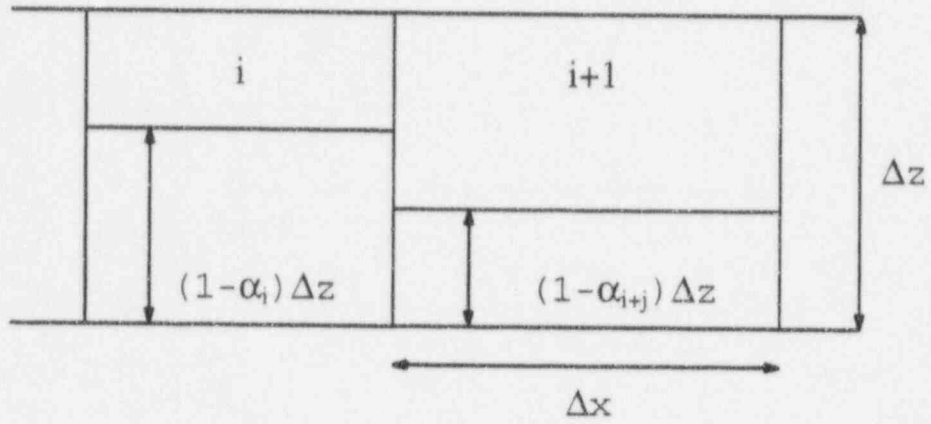


Figure 3.3-1 Void Gradient Gravity Head

3.4 References

- 3-1 D.R. Liles et.al., *TRAC-PF1/MOD1 Correlations and Models*, NUREG/CR-5069, December 1988.
- 3-2 J.A. Borkowski et. al., *TRAC-BF1/MOD1 Models and Correlations*, NUREG/CR-4391, August 1992.
- 3-3 G. Kocamustafaogullari, *Thermo-Fluid Dynamics of Separated Two-Phase Flow*, Ph. D. thesis, Georgia Institute of Technology, December 1971.
- 3-4 M. Ishii, *Thermo-Fluid Dynamic Theory of Two-Phase Flow*, Collection de la Direction des Études et Recherches D'Électricité de France, Eyrolles, Paris, 1981.
- 3-5 A.E. Bergles, J.S. Collier, J.M. Delhaye, G.F. Hewitt and F. Mayinger, *Two-Phase Flow and Heat Transfer in the Power and Process Industries*, Hemisphere Publishing Corporation, New York, McGraw-Hill Book Co., New York, 1981.
- 3-6 F.L. Addessio, *A Review of the Development of Two-Fluid Models*, NUREG/CR-2146, August 1981.
- 3-7 H.B. Stewart and B. Wendroff, *Two-Phase Flow: Models and Methods*, Journal of Computational Physics, 56, p 363-409, 1984.
- 3-8 H.B. Stewart, *Stability of Two-Phase Flow Calculation Using Two-Fluid Models*, Journal of Computational Physics, 33, p 250-270, 1979.
- 3-9 J.H. Stuhmiller, *A Review of the Rational Approach to Two-Phase Flow Modeling*, Jaycor, Del Mar, California, PB-255 548, July 1976.
- 3-10 H. Lamb, *Hydrodynamics*, Dover Publications, New York.
- 3-11 K.H. Chu and B.S. Shiralkar, *Prediction of Critical Power Based on a Two Fluid and Multi-Field Model*, Fourth International Meeting on Nuclear Thermal Hydraulics, Operation and Safety, 1993.
- 3-12 V.H. Ransom et. al., *RELAP5/MOD1 Code Manual, Volume I: System Models and Numerical Methods*, NUREG/CR-2070, March 1982.
- 3-13 G.B. Wallis, *One-Dimensional Two-Phase Flow*, McGraw-Hill Book Co., New York, 1969.
- 3-14 D.D. Jones, *Subcooled Counter Current Flow Limiting Characteristics of the Upper Region of a BWR Fuel Bundle*, General Electric Company, NEDG-NUREG-23549, 1977.
- 3-15 J.D. Duncan and J.E. Leonard, *BWR Standby Cooling in Boiling Water Reactors Under Simulated Loss-of-Coolant Conditions*, BWR-FLECT Final Report, 6, GEAP-13190, 1971.

4.0 Heat Conduction Model

TRACG solves the heat conduction equation for the fuel rods and other structural materials in the system. The structures include the pipe walls for the one-dimensional (1-D) components, the outer wall of the vessel component, and internal heat slabs in the vessel component. For the 1-D component walls, the inside heat transfer is to the fluid in the component. The outside heat transfer can be to the fluid in any other component. The internal heat slabs in the vessel component can be placed either completely inside a vessel cell or at the boundary between two vessel cells, either in the axial or the radial direction.

The nomenclature used for the heat conduction equation is as follows:

Nomenclature

A	=	surface area
C_p	=	specific heat
h	=	heat transfer coefficient
k	=	conductivity
M	=	mass
q	=	heat flux
r	=	radial dimension
q''	=	heat flux
q'''	=	volumetric heat generation rate
t	=	time
T	=	temperature
z	=	axial dimension

Greek Symbols

ρ	=	density
θ	=	indicator for implicit/explicit integration (hydraulic model)
ζ	=	indicator for implicit/explicit integration (heat conduction model)
	=	length measured in the direction normal to the surface

Subscripts

gap	=	fuel gas gap
v	=	vapor
l	=	liquid
w	=	wall
i	=	inner surface

- o = outer surface
- j = node number
- rad = thermal radiation
- N = last node number
- M = last node number in fuel (next to the gap)

Superscript

- n = time step number

4.1 Governing Equation for Heat Conduction in Solid Materials

Because the heat flux in solid material is a vector quantity, the following general equation describes the heat conduction process in an arbitrary geometry:

$$\rho C_p \frac{\partial T}{\partial t} = - \nabla \cdot \bar{q} + q''' \tag{4.1-1}$$

The heat flux \bar{q} can be expressed in terms of the temperature gradient by Fourier's law of conduction [4-1]:

$$\bar{q} = - k \nabla T \tag{4.1-2}$$

Inserting Equation 4.1-2 into Equation 4.1-1 gives:

$$\rho C_p \frac{\partial T}{\partial t} = \nabla \cdot (k \nabla T) + q''' \tag{4.1-3}$$

Equation 4.1-3 does require boundary conditions on the surface of the heat structure given by:

$$- k \frac{\partial T}{\partial \zeta} = q'' \tag{4.1-4}$$

where ζ is length measured in the direction normal to the surface and q'' is the transport of thermal energy away from the surface. An adiabatic boundary condition corresponds to $q'' = 0$.

TRACG solves the heat conduction equation for the heat slabs either as a lumped slab model or using a one-dimensional model.

4.1.1 Lumped Slab Formulation of the Heat Conduction Model

The lumped slab model is used for the heat slabs internal to one vessel cell, and is given by:

$$MC_p \frac{\partial T}{\partial t} = -A \left[h_\ell (T - T_\ell) + h_v (T - T_v) \right] \quad (4.1-5)$$

No heat generation is included for the lumped slabs.

4.1.2 One-Dimensional Formulation of the Heat Conduction Model

The 1-D heat conduction model is used for the 1-D component walls and the double-sided vessel slabs. For the double-sided heat slabs connecting two axial levels, the heat conduction equation is formulated as:

$$\rho C_p \frac{\partial T}{\partial t} = \frac{\partial}{\partial z} \left(k \frac{\partial T}{\partial z} \right) + q''' \quad (4.1-6)$$

For the the double-sided heat slabs connecting two radial rings, for the 1-D component walls, and for the fuel rods, the heat conduction equation is formulated in cylindrical coordinates:

$$\rho C_p \frac{\partial T}{\partial t} = \frac{1}{r} \frac{\partial}{\partial r} \left(rk \frac{\partial T}{\partial r} \right) + q''' \quad (4.1-7)$$

The heat generation rate can either be specified through input, calculated from the kinetics model, or be a result of metal-water reaction.

The heat flux at the fuel rod or 1-D heat slab surfaces consists of convection heat transfer given by Newton's law of cooling and thermal radiation heat transfer (fuel channels only):

$$q'' = h_\ell (T - T_\ell) + h_v (T - T_v) + q''_{\text{rad}} \quad (4.1-8)$$

4.2 Finite Difference Formulation of Heat Conduction Equation

The heat conduction equation for the fuel rods and heat slabs is solved using either a lumped slab model or a 1-D model. The 1-D model can be formulated either in cartesian coordinates or in cylindrical coordinates. The lumped slab model is used for heat slabs completely internal to a single cell in the vessel component. The 1-D model using cartesian coordinates is used for heat slabs in the vessel component situated between two axial levels. The 1-D model using cylindrical coordinates is used for the fuel rods, the walls of a 1-D component, and for heat slabs in the vessel component situated between two radial rings.

4.2.1 Lumped Slab Heat Conduction

The lumped slab heat conduction model is given by:

$$\begin{aligned}
 M_w C_{pw}^n \left(T_w^{n+1} - T_w^n \right) = & \\
 & - A_w h_{w\ell} \Delta t \left[(1 - \theta) (T_w^n - T_\ell^n) + \theta (T_w^{n+1} - T_\ell^{n+1}) \right] \\
 & - A_w h_{wv} \Delta t \left[(1 - \theta) (T_w^n - T_v^n) + \theta (T_w^{n+1} - T_v^{n+1}) \right]
 \end{aligned} \tag{4.2-1}$$

In this equation, $\theta=0$ corresponds to an explicit integration of the hydraulic model, while $\theta=1$ corresponds to an implicit integration.

4.2.2 One-Dimensional Heat Conduction in Cartesian Coordinates

The 1-D heat conduction equation in cartesian coordinates is given by Equation 4.1-6. The slab is divided into N nodes as shown in Figure 4.2-1.

For the first node, $j = 1$, the linearized heat conduction equation becomes:

$$\begin{aligned}
 \Delta z \rho_1 C_{p1}^n \Delta T_{w,1}^{n+1} = & -\Delta t h_{w\ell i}^n \left[T_{w,1}^n - T_{\ell i}^n + \theta \left(\Delta T_{w,1}^{n+1} - \Delta T_{\ell i}^{n+1} \right) \right] \\
 & -\Delta t h_{wv i}^n \left[T_{w,1}^n - T_{v i}^n + \theta \left(\Delta T_{w,1}^{n+1} - \Delta T_{v i}^{n+1} \right) \right] \\
 & + \Delta t k_{1+1/2}^n \frac{T_{w,2}^n - T_{w,1}^n + \zeta \left(\Delta T_{w,2}^{n+1} - \Delta T_{w,1}^{n+1} \right)}{\Delta z} + \Delta t q''' \Delta z
 \end{aligned} \tag{4.2-2}$$

In this equation, $\theta=0$ corresponds to an explicit integration of the hydraulic model, while $\theta=1$ corresponds to an implicit integration. $\zeta=0$ corresponds to an explicit integration of the heat conduction model, while $\zeta=1$ corresponds to an implicit integration.

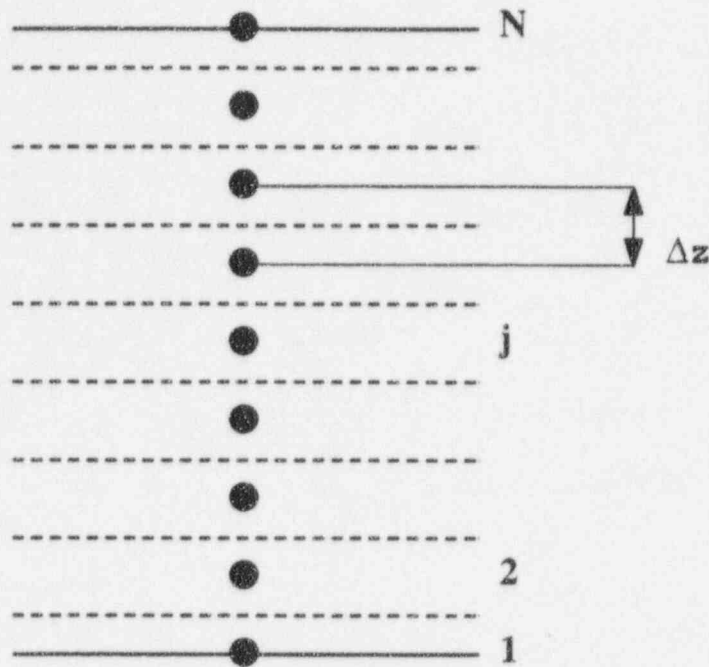


Figure 4.2-1 One-Dimensional Wall Geometry in Cartesian Coordinates

For the subsequent nodes, $1 < j < N$, the linearized heat conduction equation becomes:

$$\begin{aligned} \Delta z \rho_j C_{pj}^n \Delta T_{w,j}^{n+1} = \Delta t k_{j+\frac{1}{2}}^n \frac{T_{w,j+1}^n - T_{w,j}^n + \zeta \left(\Delta T_{w,j+1}^{n+1} - \Delta T_{w,j}^{n+1} \right)}{\Delta z} \\ + \Delta t k_{j-\frac{1}{2}}^n \frac{T_{w,j-1}^n - T_{w,j}^n + \zeta \left(\Delta T_{w,j-1}^{n+1} - \Delta T_{w,j}^{n+1} \right)}{\Delta z} \\ + \Delta t q''' \Delta z \end{aligned} \quad (4.2-3)$$

For the last node, $j = N$, the linearized heat conduction equation becomes:

$$\begin{aligned} \Delta t \rho_N C_{pN}^n \Delta T_{w,N}^{n+1} = -\Delta t h_{w\ell o}^n \left[T_{w,N}^n - T_{\ell o}^n + \theta \left(\Delta T_{w,N}^{n+1} - \Delta T_{\ell o}^{n+1} \right) \right] \\ - \Delta t h_{wv o}^n \left[T_{w,N}^n - T_{v o}^n + \theta \left(\Delta T_{w,N}^{n+1} - \Delta T_{v o}^{n+1} \right) \right] \\ + \Delta t k_{N-1/2}^n \frac{T_{w,N-1}^n - T_{w,N}^n + \zeta \left(\Delta T_{w,N-1}^{n+1} - \Delta T_{w,N}^{n+1} \right)}{\Delta z} + \Delta t q''' \Delta z \end{aligned} \quad (4.2-4)$$

4.2.3 One-Dimensional Heat Conduction in Cylindrical Coordinates

The 1-D heat conduction equation in cylindrical coordinates is given by Equation 4.1-7. The cylindrical slab is divided into N nodes, as shown in Figure 4.2-2.

For the first node, $j = 1$, the linearized heat conduction equation becomes:

$$\left(r_1 \Delta r_1 + \frac{\Delta r_1^2}{4} \right) \rho_1 C_{p1}^n \Delta T_{w,1}^{n+1} = \tag{4.2-5}$$

$$-2r_1 \Delta th_{w\ell i}^n \left[T_{w,1}^n - T_{\ell i}^n + \theta \left(\Delta T_{w,1}^{n+1} - \Delta T_{\ell i}^{n+1} \right) \right]$$

$$-2r_1 \Delta th_{wvi}^n \left[T_{w,1}^n - T_{vi}^n + \theta \left(\Delta T_{w,1}^{n+1} - \Delta T_{vi}^{n+1} \right) \right]$$

$$+ 2r_{1+1/2} \Delta tk_{1+1/2}^n \frac{T_{w,2}^n - T_{w,1}^n + \zeta \left(\Delta T_{w,2}^{n+1} - \Delta T_{w,1}^{n+1} \right)}{\Delta r_1}$$

$$+ \left(r_1 \Delta r_1 + \frac{\Delta r_1^2}{4} \right) \Delta tq'''$$

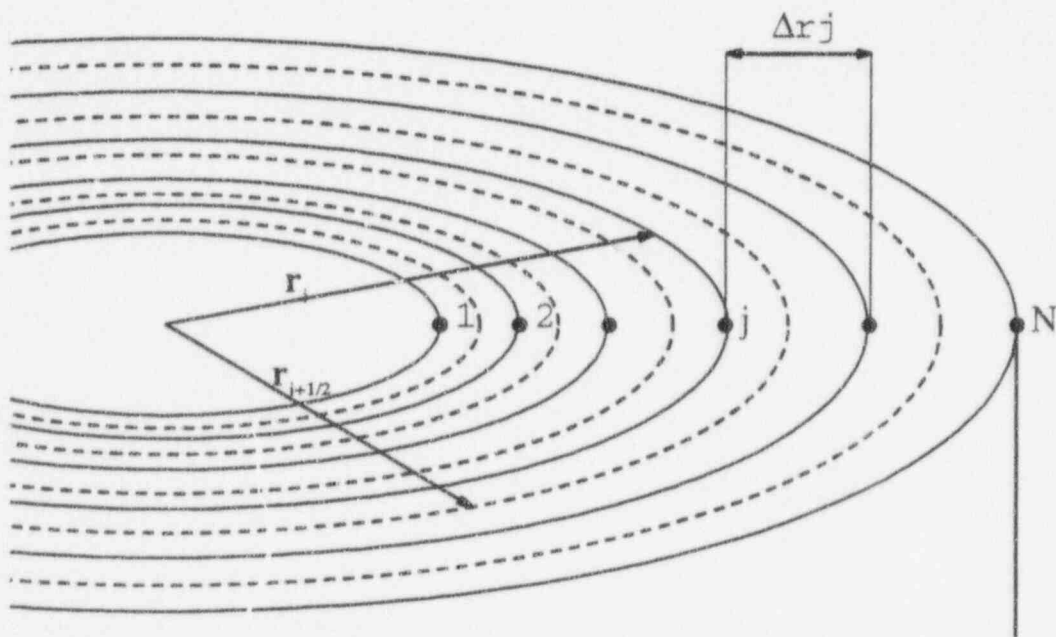


Figure 4.2-2 One-Dimensional Wall Geometry in Cylindrical Coordinates

where

$$r_{j+1/2} = \frac{r_j + r_{j+1}}{2}; \quad \Delta r_j = r_{j+1} - r_j \quad (4.2-6)$$

In this equation, $\theta=0$ corresponds to an explicit integration of the hydraulic model, while $\theta=1$ corresponds to an implicit integration. $\zeta=0$ corresponds to an explicit integration of the heat conduction model, while $\zeta=1$ corresponds to an implicit integration.

For a fuel rod (Figure 4.2-3), where $r_1 = 0$, $h_{wvi} = 0$ and $h_{wli} = 0$.

For the subsequent nodes, $1 < j < N$, the linearized heat conduction equation becomes:

$$\begin{aligned} (r_{j+1/2}^2 - r_{j-1/2}^2) \rho_j C_{pj}^n \Delta T_{w,j}^{n+1} = & \quad (4.2-7) \\ & + 2r_{j+1/2} \Delta t k_{j+1/2}^n \frac{T_{w,j+1}^n - T_{w,j}^n + \zeta (\Delta T_{w,j+1}^{n+1} - \Delta T_{w,j}^{n+1})}{\Delta r_j} \\ & + 2r_{j-1/2} \Delta t k_{j-1/2}^n \frac{T_{w,j-1}^n - T_{w,j}^n + \zeta (\Delta T_{w,j-1}^{n+1} - \Delta T_{w,j}^{n+1})}{\Delta r_{j-1}} \\ & + \Delta t q'' (r_{j+1/2}^2 - r_{j-1/2}^2) \end{aligned}$$

For the last node, $j = N$, the linearized heat conduction equation becomes:

$$\begin{aligned} \left(r_N \Delta r_{N-1} - \frac{\Delta r_{N-1}^2}{4} \right) \rho_N C_{pN}^n \Delta T_{w,N}^{n+1} = & \quad (4.2-8) \\ & - 2r_N \Delta t h_{w\ell o}^n \left[T_{w,N}^n - T_{\ell o}^n + \theta (\Delta T_{w,N}^{n+1} - \Delta T_{\ell o}^{n+1}) \right] \\ & - 2r_N \Delta t h_{wv o}^n \left[T_{w,N}^n - T_{v o}^n + \theta (\Delta T_{w,N}^{n+1} - \Delta T_{v o}^{n+1}) \right] \\ & + 2r_{N-1/2} \Delta t k_{N-1/2}^n \frac{T_{w,N-1}^n - T_{w,N}^n + \zeta (\Delta T_{w,N-1}^{n+1} - \Delta T_{w,N}^{n+1})}{\Delta r_{N-1}} \\ & + \Delta t q'' \left(r_N \Delta r_{N-1} - \frac{\Delta r_{N-1}^2}{4} \right) \end{aligned}$$

For a fuel rod (Figure 4.2-3), special considerations need to be given to the gap between the fuel pellet and the cladding. For the last node (M) in the fuel, the linearized heat conduction equation becomes:

$$\left(r_M \Delta r_{M-1} - \frac{\Delta r_{M-1}^2}{4} \right) \rho_M C_{pM}^n \Delta T_{w,M}^{n+1} = \tag{4.2-9}$$

$$+ 2r_{M+1/2} \Delta h_{\text{gap}}^n \left[T_{w,M+1}^n - T_{w,M}^n + \zeta \left(\Delta T_{w,M+1}^{n+1} - \Delta T_{w,M}^{n+1} \right) \right]$$

$$+ 2r_{M-1/2} \Delta t k_{M-1/2}^n \frac{T_{w,M-1}^n - T_{w,M}^n + \zeta \left(\Delta T_{w,M-1}^{n+1} - \Delta T_{w,M}^{n+1} \right)}{\Delta r_{M-1}}$$

$$+ \Delta t q'' \left(r_M \Delta r_{M-1} - \frac{\Delta r_{M-1}^2}{4} \right)$$

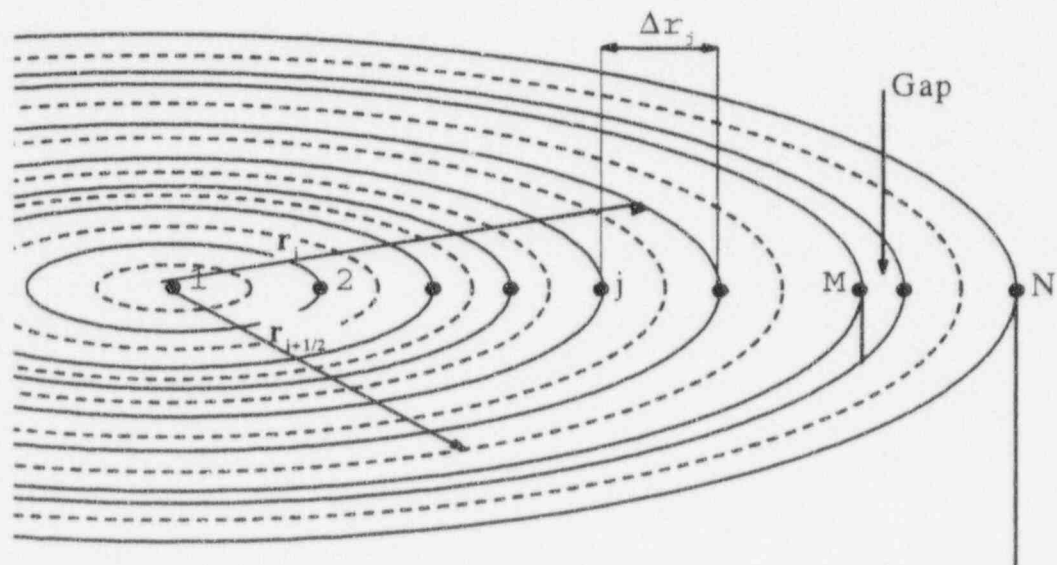


Figure 4.2-3 One-Dimensional Fuel Rod Geometry

For the first node in the cladding (M+1), the linearized heat conduction equation becomes:

$$\begin{aligned}
 & \left(r_{M+1} \Delta r_{M+1} + \frac{\Delta r_M^2}{4} \right) \rho_{M+1} C_{pM+1}^n \Delta T_{w,M}^{n+1} = \\
 & + 2r_{M+3/2} \Delta t k_{M+3/2}^n \frac{T_{w,M+2}^n - T_{w,M+1}^n + \zeta \left(\Delta T_{w,M+2}^{n+1} - \Delta T_{w,M+1}^{n+1} \right)}{\Delta r_{M+1}} \quad (4.2-10) \\
 & + 2r_{M+1/2} \Delta t h_{gap}^n \left[T_{w,M}^n - T_{w,M+1}^n + \zeta \left(\Delta T_{w,M}^{n+1} - \Delta T_{w,M+1}^{n+1} \right) \right] \\
 & + \Delta t q''' \left(r_{M+1} \Delta r_{M+1} + \frac{\Delta r_{M+1}^2}{4} \right)
 \end{aligned}$$

4.3 References

- 4-1 F.P. Incropera and D.P. DeWitt, *Fundamentals of Heat Transfer*, John Wiley & Sons, New York, 1981.

5.0 Flow Regime Map

The two-fluid model used in TRACG requires the use of auxiliary relations for the constitutive correlations in the basic conservation equations. The constitutive correlations express the rates of exchange of mass, momentum, and energy between each phase and its surroundings. These correlations take on different forms for different flow patterns. As an example, two-phase flow patterns affect the rate of vapor generation in direct contact with the walls, and this term is important in determining mass exchange between liquid and vapor. Both the exchange of energy and momentum at the interface between vapor and liquid depend on the interfacial area per unit volume and the topology of the two-phase flow. For these reasons, it is important to identify the flow regime in each hydraulic cell before proceeding with the solution of the flow equations for that cell.

The nomenclature used in this section is given below:

Nomenclature

A	cross sectional area
C_o	distribution parameter
D	diameter
D_h	hydraulic diameter
E	entrainment
E_f	fraction of wall in boiling transition
g	acceleration of gravity
G	mass flux
g_T	component of g perpendicular to flow axis
h	height of liquid in pipe
j	volumetric flux
P	pressure
Re	Reynolds Number
v	velocity
v_{gi}	drift flux velocity

Greek Symbols

α	void fraction
ρ	density
σ	surface tension
μ	dynamic viscosity

Subscripts

a	annular flow
bc	bubbly/churn flow
ℓ	liquid
tran	transition to annular flow
v	vapor

Superscript

*	Superficial velocity (e.g., j_v^*)
---	---------------------------------------

5.1 Basis for Flow Regime Map in TRACG

The constitutive correlations for shear and heat transfer in TRACG use a relatively simple flow regime map, which consists basically of two distinct patterns: (a) liquid-continuous at low void fractions and (b) vapor-continuous at high void fractions with a transition zone in between. The liquid-continuous regime applies to the single-phase liquid flow, bubbly/churn, and inverted annular flows. The vapor-continuous regime applies to the annular, dispersed droplet flow and single-phase vapor flow regimes. The transition regime involves churn to annular and churn to droplet, depending on the void fraction, flow rate and other variables.

The criterion for transition from the liquid-continuous zone is defined in terms of a transition void fraction, α_{tran} , that is a function of flow conditions and geometry.

This flow regime map is based on one that was originally suggested by Ishii [5-1] in his derivations of the drift-flux model. Ishii suggested two simple flow regime transition criteria that, in his words, "are based on the relative motion between phases and are consistent with the concept of drift-flux model".

Transition between bubbly/churn and annular flow takes place when the liquid in the film (or entrained droplets) can be lifted relative to the liquid velocity in the bubbly/churn flow regime. Transition between annular flow and dispersed droplet flow is given by the onset of entrainment. For low vapor flow, annular flow will exist and, as the vapor flux is increased, more and more entrainment will occur, causing a gradual transition to droplet flow.

The flow regime map (Figure 5.1-1) that was originally developed for vertical flow is assumed to be usable for both vertical and horizontal flow components. For horizontal flow with low velocities, however, stratification can occur. Transition to stratified flow is based on a critical Froude number.

5.1.1 Churn to Annular Transition

5.1.1.1 Technical Basis and Assumptions

The transition between churn flow and annular flow has been widely analyzed [5.1-5.4]. The criterion for transition is when the liquid in the film can be lifted by the vapor flow relative to the liquid in the churn flow regime. This criterion is satisfied at the void fraction where the same velocity is predicted for churn flow as for annular flow. Using the drift flux model, the vapor velocity for churn flow is given by:

$$v_{v, bc} = C_{o, bc}j + \bar{v}_{gj, bc} \tag{5.1-1}$$

Similarly, for annular flow, the vapor velocity is given by:

$$v_{v, a} = C_{o, a}j + \bar{v}_{gj, a} \tag{5.1-2}$$

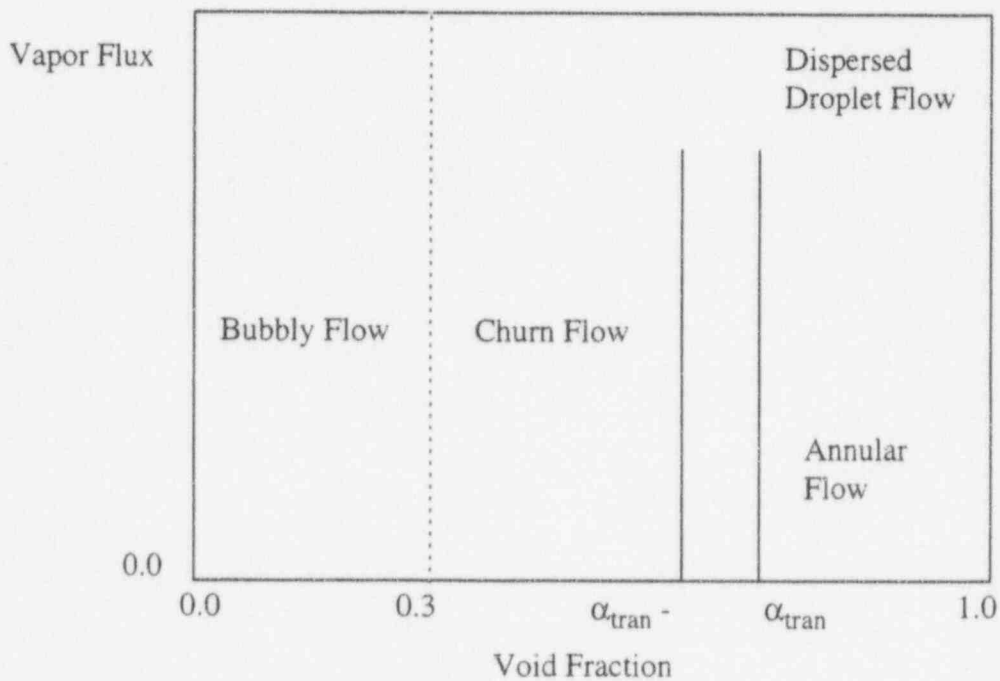


Figure 5.1-1 Flow Regime Map

The intersection of the two correlations or the condition where the velocity is the same in the two flow regimes is given by:

$$C_{o,bc}j + \bar{v}_{gj,bc} = C_{o,a}j + \bar{v}_{gj,a} \quad (5.1-3)$$

In situations involving transition to annular flow, j is relatively large, and, consequently, the dominant terms in this equation are the first term on the left-hand side and the first term on the right-hand side (in a BWR fuel channel under normal operating conditions, j is on the order of 5-10 m/sec at the transition to annular flow, while $\bar{v}_{gj} < 1$ m/sec). Neglecting \bar{v}_{gj} in the above equation and eliminating j , one gets:

$$C_{o,bc} = C_{o,a} \quad (5.1-4)$$

For annular flow, C_o is given by (Section 6.1.4):

$$C_{o,a} = 1 + \frac{1 - \alpha}{\alpha + \left(\frac{1 + 75(1 - \alpha) \frac{\rho_v}{\rho_\ell}}{\sqrt{\alpha}} \right)^{0.5}} \quad (5.1-5)$$

which, according to Ishii [5-1], can be approximated to:

$$C_{o,a} = 1 + \frac{1 - \alpha}{\alpha + 4 \sqrt{\frac{\rho_v}{\rho_\ell}}} \quad (5.1-6)$$

Inserting this expression in Equation 5.1-4 and solving for the void fraction, one gets:

$$\alpha_{\text{tran}} = \left(1 + 4 \sqrt{\frac{\rho_v}{\rho_\ell}} \right) \frac{1}{C_{o,bc}} - 4 \sqrt{\frac{\rho_v}{\rho_\ell}} \quad (5.1-7)$$

where $C_{o,bc}$ is given by (Section 6.1.3):

$$C_{o,bc} = C_{\infty,bc} - (C_{\infty,bc} - 1) \sqrt{\frac{\rho_v}{\rho_\ell}} \quad (5.1-8)$$

where

$$C_{\infty,bc} = 1.393 - 0.015 \ln(\text{Re}_\ell) \quad (5.1-9)$$

$$\text{Re}_\ell = \frac{GD_h}{\mu_\ell} \quad (5.1-10)$$

5.1.1.2 Model as Coded

The calculation of the transition void fraction to annular flow is encoded as described by Equations 5.1-7 - 5.1-10 in Section 5.1.1.1, with the limitations on $C_{o,bc}$ as described in Section 6.1.3.2.

In order to avoid discontinuities in the interfacial shear at the transition to annular flow, the transition is implemented to take place over a void fraction interval of 0.1:

$$\{\alpha_{\text{tran}} - 0.1, \alpha_{\text{tran}}\} \quad (5.1-11)$$

Churn flow exists for $\alpha < \alpha_{\text{tran}} - 0.1$ and annular flow exists for $\alpha > \alpha_{\text{tran}}$. A linear interpolation is performed for the constitutive correlations for shear and heat transfer over this interval between the correlations for churn flow and the correlations for annular flow.

5.1.1.3 Applicability

Several criteria for transition to annular flow have been proposed. Mishima and Ishii [5-4] proposed two criteria: (a) flow reversal in the liquid film section along large bubbles, and (b) destruction of liquid slugs or large waves by entrainment. A simpler criterion was proposed by Wallis [5-3], in which the transition to annular flow is given in terms of the superficial velocities:

$$j_v^* > 0.4 + 0.6j_\ell^* \quad (5.1-12)$$

where:

$$j_v^* = \frac{j_v \sqrt{\rho_v}}{(gD_h \Delta\rho)^{0.5}} \quad \text{and} \quad j_\ell^* = \frac{j_\ell \sqrt{\rho_\ell}}{(gD_h \Delta\rho)^{0.5}}$$

The TRACG criterion (Equation 5.1-11) and the Wallis criterion (Equation 5.1-12) have been compared to data by Bergles and Suo [5-5] in Figure 5.1-2. The lower bound of the transition regime (Equation 5.1-11), where the transition to annular flow is initiated, is in good agreement with the data and the Wallis criterion. It should be kept in mind that flow regime maps are based on visual interpretation of test data, which tend to be fairly subjective. The main assessment of the flow regime map should be done in connection with the interfacial shear model and based on the accuracy of void fraction prediction. As will be shown in Section 6.1, the void fraction is predicted quite accurately, generally to within a few percent.

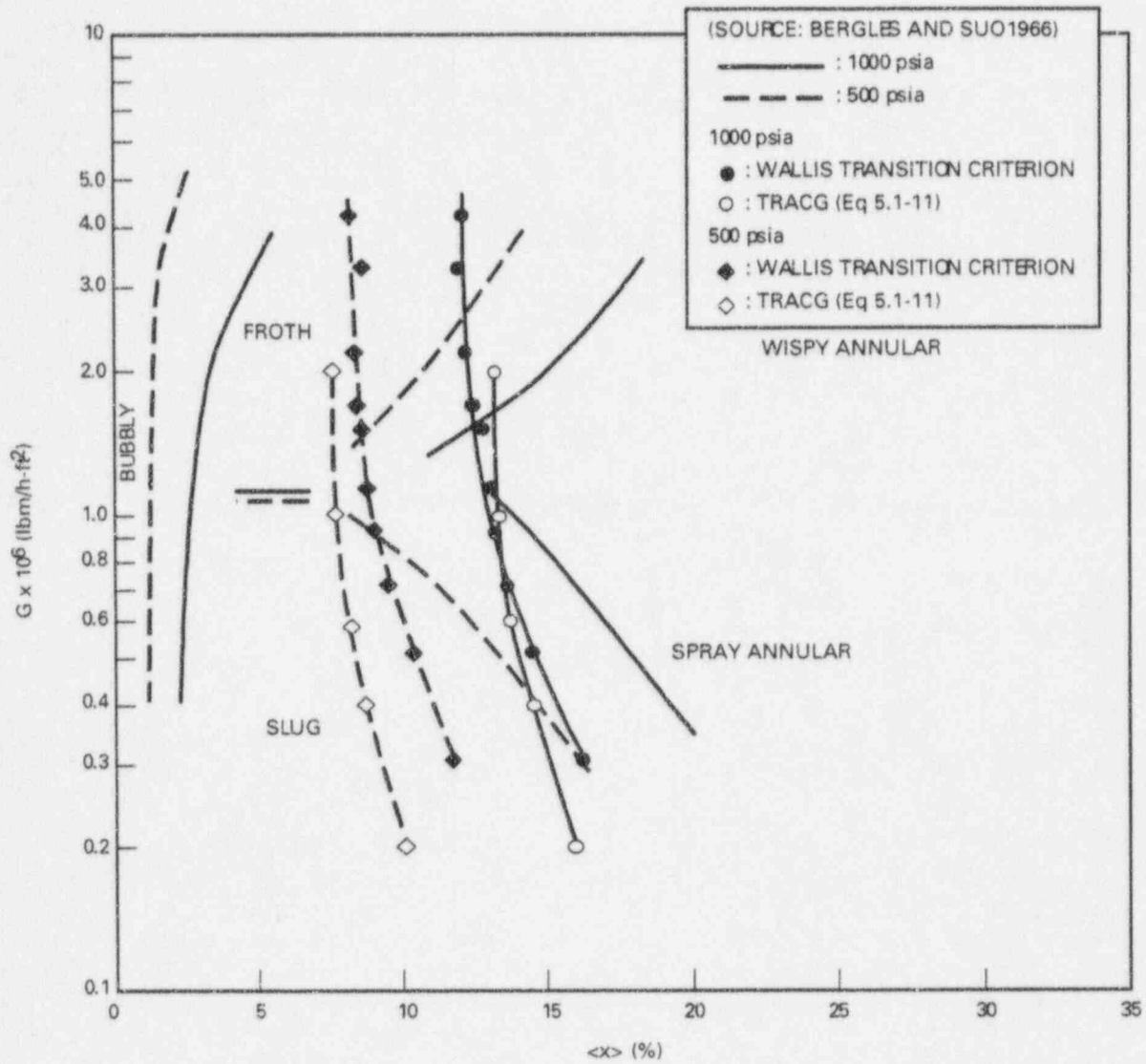


Figure 5.1-2 Flow Regime Map

5.1.2 Entrainment

The transition from a purely annular flow regime to an annular flow with dispersed droplets is given by the onset of entrainment.

5.1.2.1 Technical Basis and Assumptions

The entrainment correlation proposed by Ishii [5-6] has been adopted:

$$E = \text{tgh}(\eta) = \text{tgh}\left(7.5 \cdot 10^{-7} (j_v^*)^{2.5} (D^*)^{1.25} \text{Re}_\ell^{0.25}\right) \tag{5.1-13}$$

where

$$j_v^* = \frac{j_v}{\left[\frac{\sigma \Delta \rho g \left(\frac{\rho_v}{\Delta \rho} \right)^{0.667}}{\rho_v^2} \right]^{0.25}} \quad (5.1-14)$$

$$D^* = D_h \sqrt{\frac{g \Delta \rho}{\sigma}} \quad (5.1-15)$$

$$Re_\ell = \frac{\rho_\ell j_\ell D_h}{\mu_\ell} \quad (5.1-16)$$

5.1.2.3 Applicability

Ishii's correlation has been compared to many experimental data [5-6] for air-water systems covering the ranges:

$$0.1 < P < 0.4 \text{ MPa}$$

$$0.0095 < D_h < 0.032 \text{ m}$$

$$370 < Re_\ell < 6400$$

$$j_v < 100 \text{ m/sec}$$

The main shortcoming of the database for Ishii's entrainment correlation is the relatively limited pressure range at close to atmospheric pressure. For high pressure, however, the entrainment correlation has been indirectly validated through comparisons to void fraction data (Section 6.1.8). The excellent prediction of void fraction data ($\pm 2\%$) for pipes and rod bundles justifies the use of Ishii's entrainment correlation for high pressures (up to 7.0 MPa).

5.1.3 Horizontal Flow

For horizontal pipes, a transition from bubbly flow to stratified flow is introduced. The transition is similar to the transition to annular flow in the sense that it represents a transition from dispersed flow to separated flow. The transition from stratified to dispersed flow is derived from the condition where an instability will develop for the free surface in stratified flow based on a critical Froude number.

5.1.3.1 Technical Basis and Assumptions

For vapor flowing over a free surface, an instability will develop if the perturbation in the vapor pressure as predicted by Bernoulli's equation due to a small perturbation in the liquid level, δ , exceeds the static head corresponding to the level perturbation:

$$\rho_v v_v^2 \frac{\delta}{\alpha D_h} > \delta \Delta \rho g_T \quad (5.1-21)$$

where g_T is the component of the gravity vector perpendicular to the pipe. For a horizontal pipe $g_T = g$, while $g_T = 0$ for a vertical pipe. In general, $g_T = g \cos(\theta)$, where θ is the inclination of the pipe.

The condition for instability of the free surface is thus given by:

$$\frac{\rho_v v_v^2}{\alpha D_h \Delta \rho g_T} = 1 \quad (5.1-22)$$

or

$$\alpha_{\text{strat}} = \frac{\rho_v v_v^2}{\Delta \rho g_T D_h} \quad (5.1-23)$$

5.1.3.2 Model as Coded

Analogous to the transition to annular flow, a transition region is implemented to avoid discontinuities in the constitutive correlations. The transition is implemented to take place over a void fraction interval of 0.1.

$$\{\alpha_{\text{strat}}, \alpha_{\text{strat}} + 0.1\} \quad (5.1-24)$$

Dispersed flow exists for $\alpha < \alpha_{\text{strat}}$ and stratified flow exists for $\alpha > \alpha_{\text{strat}} + 0.1$. A linear interpolation is performed for the constitutive correlations for shear and heat transfer over this interval between the correlations for bubbly/churn flow and the correlations for stratified flow.

5.1.3.3 Applicability

Mishima and Ishii [5-8] have compared various modified Helmholtz models with data for predicting the transition between stratified and dispersed flow. The current TRACG model is a simplification of the term for the critical gas velocity recommended by Taitel and Dukler [5-7], where the coefficient $\left(1 - \frac{h_\ell}{D}\right)$ is approximated by the void fraction α and $\frac{dA_\ell}{dh_\ell}$ is approximated by $\frac{\pi}{4} D$.

A comparison of the TRACG model given by Equations 5.1-23 and 5.1-24 to Ishii's theory and the data of Wallis and Dobson [5-9] brackets the data for low flow rates and slightly underpredicts the data by about 0.2 for high flow rates. It should be noted that horizontal two-phase flow is not very significant for BWR applications, and, considering the reasonably good comparison to data, it can be concluded that the correlation for transition to stratified flow is applicable to BWRs.

5.2 Assessment and BWR Applicability

Numerous flow regime maps exist in the literature that could be used for comparisons. Many are not mechanistic and are based on subjective observations or simply based on correlations of data, often in terms of j_ℓ and j_v . Assumptions about the interfacial drag or relative velocity are required to convert this type of map to the type of map used in TRACG. Some assessments have been given in Sections 5.1.1.3, 5.1.2.3 and 5.1.3.3. The trends are generally correct, and, due to the subjective nature of determining the transition boundaries, reasonably accurate.

It is important to note that the flow regime *per se* is not used by the field equations, but rather the values for the interfacial parameters. The main assessment of the flow regime map should be done in connection with the interfacial shear model and based on the accuracy of the void fraction prediction.

In Section 6.1 it is shown that the void fraction is predicted very accurately, generally within 2-5%. Consequently, the applicability of the flow regime map is identical to the applicability of the interfacial shear mode:

$$0.1 < P < 10 \text{ MPa}$$

$$0 < G < \text{greater than } 2000 \text{ kg/m}^2\text{-sec}$$

$$\text{Onset of subcooled boiling} < T_\ell < T_{\text{sat}}$$

$$0.01 < D_h < 1.2\text{+m}$$

5.3 References

- 5-1. M. Ishii, *One-Dimensional Drift Flux Model and Constitutive Equations for Relative Motion Between Phases in Various Two-Phase Flow Regimes*, ANL-77-47, 1977.
- 5-2. Taitel, D. Bovera and A.E. Dukler, *Modeling Flow Pattern Transitions for Steady Upward Gas-Liquid Flow in Vertical Tubes*, AICLE Journal, 1980, 26, No. 3, pp. 345-354.
- 5-3. L. Wallis, *One-Dimensional Two-Phase Flow* McGraw Hill, 1969.
- 5-4. K. Mishima and M. Ishii, *Flow Regime Transition Criteria for Upward Two-Phase Flow in Vertical Tubes*, International Journal of Heat and Mass Transfer, 27 (5), 723-737, 1984.
- 5-5. A.E. Bergles and M. Suo, *Boiling Water Flow Regimes at High Pressures*, Proceedings of the 1966 Heat Transfer and Fluid Mechanics Institute, Stanford University Press, 1966.
- 5-6. M. Ishii and K. Mishima, *Correlation for Liquid Entrainment in Annular Two-Phase Flow of Low Viscous Fluid*, ANL/KAS/LWR 81-2, March 1981.
- 5-7. Y. Taitel and A.E. Dukler, AICHE J. 22 (3), 47-55, 1976.
- 5-8. K. Mishima and M. Ishii, *Theoretical Predictions of Onset of Horizontal Slug Flow*, J. Fluids Eng., 102, 441-445, December 1980.
- 5-9. G. B. Wallis and J. E. Dobson, *The Onset of Slugging in Horizontal Stratified Air-Water Flow*, Int. J. Multiphase Flow, Vol 1, 1973, p 173.

6.0 Models and Correlations

To close the set of basic equations described in Section 3, a set of constitutive correlations describing interfacial shear and heat transfer, wall friction and heat transfer is needed. These correlations define the rates of exchange of mass, momentum and energy between the phases and their surroundings. The correlations depend on the flow regime, as they take on different forms for the different flow patterns. The flow regime map defining the flow patterns as a function of the thermal-hydraulic conditions was described in Section 5. This section describes the constitutive correlations for interfacial shear and heat transfer, wall friction and heat transfer for the individual flow patterns.

The ultimate objective of the TRACG code is to analyze a wide variety of BWR transients and LOCAs. The models and correlations described in this section must be adequate for this purpose over the range of expected conditions. These ranges were derived by considering reactor startup conditions (at criticality) for the lower bound for the flow rates in the reactor vessel. The upper bound flow rates generally correspond to the reactor operation at rated conditions. Break flow following a LOCA can also result in the highest flow rate in the region of the break. For the containment, the steamline break provides an upper bound on flow rates. The void fraction range considers depressurization during a LOCA and possible uncover because of loss of inventory.

In the nomenclature, the term gas implies a general mixture of steam and noncondensable gases. The subscript v will denote a property or parameter applying to the gas mixture; the subscript s indicates a quantity applying specifically to steam, and the subscript a signifies the summation of all noncondensable gases. The subscripts f and g signify saturated liquid and steam, respectively. The following list of nomenclature applies to Section 6.

Nomenclature

a	constant; absorption coefficient; sonic velocity
A	area; constant
B	constant
B	radiosity
C	constant
C_D	drag coefficient
C_0	drift flux model distribution parameter
C_p	specific heat at constant pressure
C_v	specific heat at constant volume
CHF	critical heat flux
d_i	interfacial area per unit volume
D	diameter
D_Q	thermal diameter
e	specific total energy
E	entrainment
ECPR	experimental critical power ratio
F	wall shear; factor in Chen correlation; radiation view factor
f_{lv}	drag force per unit volume between gas and liquid phase
f_1	correlation factor for pure steam
f_2	correlation factor for noncondensable gas
f_R	friction factor
F_s	subcooled correction factor for modified Zuber correlation
g	acceleration of gravity
G	mass flux
Gr	Grashof number = $\rho^2 g \beta L^3 \Delta T / \mu^2$
h	heat transfer coefficient; specific enthalpy
H	incoming radiation
h_L	dynamic head loss term

h_{fg}	$h_g - h_f$
I	Bessel function
j^*	superficial velocity
k	thermal conductivity; constant
L	length
M_v	interfacial drag between the two phases due to difference in velocity
n	constant; variable
Nu	Nusselt number = $h D / k$
P	pressure
PCT	peak cladding temperature
Pe	Peclet number = $G D C_p / k$
Pr	Prandtl number = $\mu C_p / k$
q''	heat flux
q'''	volumetric heat generation rate
R	local peaking pattern parameter; gas constant
Re	Reynolds number = $G D / \mu$ or as defined in text
s	thickness of oxide layer
S	suppression factor in Chen correlation; specific entropy
t	time
T	temperature
v	velocity
v_{gj}	drift flux velocity
V	variable in GEXL correlation
W	molecular weight
We	Weber number = $\rho v^2 L / \sigma$
x	flow quality; noncondensable mass fraction
X	variable defined in text
Y	mole fraction; variable used in model as coded subsections
z	coordinate direction

Greek Symbols

α	void fraction
β	heat transfer coefficient from steam to droplets; volumetric coefficient of thermal expansion
χ	inverse of the Lockhart-Martinelli parameter
δ	film thickness

ε	pumping factor; emissivity
$\Phi^2_{\ell 0}$	two-phase multiplier
$\Phi^2_{\ell 0 \text{ hom}}$	homogeneous two-phase multiplier
γ	specific heat ratio = C_p / C_v ; variable in Section 6.6.8
Γ_g	volumetric vapor generation rate
Γ	mass flow of condensate per unit circumference
μ	viscosity; bias; anisotropic correction factor
ρ	density
σ	surface tension; standard deviation; Stefan-Boltzmann constant
τ	shear; transmissivity

Subscripts

a	all noncondensibles
A	annular
air	air
b	bubbly
B	bulk
BER	Berenson
c	critical
d	droplet
e	equilibrium
E	entrainment fraction
evap	evaporation
f	saturated liquid
FB	film boiling
free	free or natural convection
g	saturated steam
h	hydraulic
He	helium
HE	HEM critical flow model
i	interface
L	level
ℓ	liquid (subcooled)
ℓd	liquid departure
lam	laminar
m	mixture

mac	macroscopic
mic	microscopic
min	minimum
n	specific noncondensable gas component
NB	nucleate boiling
NC	nucleate boiling at CHF
r	relative
ref	reference
s	steam
sat	saturated
t	throat
TB	transition boiling
TP	two phase
tran	transition
turb	turbulent
u	universal
v	vapor
w	wall
Zr	Zirconium

Superscripts

I	isotropic
A	anisotropic

6.1 Interfacial Shear

Calculation of interfacial shear and momentum exchange across the interface is a necessary part of the two-fluid equation system solution. In specific terms, the interfacial shear model calculates the variable $f_{\ell v}$ in the equations of motion for vapor and liquid (Section 3). $f_{\ell v}$ represents the drag force, per unit volume, between the phases; and it is expressed in terms of average phasic velocity difference:

$$f_{\ell v} = c_i |\bar{v}_r| \bar{v}_r \quad (6.1-1)$$

where c_i is the local average interfacial drag coefficient between phases (per unit volume) and \bar{v}_r is the void-weighted average velocity difference between vapor and liquid. The local values of c_i and \bar{v}_r are dependent on flow regime, void fraction, and properties of vapor and liquid (c_i is a function of \bar{v}_r). Equation 6.1-1 gives only the generic form of $f_{\ell v}$ (its specific forms are described later). The basic principle of these calculations is to identify the prevailing flow

pattern at each hydraulic junction and then apply specific correlations for relative phasic velocity and interfacial drag to determine the momentum exchange across the interface at that junction.

6.1.1 Background

The bulk of the data available for the evaluation of the interfacial shear and the wall friction are void fraction and pressure drop data. These are also the parameters that are important and must be described accurately in a best-estimate analysis of the two-phase flow in a BWR. More fundamental data are available for the shear and the interfacial forces, and extensive basic research is continuing. However, a comprehensive set of models for the shear and interfacial forces for all flow regimes does not presently exist, and the models that do exist are primarily for idealized flow regimes. For these reasons, the development of the constitutive correlations for the interfacial shear is based on the very large database that exists for void fractions and pressure drop. The correlations are based on the following:

- For adiabatic and steady-state conditions, the two-fluid model and the drift flux model are equivalent, and drift flux parameters can be used to characterize the relative velocity, and the phase and flow distributions.
- The correlations for the interfacial shear and drag, as well as wall friction, as derived from adiabatic steady-state conditions, are applicable for transient conditions.

The interfacial shear correlations are based on the set of drift flux correlations developed by Ishii [6.1-3] from void fraction data available in literature. These models for the interfacial shear are validated through the qualification against steady-state and transient void fraction data.

6.1.2 Relation to Drift Flux Parameters

The relation between interfacial forces and drift flux parameters is discussed in detail in Reference 6.1-2. A brief summary will be given in the following subsections.

6.1.2.1 Shear and Wall Friction

The presence of wall friction creates a shear field in the two-phase flow. This shear field will interact with both phases, and thus create an interfacial force, which has its origin in the wall friction. For example, for steady-state bubbly flow, the momentum equations can be written as:

$$0 = -\alpha \frac{\partial P}{\partial x} - \alpha \rho_v g - f_{\ell v} \quad \text{[for the vapor phase]}$$

$$0 = -(1 - \alpha) \frac{\partial P}{\partial x} - (1 - \alpha) \rho_\ell g + f_{\ell v} - F_w \quad \text{[for the liquid phase]}$$

where $f_{\ell v}$ represents the shear at the interface, and F_w represents the shear between the wall and the liquid. If the pressure gradient is eliminated from the above equations, one obtains:

$$f_{\ell v} = \Delta \rho g \alpha (1 - \alpha) + \alpha F_w$$

Consequently, if the interfacial shear above was a function only of the relative velocity between the phases, the relative velocity would be dependent upon the wall friction or the Reynolds number. This, however, is not the case. Data [6.1-3, 6.1-4] indicate that the drift velocity is virtually independent of the flow rate. The interfacial shear, therefore, consists of another term with its origin in the wall friction besides a term that is a function of the relative velocity.

Following Ishii's notation [6.1-2], the local time-averaged momentum equations for the vapor and liquid phases are:

$$\alpha \rho_v \left(\frac{\partial \bar{v}_v}{\partial t} + \bar{v}_v \cdot \nabla \bar{v}_v \right) = -\alpha \nabla P + \alpha \nabla \cdot \bar{\tau} - \alpha \rho_v \bar{g} - \bar{M}_v \quad (6.1-2)$$

$$(1 - \alpha) \rho_\ell \left(\frac{\partial \bar{v}_\ell}{\partial t} + \bar{v}_\ell \cdot \nabla \bar{v}_\ell \right) = -(1 - \alpha) \nabla P + (1 - \alpha) \nabla \cdot \bar{\tau} - (1 - \alpha) \rho_\ell \bar{g} + \bar{M}_v \quad (6.1-3)$$

Here the interfacial mass transfer has been neglected and it has been assumed that each phase, as well as the interface, has the same pressure.

For one-dimensional flow, Equations 6.1-2 and 6.1-3 degenerate to:

$$\alpha \rho_v \left(\frac{\partial v_v}{\partial t} + v_v \cdot \nabla v_v \right) = -\alpha \frac{\partial P}{\partial z} + \alpha \nabla \cdot \bar{\tau}_z - \alpha \rho_v g - M_v \quad (6.1-4)$$

$$(1 - \alpha) \rho_\ell \left(\frac{\partial v_\ell}{\partial t} + v_\ell \cdot \nabla v_\ell \right) = -(1 - \alpha) \frac{\partial P}{\partial z} + (1 - \alpha) \nabla \cdot \bar{\tau}_z - (1 - \alpha) \rho_\ell g + M_v \quad (6.1-5)$$

An interpretation of the various terms on the right-hand side of Equations 6.1-4 and 6.1-5 can be obtained from Figure 6.1-1.

For the gas equation, the interpretation of the various terms is as follows:

$-\alpha \frac{\partial P}{\partial z}$ = the force on the gas due to the pressure gradient in the z-direction (the pressure is assumed to be the same for each phase)

$\alpha \nabla \cdot \bar{\tau}_z$ = the force on the gas due to the shear at the surface of the incremental volume (α is the fraction of the surface which is occupied by the gas). It is assumed that the averaged shear tension is the same for each phase, which is reasonable, because, except for surface tension and mass transfer effects, the shear is a continuous function.

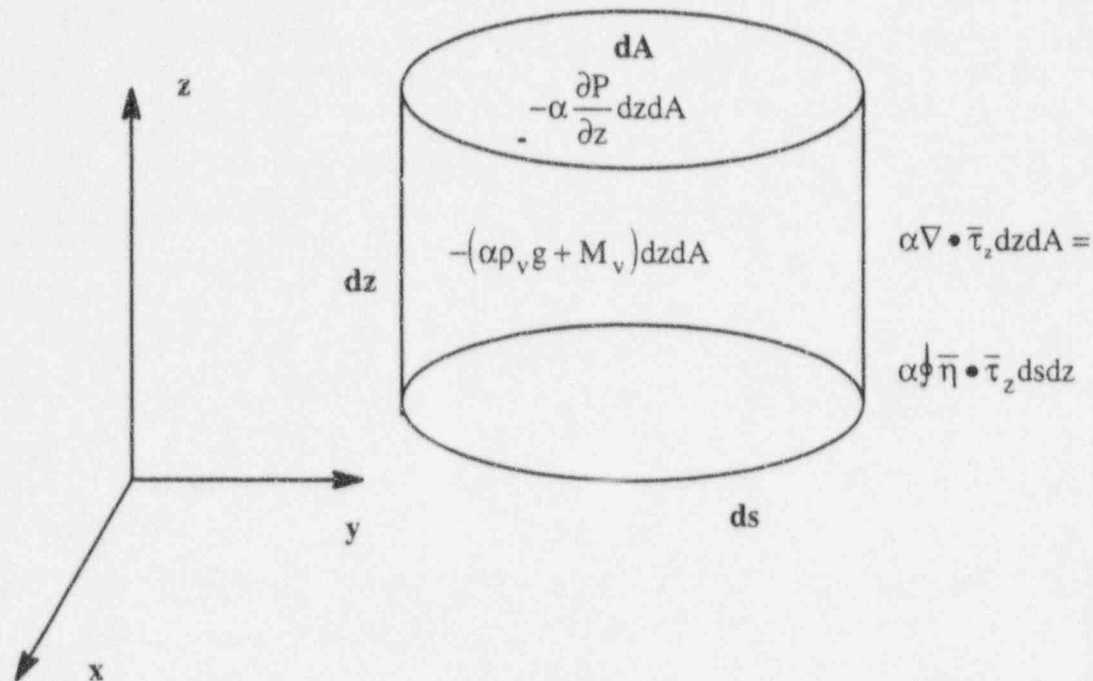


Figure 6.1-1. Right-Hand Side of Vapor Momentum Equation

$-\alpha \rho_v g$ = the body force, due to gravity, on the gas.

M_v = the interfacial drag between the phases inside the incremental volume due to a local difference in the phase velocities.

For adiabatic steady-state conditions, Equations 6.1-4 and 6.1-5 reduce to:

$$\alpha \frac{\partial P}{\partial z} - \alpha \nabla \cdot \bar{\tau}_z + \alpha \rho_v g + M_v = 0 \quad (6.1-6)$$

$$(1 - \alpha) \frac{\partial P}{\partial z} - (1 - \alpha) \nabla \cdot \bar{\tau}_z + (1 - \alpha) \rho_l g - M_v = 0 \quad (6.1-7)$$

When Equations 6.1-6 and 6.1-7 are added,

$$\frac{\partial P}{\partial z} - \nabla \cdot \bar{\tau}_z + ((1 - \alpha) \rho_l + \alpha \rho_v) g = 0 \quad (6.1-8)$$

The integration of this equation over the cross section, assuming that the densities and the pressure gradient are constant across the flow area, results in:

$$A \frac{\partial P}{\partial z} - \int_S \bar{\eta} \cdot \bar{\tau}_z ds + A(\langle 1 - \alpha \rangle \rho_\ell + \langle \alpha \rangle \rho_v)g = 0 \quad (6.1-9)$$

The integral is along the boundary (S), $\bar{\eta}$ is the normal to the boundary, and Gauss's theorem has been used. When Equations 6.1-8 and 6.1-9 are combined,

$$\nabla \cdot \bar{\tau}_z = \frac{1}{A} \int \bar{\eta} \cdot \bar{\tau}_z ds - \Delta \rho (\alpha - \langle \alpha \rangle) \quad (6.1-10)$$

Integrating the momentum equation for the gas over the cross section results in:

$$\langle \alpha \rangle A \frac{\partial P}{\partial z} - \int_A \alpha \nabla \cdot \bar{\tau}_z dA + \langle \alpha \rangle A \rho_v g + \int_A M_v dA = 0 \quad (6.1-11)$$

The second term in this equation can be evaluated using Equation 6.1-10:

$$\int_A \alpha \nabla \cdot \bar{\tau}_z dA = \langle \alpha \rangle \int \bar{\eta} \cdot \bar{\tau}_z ds - A \Delta \rho g \langle (\alpha - \langle \alpha \rangle)^2 \rangle \quad (6.1-12)$$

The left side of Equation 6.1-12 is the total amount of shear on the vapor phase. The first term on the right side is the void fraction times the wall friction. The second term is an induced shear stress due to the variance of the void fraction across the flow area:

$$f_i = A \Delta \rho g \langle (\alpha - \langle \alpha \rangle)^2 \rangle \quad (6.1-13)$$

and from which

$$\int_A \alpha \nabla \cdot \bar{\tau}_z dA = -\langle \alpha \rangle F_w - f_i \quad (6.1-14)$$

Inserting this into Equation 6.1-11 gives:

$$\langle \alpha \rangle A \frac{\partial P}{\partial z} + \langle \alpha \rangle F_w + f_i + \langle \alpha \rangle A \rho_v g + \int_A M_v dA = 0 \quad (6.1-15)$$

Similarly, for the liquid momentum equation,

$$\langle 1 - \alpha \rangle A \frac{\partial P}{\partial z} + \langle 1 - \alpha \rangle F_w - f_i + \langle 1 - \alpha \rangle A \rho_\ell g - \int_A M_v dA = 0 \quad (6.1-16)$$

The physical interpretation of the various terms in the integrated momentum equation for the gas are as follows:

$$\langle \alpha \rangle A \frac{\partial P}{\partial z} = \text{the force due to the pressure gradient}$$

$$\langle \alpha \rangle F_w = \text{induced shear stress due to the shear created by the wall friction}$$

$$\langle \alpha \rangle A \rho_v g = \text{the body force due to gravity}$$

$$\int_A M_v dA = \text{the drag force between the phases due to local velocity differences}$$

$$f_i = \text{induced shear stress due to the radial phase distribution}$$

The terms in the integrated liquid momentum equation can, of course, be interpreted in the same way.

Consequently, if the liquid phase alone is in contact with the wall, the wall friction acts alone on the liquid, giving:

$$F_{wv} = 0$$

$$F_{wl} = F_w$$

The induced shear, however, caused by the wall friction, creates an interfacial force between the phases given by:

$$\langle \alpha \rangle F_w$$

and the net forces on the phases due to the wall friction become

$$\langle \alpha \rangle F_w \quad \text{[for the gas phase]}$$

$$\langle 1 - \alpha \rangle F_w \quad \text{[for the liquid phase]}$$

Similarly, if the gas phase is in contact with the wall,

$$F_{wv} = F_w$$

$$F_{wl} = 0$$

and the interfacial force, due to the wall friction, becomes:

$$\langle 1 - \alpha \rangle F_w$$

Again, the net forces on the phases due to the wall friction become:

$$\langle \alpha \rangle F_w \quad [\text{for the gas phase}]$$

$$\langle 1 - \alpha \rangle F_w \quad [\text{for the liquid phase}]$$

It is significant to realize that the distribution of the wall shear between the phases has no impact on the pressure drop, as the total momentum equation is not affected. The distribution, however, affects the interaction between the phases and is in agreement with the experimental observation [6.1-3, 6.1-4] that the relative velocity is insensitive to flow rate.

6.1.2.2 Interfacial Drag and Phase Distribution

In Section 6.1.2.1, the interfacial force due to the wall friction was derived. The remaining interfacial forces then become a function of the interface drag due to the difference in the phase velocities, the buoyancy due to the gravity, and a force that is due to the phase distribution.

When $\frac{\partial P}{\partial z}$ and τ are eliminated from Equations 6.1-6 and 6.1-7,

$$M_v = \alpha(1 - \alpha)\Delta\rho g \quad (6.1-17)$$

The physical interpretation of this equation is that, locally, the drag is equal to the buoyancy. Integrating this equation over the cross section gives:

$$\int_A M_v dA = A\Delta\rho g \langle \alpha(1 - \alpha) \rangle \quad (6.1-18)$$

This equation, combined with Equation 6.1-13, gives the total interaction between the phases due to drag or shear:

$$\langle f_{\ell v} \rangle = f_i + \int_A M_v dA = A\Delta\rho \langle \alpha \rangle \langle 1 - \alpha \rangle \quad (6.1-19)$$

The interfacial force must be related to the velocity difference between the phases. It is conventional to define:

$$f_{\ell v} = c_i |v_r| |v_r| \quad (6.1-20)$$

Integrating Equation 6.1-20 over the cross section yields:

$$A \langle f_{\ell v} \rangle = \int_A f_{\ell v} dA = A \bar{c}_i |\bar{v}_r| |\bar{v}_r| \quad (6.1-21)$$

In this equation, \bar{v}_r is a weighted average value for the relative velocity. It is important to note that $\bar{v}_r \neq \bar{v}_v - \bar{v}_\ell$, since $\bar{v}_v = \langle \alpha v_v \rangle / \langle \alpha \rangle$ and $\bar{v}_\ell = \langle (1 - \alpha)v_\ell \rangle / \langle 1 - \alpha \rangle$ have different weight functions. We will only have $\bar{v}_r = \bar{v}_v - \bar{v}_\ell$ for a uniform phase or velocity distribution.

Locally, the drift flux velocity is related to the relative velocity by:

$$v_r = \frac{v_{gj}}{1 - \alpha} \tag{6.1-22}$$

and, consequently, an average relative velocity can be defined by:

$$\bar{v}_r = \frac{\bar{v}_{gj}}{\langle 1 - \alpha \rangle} \tag{6.1-23}$$

where $\bar{v}_{gj} = \langle \alpha v_{gj} \rangle / \langle \alpha \rangle$

Eliminating \bar{v}_{gj} using the drift flux correlation:

$$\bar{v}_v = C_o \langle j \rangle + \bar{v}_{gj}$$

where $C_o = \langle \alpha j \rangle / (\langle \alpha \rangle \langle j \rangle)$ yields:

$$\bar{v}_r = \frac{1 - \langle \alpha \rangle C_o}{\langle 1 - \alpha \rangle} \bar{v}_v - C_o \bar{v}_\ell \tag{6.1-24}$$

This expression, combined with Equation 6.1-21, results in:

$$\langle f_{\ell v} \rangle = \bar{c}_i \left| \frac{1 - \langle \alpha \rangle C_o}{\langle 1 - \alpha \rangle} \bar{v}_v - C_o \bar{v}_\ell \right| \left(\frac{1 - \langle \alpha \rangle C_o}{\langle 1 - \alpha \rangle} \bar{v}_v - C_o \bar{v}_\ell \right) \tag{6.1-25}$$

Thus, using Equation 6.1-19 and with C_o and \bar{v}_{gj} correlated from void fraction data, the interfacial interaction can be evaluated by:

$$\bar{c}_i \left| \frac{1 - \langle \alpha \rangle C_o}{\langle 1 - \alpha \rangle} \bar{v}_v - C_o \bar{v}_\ell \right| \left(\frac{1 - \langle \alpha \rangle C_o}{\langle 1 - \alpha \rangle} \bar{v}_v - C_o \bar{v}_\ell \right) = \Delta \rho g \langle \alpha \rangle \langle 1 - \alpha \rangle \tag{6.1-26}$$

6.1.3 Bubbly/Churn Flow

6.1.3.1 Technical Basis and Assumptions

For bubbly flow, it is convenient to introduce:

$$\bar{c}_i = \frac{1}{8} \frac{C_D}{d_i} \rho_\ell \quad (6.1-27)$$

where C_D is the drag coefficient for the bubbles and d_i is the interfacial area per unit volume.

The interfacial area per unit volume can be given in terms of a critical Weber number:

$$\frac{1}{d_i} = 6\alpha \frac{\rho_\ell \bar{v}_{gj}^2}{\sigma We_c (1-\alpha)^2} \quad (6.1-28)$$

Combining Equations 6.1-26, 6.1-27 and 6.1-24 gives:

$$\frac{3}{4} \alpha \frac{C_D}{We_c} \frac{\rho_\ell^2}{\sigma} \frac{\bar{v}_{gj}^4}{(1-\alpha)^4} = \Delta\rho g \alpha (1-\alpha) \quad (6.1-29)$$

Many expressions for \bar{v}_{gj} for co-current flow have been reported in the literature [6.1-4, 6.1-5], and most are of the form:

$$\bar{v}_{gj} = k \left\{ \frac{\Delta\rho g \sigma}{\rho_\ell^2} \right\}^{0.25} \quad (6.1-30)$$

where k ranges from 1.18 to 1.53. A value for k of 1.53 fits a wide range of data. Inserting Equation 6.1-30 into Equation 6.1-29 results in:

$$\frac{C_D}{We_c} = 0.2433 (1-\alpha)^5 \quad (6.1-31)$$

In order to specify the interfacial shear, the exact value of We_c is not needed; only the ratio C_D/We_c matters.

For co-current flow, the distribution parameter will range from 0 for subcooled boiling to 1.333 as a maximum value for parabolic profiles. For high flow rates or high pressure ($\rho_v \approx \rho_\ell$), the distribution parameter should approach 1. Ishii [6.1-3] recommends:

$$C_o = C_\infty - (C_\infty - 1) \sqrt{\frac{\rho_v}{\rho_\ell}} \quad (6.1-32)$$

where C_∞ is given by Nikuradse [6.1-7]:

$$C_\infty = 1.393 - 0.015 \ln(\text{Re}) \quad (6.1-33)$$

For low flow rates in large geometries, such as bubbles rising in a pool [6.1-8, 6.1-9], Equations 6.1-30 and 6.1-33 lead to an overprediction of the void fraction data. The primary reason for this is that rising bubbles tend to induce a natural circulation in large geometries with local regions of two-phase co-current upflow separated by local regions of single-phase liquid downflow. This effect is not included in the above correlations.

Assuming the local drift to be given by Equation 6.1-30, the constant k can be correlated from Wilson's data [6-9], and one obtains:

$$k = 0.73 (D^*)^{0.121} \left(\frac{\Delta\rho}{\rho_v} \right)^{0.203} (j_v^*)^{0.635} - C_o j_v^* \quad (6.1-34)$$

where:

$$D^* = D_h \sqrt{\frac{\Delta\rho g}{\sigma}} \quad j_v^* = \frac{j_v \sqrt{\rho_l}}{(\Delta\rho g \sigma)^{0.25}} \quad (6.1-35)$$

For large hydraulic diameters and low values of the volumetric flux, Equation 6.1-34 gives larger values than 1.53. TRACG uses the larger of 1.53 and the value of k predicted by Equation 6.1-34.

6.1.3.2 Model as Coded

The model for the interfacial shear for bubbly/churn flow is encoded as described by the above equations with the following limitations:

- C_o is not allowed to exceed a value of 1.333 or $1/\alpha$. The latter limit is imposed, as a value larger than this limit would cause the coefficient to the vapor velocity in Equation 6.1-24 to become negative.
- When calculating the interfacial shear from Equations 6.1-29 and 6.1-31, an expression of the following form is obtained: $\langle f_{\ell v} \rangle = \bar{c}'_1 v_r |v_r|^3$. The last term in this equation is limited to a lower value of 0.2; i.e., $\langle f_{\ell v} \rangle = \bar{c}'_1 v_r \max(0.2, |v_r|)^3$. This is a smaller value than what would be expected from Equation 6.1-30 for a wide range of pressures and thus will have no impact on the solution. This limit on the relative velocity, however, prevents the derivative of the interfacial shear with respect to the relative velocity to approach zero, which would cause numerical problems.

6.1.3.3 Applicability

The correlations for the interfacial shear for bubbly flow are based in Ishii's recommendations [6.1-3]. In his database, Ishii considered data covering a wide range of parameters:

$$0.1 < P < 12 \text{ MPa}$$

$$0.01 < D_h < 0.17 \text{ m}$$

$$-30 < j < 20 \text{ m/sec.}$$

Wilson's bubble rise data covered hydraulic diameters up to 0.48m.

6.1.4 Annular Flow

6.1.4.1 Technical Basis and Assumptions

For annular flow, c_i will be expressed as:

$$\bar{c}_i = \frac{1}{8} \frac{C_D}{d_i} \rho_\ell \quad (6.1-36)$$

with the interfacial area per unit volume given by:

$$\frac{1}{d_i} = \frac{4}{D_h} \sqrt{\alpha} \quad (6.1-37)$$

This equation holds only for a smooth film. For a rough film, the interfacial area will be increased; however, this effect of surface roughness is included in C_D .

Combining Equations 6.1-26, 6.1-36 and 6.1-37 gives:

$$\frac{1}{2} \sqrt{\alpha} C_D \frac{\rho_\ell}{D_h} \frac{\bar{v}_{gj}^2}{(1-\alpha)^2} = \Delta\rho g \alpha(1-\alpha) \quad (6.1-38)$$

Ishii [6.1-3] has analyzed the annular flow regime, using Wallis' [6.1-5] expression for the interfacial shear, and recommends:

$$\bar{v}_{gj} = \frac{(1-\alpha)^{3/2}}{\alpha + a} \sqrt{\frac{\Delta\rho g D_h}{0.015 \rho_\ell}} \quad (6.1-39)$$

where:

$$a = \sqrt{\frac{1 + 75(1 - \alpha)}{\sqrt{\alpha}}} \sqrt{\frac{\rho_v}{\rho_\ell}} \quad (6.1-40)$$

Inserting Equation 6.1-39 into Equation 6.1-38 gives:

$$C_D = 0.03\sqrt{\alpha} (\alpha + a)^2 \quad (6.1-41)$$

For the distribution parameter, Ishii [6.1-3] recommends:

$$C_o = 1 + \frac{1 - \alpha}{\alpha + a} \quad (6.1-42)$$

6.1.4.2 Model as Coded

The model for the interfacial shear for annular flow is encoded as described by the above equations with the following limitations:

- The expression for the interfacial area given by Equation 6.1-37 assumes that the wall is covered by a film no matter how thin the film is. In reality, this will not happen; at some point, the film will break up and only cover a fraction of the surface. This effect is approximated by applying a multiplier of $10(1-\alpha)$ for void fractions greater than 0.9. The purpose of this multiplier is not to model this phenomenon in great detail, but to prevent the numerical difficulty that would arise, if the interfacial shear were allowed to remain finite in the limit of α approaching 1.0
- When calculating the interfacial shear from Equations 6.1-38 and 6.1-39, an expression of the following form is obtained: $\langle f_{\ell v} \rangle = \bar{c}'_i v_r |v_r|$. The last term in this equation is limited to a lower value of 0.1; i.e., $\langle f_{\ell v} \rangle = \bar{c}'_i v_r \max(0.1, |v_r|)$. This is a smaller value than what would be expected from Equation 6.1-39 for a wide range of pressures and thus will have no impact on the solution. This limit on the relative velocity, however, prevents the derivative of the interfacial shear with respect to the relative velocity to approach zero, which would cause numerical problems.

6.1.4.3 Applicability

The correlations for the interfacial shear for annular flow are based in Ishii's recommendations [6.1-3]. In his database, Ishii considered data covering a wide range of parameters, including laminar and turbulent flow and relative velocities covering a range from 0.2 to 4 m/sec.

6.1.5 Droplet Flow

6.1.5.1 Technical Basis and Assumptions

For droplet flow, it is convenient to introduce:

$$\bar{c}_i = \frac{1}{8} \frac{C_D}{d_i} \rho_v \quad (6.1-43)$$

with interface area per unit volume given in terms of a critical Weber number:

$$\frac{1}{d_i} = 6(1 - \alpha) \frac{\rho_v \bar{v}_{gj}^2}{\sigma We_c (1 - \alpha)^2} \quad (6.1-44)$$

Combining Equations 6.1-26, 6.1-43, and 6.1-44 results in:

$$\frac{3}{4} (1 - \alpha) \frac{C_D}{We_c} \frac{\rho_v^2}{\sigma} \frac{\bar{v}_{gj}^4}{(1 - \alpha)^4} = \Delta \rho g \alpha (1 - \alpha) \quad (6.1-45)$$

Many expressions for \bar{v}_{gj} are reported in the literature [6.1-5], and most are of the form:

$$\bar{v}_{gj} = k (1 - \alpha) \left\{ \frac{\Delta \rho g \sigma}{\rho_v^2} \right\}^{0.25} \quad (6.1-46)$$

Ishii [6.1-3] recommends $k = 1.41$.

Using Equation 6.1-46 and $k = 1.41 = \sqrt{2}$, Equation 6.1-45 gives:

$$\frac{C_D}{We_c} = \frac{1}{3} \alpha \quad (6.1-47)$$

Since the droplets can be assumed uniformly distributed due to the turbulence, the distribution parameter is:

$$C_o = 1 \quad (6.1-48)$$

For large flow rates where the droplets are created by entrainment from the film, the droplet size will be determined by the initial relative velocity as they are entrained from the film on the wall. Since the film velocity is much smaller than the vapor velocity and the void fraction is

high, the initial relative velocity can be approximated by the total flux. Thus, assuming a critical Weber Number of 12, this is in agreement with Ishii's recommendations and leads to:

$$\frac{1}{d_i} = \frac{1}{2} (1 - \alpha) \frac{\rho_v j^2}{\sigma} \quad (6.1-49)$$

The droplets produced by the entrainment process can mainly be characterized as undistorted particles outside the Stokes regime, and an approximation for the drag coefficient is [6.1-3]:

$$C_D = 1.07 \alpha \text{Re}_d^{-0.5} \quad (6.1-50)$$

where:

$$\text{Re}_d = \frac{\rho_v d_d v_r}{\mu_v} \quad (6.1-51)$$

6.1.5.2 Model as Coded

The model for the interfacial shear for droplet flow is encoded as described by the above equations with the following limitations:

- When calculating the interfacial shear from Equations 6.1-46 and 6.1-47, an expression of the following form is obtained: $\langle f_{\ell v} \rangle = \bar{c}'_i v_r |v_r|^3$. The last term in this equation is limited to a lower value of 0.5; i.e., $\langle f_{\ell v} \rangle = \bar{c}'_i v_r \max(0.5, |v_r|)^3$. This is a smaller value than what would be expected from Equation 6.1-46 for a wide range of pressures and thus will have no impact on the solution. This limit on the relative velocity, however, prevents the derivative of the interfacial shear with respect to the relative velocity to approach zero, which would cause numerical problems. For high flow, the corresponding limitation is: $\langle f_{\ell v} \rangle = \bar{c}'_i v_r \max(0.1, |v_r|)$.

6.1.5.3 Applicability

The correlations for interfacial shear for droplet flow are based on Ishii's recommendations [6.1-3]. For distorted particles, the model for the drift flux velocity is equivalent to the drift flux velocity for bubbly flow and the range of applicability of the model is similar. The model is consistent with the recommendations of Wallis [6.1-5]. No specific range of applicability is given by Ishii [6.1-3] and Wallis [6.1-5] and the applicability of the model is determined by the assessment (Section 6.1.8).

6.1.6 Annular/Droplet Flow

6.1.6.1 Technical Basis and Assumptions

For dispersed annular flow, the drift flux parameters as recommended by Ishii [6.1-3] are interpolated between the annular and the droplet drift flux parameters based on the entrainment fraction:

$$\bar{v}_{gj} = \frac{(1-\alpha)(1-E)}{\sqrt{\frac{1+75(1-\alpha)}{\sqrt{\alpha}} \frac{\rho_v}{\rho_\ell}}} \sqrt{\frac{\Delta\rho g D_h (1-\alpha)(1-E)}{0.015\rho_\ell}} \quad (6.1-52)$$

$$+ \frac{E(1-\alpha)}{\alpha + E(1-\alpha)} \left\{ \begin{array}{l} \sqrt{2} \left(\frac{\Delta\rho g \sigma}{\rho_v^2} \right)^{0.25} \\ \frac{3\sigma}{\rho_v} \left(\frac{\Delta\rho g}{\mu_v \rho_v} \right)^{1/3} \frac{1}{j^2} \end{array} \right. \quad \text{for large } j^*$$

and C_o is given by:

$$C_o = 1 + \frac{(1-\alpha)(1-E)}{\alpha + \sqrt{\frac{1+75(1-\alpha)}{\sqrt{\alpha}} \frac{\rho_v}{\rho_\ell}}} \quad (6.1-53)$$

where E is the entrainment fraction defined by Equation 5.1-17.

6.1.6.2 Model as Coded

In TRACG, the entrainment fraction is defined by Equation 5.1-17. It is assumed that the fraction $(1-\alpha)E$ of the liquid exists as entrained droplets and that the fraction $(1-\alpha)(1-E)$ exists as an annular film on the wall. For the entrained droplets, the shear is calculated as described in Section 6.1.5, and for the annular film the shear is calculated as described in Section 6.1.4. The two contributions are then added to form the total interfacial shear.

6.1.6.3 Applicability

The applicability of the correlations for the annular/droplet flow regime is given by the applicability of the correlation for the annular (Section 6.1.4) and droplet (Section 6.1.5) flow regimes, as well as the applicability of the entrainment correlation.

*The minimum of the two expressions is used.

In TRACG, as in other system codes, an additional complication arises from the use of the two-fluid model. The droplets and the film will not have the same velocity. However, when a two-fluid model is used, the interfacial shear is calculated based on the average liquid velocity.

Given the above comments, the applicability of the interfacial shear model for the annular/droplet flow regime will be determined by the assessment (Section 6.1.8).

6.1.7 Modifications to Interfacial Shear

6.1.7.1 Subcooled Boiling

For subcooled boiling, the vapor is concentrated at the wall, where the liquid velocity approaches zero. Consequently, for subcooled boiling, the distribution parameter should also approach zero, and become zero at the point of net vapor generation.

6.1.7.2 Counter-Current Flow Limitations

Very few data for the void fraction exist for counter-current flow; however, a large database for counter-current flow limitation (CCFL) exists. From the drift flux correlation one gets:

$$j_v = \frac{\alpha C_o}{1 - \alpha C_o} j_\ell + \frac{\alpha \bar{v}_{gj}}{1 - \alpha C_o} \quad (6.1-55)$$

The general form for CCFL correlations is given by [6.1-12]:

$$\sqrt{\frac{j_v}{j_{v0}}} + \sqrt{\frac{j_\ell}{j_{\ell0}}} = 1 \quad (6.1-56)$$

where j_{v0} and $j_{\ell0}$ represent the intercepts with the axes. Because the drift flux correlation should describe all possible flow situations at or below the CCFL curve (Figure 6.1-2), the line given by Equation 6.1-55 for constant void fraction should be tangent to the CCFL curve.

This puts a constraint on C_o and \bar{v}_{gj} . By requiring that Equation 6.1-55 be tangent to Equation 6.1-56, we get:

$$\frac{\bar{v}_{gj}}{j_{\ell0}} = \frac{C_o (1 - \alpha C_o)}{\frac{j_{\ell0}}{j_{v0}} \alpha C_o + 1 - \alpha C_o} \quad (6.1-57)$$

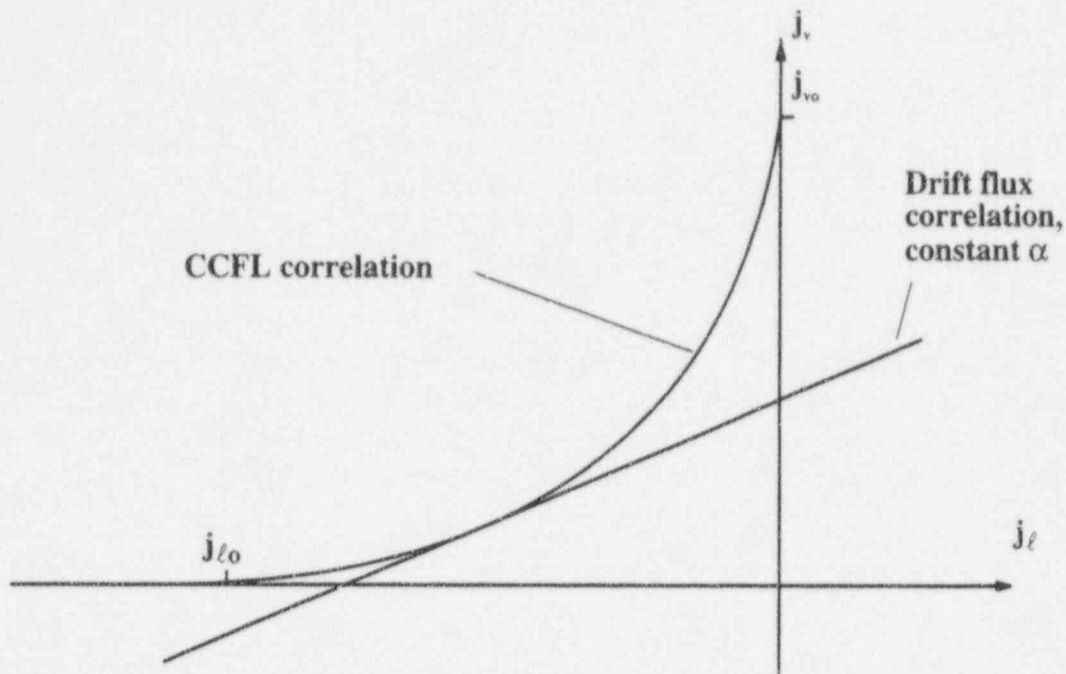


Figure 6.1-2. Drift Flux Correlation and CCFL

The CCFL correlation in TRACG utilizes the Kutateladze numbers,

$$\sqrt{K_v} + m\sqrt{K_\ell} = \sqrt{K} \quad (6.1-58)$$

where:

$$K_v = \frac{j_v \sqrt{\rho_v}}{(\Delta\rho g \sigma)^{1/4}} \quad (6.1-59)$$

$$K_\ell = \frac{j_\ell \sqrt{\rho_\ell}}{(\Delta\rho g \sigma)^{1/4}} \quad (6.1-60)$$

For counter-current flow, C_0 is not very well defined (e.g., C_0 has a singularity for $j = 0$). Consequently, \bar{v}_{gj} is determined as described in Sections 6.1.5 – 6.1.7 and C_0 is determined from Equation 6.1-57.

Even though the interfacial shear is fitted to match the CCFL correlation for counter-current flow, TRACG will check the flow rates to make sure the CCFL correlation is not exceeded (Section 3.6). The primary reason for this additional check is the discontinuity in the void fraction that often will exist at the CCFL location. This discontinuity, coupled with the use of donor-celled void fractions, can lead to an overprediction of the liquid down flow. The additional check against the CCFL correlation prevents this from happening.

6.1.7.3 Virtual Mass

The virtual mass is normally a small term compared to the other terms in the momentum equation. It is of importance only for bubbly flow and for critical flow or sudden accelerations due to abrupt area changes. The inclusion of virtual mass has a positive effect on the stability of the numerical method used for the integration of the conservation equations.

The virtual mass terms in Equations 3.1-3 and 3.1-4 are defined by:

$$k = \begin{cases} 0.5\alpha \frac{1+2\alpha}{1-\alpha} & \text{for } 0 \leq \alpha < \alpha_{\text{tran}} \\ 0.5(1-\alpha) \frac{3-2\alpha}{\alpha} & \text{for } \alpha_{\text{tran}} \leq \alpha < 1 \end{cases} \quad (6.1-61)$$

$$\rho_c = \begin{cases} \rho_\ell & \text{for } 0 \leq \alpha < \alpha_{\text{tran}} \\ \rho_v & \text{for } \alpha_{\text{tran}} \leq \alpha < 1 \end{cases} \quad (6.1-62)$$

The velocity of the dispersed phase is approximated by:

$$v_d = (1 - \alpha)v_v + \alpha v_\ell \quad (6.1-63)$$

where $\alpha_{\text{tran}} = 0.65$, represents the transition to annular flow (for horizontal flow Equation 5.1-25 is used if it produces a lower value).

The expressions for k and ρ_c are in agreement with those recommended by Zuber [6.1-11]. The velocity of the dispersed phase is v_v for $\alpha \rightarrow 0$ and v_ℓ for $\alpha \rightarrow 1$. It should be noted that the virtual mass term is only significant for bubbly flow. Thus, the calculations are not sensitive to the definition of the velocity of the dispersed phase for larger values of the void fraction. Equation 6.1-63 is chosen as a simple formulation which has the right limits.

6.1.7.4 Applicability

The applicability of the modifications to the interfacial shear is addressed through the assessment (Section 6.1.8). Subcooled boiling is present in all the heated void fraction tests, and the applicability of the modification to C_0 is covered by this assessment.

The CCFL correlation is based on data from prototypical full-scale BWR components [6.1-12] and thus the correlation is directly applicable to BWR locations such as upper tieplates and bundle inlet orifices.

The phenomenon of CCFL in the downcomer region (ECC bypass) is not of importance to BWRs because of the milder depressurization and large downcomer flow area. The low pressure injection systems will be enabled after the reactor vessel has been depressurized. There has been no evidence of any CCFL in the downcomer in any BWR LOCA test simulations. For these reasons, the TRACG interfacial shear model has not been assessed against PWR ECC bypass data. The empirical Kutateladze correlation discussed earlier is also used in the downcomer cells. This correlation is used to limit the maximum downflow of liquid corresponding to the vapor upflow rate in the cell.

Calculations performed using a Kutateladze constant of 3.2; i.e.

$$\sqrt{K_g} + \sqrt{K_\ell} = \sqrt{3.2}$$

have confirmed that CCFL will not occur in the downcomer during a typical LOCA transient in a BWR, and that it is not necessary to develop accurate models for this phenomenon.

The virtual mass model has been used for all the assessment studies, and the range of applicability given by the assessment of the interfacial shear applies to the combined model.

6.1.8 Assessment and Applicability to BWR

The interfacial shear model as described in the previous section has been extensively tested against void fraction data.

6.1.9 References

- 6.1-2 J.G.M. Andersen, K.H. Chu and J.C. Shaug, *BWR Refill-Reflood Program Task 4.7 - Model Development, Basic Models for the BWR Version of TRAC*, NUREG/CR-2673, April 1983.
- 6.1-3 M. Ishii, *One Dimensional Drift Flux Model and Constitutive Equations for Relative Motion Between Phases in Various Two-Phase Flow Regimes*, ANL-77-47, October 1977.
- 6.1-4 N. Zuber et. al., *Steady State and Transient Void Fraction in Two-Phase Flow Systems*, GEAP-5417, 1967.
- 6.1-5 G.B. Wallis, *One-Dimensional Two-Phase Flow*, McGraw-Hill Book Co. Inc., New York, 1969.
- 6.1-6 N. Zuber and J.A. Findlay, *Average Volumetric Concentration in Two-Phase Flow Systems*, Journal of Heat Transfer, 1965, 87, p453.

- 6.1-7 J. Nikuradse, *Gesetzmäßigkeit der Turbulenten Strömung in glatten Röhren*, Forch. Arb. Ing. Wes., 1932, p 356.
- 6.1-8 J.F. Wilson, R.J. Grenda and J.F. Patterson, *The Velocity of Rising Steam in a Bubbling Two-Phase Mixture*, ANS Trans., 5(1), p151-152, 1962.
- 6.1-9 P.C. Hall and K.H. Adron, *Prediction of Void Fraction in Low Velocity Bubbling Flow*, CEG j13, Rd/13/n3966, August 1978.
- 6.1-10 J.A. Findlay and G.E. Dix, *BWR Void Fraction Correlation and Data*, NEDE-21565, January 1977.
- 6.1-11 N. Zuber, *On the Dispersed Two-Phase Flow in the Laminar Flow Regime*, Chemical Engineering and Science Journal, Vol. 19, p. 897, 1964.
- 6.1-12 D.D. Jones, *Subcooled Counter Current Flow Limiting Characteristics of the Upper Region of a BWR Fuel Bundle*, General Electric Company, NEDG-NUREG-23549, 1977.
- 6.1-13 *Compendium of ECCS Research for Realistic LOCA Analysis*, NUREG-1230, December 1988.
- 6.1-14 *Reactor Safety Issues Resolved by the 2D/3D Program*, NUREG/IA-0127, July 1993.

6.2 Wall Friction and Form Losses

6.2.1 Wall Friction

6.2.1.1 Technical Basis and Assumptions

The major assumption in the calculation of wall friction is that the friction factors based on steady-state data are applicable for transients. Also, correlations for fully developed flow are utilized. These assumptions are reasonable for BWR transients as long as passages being analyzed have $L/D > 10$. This is generally true for BWR regions, except where large 3D cells are used. The errors in the use of fully developed correlations could be larger in these regions. This is discussed later in the section.

The field equations for conservation of momentum for the vapor and liquid phases contain terms resulting from the wall friction (Equations 3.1-30 and 3.1-31). These terms appear as $F_{wv} / \alpha\rho_v$ and $F_{wl} / (1 - \alpha)\rho_l$, respectively. As discussed in Section 6.1, the net force on the vapor phase due to wall friction is αF_w ; thus, the term $F_{wv} / \alpha\rho_v$ reduces to F_w / ρ_v . Similarly, the term in the liquid momentum equation reduces to F_w / ρ_l . Here, F_w is the total wall shear. In this section, the basis for calculation of the wall shear F_w is described. The total wall shear is calculated using a two-phase multiplier approach as:

$$F_w = \frac{f_\ell}{2D_h} \frac{G^2}{\rho_\ell} \phi_{\ell 0}^2, \quad (6.2-1)$$

where $\phi_{\ell 0}^2$ is the two-phase multiplier, and f_ℓ is the single-phase friction factor.

6.2.1.2 Two-Phase Friction Multiplier Approach

The frictional pressure drop in two-phase flow is conventionally correlated by means of a two-phase multiplier, which relates the overall frictional pressure drop to a reference frictional pressure drop for an equivalent single-phase flow. These models were originally motivated by the "separate cylinders" model for two-phase flow, which provided a rationale for the correlating parameters. In the Lockhart-Martinelli model [6.2-1], the reference pressure gradient is that due to the liquid flowing alone in the total cross-section; the Martinelli-Nelson correlation [6.2-2] considers a 'liquid only' pressure gradient resulting from a liquid flow equal to the total two-phase flow rate. The two-phase multiplier is correlated in terms of the ratio of the pressure gradients for liquid and vapor flowing alone. TRACG employs a modified Chisholm two-phase multiplier, $\phi_{\ell 0}^2$, which is of the Martinelli-Nelson type.

6.2.1.3 Single-Phase Friction Factor

The form of the single-phase friction factor is well established [6.2-3]. For laminar flow, the friction factor results from the exact solution for fully developed flow in circular pipes. For turbulent flow in smooth pipes, Blasius and McAdams proposed correlations that approximate the Prandtl - Von Karman - Nikuradse line over a wide range of Reynolds numbers. In 1939, Colebrook extended the expression for turbulent flow in a smooth pipe to include roughness of the pipe wall in the so-called transition region between smooth pipe flow and flow for which f is constant. Moody, in 1941, presented the Colebrook function in the well known Moody diagram. An approximation to Colebrook's function, which includes the effect of roughness, was proposed in 1947 by Moody.

6.2.1.4 Two-Phase Multiplier

The two-phase frictional multiplier used in TRACG is based on a modification to the Chisholm correlation [6.2-4]. Following a traditional separated flow approach, Chisholm proposed a correlation of the form:

$$\frac{\Delta P_{TP}}{\Delta P_{\ell 0}} = \Phi_{\ell 0}^2 = (1-x)^2 \left(1 + \frac{C}{X} + \frac{1}{X^2} \right) \quad (6.2-3)$$

where X is the Lockhart-Martinelli parameter given by:

$$1 / X^2 = \frac{f_v x^2}{\rho_v} \bigg/ \frac{f_\ell (1-x)^2}{\rho_\ell} = \zeta \frac{x^2}{(1-x)^2} \quad (6.2-4)$$

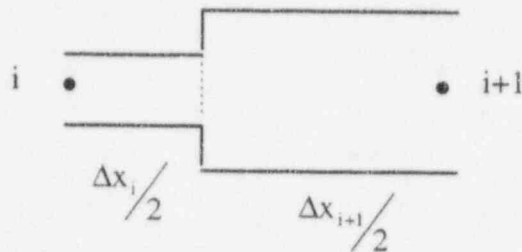
6.2.1.5 Model As Coded

The calculation of the wall friction is encoded as described by Equations 6.2-1. However, there are some limitations on specific variables that should be noted. A minimum value of 10^{-5} is used for the hydraulic diameter whenever the input value is less than this minimum value for evaluating the Reynolds number. A minimum value of the absolute value of the mass flux used in the Reynolds number is obtained by calculating the mass flux with a mixture velocity of 0.1 m/s. These imposed lower limits do not adversely affect the application of TRACG. They prevent division by zero for low flow where the frictional pressure drop is insignificant.

The evaluation of the wall friction requires a combination of cell-edged and cell-centered quantities. The cell-edged quantities of phase velocity, hydraulic diameter, and surface roughness are used as is. The mass fluxes are donor-celled based on the phase velocity. The densities and viscosities are linearly interpolated based on the lengths of the adjacent cells as follows:

$$\rho = \frac{\Delta x_i \rho_i + \Delta x_{i+1} \rho_{i+1}}{\Delta x_i + \Delta x_{i+1}}$$

The wall friction from cell-center to cell-center is calculated assuming two pipe segments, each of a length equal to one half the cell length:



For the left half cell, the average mass flux is $G_{i+1/2}^i = G_{i+1/2} \frac{A_{i+1/2}}{\text{Vol}_i / \Delta x_i}$ and similarly for the right half cell, the average mass flux is $G_{i+1/2}^{i+1} = G_{i+1/2} \frac{A_{i+1/2}}{\text{Vol}_{i+1} / \Delta x_{i+1}}$. For a constant cross-section pipe, $G_{i+1/2}^i = G_{i+1/2}$. A linear interpolated mass flux based on the cell length is used for the calculation of the wall friction:

$$\bar{G} = \frac{\Delta x_i}{\Delta x_i + \Delta x_{i+1}} G_{i+1/2}^i + \frac{\Delta x_{i+1}}{\Delta x_i + \Delta x_{i+1}} G_{i+1/2}^{i+1}$$

The wall friction is applied to one-dimensional and three-dimensional components in a consistent manner.

6.2.1.6 Applicability

The single-phase friction factor represented by the Moody diagram has a tolerance of $\pm 5\%$ for values of Re from 4000 to 10^7 , and for values of f up to 0.05. Below 4000, the range of Reynolds numbers is covered by laminar flow and a transition region with a slightly higher uncertainty. The uncertainty is of the order of 10% for non-smooth pipe data. Data for non-circular channels are also well predicted with the concept of the hydraulic diameter. Data for triangular channels fall about 3% under the Moody smooth line, and for square channels about 10% under the Moody line for Reynolds numbers between 10,000 and 200,000 [6.2-6].

For two-phase flow, the majority of the comparisons with the modified Chisholm correlation have been made for rod bundle data. It should be noted that the measured pressure drop will include both frictional and static head components for vertical flow. Thus, it is important to use a consistent set of void fraction and frictional pressure drop models in analyzing such data. The void correlation used in the data reduction produces almost identical results as TRACG.

Idsinga, Todreas and Bowring [6.2-7] tested 18 two-phase friction pressure drop models and correlations against 2200 experimental steam-water pressure drop measurements under adiabatic conditions and 1230 in diabatic flow conditions. The data represented several geometries and had the following property ranges :

Pressure	1.7 - 10.3 MPa
Mass flux	270 - 4340 kg/m ² -s
Quality	Subcooled to 100%
Hydraulic diameter	2.3 - 33 mm

The Chisholm correlation was among those tested. The authors concluded that the correlation performed better for low pressure data (1.7 - 6.2 MPa) than for the high pressure data (6.2 - 10.3 MPa). While these conclusions are not directly applicable to the modified Chisholm correlation, it is reasonable to assume that its application at lower pressures will not lead to large errors.

Applicability to Containment Volumes

The correlations are applicable to containment flow paths such as Passive Containment Cooling Condensers (PCC) piping, headers and tubes, and the main vents which are adequately represented by pipes. The range of applicability is as quoted earlier. These are the flow paths of importance in the containment. Frictional pressure drops in the large open areas of the drywell and wetwell are small after the initial blowdown. However, they do determine the global flow patterns and natural circulation flows in these regions. The application of the friction factors and two-phase multipliers, which are based on fully developed flows in pipes, will have larger margin for error for large 3-D cells.

It should be noted that the friction factors are used in the same way in TRACG as in other codes such as GOTHIC [6.2-12], which are specifically meant for containment analysis, and have been extensively qualified for these applications.

6.2.2 Form Losses at Abrupt Expansions and Contractions

6.2.2.1 Technical Basis and Assumptions

The basic assumption underlying the formulation of local form losses at abrupt expansions and contractions is that the transient flow process can be approximated as a quasi-steady flow process that is instantaneously satisfied by the upstream and downstream conditions (i.e.,

transient inertia, mass and energy storage are neglected at abrupt area changes). However, the upstream and downstream flows are treated as fully transient flows.

The quasi-steady approach can be justified on the grounds that available loss correlations are based on data taken during steady processes, but transient investigations [6.2-8] have verified the adequacy of the assumption. The volume of fluid and associated mass, energy and inertia at points of abrupt area change is generally small compared with the volume of upstream and downstream fluid regions. These transient effects are approximated by lumping them into the upstream and downstream volumes. In general, the quasi-steady approach is consistent with modeling of other important phenomena in transient codes (i.e., heat transfer, pumps and valves).

6.2.2.2 Single-Phase Flows

In steady, incompressible flow, losses at an area change are modeled by the inclusion of an appropriate dynamic head loss term, h_L , in the one-dimensional modified Bernoulli equation:

$$\left(v^2 / 2 + P / \rho \right)_1 = \left(v^2 / 2 + P / \rho \right)_2 + h_L; \quad (6.2-6)$$

$$h_L = Cv^2 / 2$$

The particular form of the dynamic head loss is obtained by employing the Bourda-Carnot [6.2-9] assumption for calculating losses associated with the expansion part of the flow process. For a contraction, the loss corresponds to an expansion from the vena contracta. TRACG does not compute these local loss coefficients. The loss coefficient C is input by the user based on the geometry of the flow. In the absence of an input loss, TRACG will calculate the reversible pressure change given by the Bernoulli equation. (TRACG does estimate these losses, but this is only used as an input check.)

6.2.2.3 Two-Phase Flows

The flow through an abrupt area change can be visualized by considering each phase to be flowing in a phasic stream tube. The velocities and volume fractions are calculated from the transient flow equations in the upstream and downstream regions. Within the area change region, the phases are coupled through the interphase drag and a common pressure gradient. The gradient in relative velocity can be large at points of abrupt area changes. Since each phase is governed by a modified Bernoulli type of equation, it is reasonable to assume that losses associated with changes in phasic flow area can be modeled by separate dynamic pressure loss terms for both the liquid and gas phases. However, the interfacial drag effects are important at abrupt area changes. These will affect the local slip between the phases and the effective phasic areas.

This pressure drop is apportioned to each phase in proportion to its volume fraction. The single-phase loss coefficient C must be input by the user. In the absence of an input loss, TRACG will calculate a 'reversible' pressure change consistent with the momentum equations.

6.2.2.4 Model as Coded

The single-phase loss coefficient is input separately for forward and reverse flow direction. The sign of the total mass flux will determine which loss coefficient is applied:

$$\begin{aligned}
 C_{i+1/2} &= C_{\text{forward}} && \text{if } G_{i+1/2} \geq 1.0 \\
 &= C_{\text{reverse}} && \text{if } G_{i+1/2} < -1.0 \\
 &= 0.5[(1 - G_{i+1/2})C_{\text{reverse}} + (1 + G_{i+1/2})C_{\text{forward}}] && \text{if } -1 \leq G_{i+1/2} < 1.0
 \end{aligned}$$

where G is based on the volumetric fluxes normalized to a Kutateladze number (i.e., an interpolation is performed for mass fluxes where counter-current flow is possible). The frictional pressure drop is generally insignificant for counter-current flow.

Singular losses are applied to one-dimensional and three-dimensional components in a consistent manner.

6.2.2.5 Applicability

The model used in TRACG has been extensively tested for pressure drop across spacers and bundle upper tie plates. The range of conditions is similar to that for the frictional pressure drop data.

Husain, Choe and Weisman [6.2-10] have made extensive comparisons of pressure drop across abrupt area changes with separated flow and homogeneous flow models. They quote the following statistics:

For Abrupt Expansions:

Mass Flux (kg/m ² -s)	Homogeneous Model		Slip Flow	
	Mean Error	σ	Mean Error	σ
<680	0.60	0.94	-0.02	0.64
<1360	0.49	0.82	-0.03	0.54
>1360	0.05	0.11	-0.08	0.09
>2720	0.10	0.06	-0.00	0.08
All	0.42	0.77	-0.04	0.49

For Abrupt Contractions:

Mass Flux (kg/m ² -s)	Homogeneous Model		Slip Flow	
	Mean Error	σ	Mean Error	σ
<680	-0.075	0.30	-0.09	0.28
<1360	-0.16	0.09	-0.17	0.12
> 2040	-0.05	0.01	-0.17	0.02
>2720	-0.05	0.00	-0.16	0.00
All	0.03	0.27	-0.00	0.25

The numbers are shown as fractions of the mean value.

This indicates that the homogeneous flow model works well for contractions but not as well for expansions. The statistics do not apply to the TRACG model, which uses the homogeneous multiplier only for the irreversible pressure drop; but they indicate the likely errors in its application to expansions, which are in the acceptable range.

Applicability to Containment Volumes

The formulations for form losses at abrupt expansions and contractions are applicable to pipe geometries in the containment such as the PCC inlet piping, headers and tubes, and the vent pipes and horizontal vents. These involve inlet and exit losses and losses at bends in the piping. Form losses are not as important in the large three-dimensional cells, where large changes in area are not common. The same formulation is applied in these regions.

6.2.3 Assessment and Applicability to BWR

The models for wall friction and form losses have been assessed against experimental data and other correlations. Reactor data at natural circulation have been analyzed with TRACG. TRACG containment calculations have been compared to appropriate test results.

6.2.4 References

- 6.2-1 R.W. Lockhart and R.C. Martinelli, *Proposed Correlation of Data for Isothermal Two-Phase Two-Component Flow in Pipes*, Chem. Eng. Progr. **45**, pp. 39 - 48, 1949.
- 6.2-2 R.C. Martinelli and D.B. Nelson, *Prediction of Pressure Drops During Forced Circulation Boiling of Water*, Trans. ASME **70**, pp. 695 -702, 1948.
- 6.2-3 J. Waggener, *Friction Factors for Pressure Drop Calculations*, Nucleonics, **19** (11), November 1961.

- 6.2-4 D. Chisholm, *Pressure Gradients Due to Friction During the Flow of Evaporating Two-Phase Mixtures in Smooth Tubes and Channels*, Int. J. Heat Mass Transfer 16, pp. 347 - 358, 1973.
- 6.2-6 R.G. Deissler and M.F. Taylor, *Analysis of Turbulent Flow and Heat Transfer in Non-Circular Passages*, NACA-TN4384, 1958.
- 6.2-7 W. Idsinga, N. Todreas and R. Bowring, *An Assessment of Two-Phase Pressure Drop Correlations for Steam-Water Systems*, Int. J. Multiphase Flow, 3, pp. 401-413, 1977.
- 6.2-8 J. Weisman, T. Ake, R. Knott, *Two-Phase Pressure Drop Across Abrupt Area Changes in Oscillatory Flow*, Nuclear Science and Engineering, 61, 1976, pp. 297-309.
- 6.2-9 J.K. Vennard, Elementary Fluid Mechanics, 4th Edition, New York; John Wiley and Sons, 1965.
- 6.2-10 A. Husain, W.G. Choe, J. Weisman, *The Applicability of the Homogeneous Flow Model to Pressure Drop in Straight Pipe and Across Area Changes*, Report COO-2152-16, University of Cincinnati.
- 6.2-12 T.L. George, et al, *GOTHIC Containment Analysis Package*, Version 3.4e, Vol. 1: Technical Manual, EPRI TR-103053-V1, October 1993.

6.3 Critical Flow

This section details the equilibrium critical flow model employed in the TRACG computer code. The critical flow model used in TRACG is applicable for a coarse-mesh nodalization and is based on a semi-empirical approximation of the choking criteria derived from the general one-dimensional, two-phase fluid field equations. The critical flow model also allows for the simulation of choking when noncondensable gases are present. The principal motivation for using a choked flow limitation model was to improve code efficiency and run times. In the past, it was found that modeling choked flow using the finite-difference approximation to the basic conservation equations required extremely fine cell nodalization in the vicinity of the break plane. As a consequence, simulating break transients generally led to prohibitively costly calculations. The choked flow model was developed in several stages by a number of individuals [6.3-1,2,3,4].

The remainder of this section is organized as follows. Section 6.3.1 documents the technical basis and assumptions used to formulate the choking criteria in TRACG. Section 6.3.2 documents the general methodology and implementation details for calculating the thermodynamic properties at the choke plane. Sections 6.3.3.1, 6.3.3.2, and 6.3.3.3 document the two-phase/two-component, single-phase/two-component vapor, and single-phase liquid flow models, respectively. Section 6.3.4 documents the closure relations needed to calculate the choke plane phasic velocities. Section 6.3.5 discusses the applicability of the TRACG choking model.

6.3.1 Technical Basis and Assumptions

Choking occurs when the mass flow in a pipe becomes independent of the downstream conditions. Therefore, a further reduction in the downstream pressure will not change the mass flow rate. The reason choking occurs is that acoustic signals can no longer propagate upstream to affect the properties that determine the mass flow rate at the choke plane. The choking model employs a flow-limiting scheme that uses a linear function of the cell junction phasic velocities and compares this expression to the calculated local sonic velocity for the junction. If this linear function exceeds the local sound speed, the choking model is employed to limit flow at that particular junction. The quantitative details of how this is done will be identified later in this section. The choking model used in TRACG is similar to that used in TRAC-BF1/MOD1 [6.3-22], which is based on the RELAP5/MOD1 model originally developed by Ransom and Trapp [6.3-5,6,7,8].

Originally, the TRACG choking model was based on a characteristic analysis of the partial differential equations governing the flow response. However, it has been found empirically that a much simplified criterion relating the throat Homogenous Equilibrium Mixture (HEM) sonic velocity and throat phasic velocities, void fractions, and densities may be used in

place of the detailed theoretical expression and still yield good code/data comparisons. The simplified criterion that indicates choked flow is:

$$\left| \frac{\alpha_v \rho_\ell v_v + \alpha_\ell \rho_v v_\ell}{\alpha_v \rho_\ell + \alpha_\ell \rho_v} \right| \geq a_{HE} \quad (6.3-1)$$

The choking model consists of five different regimes, identified in Table 6.3-1. These regimes are based on cell-centered void conditions immediately upstream of the choke plane. Each of these regimes is simulated in the TRACG. In each case, the method used to calculate the homogeneous sound speed a_{HE} is slightly different. The presence of noncondensable gases introduces an additional degree of complexity in the approximation of a_{HE} . The presence of noncondensable gases is accounted for in all of the break flow regimes with one exception. Noncondensable gases at the break choke plane are ignored for the low void regime (Table 6.3-1) when the Alamgir-Jones-Lienhard (AJL) correlation is used. In the subcooled blowdown regime, the effects of noncondensibles on the local sonic speed are assumed to be small and are therefore ignored.

6.3.2 Implementation Details

This section summarizes how the choking model is implemented in TRACG. The choking model is implemented in only one-dimensional components. The critical flow model is called by the subroutine TFIDE, which is the subroutine to solve the governing equations for one-dimensional TRACG components. TFIDE passes donor cell parameters based on new-time velocities to CHOKER. Tables 6.3-2 and 6.3-3 summarize the principal variables passed to CHOKER and the calculated output variables. The alphanumeric identifiers in Tables 6.3-2 and 6.3-3 should not be necessarily interpreted as subroutine call arguments. After CHOKER has been entered, control is passed to a particular model, depending on the void conditions defined in Table 6.3-1. Each model that is invoked follows the same computational sequence:

1. The throat pressure and temperature conditions are calculated. The subroutine THERMO is called to calculate additional thermodynamic properties at the throat conditions.
2. The throat sonic speed is calculated and the choking criteria evaluated to determine if the flow is choked.
3. If the flow is not choked, control is returned to TFIDE.
4. If choking criteria are met, new-time throat velocities and derivatives are recalculated. To calculate the derivatives, the throat pressure is perturbed by 1% and a second pass is made to calculate the liquid and vapor velocities. The choked derivatives are calculated by dividing the change in the choked velocity calculated between passes by the pressure perturbation.

5. Control is returned to TFIDE with the new calculated junction phasic velocities and derivatives.

The following sections detail how CHOKE calculates the throat conditions, the details of particular models that are invoked, and how they are implemented in the code.

Table 6.3-1
Equilibrium Critical Flow Regimes

Void Fraction	Regime	Correlation
$\alpha \leq 0.01$	liquid	Alamgir-Jones-Lienhard
$0.01 < \alpha < 0.1$	transition	Interpolate between liquid and two-phase
$0.1 < \alpha < 0.999$	two-phase	Homogeneous equilibrium sound speed
$0.999 < \alpha < 0.9999$	transition	Interpolate between two-phase and gas only
$0.9999 \leq \alpha$	gas only	HEM with adiabatic gas approximation

6.3.2.1 Methodology for the Calculation of Choke Plane Thermodynamic Properties

This section details the principal method used to calculate choke plane thermodynamic properties and how this method is implemented in the TRACG code. In order to calculate a_{HE} , the cell break plane conditions must first be approximated. In the TRACG finite-differencing scheme, fluid properties are calculated as cell-centered quantities. As a consequence, approximation techniques must be employed to estimate gradients in fluid conditions between the cell center and cell edge choke plane. In TRACG, a half cell momentum (Figure 6.3-1) balance approximation is used to estimate the junction pressure. It is assumed that the area change from the cell center to the cell face is not too abrupt. Hence, form loss effects are not accounted for in the approximation. The throat pressure is evaluated using Bernoulli's theorem, and accounting for the wall friction in the half cell:

$$P_t = P_c - \frac{\rho_{mt} v_{mt}^2}{2} + \frac{1}{2} \left[\rho_{mc} - (\alpha_{vc} \rho_{vc} + \alpha_{lc} \rho_{lc}) f \frac{L}{D_H} \right] v_{mc}^2 \quad (6.3-2)$$

where the subscripts t and c designate cell throat and center locations. The subscript m designates mixture conditions. The parameters V_{mc} , V_{mt} , ρ_{mc} , and ρ_{mt} are mixture velocities and densities at the cell center and throat, respectively (Figure 6.3-1). The parameter f is friction factor. The L and D_H parameters are the upstream cell half length and throat hydraulic diameter, respectively.

The Bernoulli equation (Equation 6.3-2) was evaluated by assuming that the mixture velocities rather than the phasic velocities are sufficient to calculate throat properties. The

Table 6.3-2
Input Call Parameters to CHOKe Subroutine

Variable	Parameter
DXC	Donor cell length
HD	Hydraulic diameter
WFL	Wall friction factor, liquid
WFV	Wall friction factor, vapor
ALP	Donor cell void fraction
PC	Donor cell upstream pressure
PD	Donor cell downstream pressure
RL	Donor cell density, liquid
RV	Donor cell density, vapor
SIGMA	Donor cell surface tension
TL	Donor cell temperature, liquid
TV	Donor cell temperature, vapor
VMC	Donor cell mixture velocity
VMO	Old-time mixture velocity
VL	Throat junction velocity, liquid
VV	Throat junction velocity, vapor
DFLDP	Derivative of VL with respect to pressure
DFVDP	Derivative of VV with respect to pressure
ICHOKE	Choking flag
ROAX	Donor cell total noncondensable density
IEOS	Gaseous phase equation-of-state flag
AVMO	Old-time HE sonic velocity

Table 6.3-3
Outputs from Subroutine CHOKE

Variable	Parameter
VL	Throat liquid velocity
VV	Throat vapor velocity
DFLDP	Derivative of VL with respect to pressure
DFVDP	Derivative of VV with respect to pressure
ICHOKE	Choking status flag

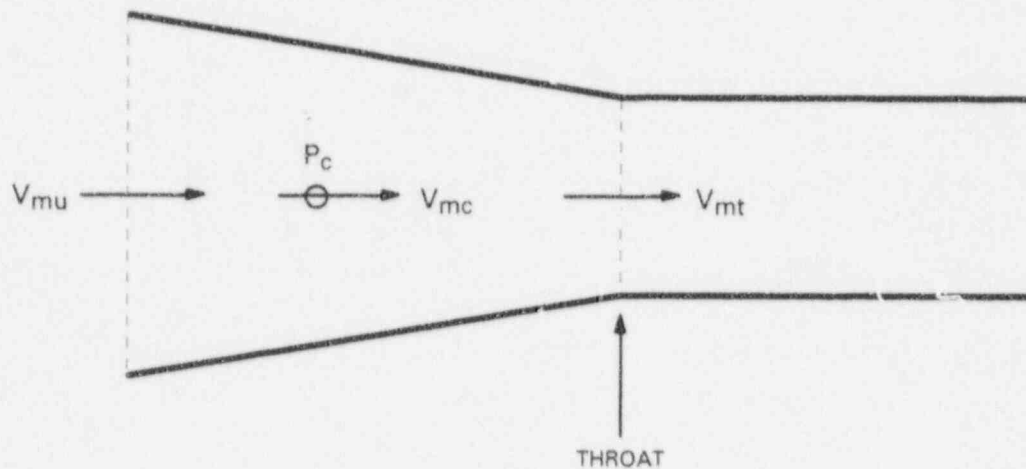


Figure 6.3-1. Choking Cell Configuration

mixture densities and velocities in Equation 6.3-2 are defined in Equations 6.3-3 to 6.3-8. The details for each type of flow are provided in Sections 6.3.3.1, 6.3.3.2 and 6.3.3.3.

Because of inherent limitations in the TRACG finite-difference solution scheme, additional approximations have been made to evaluate V_{mc} , V_{mt} and ρ_{mt} . In particular, the finite-difference scheme solves the field equations so that the phasic velocities are calculated only at cell edges. Cell-donored quantities, including the pressure, phase densities, temperatures and void fractions, are calculated only as cell-centered parameters. The mixture densities and velocities in Equation 6.3-2 are calculated as follows:

$$\rho_{mc} = \alpha_{vc}\rho_{vc} + \alpha_{lc}\rho_{lc} \quad (6.3-3)$$

$$V_{mt}^* = \frac{\alpha_{vc}\rho_{vc}V_{vt} + \alpha_{lc}\rho_{lc}V_{lt}}{\alpha_{vc}\rho_{vc} + \alpha_{lc}\rho_{lc}} \quad (6.3-4)$$

$$v_{mt} = \frac{v_{mt}^*}{c_{vena}} \quad (6.3-5)$$

The throat area is the minimum of the actual throat area and a vena contracta in the throat. The loss coefficient in the throat is related to the vena contracta through the following approximation:

$$c_{vena} = \frac{1}{\frac{A_t}{Vol_d / \Delta x_d} + \sqrt{c_{loss}}} \quad (6.3-6)$$

This is equivalent to basing the loss coefficient on an abrupt expansion from $A_t c_{vena}$ to the downstream area $Vol_d / \Delta x_d$. The vena contracta is limited to a minimum value of 0.75.

$$v_{mc} = v_{mt}^* \frac{A_t}{Vol_c / \Delta x_c} \quad (6.3-7)$$

The cell edge velocities and cell-centered densities and void functions are quantities calculated at the previous computational time step that are passed to the CHOKe subroutine. The quantities from Equations 6.3-3 through 6.3-7 are calculated and used to evaluate Equation 6.3-2. The density ratio ρ_{mt} / ρ_{mc} is calculated at the previous time step, with ρ_{mt} being estimated using CHOKe. The expression for the throat mixture velocity V_{mt} is a logical consequence of the code finite-differencing scheme. The approximation for V_{mt} is done by equating the mass fluxes with cell and throat-donored densities so that $\rho_{mc} V_{mt}^* = \rho_{mt} V_{mt}$. The mixture velocity V_{mt}^* is the effective velocity weighted with the cell-centered mixture density, whereas V_{mt} is weighted with the throat mixture density. Use of V_{mt} improves the accuracy of the throat pressure P_t calculation when compressibility effects are important.

The expression used to approximate the cell-centered mixture velocity V_{mc} is based on the assumption (Figure 6.3-1) that the flow area at the cell center upstream of the choke plane is given by $Vol / \Delta x$. By assuming constant volumetric flow, we have the following relationship between the cell-centered and upstream mixture velocities:

$$A_c v_{mc} = A_t v_{mt}^* \quad (6.3-8)$$

where

$$A_c = \frac{Vol_c}{\Delta x_c} \quad (6.3-9)$$

Equation 6.3-9 is substituted into Equation 6.3-8 and the result is rearranged to get Equation 6.3-7.

Once P_t has been calculated at the choke plane, the phasic temperatures at this location are calculated using assumptions dependent on the break upstream void fraction conditions and whether noncondensibles are present. The choking model assumes that the throat void fraction is equal to the calculated void fraction of the cell immediately upstream of the choke plane. Once the phasic temperatures and throat pressure have been calculated at the break plane, they are used to evaluate the remaining thermodynamic properties needed to calculate the sonic speed. Once a_{HE} is calculated, the appropriate tests for choking using Equation 6.3-1 are performed.

Table 6.3-4 summarizes the assumptions used to calculate the key throat parameters (pressure and phasic temperatures) and the associated sonic models used in the code. This table also makes reference to the presence of noncondensable gases, which will be discussed in later sections. Additional details of the assumptions used to calculate the break plane thermodynamic conditions and corresponding sonic velocity for different types of flow are presented in the following sections.

6.3.3 Calculation of Local Sonic Velocity

6.3.3.1 Two-Component/Two-Phase Flow

The two-component/two-phase (TCTP) HEM critical flow model used in TRACG was developed by Phillips et. al [6.3-3,7]. This model is based exclusively on theoretical grounds and employs several simplifying assumptions to enable one to derive an expression for the equilibrium sonic mixture velocity. This section will deal with several variations of the TCTP model employed in the TRACG code. The variations include the following:

- Noncondensibles/water mixture for $\alpha_v \leq 0.01$.
- Steam/water mixture for $\alpha_v \leq 0.01$.
- General TCTP model with steam/water/noncondensibles mixture applied to void fraction regimes:

$$0.01 \leq \alpha_v \leq 0.1$$

$$0.1 \leq \alpha_v \leq 0.999$$

$$0.999 \leq \alpha_v \leq 0.9999$$

- Noncondensibles /steam mixture formulation covers void regime $\alpha_v \geq 0.9999$.

Table 6.3-4
Summary of TRACG Choking Correlations and Throat Conditions

Void Fraction Range	Two-Phase Liquid Steam Throat Conditions	Two-Phase Two-Component Throat Conditions	Water With Noncondensable Throat Conditions	Steam With or Without Noncondensable Throat Conditions	Sonic Velocity Correlation
Case 1 $\alpha_v \leq 0.01$	$P_T = \text{SATPRS}$ (T_{lc}) $T_l = T_{\text{SAT}}(P_T)$ $T_g = T_l$	Noncondensable gas effects ignored throat conditioning same as left box.	Noncondensable gas effects ignored throat conditioning same as left box.	N/A	Use maximum of AJL and HEM correlation. See Section 6.3.3.3.
Case 2 $0.01 \leq \alpha_v \leq 0.1$	Throat conditions based on information in box above or box below.	Throat conditions based on information in box above or box below.	Throat conditions based on information in box above or box below.	N/A	Use HEM sonic model (α_v reset to 0.1) or AJL model. Interpolate with cubic spline.
Case 3 $0.1 \leq \alpha_v \leq 0.999$	P_T calculated from Bernoulli equation $T_g = T_{\text{SAT}}(P_T)$ $T_g = T_l$ Assume $\frac{d\alpha_v}{dP} \neq 0$	P_T calculated from Bernoulli equation equilibrium throat temperature T_{EQ} calculated with Taylor series approx. $T_{\text{EQ}} = T_l = T_{\text{NC}} = T_g$ Assume $\frac{d\alpha_v}{dP} \neq 0$	P_T calculated from Bernoulli equation liquid throat temp. set equal to cell center liquid temp. $T_{\text{NC}} = T_l$ Assume $\frac{d\alpha_a}{dP} = 0$	N/A	HEM sonic velocity model.
Case 4 $0.999 < \alpha_v < 0.9999$	Throat conditions based on information in box above or box below.	Throat conditions based on information in box above or box below.	Throat conditions based on information in box above or box below.	N/A	Interpolate between box above and box below.
Case 5 $0.9999 < \alpha_v$	N/A	N/A	N/A	For perfect gas P_T, T_v calculated from Adiabatic law $T_v = T_a$ For HEM case P_T is same value but, $T_v = T_a = T_{\text{SAT}}(P_T)$	Max $\left[\begin{array}{l} \text{HEM model} \\ \text{with } \frac{d\alpha_v}{dP} = 0, \\ \text{HEM model} \\ \text{with } \frac{d\alpha_v}{dP} \neq 0, \end{array} \right]$

The general expression for the local HEM sonic velocity is:

$$a_{HE} = \left(\frac{\partial P}{\partial \rho} \right)_S^{1/2} \quad (6.3-10)$$

where the subscript S corresponds to constant entropy of the derivative P with respect to ρ . In order to derive a tractable expression for a_{HE} in terms of thermodynamic quantities and derivatives, a number of simplifying assumptions have been made:

1. Each fluid component is in thermal equilibrium with itself (i.e., there are no temperature gradients).
2. The flow process is isentropic. Nonequilibrium interfacial heat and mass transfer are not directly considered.
3. Noncondensable gases occupy the same volume as the steam and they obey the Gibbs-Dalton law of partial pressures.
4. The noncondensable gases are chemically and mechanically inert (i.e., they do not dissolve into or evolve from the liquid, or form new compounds with water molecules).
5. The noncondensable gases are ideal gases.
6. Multi-dimensional and turbulence effects are not considered.
7. The fluid is homogenous. Stratification and/or other flow-map-dependent phenomena that could affect the sonic velocity are precluded. For critical flow the velocities are so large that stratification will not occur.

The above assumptions, with some exceptions, also apply to the critical flow models documented in Sections 6.3.3.2 and 6.3.3.3. With regard to assumptions 1 and 2, TRACG assumes a mixture equilibrium temperature at the choke plane that is calculated according to which break flow regime (Table 6.3-4) is considered. Under certain circumstances, the equilibrium assumption may break down [6.3-1,2,3]. In particular, for break assemblies of very short length, nonequilibrium transport behavior may be important. This occurs when the liquid and vapor phase at the choke plane have not had adequate time to relax to thermal equilibrium. However, it was judged that, in most cases, the equilibrium assumption is reasonable except in the low liquid void regime (Table 6.3-1). Modifications to assumption 2 under these circumstances are detailed in Section 6.3.3.3.

With respect to assumptions 3-5, the class of problems is confined to situations where noncondensable gases cannot interact chemically with the liquid-steam mixture. This may not produce accurate results for certain classes of problems where significant quantities of dissolved gases are hypothesized to come out of solution as the liquid decompresses at the choke plane

[6.3-9]. Assumption 6 may require code input adjustments to account for break flow geometry effects. The effects of break geometry near the choke plane are discussed by a number of authors [6.3-9 - 16]. In general, the use of a one-dimensional critical flow model approximation requires that a discharge coefficient be employed to account for two- or three-dimensional geometry effects [6.3-10]. Since there is a wide range of possible break flow geometries, there is no particular universal discharge coefficient that is applicable to all situations.

Using the formulation detailed in Appendices D and E, the following equations show how the HEM sonic speed is derived for either a steam-liquid or noncondensable-steam-liquid mixture. The general form of the isentropic derivative for the reciprocal of the sonic velocity squared is:

$$a_{HE}^{-2} = \left(\frac{\partial \rho}{\partial P} \right)_S = \alpha_v \left(\frac{\partial \rho_a}{\partial P} \right)_S + \alpha_v \left(\frac{\partial \rho_s}{\partial P} \right)_S + \alpha_\ell \left(\frac{\partial \rho_\ell}{\partial P} \right)_S - (\rho_a + \rho_s - \rho_\ell) \left(\frac{\partial \alpha_v}{\partial P} \right)_S \quad (6.3-11)$$

In the liquid/noncondensable regime, $\left\{ \frac{\partial \alpha_v}{\partial P} \right\}_S = 0$, so that Equation 6.3-11 reduces to:

$$a_{HE} = \left[\alpha_v \left(\frac{\partial \rho_a}{\partial P} \right)_S + \alpha_v \left(\frac{\partial \rho_s}{\partial P} \right)_S + \alpha_\ell \left(\frac{\partial \rho_\ell}{\partial P} \right)_S \right]^{-1/2} \quad (6.3-12)$$

The individual isentropic derivatives in Equation 6.3-12 are given by the general formula for a pure substance derived in Appendix D and is:

$$\left(\frac{\partial \rho}{\partial P} \right)_S = \left(\frac{\partial \rho}{\partial P} \right)_T - \frac{T \left(\frac{\partial \rho}{\partial T} \right)_P^2}{\rho^2 \left[\left(\frac{\partial e}{\partial T} \right)_P - \frac{P}{\rho^2} \left(\frac{\partial \rho}{\partial T} \right)_P \right]} \quad (6.3-13)$$

where the state variables, such as ρ , are for the liquid or noncondensable. In the case where we are modeling a single-phase vapor/noncondensable mixture ($\alpha_v \approx 1$), Equation 6.3-12 becomes:

$$a_{HE} = \left[\left(\frac{\partial \rho_a}{\partial P} \right)_S + \left(\frac{\partial \rho_s}{\partial P} \right)_S \right]^{-1/2} \quad (6.3-14)$$

where the individual isentropic derivatives are again evaluated using Equation 6.3-13 and the appropriate values for ρ and e .

In situations where the steam/liquid phases coexist, the general expression for the homogenous sound speed can be expanded using Equation 6.3-11. In this situation, the

isentropic derivative $\left\{ \frac{\partial \alpha_v}{\partial P} \right\}_S \neq 0$; and we have a significantly more complex expression. The expansion of the individual isentropic derivatives into algebraic expressions containing non-isentropic derivatives is somewhat long and is detailed in Appendix E. In the limit where the noncondensable gas density becomes zero, Equation 6.3-11 can be expressed as:

$$a_{HE} = \left(\frac{\partial \rho}{\partial P} \right)_S^{-1/2} = \left(\frac{\rho}{\rho_\ell \rho_g} \Omega \right)^{-1/2} \quad (6.3-15)$$

where

$$\Omega = \alpha_v \rho_\ell \left(\frac{\partial \rho_s}{\partial P} \right)_S + \alpha_\ell \rho_s \left(\frac{\partial \rho_\ell}{\partial P} \right)_S - \Lambda \quad (6.3-16)$$

$$\Lambda = \frac{\rho_s - \rho_\ell}{S_s - S_\ell} \left[\alpha_v \rho_g \left(\frac{\partial S_s}{\partial P} \right)_S + \alpha_\ell \rho_\ell \left(\frac{\partial S_\ell}{\partial P} \right)_S \right] \quad (6.3-17)$$

Prior to calculating the value of the sonic velocity, the throat thermodynamic conditions must be evaluated. The general outline for calculating the throat pressure was given in Section 6.3.2.1, using Equation 6.3-2. This section describes further details as to how the throat temperature and partial pressures are calculated. The methodology used depends on the particular break flow regime. This section considers Cases 1-3 in Table 6.3-4. Case 4 will be documented separately in Section 6.3.3.2. Table 6.3-4 summarizes how the throat conditions are calculated for Cases 1-4.

Relative to the steam-water case, P_t is calculated with Equation 6.3-2. The throat temperature of the liquid is assumed to be the upstream cell-centered liquid temperature ($T_{\ell c}$). The noncondensable gas throat temperature is set equal to the liquid temperature. In the situation where there is a steam-liquid mixture at the cell center upstream of the break plane, Equation 6.3-2 is again used; and the steam-liquid mixture is assumed to be in equilibrium with the throat steam and liquid temperatures set equal to the saturation temperature at the throat pressure, P_t .

For the steam-liquid-noncondensable situation, the total throat pressure P_t is again calculated with Equation 6.3-2. However, the effect due to partial pressure complicates matters for estimating the throat temperature. The steam-liquid-noncondensable temperature is calculated using a Taylor series approximation to account for the steam partial pressure [6.3-3]. Given the cell-centered pressure P_c , which is the sum of the vapor and noncondensable partial pressures, the steam partial pressure P_s at the throat is expanded as:

$$P_{st} (P_c + \Delta P) = P_s (P_c) + \Delta P \left(\frac{\partial P_s}{\partial P} \right)_{P=P_c} \quad (6.3-18)$$

where from Dalton's law, the cell-centered pressure upstream of the throat is

$$P_c = P_a + P_s \quad (6.3-19)$$

and the pressure increment to the throat is

$$\Delta P = P_t - P_c \quad (6.3-20)$$

In the above expansion, the steam throat partial pressure is calculated with a Taylor series expansion, where P_s is the dependent variable and P_c is the independent variable. The derivative of P_s with respect to P evaluated at $P = P_c$ is given by:

$$\left(\frac{\partial P_s}{\partial P} \right)_{P=P_c} = \left(\frac{\partial T}{\partial P} \right)_S \left(\frac{dP_s}{dT} \right)_{T=T_{sat}(P_c)} \quad (6.3-21)$$

The isentropic part of the derivative $\left(\frac{\partial T}{\partial P} \right)_S$ is a fairly complex expression. Its expansion into its basic components is detailed in Appendix E. The equilibrium throat steam-liquid-noncondensable temperature is then

$$T_{eq} = TSAT(P_{st}) \quad (6.3-22)$$

where TSAT is the saturation temperature evaluated at the throat pressure P_{st} .

6.3.3.2 Single-Phase One- or Two-Component Vapor Flow

The seven principal simplifying assumptions employed in Section 6.3.3.1 to calculate a_{HE} are also employed in the single-phase, one/two-component vapor choking formulation. This choking model presently employs two methods for calculating the sonic speed. The first approximation models the steam as a "perfect gas" (in the sense that there is no potential for vapor condensation). This is a valid approximation when the throat temperature of the steam is well above saturation conditions so that the isentropic derivative $\left\{ \frac{\partial \alpha_v}{\partial P} \right\}_S = 0$. The second approximation employs the generalized HE formulation from Section 6.3.3.1. In this formulation, the isentropic derivative $\left\{ \frac{\partial \alpha_v}{\partial P} \right\}_S$ is not equal to zero. This formulation fully accounts for the vapor equation of state deviations from the "perfect gas" approximation when the calculated throat temperature is near saturation conditions.

In the first approximation, the steam and noncondensable mixture are assumed to approximate a perfect gas with zero friction losses between the cell center and downstream choke

plane. Under these conditions, the cell-centered total pressure, temperature, and density are approximated within the adiabatic choked flow perfect gas formulation [6.3-17] which gives:

$$P_t = P_c^* \left(1 + \frac{\gamma-1}{2}\right)^{\left(\frac{\gamma}{\gamma-1}\right)} \quad (6.3-23)$$

$$P_c^* = P_c + \frac{\rho_c V_c^2}{2} \quad (6.3-24)$$

$$T_t = T_c \left(1 + \frac{\gamma-1}{2}\right)^{-1} \quad (6.3-25)$$

$$\rho_t = \rho_c \left(1 + \frac{\gamma-1}{2}\right)^{\left(\frac{\gamma}{\gamma-1}\right)} \quad (6.3-26)$$

where the specific heat ratio is density-averaged

$$\gamma = \frac{\bar{C}_P}{\bar{C}_V} = \frac{X_a C_{P_a} + (1 - X_a) C_{P_s}}{X_a C_{V_a} + (1 - X_a) C_{V_s}} \quad (6.3-27)$$

$$X_a = \frac{\rho_a}{\rho_t} \quad (6.3-28)$$

Assuming constant noncondensable mass fraction X_a gives a noncondensable throat density

$$\rho_{at} = X_a \rho_t \quad (6.3-29)$$

The throat partial pressure of the steam becomes:

$$P_{st} = P_t - \rho_{at} R T_a \quad (6.3-30)$$

The conditions at the throat are thus completely specified.

The above throat pressure and temperature conditions are then used by THERMO to calculate the remaining thermodynamic parameters and derivatives to evaluate the equations for the isentropic sound speed. In the limit $\alpha_v = 1$, Equation 6.3-11 reduces to:

$$a_{HE} = \left[\left(\frac{\partial \rho_a}{\partial P} \right)_S + \left(\frac{\partial \rho_s}{\partial P} \right)_S \right]^{-1/2} \quad (6.3-31)$$

where the individual isentropic derivatives are evaluated at $T_t = T_a = T_s$.

In the second formulation of the sonic speed, the vapor and noncondensable temperature are set equal to TSAT (P_{st}), or the saturation temperature at the throat partial steam pressure. Since the vapor state is now on the saturation curve, the isentropic derivative $\left\{ \frac{\partial \alpha_v}{\partial P} \right\}_S$ is not equal to zero even though $\alpha_\ell = 0$. From Appendix E, the generalized HEM sonic velocity in the limit $\alpha_v = 1$ reduces to:

$$a_{HE}^{-2} = \frac{\rho}{\rho_\ell \rho_s} \left\{ \rho_s \left(\frac{\partial \rho_a}{\partial P} \right)_S + (\rho_\ell - \rho_a) \left(\frac{\partial \rho_s}{\partial P} \right)_S - \frac{\rho_a + \rho_s - \rho_\ell}{S_s - S_\ell} \left[\rho_a \left(\frac{\partial S_a}{\partial P} \right)_S + \rho_s \left(\frac{\partial S_s}{\partial P} \right)_S \right] \right\} \quad (6.3-32)$$

TRACG calculates the sonic speed using both Equations 6.3-32 and 6.3-33 and uses the maximum value in the criteria for choking.

6.3.3.3 Single-Phase Liquid Flow

This section documents the single-phase liquid critical flow model used in TRACG. The terminology single-phase liquid is used in the sense that the vapor and/or noncondensable void fraction is either negligible or nonexistent. The single-phase liquid critical flow model employs two approximations for calculating the sonic velocity. The first method uses the approach developed by Alamgir, Jones and Lienhard (AJL) [6.3-18,19,20] to correlate the sonic velocity. This approach is called the AJL model or correlation. The second method employs a modified HEM approximation. After the sonic speed for each scheme is calculated, the maximum value is used in the choking criterion formulation. The single-phase liquid model is activated when the cell vapor void fraction immediately upstream of the break plane satisfies the criteria $\alpha \leq 0.01$.

The seven principal assumptions employed to calculate the choke plane a_{HE} in Sections 6.3.3.1 and 6.3.3.2 are modified for the single-phase liquid critical flow model. These modifications are:

- Vapor or noncondensibles immediately upstream of the break plane are assumed to be insignificant and are not donored to the cell choke plane.
- The AJL model quantifies turbulent fluctuations and nonequilibrium nucleation phenomena at the choke plane.

When high-pressure, high-temperature water is suddenly decompressed, it transitions from a subcooled or saturated state to a superheated state. As a consequence, the throat pressure of the flashing liquid can be much lower than the choke plane saturation pressure. Such enhanced depressurization can be driven by turbulent fluctuations or by bubble nucleation effects as the

liquid exits the choke plane. The pressure undershoot $\Delta P(a_s)$ at the throat is related to the sonic speed via the correlation:

$$P_{\text{sat}}(T_\ell) - P_t = \Delta P(a_s) \quad (6.3-33)$$

$$\Delta P(a_s) = (CA + CB a_s^{2.4})^{1/2} - CC a_s^2 \quad (6.3-34)$$

where

$$CA = \frac{0.258 \sigma^{3/2} \left(\frac{T_\ell}{T_{\text{crit}}} \right)^{13.76}}{(kT_{\text{crit}})^{1/2} \left(1 - \frac{\rho_g}{\rho_\ell} \right)} \quad (6.3-35)$$

$$CB = \left[\frac{(13.25) (9.866 \times 10^{-12}) \rho_\ell \left(\frac{dA}{dx} \right)_t}{A_t} \right]^{0.8} \quad (6.3-36)$$

$$CC = 0.072 \rho_\ell \left(\frac{A_t}{A_u} \right)^2 \quad (6.3-37)$$

σ = surface tension

k = Boltzmann constant

$\left(\frac{dA}{dx} \right)_t$ = rate of area change

T_{crit} = critical fluid temperature

$P_{\text{sat}}(T_\ell)$ = saturation pressure at the liquid temperature in the cell adjacent to the choking plane

The first term in Equation 6.3-34 represents the depressurization driven by nucleation effects formulated by Alamgir and Lienhard [6.3-18]. The second term developed by Jones [6.3-19,20] represents the additional pressure losses because of increased turbulence due to flashing. In the formulation implemented in TRACG, turbulence driven by acceleration effects (break geometry area gradients) is assumed to be much larger than wall friction effects. As a consequence, wall friction is ignored in the implementation of the AJL correlation in TRACG. The 0.072 coefficient is a best estimate of the turbulent intensity index in Equation 6.3-34. This number is

recommended unless there is a clear and substantially different value known *a priori* for a particular break geometry.

For closure, the second equation used to relate the throat pressure with the sonic speed is:

$$P_c + \frac{\rho_m V_{mc}^2}{2} = P_t + \frac{\rho_m a_s^2}{2} \quad (6.3-38)$$

Equation 6.3-38 is obtained by applying the Bernoulli equation (Equation 6.3-2) assuming no wall friction and sonic velocity in the throat. Equations 6.3-34 and 6.3-38 are solved in the TRACG solution scheme by eliminating P_t and finding a_s from the transcendental equation:

$$a_s - \sqrt{\frac{2}{\rho_\ell} [DPP + \Delta P(a_s)]} + V_{mc}^2 = 0 \quad (6.3-39)$$

where

$$DPP = \text{Max} [0, P_c - P_{\text{sat}}(T_\ell)] \quad (6.3-40)$$

Equation 6.3-39 is solved iteratively using a standard Newton-Raphson technique.

The sonic speed is calculated using a second approximation with Equation 6.3-13. Here, the throat temperature is set equal to T_ℓ and the pressure is set equal to $P_{\text{sat}}(T_\ell)$, where T_ℓ is the cell-centered liquid temperature upstream of the throat. In the second approximation, it is assumed that the liquid has decompressed to a saturated state at the break plane. The final sonic velocity becomes $\text{Max} [a_s, a_{\text{HE}}]$, where a_{HE} is the liquid single-phase homogenous sound speed from Equation 6.3-14.

In the course of doing simulations with early versions of the TRACG choking model, numerical oscillations in the break mass flow rate were observed when the throat conditions were near the subcooled sonic regime [6.3-4]. If the conditions upstream of the break plane transition from subcooled to saturated conditions, large reductions in the throat sonic velocity will occur. To prevent large discontinuous changes in the sonic velocity, a cubic spline interpolation scheme has been employed in the transition region $0.01 \leq \alpha_v \leq 0.1$. In this α_v range, both the TCTP homogeneous equilibrium and single-phase liquid models are separately used to calculate the break plane sonic speed. The cubic spline interpolation yields the transition sonic speed:

$$a_t = W a_{\text{HE}} + (1 - W) a_s \quad (6.3-41)$$

where

$$W = 3\alpha_T^2 - 2\alpha_T^3 \quad (6.3-42)$$

$$\alpha_T = \frac{\alpha_v - 0.01}{0.1 - 0.01} \quad (6.3-43)$$

6.3.4 Determination of Choked Flow Phasic Velocities

Once a particular regime has been picked and the corresponding sonic speed calculated, Equation 6.3-1 is employed to test for choking conditions. Because of the half-cell donoring scheme, Equation 6.3-1 is implemented in TRACG with the following modifications.

The sonic speed calculated from cell edge throat properties is first multiplied by the throat mixture density ratio so that:

$$a_s^* = a_s \left(\frac{\rho_{mt}}{\rho_{mc}} \right) \quad (6.3-44)$$

This modification was used to partially account for the difference in throat mass flux used in the cell continuity equation (due to cell-centered donoring) and the velocity that would exist if the throat density were used instead. If the choking criteria are satisfied, the new-time throat mixture velocity is set equal to the sonic velocity and then calculated using a relaxation scheme:

$$a_s^{*n+1} = a_s^{*n} + \text{RELAX} (a_s^{*n} - a_s^{*n+1}) \quad (6.3-45)$$

where

$$\text{RELAX} = \max \{0.1, 1 - \exp(-20 \Delta t)\} \quad (6.3-46)$$

where n and $n+1$ refer to old and new times, respectively. The relaxation algorithm is used to ensure numerical stability. Calculating the throat sonic velocity is not sufficient to advance the momentum solution to the next time step, since the two throat edge velocities must first be specified.

Two equations are needed to solve for the two unknown throat edge velocities. The solution scheme (except for single-phase vapor choking) uses the following two equations:

$$a_s^* = \frac{\alpha_v \rho_\ell v_v + \alpha_\ell \rho_v v_\ell}{\alpha_v \rho_\ell + \alpha_\ell \rho_v} \quad (6.3-47)$$

and

$$C_v v_v + C_\ell v_\ell = \text{RHS} \quad (6.3-48)$$

where

a_s^* = calculated sonic speed

v_ℓ, v_v = choke plane cell edge liquid and vapor velocities

C_ℓ, C_v, RHS = TRACG momentum equation solution constants calculated from TFIDE.

For single-phase one- or two-component vapor choking, Equations 6.3-47 and 6.3-48 are replaced by the simple relationships:

$$v_\ell = v_v = a_s^* \quad (6.3-49)$$

In general, the above formulation allows for slip between the phases at the choke plane. In order to advance the TRACG momentum solution scheme in time, the velocity derivatives with respect to pressure must be calculated. The derivatives are calculated by perturbing the previously calculated throat pressure by 1% in the subroutine CHOKE. The sonic speed and junction velocities are then recalculated. The phasic velocity derivatives are then calculated as follows:

$$\frac{\Delta v_\ell}{\Delta P_t} = \frac{v_\ell(P_t + \Delta P_t) - v_\ell(P_t)}{\Delta P_t} \quad (6.3-50)$$

$$\frac{\Delta v_v}{\Delta P_t} = \frac{v_v(P_t + \Delta P_t) - v_v(P_t)}{\Delta P_t} \quad (6.3-51)$$

where (ΔP_t) is the 1% throat pressure variation. It should be noted that the phasic velocities, calculated by CHOKE and passed back to TFIDE when the flow is choked, are calculated at P_t and not at $(P_t + \Delta P_t)$.

6.3.5 Applicability

The two-phase critical flow models described in Sections 6.3.1 through 6.3.4 contain a number of simplifying assumptions. The most important limitation is that the TRACG choking model is inherently one-dimensional. Break flow geometry must be considered as a factor in simulating a particular scenario. If the modeled break configuration is strongly affected by multi-dimensional hydrodynamic phenomena, a discharge coefficient may have to be used.

The TRACG sonic speed formulation (with the exception of the AJL correlation, which considers turbulence and nucleation) assumes that nonhomogeneous or nonequilibrium processes are not significant. As a consequence, the sonic speed at the choke plane is derived with the assumption that the liquid and vapor phases have relaxed to thermodynamic equilibrium. In reality the degree of break plane nonhomogeneity is dependent on the flow map, while the degree of nonequilibrium is determined by interfacial transport processes and the time needed to relax to

equilibrium. The primary dependence on flow regimes is accounted for by using the void fraction to select which model and corresponding simplifications are most appropriate together with use of the individual component densities in evaluating the sonic velocity. This simple approach and the assumption of thermodynamic equilibrium are justified by assessing the calculated results against data.

6.3.6 Assessment and Applicability to BWR

Assessment work using the TRACG critical flow model has generally yielded very good results. The methodology for calculating the choke plane phasic velocities has generally yielded accurate comparisons versus experimental data with regard to calculated mass flow rates and system depressurization responses [6.3-1,2,3,4,21].

Break flow studies based on the TRACG predictions versus data from 11 tests in five different test facilities (PSTF, TLTA, FIST, FIX, Marviken) show that TRACG slightly overpredicts the data.

6.3.7 References

- 6.3-1 S.T. Free, Equilibrium Critical Flow Model Development, WR-CD-024, June 1980.
- 6.3-2 J.W. Spore, *Improvements in the TRAC-801 Choking Model*, WR-CD-81-053, July 1981.
- 6.3-3 R.E. Phillips, *Two-Phase Two-Component Choking Model*, EGG-CDD-5977, August 1982.
- 6.3-4 D.D. Taylor, *Improvements to Subcooled Choking Model*, IS-SAAM-80-025, August 1983.
- 6.3-5 V.H. Ransom and J.A. Trapp, *RELAP5 Progress Summary Analytical Choking Criterion For Two-Phase Flow*, CDAP-TR-013, 1978.
- 6.3-6 V.H. Ransom and J.A. Trapp, "The RELAP5 Choked Flow Model and Application to a Large Scale Flow Test," *Proceedings of the ANS/ASME/NRC International Topical Meeting on Nuclear Reactor Thermal-Hydraulics, Saratoga Springs, NY*, October 508, 1980, pp. 799-819.
- 6.3-7 V.H. Ransom et al., *RELAP5/MOD2 Code Manual, Volume 1*, NUREG/CR-4312, EGG-2396, August 1985.
- 6.3-8 J.A. Trapp and V.H. Ransom, "A Choked-Flow Calculation Criterion for Nonhomogeneous, Nonequilibrium Two-Phase Flows," *International Journal of Multiphase Flow*, 8, 6, 1982, pp. 669-681.
- 6.3-9 Y.Y. Hsu et al., *Transport Processes in Boiling and Two-Phase Systems*, American Nuclear Society, La Grange Park, IL, 1986.

- 6.3-10 J.R. Travis et al., "Multidimensional Effects in Critical Two-Phase Flow," *Nuclear Science and Engineering*, 68, 1978.
- 6.3-11 G.L. Sozzi and W.A. Sutherland, *Critical Flow of Saturated and Subcooled Water at High Pressure*, NEDO-13418, 1975.
- 6.3-12 R.E. Henry et al., "The Two-Phase Critical Flow of One Component Mixtures in Nozzles, Orifices, and Short Tubes," *Journal of Heat Transfer*, May 1981.
- 6.3-13 R.E. Henry, "The Two-Phase Critical Discharge of Initially Saturated Subcooled Liquid," *Nuclear Science Engineering*, 41, 3, 1970, pp. 336-343.
- 6.3-14 H.K. Fauske, "The Discharge of Saturated Water Through Tubes," *Chemical Engineering Progress Series*, 61, 59, 1965, pp. 210-216.
- 6.3-15 D.K. Edmonds and R.V. Smith, "Comparison of Mass Limiting Two-Phase Flow in a Straight Tube and in a Nozzle," *Symposium on Two-Phase Flow, 1, University of Exeter, England, 1966*, pp. G401-G414.
- 6.3-16 R.E. Henry, *A Study of One- and Two-Component, Two-Phase Critical Flows at Low Qualities*, ANL-7430, March 1968.
- 6.3-17 A.H. Shapiro, *The Dynamics and Thermodynamics of Compressible Flow, 1*, New York: Ranald Press, 1953.
- 6.3-18 M.D. Alamgir and J.H. Lienhard, "Correlation of Pressure Undershoot During Hot Water Depressurization," *ASME Journal of Heat Transfer*, 103, 1981, pp. 52-73.
- 6.3-19 N. Abuaf, O.C. Jones, Jr., and B.J.C. Wu, *Critical Flashing Flow in Nozzles with Subcooled Inlet Conditions*, BNL-NUREG-27512, 1980.
- 6.3-20 O.C. Jones, Jr., "Flashing Inception in Flowing Liquids," *ASME Journal of Heat Transfer*, 102, 1980, pp. 439-444.
- 6.3-21 B.L. Charboneau, *Overview of TRAC-BD1/MOD1 Assessment Studies*, NUREG/CR-4428, EGG-2422, November 1985.
- 6.3-22 S.Z. Rouhani et al., *TRAC-BF1/MOD1 Models and Correlations*, NUREG/CR-4391, EGG-2680, R4, August 1992.

6.4 Two-Phase Level Model

In the normal TRACG solution of the fluid flow equations, the mean cell void fraction is assumed to exist uniformly throughout each hydrodynamic fluid cell. If a phase boundary or liquid level exists in the cell, the numerical solution to the fluid flow equations results in an artificially high diffusion of vapor in one direction and liquid in the other. To minimize this artificial diffusion, it is necessary to accurately predict the existence of two-phase levels that may occur in vertically oriented cells and to take proper account for this in the numerical solution of the flow equations. The TRACG two-phase level tracking model was developed for this purpose. The model provides the capability of maintaining the sharp void fraction discontinuity across a two-phase level that occurs in vertical components.

The TRACG level tracking model consists of two parts:

1. Detection of two-phase levels plus calculation of their positions, velocities, and void fractions above and below the phase boundaries.
2. Appropriate modification to the equations governing the flow when a two-phase level is present.

Part 2 above is discussed in Subsection 6.4.3. Part 1 may be further divided into two sections: (1) detection of two-phase levels and (2) calculation of the parameters necessary to describe the propagation of fluid above and below the phase boundaries.

6.4.1 Level Detection

The first step in detecting a two-phase level is the determination of the type of vertical void profile existing around a particular cell. The level detection logic required for a normal (increasing in the vertical direction) void profile is not the same as the logic required for an inverted (decreasing in the vertical direction) void profile. Once the type of void profile has been established, the model must determine if the conditions in the cell indicate the existence of a two-phase level. Although different logic is used depending on the void profile, the use of cell average void fraction differences to initiate the level calculations is common to all conditions. Generally, a level is assumed to exist in cell j if (Figure 6.4-1):

$$(\alpha_{j+1} - \alpha_j) \geq \Delta\alpha_{\text{cut}} \quad \text{and} \quad \alpha_{j+1} \geq \alpha_{\text{cut}} \quad (6.4-1)$$

provided that no level exists in cell $(j+1)$ or cell $(j-1)$. Here, $\Delta\alpha_{\text{cut}}$ is a predetermined cutoff value. A value of 0.2 is recommended for $\Delta\alpha_{\text{cut}}$ and 0.9 is recommended for α_{cut} . Once a level has been established in a cell, these criteria are not used. The level calculation is therefore not sensitive to the precise value of $\Delta\alpha_{\text{cut}}$ as long as a reasonable value is chosen. The value of α_{cut} is used to prevent spurious level indications when the $\Delta\alpha_{\text{cut}}$ criteria are satisfied. The recommended value has been used for all TRACG qualification cases.

An inverted void profile is detected when the decrease in void fraction from cell (j) to cell (j+1) is greater than a predetermined cutoff value similar to $\Delta\alpha_{cut}$. The recommended value for the inverted level $\Delta\alpha_{cut}$ is 0.1. If a void inversion is detected, the normal void profile level criterion (Equation 6.4-1) is applied to the cells above and below the inversion boundary. For cells below a void inversion, the α_{cut} criterion is not applied.

6.4.2 Calculation of Level Parameters

The parameters necessary to describe a two-phase level are (1) the position and velocity of the level and (2) the void fractions above and below the level. Figure 6.4-1 shows a simplified diagram of a two-phase level established in a normal void profile situation.

For a normal void profile ($\alpha_{j+1} \geq \alpha_j \geq \alpha_{j-1}$), the two-phase level parameters in cell j can be obtained from the conditions in the vessel cells above and below cell j. The position of the level in cell j can be described by the equation:

$$\Delta z_{Lj} = \Delta z_j \left(\frac{\alpha_j^+ - \alpha_j}{\alpha_j^+ - \alpha_j^-} \right) \quad (6.4-2)$$

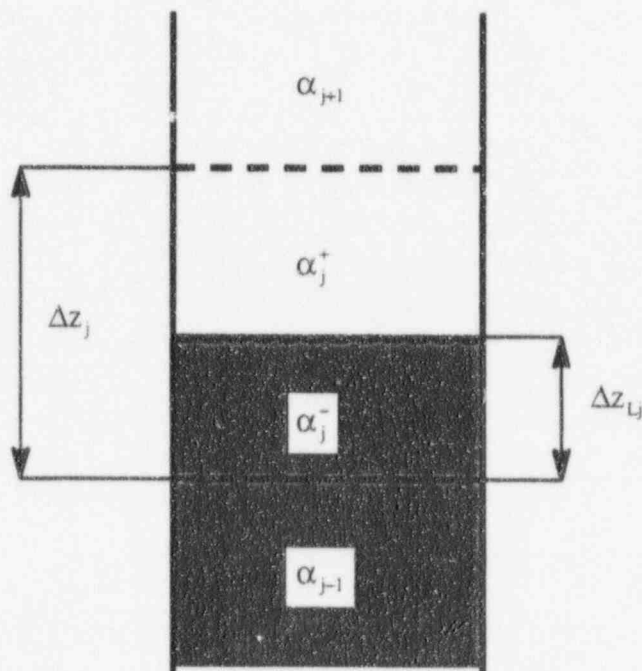


Figure 6.4-1. Two-Phase Level with Normal Void Profile

where α^+ and α^- are the void fractions above and below the level. For normal void profile conditions, the void fraction below the level α_j^- is assumed to be equal to the void fraction in the cell below, i.e.:

$$\alpha_j^- = \alpha_{j-1} \quad (6.4-3)$$

In the absence of entrainment of liquid from below the level, the void fraction above the level, α_j^+ , is assumed to be equal to the void fraction in the cell above:

$$\alpha_j^+ = \alpha_{j+1} \quad (6.4-4)$$

Entrainment lowers the void fraction given by Equation 6.4-4. The mass flux of entrained liquid ($G_{\ell ent}$) is calculated from the correlation of Rosen [6.4-1] as:

$$G_{\ell ent} = \left[3 \cdot 10^{-5} (C_K^{0.5} + 530.0 C_K^{2.1}) \left(\frac{\rho_\ell - \rho_v}{\rho_v} \right)^{0.5} \right] j_v \rho_v \quad (6.4-5)$$

$$C_K = \frac{2 D_{\max} j_v}{v_{\text{crit}} \left(\frac{\rho}{g (\rho_\ell - \rho_v)} \right)^{0.5}} \quad (6.4-6)$$

$$v_{\text{crit}} = 2 \left(\frac{\sigma g (\rho_\ell - \rho_v)}{\rho_v^2} \right)^{0.25} \quad (6.4-7)$$

$$D_{\max} = 0.3375 \frac{\rho_v v_v^2}{g (\rho_\ell - \rho_v)} \quad (6.4-8)$$

In these expressions, all fluid properties are for the cell in question and j_v and v_v are for the upper cell boundary. For positive liquid velocity at the top of the cell, the liquid mass flux may also be represented as:

$$G_{\ell ent} = (1 - \alpha_j^+) \rho_\ell v_\ell \quad (6.4-9)$$

from which the above-level void fraction, α_j^+ , is computed to be:

$$\alpha_j^+ = 1 - \frac{G_{\ell ent}}{\rho_\ell v_\ell} \quad (6.4-10)$$

For negative liquid velocity at the top of the cell, the entrainment is assumed to be zero and α_j^+ is assumed equal to the void fraction in the cell above (Equation 6.4-4).

The level velocity, v_{Lj} , is calculated as the time derivative of the level position:

$$v_{Lj} = \frac{\Delta z_j \left(\frac{\Delta \alpha_j}{\Delta t} \right) - \Delta z_{Lj} \left(\frac{\Delta \alpha_j^-}{\Delta t} \right) - (\Delta z_j - \Delta z_{Lj}) \left(\frac{\Delta \alpha_j^+}{\Delta t} \right)}{\alpha_j^- - \alpha_j^+} \quad (6.4-11)$$

The level velocity is used to predict when a two-phase level will leave a cell. In the event the level does exit a cell, the level velocity is used to predict the new velocity conditions at the boundary the level has crossed.

For a normal void profile, the two-phase level is completely described by Equations 6.4-2 to 6.4-11. However, if the two-phase level is in a cell below a void profile inversion ($\alpha_{j+1} < \alpha_j$) or flow area reduction, Equations 6.4-4 and 6.4-10 cannot be used to determine the void fraction above the level without modification. In this situation, it is assumed that:

$$\alpha_j^+ = 0.999 \quad (6.4-12)$$

and the two-phase level can be described by Equations 6.4-2, 6.4-3, 6.4-10, and 6.4-11. For a two-phase level occurring above a void fraction inversion ($\alpha_j < \alpha_{j-1}$) or flow area reduction, the void fraction below the level is evaluated using the drift flux model:

$$\alpha_j^- = \frac{j_v^-}{C_o j^- + \bar{v}_{gj}} \quad (6.4-13)$$

where C_o and \bar{v}_{gj} are determined assuming bubbly/churn flow (Section 6.1.3), and j_v^- and j^- are the vapor and mixture volumetric flux below the level, respectively.

6.4.3 Model As Coded

The two-phase level model is available for both three-dimensional and one-dimensional components. There are differences in the implementation for the two component types. For this reason, the as-coded details of the model will be described separately.

6.4.3.1 Three-Dimensional Component

The discretized governing equations described in Section 3.2 are impacted by the presence of a level through the void fraction axial donor celling as follows:

$$\phi_{i+1/2}^d = \begin{cases} \phi_i & v_{i+1/2} \geq 0 \text{ and no level exists in cell } i \\ \phi_i^+ & v_{i+1/2} \geq 0 \text{ and a level exists in cell } i \\ \phi_{i+1} & v_{i+1/2} < 0 \text{ and no level exists in cell } i + 1 \\ \phi_{i+1}^- & v_{i+1/2} < 0 \text{ and a level exists in cell } i + 1 \end{cases}$$

If an average property is required at a cell boundary, the above or below level void fraction is used for interpolation if a level exists.

The donor celling for source connections to the vessel for flow from vessel cell i is impacted in a similar fashion as follows:

$$\phi_s^d = \begin{cases} \phi_i & \text{if no level exists in cell } i \\ \phi_i^+ & \text{if level position is below connection} \\ \phi_i^- & \text{if level position is above connection} \end{cases}$$

The donor celled property is interpolated between the above and below values as a level crosses the source connection area.

The pressure drop from cell center to cell center in the momentum equation is also adjusted to account for a level in the cell. The pressure difference is modified to reflect the fluid conditions that exist at the cell boundary. In Figure 6.4-1, the hydrostatic head between cells j and $j+1$ is modified by adjusting the cell j pressure used in the momentum equation as follows:

$$P_j^* = P_j + (\rho_\ell - \rho_v)(\alpha^+ - \alpha^-)g \left(\Delta z_{Lj} - \frac{\Delta z_j}{2} \right) \quad (6.4-14)$$

This modification, together with the use of averaged void fractions as discussed above for the cell boundary, gives both the correct static head between cells and the correct pressure gradient and relative velocity at the cell boundary.

The interfacial heat transfer and shear are also impacted by a two-phase level. Above and below level heat transfer coefficients are calculated and volume weighted using the level position. A free surface convection component is added to account for free surface heat transfer. Interfacial heat transfer is described in Section 6.5. The interfacial shear is evaluated at the conditions present at the cell boundary when a level exists.

When a level crosses a boundary, there is a discontinuity in the void fraction and phase velocity at the boundary. To account for this, the phase velocities are modified when a level crosses a cell boundary using the jump conditions:

$$\begin{aligned}
 v_L &= \frac{-j_v^- + j_v^+}{\alpha^+ - \alpha^-} && \text{for } v_L < 0 \\
 v_L &= \frac{j_\ell^- - j_\ell^+}{\alpha^+ - \alpha^-} && \text{for } v_L > 0
 \end{aligned}
 \tag{6.4-15}$$

For a falling level, the modified old time vapor velocity becomes:

$$(v_v)_{j-1} = \frac{\alpha_j^- (v_v)_{j-1} - (\alpha_j^- - \alpha_j^+) v_{Lj}}{\alpha_j^+}
 \tag{6.4-16}$$

The liquid velocity at the boundary is adjusted using the above vapor velocity and the drift flux correlation with parameters appropriate for droplet flow as described in Section 6.1.5. For the falling level:

$$(v_\ell)_{j-1} = (v_v)_{j-1} - 1.41 \left(\frac{\Delta \rho g \sigma}{\rho_v^2} \right)^{0.25}
 \tag{6.4-17}$$

The evaluation of a rising level is handled in the same manner. In this case, the vapor velocity is adjusted using the liquid velocity modified using the jump condition and the drift flux correlation with parameters appropriate for bubbly flow (Section 6.1.3).

6.4.3.2 One-Dimensional Component

The level model is available in a one-dimensional (1-D) component cell that is vertically oriented. The level detection and calculation of level parameters are consistent with the three-dimensional (3-D) component. The major difference between the implementation is that, unlike the 3-D component, the 1-D component model does not affect the donor celling of void fraction at cell boundaries. For the 1-D component, the level model impact is limited to the interfacial heat transfer calculation within the cell. Above and below level heat transfer coefficients are calculated and volume weighted using the level position. A free surface convection component is added to account for free surface heat transfer. The absence of any special treatment for the convected void fraction in the presence of a level can be accounted for through nodalization. The 1-D component will require a finer nodalization in the vicinity of a two-phase level. Assessment of the use of the level model for 1-D components is provided in Section 7.11.

6.4.4 Applicability

The applicability of the level model is controlled by the assumptions used in the model development, in particular, the assumptions regarding the setting of the above and below void fractions. It is assumed that these values can be assigned the values of adjacent cells. Implicit in this assumption is that there is no significant change in void fraction for cells below or above the level position. An adjustment is made for entrainment for the above level void fraction but there is no provision for the existence of a void profile below the level. In situations where a significant void profile exists below the two-phase level, the nodalization must be sufficient to provide the necessary below level detail to avoid discontinuities in the level position. In addition to the model assumptions, the model applicability depends on the applicability of the interfacial shear and heat transfer models used to determine the void fraction.

6.4.5 Assessment

Assessment of the level model is provided by the PSTF level swell tests [6.4-2]. The PSTF facility consists of a 4.27m tall vessel with an internal diameter of 1.19m. A blowdown pipe is connected to the bottom of the vessel and could be fitted with different nozzles. In some tests, the blowdown pipe contained a vertical section with its inlet in the upper portion of the vessel at an elevation of 3.2m. In all cases, the vessel was partially filled with water, heated and pressurized to 7.2 MPa. A rupture disk at the end on the blowdown pipe was broken, allowing the system to depressurize.

For the cases where the blowdown pipe contained the vertical section, the break flow was primarily steam flow and the system depressurized quickly. In these tests, the liquid in the vessel flashed, causing the liquid level to rise initially and subsequently subside toward the end of the depressurization. The level swell is generally well predicted for these tests. The primary cause of the difference between the measured and calculated void fractions and the corresponding level positions is the uncertainty in the cross sectional distribution of the vapor resulting from the flashing of liquid during the rapid depressurization.

For cases where the vertical section was omitted, the system initially depressurized slowly as the break flow was primarily liquid and two-phase flow. During this period, the level dropped slowly. When the level uncovered the entrance to the blowdown pipe, the depressurization rate increased. The increased depressurization rate caused increased flashing of the liquid and the level drop subsided. The level movement is well predicted for these tests, indicating a good prediction of the void fraction. In these tests, the slower depressurization results in less uncertainty in the cross-sectional vapor distribution.

Visible in the TRACG level predictions are small discontinuities in the level position. These discontinuities result from the change in below level void fraction that occurs when a level crosses a cell boundary. Whenever a void profile exists below the level, the nodalization must provide sufficient detail below the level to minimize these discontinuities. The impact on the results for these tests is insignificant, indicating an acceptable nodalization.

The above separate effects assessment of the level model is supplemented by integral system testing and plant data comparisons.

6.4.6 References

- 6.4-1 A. Rosen et. al., *Teploenergetica*, 11, p 59, 1976.
- 6.4-2 J.A. Findlay, *BWR Refill-Reflood Program Task 4.8 - Model Qualification Task Plan*, General Electric Company, GEAP-24898, August 1981.

6.5 Interfacial Heat Transfer

Interfacial heat transfer models are needed for the closure of the two-phase equation system solution (Section 3.1). Interfacial heat transfer rates are part of the vapor and liquid conservation energy equations and determine the interfacial mass exchange rate Γ_g , which appears in the vapor and liquid mass and energy conservation equations. This section describes models and correlations incorporated into the TRACG interfacial heat transfer model, their technical bases and limitations.

6.5.1 Background

The TRACG interfacial heat transfer model is based on the assumption that the liquid-vapor interface is always at saturation temperature corresponding to the local partial steam pressure. Energy exchange rate at the interface provides the necessary mass exchange to maintain the interface at saturation temperature. The total heat exchange and mass transfer at the interface are functions of the volume-averaged liquid-interface heat transfer rate $q_{\ell i}$ and vapor-interface heat transfer rate q_{vi} :

$$q_{\ell i} = A_i h_{i\ell} (T_\ell - T_{\text{sat}}) \quad ; \quad q_{vi} = A_i h_{iv} (T_v - T_{\text{sat}}) \quad , \quad (6.5-1)$$

where A_i is the interfacial area per unit volume and $h_{i\ell}$ and h_{iv} are liquid-interface and vapor-interface convective heat transfer coefficients. Energy exchange at the vapor-liquid interface leads to mass exchange at the interface Γ_g due to evaporation ($\Gamma_g > 0$) or condensation ($\Gamma_g < 0$) processes at the interface:

$$\Gamma_g = \frac{q_{\ell i} + q_{vi}}{h_{fg}} \quad (6.5-2)$$

Equations 6.5-1 and 6.5-2 represent the energy and mass exchange between phases at the interface and appear in the mass and energy conservation equations (Section 3.1). According to Equation 6.5-1, interfacial area A_i and interfacial heat transfer coefficients $h_{i\ell}$ and h_{iv} have to be defined (based on the flow regime) to calculate energy and mass exchange at the interface and to close the thermal-hydraulic system of equations.

The interfacial heat transfer model described below is closely related to the interfacial shear model (Section 6.1) and incorporates the same flow regime map (Section 5.1.1). The entrainment model described in Section 5.1.2 is used to determine the fraction of the entrained liquid.

6.5.2 Interfacial Area

The calculations of the interfacial heat transfer require the specification of the interfacial area A_i and heat transfer coefficients $h_{i\ell}$ and h_{iv} . The experimental data will generally lead only

to information about their product. The models for the interfacial area described in the following sections are mostly based on the models proposed by Ishii [6.5-1], which were used [6.5-2, 6.5-3] to determine the interfacial shear (Section 6.1). For this reason, the database that was used to confirm the drift flux parameters for the interfacial shear model is applicable to the interfacial heat transfer model (interfacial area calculations). For some flow regimes (bubbly-churn flow, droplet flow), the interfacial area is defined by a maximum stable particle size, which is a function of a critical Weber number. In the calculation of the interfacial shear, only the ratio of the drag coefficient C_D and critical Weber number We_c has to be correlated (Section 6.1), and there is no need to calculate interfacial area A_i . This is not the case in the interfacial heat transfer calculations, where the value of the interfacial area A_i has to be defined for all the flow regimes to calculate interfacial heat flux (Equation 6.5-1).

6.5.3 Bubbly/Churn Flow

6.5.3.1 Technical Basis and Assumptions

The interfacial area in bubbly flow regime depends on the number of bubbles and average bubble diameter:

$$A_{ib} = N_b \pi d_b^2 \quad (6.5-3)$$

The number of bubbles N_b is related to the void fraction:

$$N_b = \frac{6\alpha}{\pi d_b^3} \quad (6.5-4)$$

Substituting Equation 6.5-4 into Equation 6.5-3, one obtains the expression for the interfacial area:

$$A_{ib} = \frac{6\alpha}{d_b} \quad (6.5-5)$$

The bubble diameter is calculated from critical Weber number:

$$d_b = \frac{\sigma We_c}{\rho_l v_{rb}^2}$$

A maximum critical Weber number for the stable spherical particles is typically 12-13 [6.5-1, 6.5-4]. In reality, a spectrum of bubbles will exist with a critical Weber number of 13 representing the maximum bubble diameter. A value of half the maximum bubble size is chosen for the average bubble diameter d_b .

The relative phasic velocity is calculated similar to Section 6.1:

$$v_{rb} = \frac{\bar{v}_{gj}}{1 - \alpha}$$

The same correlation for the cross-sectional average vapor drift velocity \bar{v}_{gj} is used in the interfacial heat transfer and interfacial shear models (Section 6.1):

$$\bar{v}_{gj} = k \left\{ \frac{\Delta \rho g \sigma}{\rho_\ell^2} \right\}^{0.25}, \quad \text{where } k = 1.53 \quad (6.5-6)$$

The heat transfer coefficient $h_{i\ell,b}$ between the continuous liquid phase and bubbly interface is calculated based on modified Lee-Ryley model and the corresponding correlation for the Nusselt number [6.5-2, 6.5-3, 6.5-5, 6.5-6, 6.5-8]:

$$Nu_{\ell,b} = 2 + 0.74 \sqrt{Re_b}; \quad Re_b = \frac{\rho_\ell v_{rb} d_b}{\mu_\ell} \quad (6.5-7)$$

The original correlation is based on measurements of the evaporation rate of small droplets [6.5-6]. The vapor properties in the original correlation are replaced with liquid properties and a factor of $Pr^{1/3}$, which is a part of the original correlation, is omitted [6.5-5, 6.5-8]. This has no significant impact, since $Pr \approx 1$ for water. Heat transfer coefficient $h_{i\ell,b}$ corresponding to the liquid side is given by:

$$h_{i\ell,b} = \frac{Nu_{\ell,b} k_\ell}{d_b} \quad (6.5-8)$$

Correlation for the heat transfer coefficient between vapor and bubble interface is based on the solution of the heat conduction equation for a spherical solid particle. For the fully developed temperature profile, this solution leads to $h_{iv,b} = 2\pi^2 k_v / 3d_b$ [6.5-7]. Due to relative motion between the bubbles and liquid, internal circulation will occur. The empirical factor $2.7\mu_\ell/\mu_v$ [6.5-19] is applied to account for this circulation and the final form for the $h_{iv,b}$ is:

$$h_{iv,b} = \frac{2}{3} \pi^2 \frac{k_v}{d_b} \left[2.7 \frac{\mu_\ell}{\mu_v} \right] \quad (6.5-9)$$

6.5.3.2 Model as Coded

Bubbly churn flow is realized when the criteria for the liquid continuous flow regime $\alpha < \alpha_{\text{tran}} - 0.1$ are satisfied (Section 5.1). Calculation of the heat transfer factors $(Ah)_{i\ell,b}$ and $(Ah)_{iv,b}$ is based on equations described in Section 6.5.3.1 with the following limitations. The

minimum number of bubbles per unit volume is limited to 10^7 . Limitation on bubble diameter is $0.0005\text{m} < d_b < 0.5D_h$.

6.5.3.3 Applicability

Because the calculation of the interfacial area is based on flow-regime, and is closely related to interfacial shear model, the applicability of these calculations corresponds to the range of data described in Sections 5 and 6.1. The original Lee-Ryley correlation, which provides the basis for calculations of the heat transfer coefficient between the liquid and bubble interface, was developed based on data on measured evaporation rates of small droplets, due to heat transfer from hot air or superheated steam. Because this correlation has been developed for small spherical particles, it is reasonable to apply it for small bubbles. Assessments presented in Reference 6.5-8 and Section 6.5.8 provide the justification for this correlation.

While a detailed discussion on derivation of the heat transfer factor on the vapor side has been presented in the previous section, it should be noted that, because of the small bubble diameter and low heat capacity of the vapor, the vapor temperature is very close to saturation temperature and the interfacial heat transfer model is insensitive to the value of the vapor side heat transfer coefficient.

6.5.4 Annular Flow

6.5.4.1 Technical Basis and Assumptions

In this flow regime, interfacial heat transfer and mass exchange occur at the surface of the liquid film on the walls. The interfacial area per unit volume in the annular film flow regime is a function of the average film thickness δ . The volume fraction α_f , which is occupied by liquid film, is:

$$\alpha_f = 1 - \alpha \quad (6.5-10)$$

The average film thickness δ and vapor-film interfacial area A_{if} per unit volume are given by the film fraction α_f and hydraulic diameter D_h . Assuming a tubular cross-section, one obtains:

$$\delta = \frac{D_h}{2} (1 - \sqrt{\alpha}); \quad A_{if} = \frac{4}{D_h} \sqrt{\alpha} \quad (6.5-11)$$

Equation 6.5-11 predicts a finite interfacial area $A_i = \frac{4}{D_h}$ and a film thickness approaching zero as the void fraction approaches one. In reality, at some point the film will break up and not cover the entire surface. TRACG uses a model for the minimum stable film thickness to model this breakup. The average film thickness δ is limited by the minimum film thickness δ_{min} :

$$\delta = \max \{ \delta, \delta_{min} \}$$

The expression for δ_{\min} is derived from the theory of minimum stable film flow [6.5-5] and defined as:

$$\delta_{\min} = \min \left\{ C \cdot \left[\frac{18\sigma\mu_\ell^2}{g^2\rho_\ell^3} \right]^{0.2}, \left[\frac{6\sigma\mu_\ell^2}{\rho_\ell\tau^2} \right]^{1/3} \right\} \quad (6.5-12)$$

where the interfacial shear stress is approximated by:

$$\tau = 0.005 \frac{\rho_v v_v^2}{2}$$

The original correlation for the minimum film thickness [6.5-5] has the form:

$$\delta_{\min} = \left[\frac{18\sigma\mu_\ell^2}{g^2\rho_\ell^3} \right]^{0.2}$$

The empirical factor C is set to 0.5 based on comparisons with the boiling transition correlation (Section 6.6.2).

The corresponding value for α_f is:

$$\alpha_{f,\min} = 1 - \left(1 - 2 \frac{\delta_{\min}}{D_h} \right)^2$$

The film thickness δ will decrease as α_f decreases but remains constant after it reaches the minimum thickness δ_{\min} . When $\alpha_f < \alpha_{f,\min}$, the vapor-film interfacial area is defined as:

$$A_{if} = \frac{4}{D_h} \sqrt{1 - \alpha_{f,\min}} \left[\frac{\alpha_f}{\alpha_{f,\min}} \right] \quad (6.5-13)$$

which is consistent with Equation 6.5-11 when $\alpha_f = \alpha_{f,\min}$ and provides the right trend ($A_{if} = 0$ when $\alpha_f = 0$).

Combining Equation 6.5-11 and Equation 6.5-13, one obtains:

$$A_{if} = \begin{cases} \frac{4}{D_h} \sqrt{1 - \alpha_f} & \text{for } \alpha_f > \alpha_{f,\min} \\ \frac{4}{D_h} \sqrt{1 - \alpha_{f,\min}} \left[\frac{\alpha_f}{\alpha_{f,\min}} \right] & \text{for } \alpha_f < \alpha_{f,\min} \end{cases} \quad (6.5-14)$$

The heat transfer coefficient $h_{iv,f}$ between the vapor phase and film interface is calculated according to Reference 6.5-8 and based on Theofanous's model [6.5-9]. The original model has the form:

$$St = 0.02 \sqrt{L/D} \quad (6.5-15)$$

As suggested in Reference 6.5-8, the modified version does not include the shape factor $\sqrt{L/D}$ and has the following form:

$$St = \frac{h_{i\ell}}{\rho_\ell C_{p\ell} v_v} = 0.02 \quad (6.5-16)$$

The heat transfer coefficient on the vapor side is obtained from Equation 6.5-16 by substituting corresponding vapor properties, which yields:

$$h_{iv,f} = 0.02 \rho_v C_{p,v} v_v \quad (6.5-17)$$

For the liquid side, the heat transfer coefficient is given by the analytical solution of the heat conduction equation across a thin liquid film, assuming a linear temperature profile [6.5-2]:

$$h_{i\ell,f} = 2 \frac{k_\ell}{\delta} \quad (6.5-18)$$

The presence of noncondensibles affects the interfacial heat transfer calculations in several ways. First, the saturation temperature T_{sat} in Equation 6.5-1 is calculated based on steam partial pressure. Second, the heat transfer coefficient on the liquid side is multiplied by a factor C_{ncg} to reduce the overall heat transfer at the interface [6.5-19]:

$$C_{ncg} = \min \left\{ 1.0, 0.168 \left(\frac{\alpha \rho_s^2}{(1-\alpha) \rho_a \rho_\ell} \right)^{0.1} \right\}$$

6.5.4.2 Model as Coded

Calculation of the heat transfer factors $(Ah)_{i\ell,f}$ and $(Ah)_{iv,f}$ is based on equations described in Section 6.5.4.1 with the following limitations for the interfacial heat transfer coefficients: $h_{i\ell,f} > h_{i\ell,free}$, $h_{iv,f} > h_{iv,free}$, where the heat transfer coefficients at free surface $h_{i\ell,free}$, $h_{iv,free}$ are defined according to Section 6.5.8.

The maximum value of the heat transfer coefficient on the liquid side is based on the constant Stanton number criteria (Section 6.5.4.1):

$$h_{i\ell f} < 0.02 \rho_{\ell} C_{P,\ell} v_f, \quad v_f = \frac{\delta^2 g \Delta \rho}{3 \mu_{\ell}}$$

where v_f is the film velocity derived from a simple force balance on a falling film, assuming viscous flow and a linear velocity distribution in the film. The minimum values of $\alpha \rho_s^2$ and $(1-\alpha) \rho_a \rho_{\ell}$ (C_{ncg} factor) are limited to 10^{-8} .

6.5.4.3 Applicability

The constant Stanton number criterion is frequently used to calculate the heat transfer coefficients. A constant Stanton number approach was suggested by various investigators for predicting the condensation rates on highly turbulent subcooled liquid jets. A comprehensive review of these studies is presented in Reference 6.5-9. Some of these models, such as Theofanous's model, include a correction factor. The Theofanous model, which is based upon the diffusion of turbulent eddies, covers a wide range of Reynolds numbers: $4.5 \times 10^3 < Re < 5 \times 10^5$ and was originally suggested for the highly turbulent liquid jets. Because the correction factor L/D is based upon shape factor of the jet, this factor is ignored in TRACG [6.5-8]. Assessments presented in Reference 6.5-8 and Section 6.5.8 provide the justification for this correlation.

The heat transfer coefficient for the liquid side is based on the analytical solution of the heat conduction equation for the thin liquid film. It should be noted that, because the film is very thin ($10^{-4} - 10^{-5}$ m for typical BWR conditions) the heat capacity is low and the temperature will be very close to saturation temperature. Consequently, the interfacial heat transfer factor model is insensitive to the exact value of the heat transfer coefficient on the liquid side. Similarly, when the wall is covered by a film, the vapor core will be close to thermal equilibrium with the interface. Therefore, the vapor temperature is not sensitive to the exact value of the heat transfer coefficient on the vapor side.

6.5.5 Droplet Flow

6.5.5.1 Technical Basis and Assumptions

In this regime, interfacial heat transfer and mass exchange occur at the vapor-to-droplet interface. The interfacial area in the droplet flow regime depends on the number of droplets and average droplet diameter. The volume fraction α_d occupied by a droplet is:

$$\alpha_d = 1 - \alpha$$

The interfacial area in the droplet flow regime depends on the number of droplets and average droplet diameter:

$$A_{id} = N_d \pi d_d^2 \quad (6.5-19)$$

The number of droplets N_d is related to the droplet fraction:

$$N_d = \frac{6\alpha_d}{\pi d_d^3} \quad (6.5-20)$$

Substituting Equation 6.5-20 into Equation 6.5-19, one obtains the expression for the interfacial flow area:

$$A_{id} = \frac{6\alpha_d}{d_d} \quad (6.5-21)$$

Droplet diameter is calculated from the critical Weber number [6.5-1]. For low flow rates, the relative vapor-liquid velocity is used:

$$d_d = \frac{\sigma We_c}{\rho_v v_{rd}^2}; \quad v_{rd} = \frac{\bar{v}_{gj}}{1-\alpha}$$

For large flow rates where the droplets are created by entrainment from the film, the droplet size will be determined by the initial relative velocity as they are entrained from the film on the wall. Since the film velocity is much smaller than the vapor velocity and the void fraction is high, the initial relative velocity can be approximated by the total flux (Section 6.1), and the droplet diameter is defined as:

$$d_d = \frac{\sigma We_c}{\rho_v j^2}$$

Combining these two expressions, the final equation for the droplet diameter is:

$$d_d = \frac{\sigma We_c}{\rho_v \max(v_{rd}^2, j^2)} \quad (6.5-22)$$

The relative velocity v_{rd} is related to the vapor drift velocity \bar{v}_{gj} by [6.5-4]:

$$v_{rd} = \frac{\bar{v}_{gj}}{1-\alpha} = 1.41 \left\{ \frac{\Delta \rho g \sigma}{\rho_v^2} \right\}^{0.25} \quad (6.5-23)$$

A maximum critical Weber number for the droplets is typically 12–13 [6.5-1,6.5-4]. In reality, a spectrum of droplets will exist with a critical Weber number of 13 representing the maximum droplet diameter. A value of half the maximum droplet size is chosen for the average droplet diameter d_d .

Similar to bubbly flow, the Lee-Ryley correlation [6.5-6] is used to calculate the interfacial heat transfer coefficient at the vapor-to-droplet interface:

$$\text{Nu}_{v,d} = 2 + 0.74\sqrt{\text{Re}_d} \text{Pr}_v^{1/3}; \quad \text{Re}_d = \frac{\rho_v v_{rd} d_d}{\mu_v} \quad (6.5-24)$$

$$h_{iv,d} = \frac{\text{Nu}_{v,d} k_v}{d_d}$$

The heat transfer coefficient on the liquid side is defined as [6.5-7]:

$$h_{il,d} = \frac{2}{3} \pi^2 \frac{k_\ell}{d_d} \cdot 2.7 \quad (6.5-25)$$

Equation 6.5-25 is similar to Equation 6.5-9 and is based on the analytical solution of the heat conduction equation for a spherical solid particle. The empirical factor 2.7 is applied to account for internal circulation (Section 6.5.3.1). In the presence of noncondensibles, the heat transfer coefficient on the liquid side is modified as for the annular flow regime (Section 6.5.4.1).

6.5.5.2 Model as Coded

Calculation of the heat transfer factors $(Ah)_{il,d}$ and $(Ah)_{iv,d}$ is based on equations described in Section 6.5.5.1 and implemented with the following limitation for the droplet diameter:

$$2 \cdot 10^{-4} \text{ m} \leq d_d \leq \frac{D_h}{4}$$

6.5.5.3 Applicability

The Lee-Ryley correlation is based on measurements of evaporation of a water droplet for the following range of variables: droplet diameter 0.006–0.03m, droplet Reynolds number 64–250. The Lee-Ryley correlation is very consistent with the correlation reported in Reference 6.5-20, where the heat transfer to spheres is considered over a wide range of conditions: sphere diameter 0.013–0.04m, Reynolds number 20–2000. A comprehensive review of heat transfer data for sphere is also presented in Reference 6.5-20. It is noted [6.5-6, 6.5-20] that the form

$$\text{Nu} = 2 + B \cdot \text{Re}^{0.5} \text{Pr}^{1/3}$$

has been firmly established by a number of authors for heat transfer to spherical particles under forced convection conditions. All the available data in the range $20 < \text{Re} < 2000$ has been best fit

to obtain the resulting coefficient: $B = 0.63$ (heat transfer in air), $B = 0.79$ (heat transfer in water). The correlation suggested in Reference 6.5-20, which covers heat transfer in air and water and predicts the data with an error no greater than 10%, has the form:

$$Nu = 2 + 0.72 \cdot Re^{0.5} Pr^{1/3}$$

This correlation is almost identical to the Lee-Ryley correlation (the difference is within 4%). Based on results presented in References 6.5-6 and 6.5-20, it can be concluded that Lee-Ryley correlation is applicable over the wide range of conditions that would be present in the reactor vessel and containment.

Because of the small droplet diameter, the liquid temperature is very close to saturation temperature. Thus, the interfacial heat transfer model is relatively insensitive to the liquid side heat transfer coefficient.

6.5.6 Annular/Droplet Flow

In the annular/droplet flow regime, liquid is distributed between the liquid film and droplets based on the entrainment model (Section 5.1.2). The total vapor-liquid interfacial area is the sum of the vapor-to-liquid film interfacial area and vapor-to-droplet interfacial area. The fraction of the entrained liquid is defined by entrainment coefficient E . The volume fractions occupied by liquid film α_f and droplets α_d are:

$$\alpha_f = (1 - \alpha)(1 - E), \quad \alpha_d = (1 - \alpha)E \quad (6.5-26)$$

If the vapor continuous flow regime exists ($\alpha > \alpha_{\text{tran}}$), the heat transfer factors $(Ah)_{il,fd}$ and $(Ah)_{iv,fd}$ are defined as:

$$(Ah)_{il,fd} = (Ah)_{il,f} + (Ah)_{il,d} \quad (6.5-27)$$

$$(Ah)_{iv,fd} = (Ah)_{iv,f} + (Ah)_{iv,d}$$

where heat transfer factors for the film and droplet regimes are defined in Section 6.5.3.1 and 6.5.4.1.

In the presence of noncondensibles, the heat transfer coefficient on the liquid side is modified as for the annular flow regime (Section 6.5.4.1).

6.5.7 Transition to Annular Flow

In the transition region ($\alpha_{\text{tran}} - 0.1 < \alpha < \alpha_{\text{tran}}$), linear interpolation for the heat transfer factors is applied to provide smooth transition from the liquid continuous to vapor continuous flow regime.

6.5.8 Free Surface in Vertical Pipes or 3D Cells

6.5.8.1 Technical Basis and Assumptions

When a level is established in a vertical pipe or 3D cells, natural, or free, convection is observed in the vicinity of the level. TRACG provides the capability to calculate heat and mass exchange at the free surface. Free-convection heat-transfer coefficients can generally be represented as a function of Grashof and Prandtl numbers for a variety of circumstances:

$$\text{Nu} = \text{Nu}(\text{GrPr})$$

The correlation for average heat transfer coefficient from the horizontal plates [6.5-10] is incorporated in TRACG to evaluate interfacial heat transfer at a free surface:

$$H_{iv} = 45.04k_v |T_v - T_{\text{sat}}|^{0.3333}; \quad H_{i\ell} = 45.04k_\ell |T_{\text{sat}} - T_\ell|^{0.3333} \quad (6.5-28)$$

In the presence of noncondensibles, saturation temperature is calculated based on steam partial pressure, and heat transfer coefficient in the liquid side is modified based on Sparrow [6.5-11] and Uchida [6.5-12] results. The Sparrow results are applied when the mass fraction of noncondensibles is less than 0.1, and Uchida results are applied when the mass fraction of noncondensibles is greater than 0.1 (Figure 6.5-1).

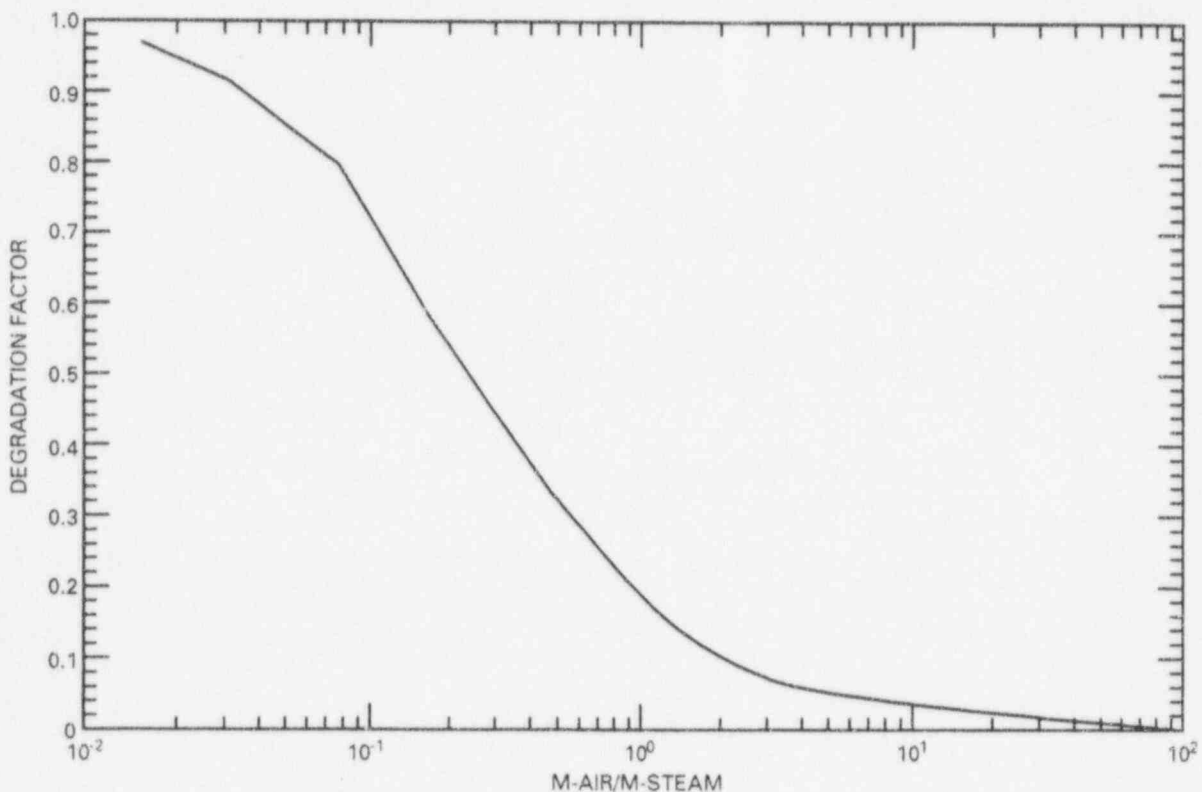


Figure 6.5-1. Sparrow-Uchida Degradation Factor

6.5.8.2 Model as Coded

Calculations of the interfacial heat transfer at free surface are encoded as described in Section 6.5.8.1.

6.5.8.3 Applicability

The correlation (Equation 6.5-28) has been derived for turbulent flow with $GrPr > 10^9$. The applicability is evaluated through the assessment.

6.5.9 Horizontal Stratified Flow in a Pipe

6.5.9.1 Technical Basis and Assumptions

In a horizontal pipe stratified flow will exist if the void fraction is greater than a critical void fraction given by a critical Froude number (Section 5.1.3).

For horizontal stratified flow the interfacial area per unit volume is approximated from the void fraction by:

$$A_i = \frac{16\sqrt{\alpha(1-\alpha)}}{\pi D_h} \quad (6.5-29)$$

The interfacial heat transfer is calculated using the same correlations as for annular flow.

6.5.9.2 Model as Coded

The calculation of the interfacial heat transfer for horizontal stratified flow is encoded as described in Section 6.5.9.1.

6.5.9.3 Applicability

The applicability of the interfacial heat transfer for horizontal stratified flow is assumed to be the same as the applicability for annular flow, and evaluated through assessment.

6.5.10 Upper and Lower Limits for the Interfacial Heat Transfer

In order to avoid numerical difficulties, upper and lower limits have been implemented for the interfacial heat transfer. A lower limit has been implemented to maintain some coupling (mass and energy) between the liquid and vapor field for all conditions. The lower limits are given by:

$$A_i h_{iv} > 2.0 \cdot 10^{-3} \rho_v$$

$$A_i h_{i\ell} > 2.0 \cdot 10^{-4} \rho_\ell$$

Upper limits have been implemented to prevent the partial differential equations from becoming stiff:

$$A_i h_{iv} < 5.5 \cdot 10^6 \rho_v \alpha(1-\alpha)$$

$$A_i h_{i\ell} < 10^8 \rho_v \alpha(1-\alpha)$$

It is recognized that there is no physical basis for these limits; they have been implemented strictly for numerical reasons. The limits, however, have been chosen such that there is no impact on the heat transfer for all reasonable scenarios for BWRs.

6.5.11 Assessment and Application to BWR

Separate assessment of all the models and correlations incorporated into the interfacial heat transfer model is not possible because of the limited range of test data. Test data for the separate effects are described in the previous sections. The overall assessment of the TRACG interfacial heat transfer model can be performed by selecting a set of steady-state and transient regimes with a strong dependency on the interfacial heat transfer. This approach is typical and has been used (for example) by TRAC-PF1 [6.5-8] developers by selecting the ECC injection to qualify the interfacial heat transfer model. The assessments included examples of subcooled boiling and film boiling where interfacial heat transfer effects were significant.

6.5.12 References

- 6.5-1 M. Ishii, *One-Dimensional Drift-Flux Model and Constitutive Equations for Relative Motion Between Phases in Various Two-Phase Flow Regimes*, ANL-77-47, October 1977.
- 6.5-2 J.G.M. Andersen and K.H. Chu, BWR Refill-reflood Program Task 4.7 -- Constitutive Correlations for Shears and Heat Transfer for BWR Version of TRAC, GEAP-24940, December, 1981.
- 6.5-3 J.G.M. Andersen, K.H. Chu and J.C. Shaug, *BWR REFILL/REFLOOD Program Task 4.7 - Model Development, Basic Models for the BWR Version of TRAC*, GEAP-22051, NUREG/CR-2573, EPRI NP-2375, April 1983.
- 6.5-4 B. Wallis, *One-Dimensional Two-Phase Flow*, McGraw-Hill Book Co., Inc., New York, 1969.
- 6.5-5 J.A. Borkowski and N.L. Wade, *TRAC-BF1/MOD1 Models and Correlations*, NUREG/CR-4391 EGG-2680 R4, 1992.
- 6.5-6 K. Lee and D.J. Ryley, *The Evaporation of Water Droplets in Superheated Steam*, Journal of Heat Transfer, November 1968, pp. 445-451.
- 6.5-7 J.G.M Andersen and H. Abel-Larsen, *CORECOOL - Model Description of the Programme*, Department of Reactor Technology, Riso National Laboratory, Denmark, RISO-M-21380, November 1980.

- 6.5-8 D.R. Liles, et al., *TRAC-PF1/MOD1 Correlations and Models*, NUREG/CR-5069 LA-11208-MS R4, 1988.
- 6.5-9 T.G. Theofanous, *Modeling of Basic Condensation Processes*, presented at the U. S. Nuclear Regulatory Commission Condensation Workshop, Silver Spring, Maryland, May 1979.
- 6.5-10 J.P. Hollman, *Heat Transfer*, 3rd Ed, New York: McGraw-Hill, Inc. 1972.
- 6.5-11 J.G. Collier, *Convective Boiling and Condensation*, McGraw-Hill, Inc, 1972.
- 6.5-12 H. Uchida, A. Oyama and M. Togo, *Evaluation of Post-Incident Cooling Systems of Light Water Power Reactors*, Third International Conference on the Peaceful Uses of Atomic Energy, Vol. 13, Geneve, 1964.
- 6.5-13 H. Christensen, *Power-to-Void Transfer Function*, ANL6385, July 1961.
- 6.5-14 D.G. Morris, et. al., *A Preliminary Evaluation of Rod Bundle Post-CHF Heat Transfer to High Pressure Water in Transient Upflow, Interim Report for THTF Test 3-06-6B*, ORNL, November 1980.
- 6.5-15 J.A. Findlay, *BWR Refill-Reflood Program Task 4.8 - Model Qualification Task Plan*, General Electric Company, GEAP-24898, August 1981.
- 6.5-16 D.D. Jones, J.E. Leonard, K.H. Sun and G.E. Dix, *Calculation of Counter Current Flow Limiting Conditions in BWR Geometry*, NEDE-13430, San Jose, CA, 1975.
- 6.5-17 R.T. Lahey, Jr., and F.J. Moody, *The Thermal-Hydraulics of a Boiling Water Reactor*, 1984.
- 6.5-18 A.R. Edwards and T.P. O'Brien, *Studies of Phenomena Connected with the Depressurization of Water Reactors*, Journal of the British Nuclear Energy Society, Vol 9, pp 125-135, April 1970.
- 6.5-19 Minutes of the Advanced Code Review Group Meeting, NRC Willste Building, Silver Spring, Maryland, January 25, 1980.
- 6.5-20 P.N. Rowe, K.T. Claxton and J.B. Lewis, *Heat and Mass Transfer from a Single Sphere in an Extensive Flowing Fluid*, Trans. Instn. Chem. Engrs., 43, T14-T31, 1965.
- 6.5-22 F.D. Shum et. al, *SAFER Model for Evaluation of Loss-of-Coolant Accidents for Jet Pump and Non-Jet Pump Plants, Volume 1*, NEDE-30996P, June 1986.

6.6 Wall Heat Transfer

This section describes all models used in TRACG for the exchange of energy between the fluid and the solid walls of each hydraulic volume. The basis for the correlations, the situations to which they apply, and their implementation are discussed.

6.6.1 Background

Wall heat transfer encompasses many different regimes, including (1) single-phase heat transfer (liquid or gas, forced or natural circulation), (2) two-phase heat transfer (nucleate boiling, film boiling, condensation) and (3) thermal radiation. Most of these are contained in what is referred to as the boiling curve shown in Figure 6.6-1.

- The left most part of the curve represents single-phase convection to liquid in which the fluid motion can result from an imposed pressure difference or can result from density differences (natural convection).

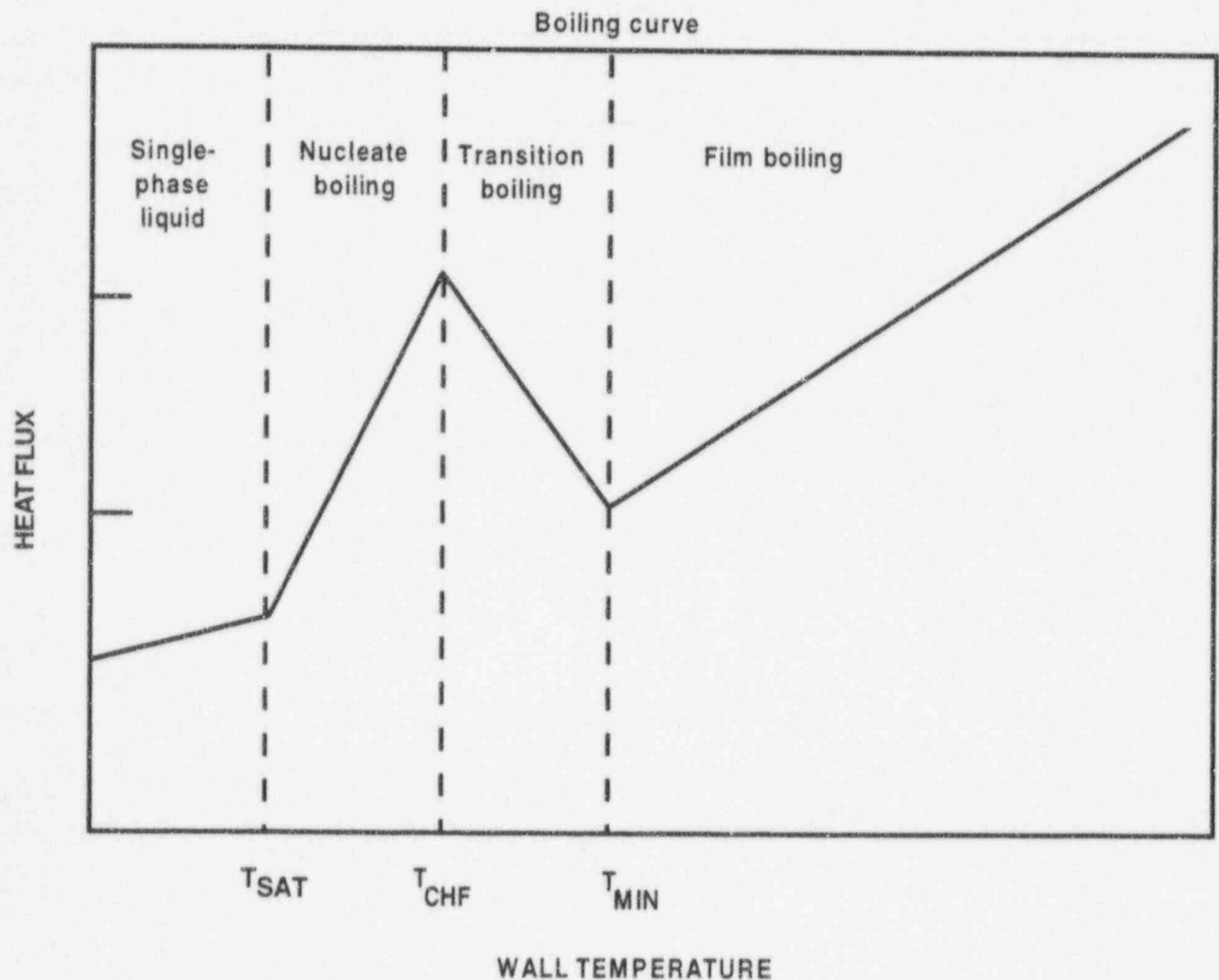


Figure 6.6-1. Boiling Curve

- As the wall temperature rises sufficiently above the saturated conditions, nucleate boiling occurs. Initially, the bulk liquid may still be subcooled. This regime is also called the isolated bubble regime and is characterized by high heat transfer rates. Bulk saturated nucleate boiling and forced convection vaporization are other boiling regimes.
- The critical heat flux (CHF) occurs when the heat flux reaches a maximum prior to degradation in heat transfer.
- As the wall temperature increases past the point of the CHF, transition boiling occurs. At low vapor content, this phenomenon is known as Departure from Nucleate Boiling (DNB). In this regime, the local vapor generation is so great that the drag on the liquid moving toward the surface prevents it from completely wetting the surface. As a result, the heat transfer decreases. For BWRs, high quality CHF is more relevant. This corresponds to the dryout of the liquid film at the wall, resulting in reduced heat transfer. In an increasing heat flux experiment, transition boiling would not be encountered. The local minimum at the end of the transition boiling regime is termed the minimum heat flux or the minimum stable film boiling temperature.
- When the entire boiling surface becomes blanketed with vapor, the regime is the film boiling regime. The heat flux then begins to increase with increasing superheat, and radiation effects become more important.
- Convection to single-phase (super-heated) steam.

The heat transfer in each of these boiling regimes or the transition points between regimes are predicted by correlations developed specifically for a particular regime. For a given set of local thermal-hydraulic conditions, a unique wall heat transfer mode is assigned. In a similar manner to the boiling curve, the heat transfer at the wall is divided into the following modes:

- Single-phase liquid convection mode
- Subcooled and nucleate boiling mode
- Transition boiling mode
- Film boiling mode
- Single-phase vapor convection

Additionally, the following modes of heat transfer are considered:

- Condensation
- Thermal radiation
- Quenching heat transfer

Each mode has a correlation to predict the amount of heat transfer. Sections 6.6.3 through 6.6.14 discuss each correlation along with its implementation and applicability. Section 6.6.2 discusses the logic selection and Section 6.6.15 assesses the correlations.

6.6.2 Heat Transfer Selection Logic

The wall heat transfer coefficient depends on the fluid condition and the wall conditions (Table 6.6-1 and Figure 6.6-2):

For single-phase liquid ($\alpha=0$), convective heat transfer will exist up to the point of net vapor generation for subcooled boiling ($h_\ell = h_{\ell d}$).

For two-phase flow with void fractions below the transition to annular flow (Section 5), several heat transfer regimes can exist. For subcooled wall temperatures, liquid convection will exist at the wall while condensation will take place at the bubble interface if $T_\ell < T_{\text{sat}}$. For superheated wall temperatures up to the point of boiling transition, either subcooled ($x_e < 0$) or nucleate boiling ($x_e > 0$) will exist dependent on the equilibrium quality. Nucleate boiling will exist up to the point where boiling transition occurs ($x_e < x_c$ and $T_w < T_{\text{CHF}}$ dependent on the boiling transition correlation). If boiling transition has occurred, transition boiling will exist if the wall temperature is less than the minimum point on the boiling curve ($T_w < T_{\text{min}}$) and sufficient liquid is present for rewet ($x_e < x_c$); otherwise, film boiling will exist.

For two-phase flow conditions with void fractions above the transition to annular flow, several heat transfer regimes can exist. For subcooled wall temperatures, film condensation will occur. For superheated wall temperatures up to the point of boiling transition, forced convection vaporization will exist. Forced convection vaporization will exist up to the point where boiling

Table 6.6-1
Selection Logic for Wall Heat Transfer

Fluid Condition	Wall Conditions			
	No Boiling Transition		Boiling Transition	
Flow Regime	$T_w < T_{\text{sat}}$	$T_{\text{sat}} < T_w < T_{\text{CHF}}$	$T_{\text{CHF}} < T_w < T_{\text{min}}$	$T_{\text{min}} < T_w$
$\alpha = 0$	Liquid Convection	Liquid Convection	N/A	N/A
$0 < \alpha < \alpha_{\text{tran}}$	Liquid Convection	Subcooled/ Nucleate Boiling	Transition Boiling	Film Boiling
$\alpha_{\text{tran}} < \alpha < 1$	Condensation	Forced Convection Vaporization	Transition Boiling	Film Boiling
$\alpha = 1$	N/A	Vapor Convection	Vapor Convection	Vapor Convection

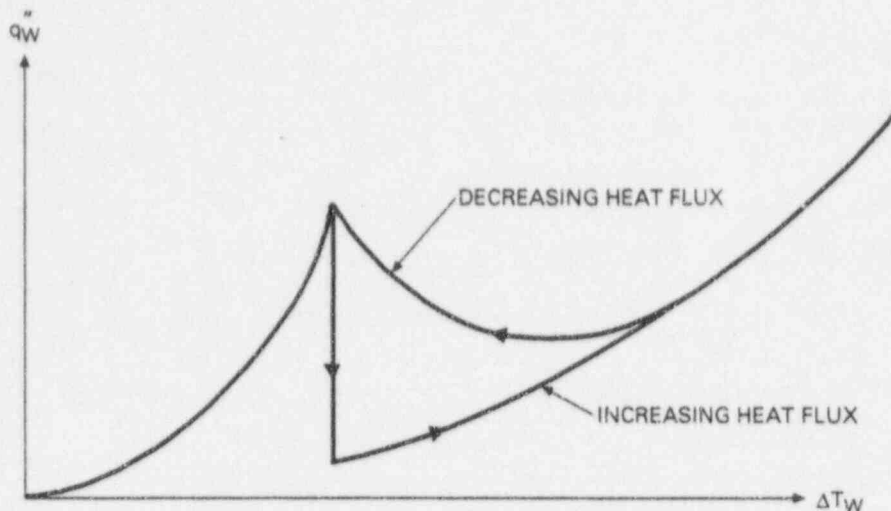


Figure 6.6-2. Selection Logic for Wall Heat Transfer Coefficient

transition occurs ($x_e < x_c$ and $T_w < T_{CHF}$ dependent on the boiling transition correlation). If boiling transition has occurred, transition boiling will exist if the wall temperature is less than the minimum point on the boiling curve ($T_w < T_{min}$) and sufficient liquid is present for rewet ($x_e < x_c$); otherwise, film boiling or vapor convection will exist.

For single-phase vapor ($\alpha=1$), convective heat transfer will exist for all wall temperatures above the saturation temperature ($T_w > T_{sat}$).

When the wall goes into boiling transition ($x_e > x_c$ and $T_w > T_{CHF}$ dependent on the boiling transition correlation), the heat transfer regime will change from nucleate boiling to film boiling. Transition boiling will only be entered from the film boiling mode if two criteria are met: (1) the wall temperature is sufficiently low ($T_w < T_{min}$) and (2) there is sufficient liquid to allow rewet ($x_e > x_c$ and $T_w > T_{CHF}$).

6.6.3 Single-Phase Convection to Liquid

Liquid single-phase wall heat transfer is broken down into three different categories: (1) laminar forced convection; (2) turbulent forced convection, and (3) natural convection.

6.6.3.1 Technical Basis and Assumptions

The heat transfer to liquid is given by the maximum heat transfer coefficient calculated by the liquid laminar, natural convection, and turbulent heat transfer correlations:

$$h_\ell = \max \{ h_{\ell,turb}, h_{\ell,lam}, h_{\ell,free} \} \quad (6.6-1)$$

Laminar flow heat transfer is given by the Rohsenow-Choi equation [6.6-1]:

$$h_{\ell, \text{lam}} = 4.0 \frac{k_{\ell}}{D_h} \quad (6.6-2)$$

This represents a compromise between the analytical solutions for uniform wall heat flux ($Nu = 4.364$) and for constant surface temperature ($Nu = 3.658$). The solutions were developed for a fully developed parabolic profile and therefore are suitable for only laminar flow.

For turbulent flow, the heat transfer is given by the Dittus-Boelter correlation [6.6-2]:

$$h_{\ell, \text{turb}} = 0.023 \frac{k_{\ell}}{D_h} \left(\frac{G_{\ell} D_h}{\mu_{\ell}} \right)^{0.8} \left(\frac{C_{p, \ell} \mu_{\ell}}{k_{\ell}} \right)^{0.4} \quad (6.6-3)$$

For natural convection flows, both laminar and turbulent, the heat transfer is given by [6.6-3]:

$$h_{\ell, \text{free}} = 0.12 k_{\ell} \left\{ \frac{-g \rho_{\ell} \frac{\partial \rho_{\ell}}{\partial T_{\ell}} C_{p, \ell} |T_w - T_{\ell}|}{\mu_{\ell} k_{\ell}} \right\}^{0.333} \quad (6.6-4)$$

6.6.3.2 Model as Coded

Calculations of the heat transfer coefficient to the liquid h_{ℓ} are based on equations described in Section 6.6.3.1. The Chen correlation (Section 6.6.4.1) is used to calculate heat transfer coefficient for the turbulent flow $h_{\ell, \text{turb}}$. The value of the Chen F-factor is set equal to one and the microscopic term is set to zero. Under these conditions, the Chen correlation transforms into Dittus-Boelter correlation.

6.6.3.3 Applicability

As stated above, the Rohsenow-Choi correlation was derived analytically for laminar, parabolic flow in a circular tube. The analytic solutions for noncircular cross-sectional geometries are similar to Rohsenow-Choi for aspect ratios not greater than 3. For aspect ratios greater than 3, Rohsenow-Choi will underpredict heat transfer; up to 50% for very large aspect ratios. At low flow rates, natural convection forces may distort the parabolic profile assumed in Rohsenow-Choi. This will likely cause Rohsenow-Choi to underpredict heat transfer. If Equation 6.6-4 predicts a higher heat transfer coefficient, then TRACG will use that value.

A large database exists for single-phase turbulent heat transfer. The Dittus-Boelter correlation represents the data within $\pm 25\%$ [6.6-4]. Figure 6.6-3 shows a comparison of Dittus-Boelter with data [6.6-4]. The correlation has been successfully and widely used for over 50 years for both nuclear and non-nuclear applications. It was originally developed for turbulent flow in smooth tubes for application to automobile radiators. For moderate temperature differences, the correlation is valid for forced flows within the following ranges [6.6-5]:

$$0.7 < Pr < 160$$

$$Re > 6000$$

$$L/D > 60$$

For moderate to high temperature differences, Dittus-Boelter appears to overpredict heat transfer for gases by 10 to 25% [6.6-6]. The correlation uses the bulk temperature of the fluid to determine the thermodynamic properties. Some authors [6.6-7] recommend a property correction for wide temperature differences. However, the correlation for many practical cases of interest can be used without any property correction to yield reasonably accurate estimation of the single-phase heat transfer coefficients in rod bundles [6.6-8].

In the development of the correlation, the entrance effect was neglected and is similarly neglected in the application in the code. For turbulent flow, the effects of the entrance flow are generally small. For flows over small lengths, the entrance region will have a more pronounced effect and the correlation will underpredict the actual heat transfer.

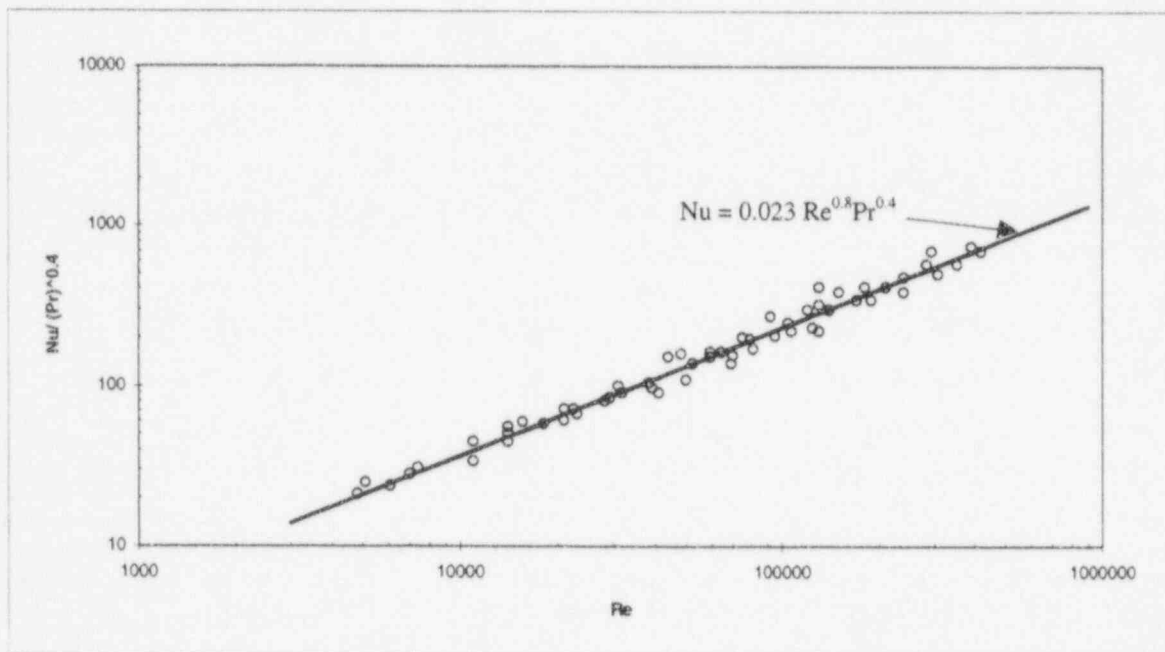


Figure 6.6-3. Dittus-Boelter Correlation Plotted Along with Data for Forced, Turbulent Convection in Tubes

Transition from laminar flow in pipes to turbulent flow in pipes is generally viewed to occur at $Re = 2300$. Laminar flows can be maintained to Reynolds numbers an order of magnitude larger than 2300 if the surfaces are smooth and there are no disturbances. Flows in the range $2300 < Re < 6000$ often oscillate between laminar and turbulent flow. As a result the spread in experimental data in this range is large and no known correlations exist in this transition region. However, for practical applications, pipes will not be smooth or will be of a varying shape or diameter. This will tend to cause laminar flows near or greater than $Re = 2300$ to become turbulent. For this reason, a sensible approach is to take the maximum of the laminar and turbulent correlations.

The natural convection correlation used in TRACG was developed for use for turbulent natural convection for values of $GrPr$ greater than 10^8 . The form of this correlation, $(GrPr)^{0.33}$, was analytically derived by Bailey [6.6-12] using a turbulent integral analysis. Figure 6.6-4 shows that the correlation agrees well with data for $GrPr$ greater than 10^7 . As $GrPr$ decreases, the correlation will underpredict the data by an increasing amount. However, TRACG will pick the largest heat transfer coefficients predicted by the turbulent, laminar and natural convection correlations. Below $GrPr = 4.1 \times 10^4$, the heat transfer coefficient used by TRACG will be $Nu = 4.0$ because the value predicted by Equation 6.6-4 will be less than $Nu = 4.0$. The correlation agrees with the data in Figure 6.6-3 above $GrPr = 4.1 \times 10^4$ to approximately 65%. This is the recommended value to be used in any sensitivity studies. It should be noted that results of turbulent correlations at identical conditions can vary by 100% [6.6-9].

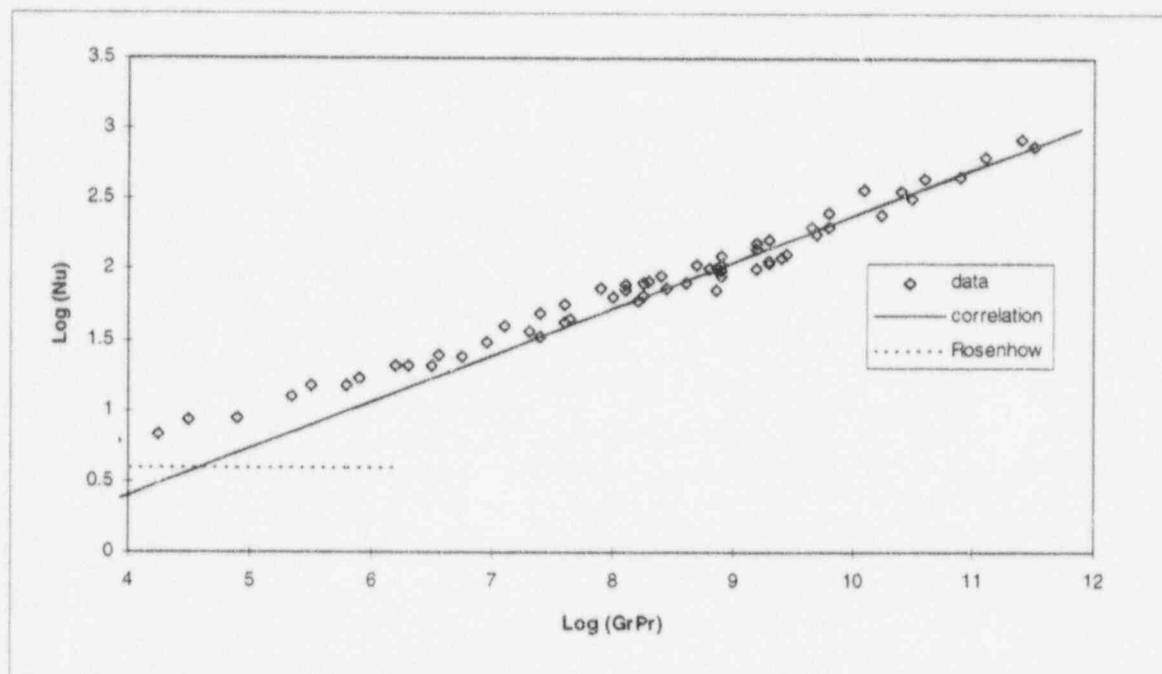


Figure 6.6-4. Fishenden and Saunders Correlation (Equation. 6.6-4)
Plotted Against Natural Convection Data for Vertical Surfaces

Equation 6.6-4 was developed for vertical flat plate natural convection. The error in applying it to vertical cylinders is less than 5% [6.6-10] when

$$\frac{D}{L} \geq 35 \cdot (\text{Gr})^{-0.25} \quad (6.6-5)$$

While there is no known experimental basis for applying this correlation to internal flow, RELAP5/MOD2 [6.6-23] applied a similar correlation to internal flow with apparent success. The form of the equation, $(\text{GrPr})^{0.33}$, makes the heat transfer coefficient independent of the chosen characteristic length.

For containment applications, natural convection from non-vertical walls may be important. Equation 6.6-4 is very similar to the correlation in Holman [6.6-4] for natural convection from the upper surface of a horizontal heated plate or the lower surface of a cooled plate, $\text{Nu} = 0.15(\text{GrPr})^{1/3}$. For the opposite situation of natural convection from the upper surface of a cooled plate or the lower surface of a heated plate, Equation 6.6-4 will underpredict the heat transfer coefficient by 8% at GrPr of 10^5 and will overpredict the heat transfer coefficient by 550% at GrPr of 10^{11} compared to the appropriate correlation in Holman [6.6-4]. The main impact for containment response of the overprediction of this coefficient occurs in the heat transfer from the diaphragm floor to the wetwell airspace. This causes an increase in the containment pressure and is therefore, conservative.

6.6.4 Subcooled and Nucleate Boiling

For subcooled boiling and nucleate boiling, the heat transfer is given by Chen's correlation [6.6-11]. An option is available to use the Forster-Zuber correlation for pool boiling in the IC and PCC pools.

6.6.4.1 Technical Basis and Assumptions

Chen argued that the heat transfer coefficient for saturated convective boiling is equal to the sum of the macroscopic (bulk convective) contribution h_{mac} and the microscopic (nucleate boiling) contribution h_{mic} :

$$q''_{w,\ell} = F h_{\text{mac}} (T_w - T_\ell) + h_{\text{mic}} (T_w - T_s(P)) \quad (6.6-6)$$

where F is a factor that modifies the convective part to account for increased heat transfer due to agitation caused by vapor bubble formation.

The macroscopic or convective portion is represented by the Dittus-Boelter correlation (Equation 6.6-3). The microscopic contribution to the overall heat transfer coefficient is given by a modified version of the Forster and Zuber [6.6-13] relation for the heat transfer coefficient for nucleate pool boiling:

$$h_{mic} = 0.00122 \frac{k_{\ell}^{0.79} C_{p,\ell}^{0.45} \rho_{\ell}^{0.49}}{\sigma^{0.5} \mu_{\ell}^{0.29} h_{fg}^{0.24} \rho_g^{0.24}} (\Delta T_w)^{0.24} (\Delta P_w)^{0.75} S \quad (6.6-7)$$

where S corrects the fully developed nucleate boiling prediction in h_{mic} to account for the fact that as the macroscopic convective effect increases in strength, nucleation is more strongly suppressed.

The factors F and S are given by Reference 6.6-14 as:

$$F = \begin{cases} 1.0 & \text{if } \chi_{tt} \leq 0.10 \\ 2.35(\chi_{tt} + 0.213)^{0.736} & \text{if } \chi_{tt} > 0.10 \end{cases} \quad (6.6-8)$$

where

χ_{tt} = Inverse of the Lockhart - Martinelli parameter

$$= \left(\frac{x}{1-x} \right)^{0.9} \left(\frac{\rho_{\ell}}{\rho_g} \right)^{0.5} \left(\frac{\mu_g}{\mu_{\ell}} \right)^{0.1} \quad (6.6-9)$$

$$\Delta T_w = T_w - T_{sat}$$

$$\Delta P_w = P_{sat}(T_w) - P_{sat}$$

$$S = \begin{cases} (1 + 0.12 \text{Re}_{TP}^{1.14})^{-1} & \text{if } \text{Re}_{TP} < 32.5 \\ (1 + 0.42 \text{Re}_{TP}^{0.78})^{-1} & \text{if } 32.5 \leq \text{Re}_{TP} < 50.9 \\ 0.1 & \text{if } \text{Re}_{TP} \geq 50.9 \end{cases} \quad (6.6-10)$$

$$\text{Re}_{TP} = \frac{G_{\ell} D_h}{\mu_{\ell}} F^{1.25} 10^{-4} \quad (6.6-11)$$

During subcooled boiling, vaporization may occur at the heated surface before the mean temperature of the cooling liquid reaches the saturation point. This phenomenon is caused by a nonuniform temperature distribution in the liquid.

In TRACG, each computational cell is assumed to have a uniform temperature distribution and the volumetric vaporization rate is given by:

$$\Gamma_g = - \frac{q_{i\ell}'' + q_{iv}''}{h_{fg}} \quad (6.6-12)$$

where:

$$q_{i\ell}'' = h_{i\ell} (T_{sat} - T_\ell) \frac{A_i}{V} \quad (6.6-13)$$

$$q_{iv}'' = h_{iv} (T_{sat} - T_v) \frac{A_i}{V} \quad (6.6-14)$$

This means that no vapor will be generated until the liquid reaches its saturation point and the void fraction will not be correctly predicted during subcooled boiling, unless specific models are introduced for subcooled boiling.

The Rouhani-Bowring model [6.6-15] for subcooled boiling energy distribution, along with the Saha-Zuber model [6.6-16] for subcooled boiling initiation, have been implemented into TRACG. The models are summarized by the following equations:

$$q_w'' = q_\ell'' + q_{evap}'' \quad (6.6-15)$$

where q_w'' is the wall heat flux which goes to heat up the liquid

$$q_\ell'' = \begin{cases} q_w'' & \text{if } h_\ell \leq h_{\ell d} \\ q_w'' \frac{h_f - h_\ell}{h_f - h_{\ell d}} \left(1 + \frac{h_\ell - h_{\ell d}}{h_f - h_\ell} \frac{\varepsilon}{1 + \varepsilon} \right) & \text{if } h > h_{\ell d} \end{cases} \quad (6.6-16)$$

and q_{evap}'' is the liquid side heat flux which goes to vaporize the liquid.

The pumping factor is given by:

$$\varepsilon = \frac{\rho_\ell (h_f - h_\ell)}{\rho_g h_{fg}} \quad (6.6-17)$$

The subcooled departure enthalpy is given by:

$$h_{\ell d} = \begin{cases} h_f - 154 \frac{q_w''}{\rho_\ell v_\ell} & \text{if } Pe > 70000 \\ h_f - 0.0022 \frac{q_w'' D_h C_{p,\ell}}{k_\ell} & \text{if } Pe < 70000 \end{cases} \quad (6.6-18)$$

where:

$$Pe = \frac{G_\ell D_h C_{p,\ell}}{k_\ell} \quad (6.6-19)$$

The expression for $q_{i,\ell}$ is then modified to:

$$q_{i,\ell} = A_i h_{i,\ell} (T_s - T_\ell) - A_w q''_{\text{evap}} \quad (6.6-20)$$

Hence, vapor can be generated even if the liquid temperature is below saturation.

TRACG also has an option to simulate pool boiling whereby F in Equation 6.6-6 is set to zero and S is set to 1. This is used only in the IC and PCC pools. The correlation then becomes the modified Forster-Zuber correlation. In this situation, TRACG takes the maximum value of the Forster-Zuber correlation

$$h_{F-Z} = 0.00122 \frac{k_\ell^{0.79} C_{p,\ell}^{0.45} \rho_\ell^{0.49}}{\sigma^{0.5} \mu_\ell^{0.29} h_{fg}^{0.24} \rho_g^{0.24}} (\Delta T_w)^{0.24} (\Delta P_w)^{0.75}$$

and the Dittus-Boelter correlation

$$h_{\ell, \text{turb}} = 0.023 \frac{k_\ell}{D_h} \left(\frac{\rho_\ell v_\ell D_h}{\mu_\ell} \right)^{0.8} \left(\frac{C_{p,\ell} \mu_\ell}{k_\ell} \right)^{0.4}$$

6.6.4.2 Model as Coded

Calculations of the heat transfer coefficient to the liquid h_ℓ are based on equations described in Section 6.6.4.1. The suppression factor, S , should approach zero as $\alpha \rightarrow 1$. To ensure the right trend the following internal procedure is used. When void fraction exceeds 0.95, the calculated suppression factor is modified according to the following equations:

$$S = f_\alpha \cdot S, \text{ where } f_\alpha = X_\alpha^2 (3 - X_\alpha), X_\alpha = 20 * (1 - \alpha)$$

For annular flow, the heat transfer coefficient is reduced if the film thickness is less than the minimum film thickness (Section 6.5.4) and only a fraction (W_f) of the wall is wetted. This is accomplished by the following multiplier to the wall area in contact with the liquid.

$$h_{mult} = (1 - x_2) + x_2 W_f$$

where $x_2 = 0$ for bubbly/churn flow and $x_2 = 1$ for annular flow. x_2 is linearly interpolated from 0 to 1 at the transition to annular flow.

6.6.4.3 Applicability

The original database for the Chen correlation covered the following ranges:

- Pressure: 0.09 to 3.48 MPa
- Mass Flow: 54 to 4070 kg/(m²-s)
- Quality: 0.0 to 0.7

The pressure range has been extended up to 6.9 MPa [6.6-17]. The specific experimental geometries and conditions for the database are shown in Table 6.6-2. The results of the comparison of the Chen correlation with previous correlations is shown in Table 6.6-3. The Chen correlation has by far the lowest average percentage deviations. A standard deviation of 11.0% is appropriate to use for sensitivity studies for convective boiling.

Table 6.6-2
Range of Conditions for Data Used
in Testing Correlations [6.6-17]

Fluid	Geometry	Flow	Pressure (Pa x 10 ⁻⁵)	Liquid inlet velocity (m/s)	Quality (wt%)	Heat flux (kW/m ²)
Water	Tube	Up	0.55-2.76	0.06-1.45	15-71	88-630
Water	Tube	Up	2.9-34.8	0.24-4.5	3-50	205-2400
Water	Tube	Down	1.1-2.1	0.24-0.82	2-14	44-158
Water	Annulus	Up	1	0.06-0.27	1-59	100-500
Methanol	Tube	Up	1	0.3-0.76	1-4	22-54
Cyclohexane	Tube	Up	1	0.4-0.85	2-10	9.5-41
Pentane	Tube	Up	1	0.27-0.67	2-12	9.5-38
Heptane	Tube	Up	1	0.3-0.73	2-10	6.2-28
Benzene	Tube	Up	1	0.3-0.73	2-9	12.5-41

Table 6.6-3
Comparison of Correlations [6.6-17]

Average Percentage Deviations for Correlations

Data	Dengler and Addoms	Guerrieri and Talty	Bennett <i>et al.</i>	Schrock and Grossman	Chen
Dengler and Addoms (water)	30.5	62.3	20.0	20.3	14.7
Schrock and Grossman (water)	89.5	16.4	24.9	20.0	15.1
Sani (water)	26.9	70.3	26.5	48.6	8.5
Bennet <i>et al.</i> (water)	17.9	61.8	11.9	14.6	10.8
Guerrieri and Talty (methanol)	42.5	9.5	64.8	62.5	11.3
Guerrieri and Talty (cyclohexane)	39.8	11.1	65.9	50.7	13.6
Guerrieri and Talty (benzene)	65.1	8.6	56.4	40.1	6.3
Guerrieri and Talty (heptane)	61.2	12.3	58.0	31.8	11.0
Guerrieri and Talty (pentane)	66.6	9.4	59.2	35.8	11.9
Combined average for all data	38.1	42.6	32.6	31.7	11.0

For situations such as the PCC and IC pool where the boiling is known to be pool boiling, the Forster-Zuber correlation is used (Equation 6.6-6 with $F = 0$ and $S = 1$). The Forster-Zuber correlation was developed for pool boiling heat transfer and is one of the most frequently quoted pool boiling correlations. The pressure range of the data used in the Forster-Zuber correlation was 1 to 50 bar.

Figure 6.6-5 shows a comparison at 1.0 MPa of the Forster-Zuber correlation with two other pool boiling correlations - - Rohsenow and Stephan-Abdelsalam [6.6-11]. The heat transfer coefficient predicted by Forster-Zuber falls between the other two correlations over a majority of the values of superheat. As the wall superheat approaches the value at the critical heat flux, Forster-Zuber predicts less heat transfer than both of the other correlations.

Regarding subcooled boiling and differing geometries, Carey in his book [6.6-11] writes: "First, because the subcooling of the liquid pool has virtually no effect on the resulting heat transfer rate, the pool boiling correlations are generally regarded as being valid for both subcooled and saturated nucleate boiling. Second, it has also been observed that a pool boiling heat transfer correlation developed for one heated surface geometry in one specific orientation often works reasonably well for other geometries and/or other orientations. Hence, although a correlation was developed for a specific geometry and orientation, it may often be used, at least as a good approximation, for others as well."

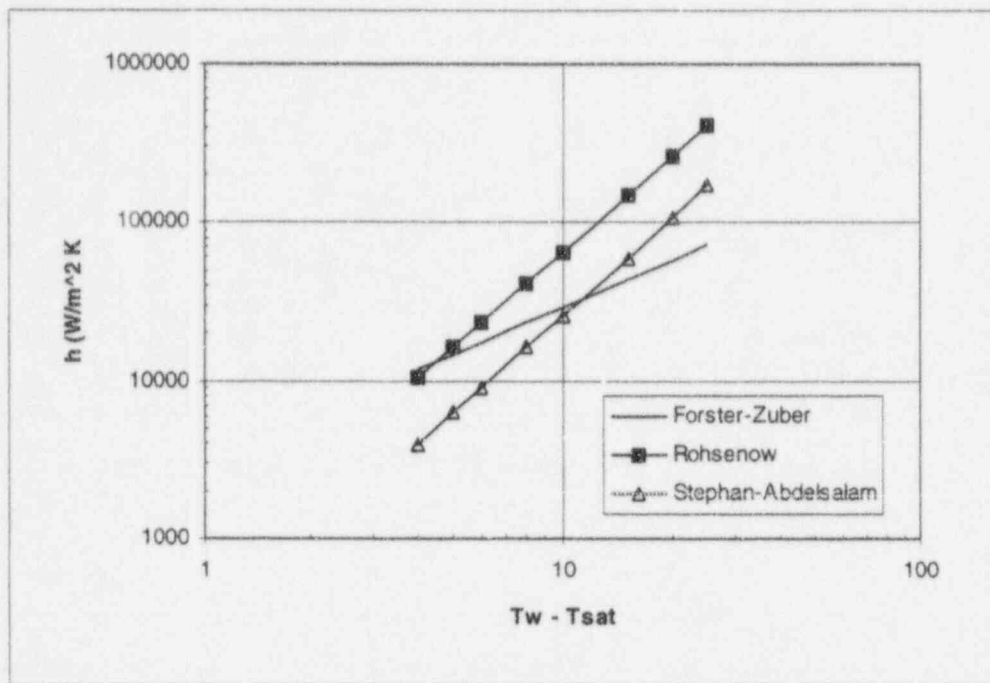


Figure 6.6-5. Heat Transfer Coefficients Predicted by Three Pool Boiling Correlations vs. Wall Superheat

6.6.5 Single-Phase Convection to Vapor

In a similar manner as liquid single-phase wall heat transfer, single-phase convection to vapor is broken down into three different categories: (1) laminar forced convection, (2) turbulent forced convection, and (3) natural convection.

6.6.5.1 Technical Basis and Assumptions

The heat transfer is calculated using the maximum heat transfer coefficient calculated by the laminar, turbulent or natural convection correlations:

$$h_v = \max \{ h_{v,lam}, h_{v,free}, h_{v,turb} \} \tag{6.6-21}$$

The natural convection correlation is given by McAdams [6.6-18]:

$$h_v = 0.13 \frac{k_v}{D_h} \left[\frac{D_h^3 \rho_v^2 g |T_w - T_v|}{\mu_v^2 T_v} \right]^{1/3} \left(\frac{C_{p,v} \mu_v}{k_v} \right)^{1/3} \tag{6.6-22}$$

The Rohsenow-Choi equation (Equation 6.6-1) is used for laminar forced convection. The Dittus-Boelter correlation (Equation 6.6-3) is used for the turbulent forced convection, $h_{v, turb}$. The vapor properties are used in Equations 6.6-1 and 6.6-3 instead of the liquid properties. When $T_w > T_v$, the heat transfer coefficient predicted by Dittus-Boelter is multiplied by a factor $\sqrt{T_v/T_w}$ to account for variation in vapor properties.

6.6.5.2 Model as Coded

Calculations of the heat transfer coefficient to vapor are encoded as described in Section 6.6.5.1.

6.6.5.3 Applicability

There is no fundamental difference between heat transfer to a single-phase vapor and heat transfer to a single-phase liquid. Most correlations apply to both vapors and liquids. The Dittus-Boelter correlation and the Rohsenow-Choi equation are exactly the same as that used in Section 6.6.3. The McAdams correlation (Equation 6.6-22) is almost identical to the Fishenden and Saunders correlation (Equation 6.6-4). The heat transfer coefficient differs by the choice of constants, 0.13 versus 0.12. The fact that there are two natural convection correlations, rather than one, relates to historical, not technical, reasons of the way the code was developed. The applicability and accuracy can be considered equal to what was presented in Section 6.6.3.3.

6.6.6 Boiling Transition Criteria

Boiling curves generally exhibit a maximum or critical heat flux at the transition between nucleate and transition boiling. The correlations presented in this section define the point where a shift is made from the nucleate boiling correlations to the transition boiling correlations, or vice-versa.

6.6.6.1 Technical Basis and Assumptions

There are four options for the boiling transition criteria:

- (1) Modified Zuber and Biasi correlations
- (2) CISE-GE and modified Zuber critical quality correlations
- (3) Modified CISE-GE critical quality and modified Zuber correlations
- (4) GEXL correlations

For Option 1, which is used for all components except the channel component, the critical heat flux is given by the modified Zuber correlation in low and counter-current flow conditions, while in high flow conditions, it is given by the Biasi correlation. The cutoff value for low and high flow conditions is $100 \text{ kg/m}^2\text{-s}$ for upflow and $240 \text{ kg/m}^2\text{-s}$ for downflow.

The modified Zuber correlation [6.6-19, 6.6-20] is given by:

$$q''_{CHF} = 0.1179(1 - \alpha)\rho_g h_{fg} \left[\frac{\sigma g \Delta \rho}{\rho_g^2} \right]^{1/4} \quad (6.6-23)$$

$$+ (1 - \alpha) 0.696 F_s \left[\rho_\ell c_{p,\ell} k_\ell \right]^{1/2} \left[\frac{g \Delta \rho}{\sigma} \right]^{1/4} \left[\frac{\sigma g \Delta \rho}{\rho_g^2} \right]^{1/8}$$

where F_s is a subcooled correction factor given by:

$$F_s = \begin{cases} T_s - T_\ell & \text{if } T_\ell < T_s \\ 0 & \text{if } T_\ell > T_s \end{cases} \quad (6.6-24)$$

The Biasi correlation [6.6-27] is given by:

$$q''_{CHF} = \max(q_1, q_2)$$

$$q_1 = \frac{3.78 \times 10^7}{(100D_h)^n \left(\frac{G}{10}\right)^6} h_p (1 - x)$$

$$q_2 = \frac{1.883 \times 10^7}{(100D_h)^n \left(\frac{G}{10}\right)^{1/6}} \left[\frac{f_p}{\left(\frac{G}{10}\right)^{1/6}} - x \right]^{1/4} \quad (6.6-25)$$

$$h_p = -1.159 + 0.149P \cdot e^{-0.019P} + \frac{8.99P}{10 + P^2}$$

$$f_p = 0.7249 + 0.099P \cdot e^{-0.032P}$$

where P is pressure in bars and:

$$n = \begin{cases} 0.4 & \text{for } D_h \geq 0.01 \text{ m} \\ 0.6 & \text{for } D_h < 0.01 \text{ m} \end{cases} \quad (6.6-26)$$

The temperature at critical heat flux, T_{CHF} , is obtained by solving the following equation:

$$q''_{CHF} = h_{Chen}(T_{CHF} - T_{sat}) \quad (6.6-27)$$

Onset of boiling transition will take place when the wall temperature is higher than T_{CHF} .

In Options 2 or 3, the departure from nucleate boiling is defined by the critical quality instead of critical heat flux as in the Zuber and Biasi Correlations. The critical quality is given by the CISE-GE or modified CISE-GE correlation shown below [6.6-15]:

$$x_c = C \frac{A L_{B1}}{B + L_{B1}} \quad (6.6-28)$$

where:

$$A = 1.055 - 0.013 \left(\frac{P - 4.137 \times 10^6}{2.758 \times 10^6} \right)^2 - 0.909 \left(\frac{G}{10^3} \right) + 0.493 \left(\frac{G}{10^3} \right)^2 - 0.114 \left(\frac{G}{10^3} \right)^3$$

$$B = 0.457 + 1.476 \left(\frac{G}{10^3} \right) - 0.489 \left(\frac{G}{10^3} \right)^2$$

$$C = \begin{cases} 1.24 / F_L & \text{for Option 3} \\ (1.24 / F_L)^{1/2} & \text{for Option 2} \end{cases}$$

in which:

$$L_{B1} = \begin{cases} L_B & \text{for Option 2} \\ (P_h / P_{h,7}) L_B & \text{for Option 3} \end{cases}$$

$P_{h,7}$ = Heated perimeter of a 7x7 bundle

F_L = Relative rod power

L_B = the heated length over which the steam quality is greater than zero

During co-current flow, the heat transfer mode at the wall will change from nucleate boiling mode to film boiling mode whenever the local equilibrium quality exceeds the critical quality. The CISE-GE and the modified CISE-GE correlations are rarely used in TRACG.

The GEXL correlation, which is recommended for applications to BWR fuel bundles, is applied for Option 4. The correlation is described in detail in Reference 6.6-21 and has been approved by the NRC. A summary is included here.

The correlation, expressed in the most general terms, is:

$$x_c = x_c(L_B, D_Q, G, P, R, L_A, L_H) \quad (6.6-29)$$

where

- x_c = Bundle average critical quality
- L_B = Distance from the initiation of bulk boiling to the boiling transition point
- D_Q = Thermal diameter (four times the ratio of total flow area to total rod perimeter, including unheated rods when any are present)
- G = Mass flux ($\text{kg}/\text{m}^2\text{-s}$)
- P = System pressure (MPa)
- R = A parameter which characterizes the local peaking pattern with respect to the most limiting rod
- L_A = Annular length
- L_H = Heated length

A more specific form of the GEXL correlation is:

$$x_c = \sum_{I=1}^{26} A(I) \times V(I) \quad (6.6-30)$$

where $A(I)$ is a set of constants which are fuel type specific.

6.6.6.2 Model as Coded

Calculations of the boiling transition criteria are based on equations described in Section 6.6.6.1. If Option 1 is chosen, then the Biasi correlation is used for high flow rate ($G > G_2$) and the Zuber correlation is used for low flow rates ($G_1 < G$). Linear interpolation for critical heat flux is applied within the region $G_1 < G < G_2$. The cutoff values for G_1 and G_2 are:

$$G_1 = 100 \text{ kg}/(\text{m}^2\text{s}) \text{ for upflow} \quad \text{and} \quad G_1 = 240 \text{ kg}/(\text{m}^2\text{s}) \text{ for downflow}$$

$$G_2 = 300 \text{ kg}/(\text{m}^2\text{s}) \text{ for upflow} \quad \text{and} \quad G_2 = 440 \text{ kg}/(\text{m}^2\text{s}) \text{ for downflow}$$

The Biasi correlation is modified for high void fraction to satisfy the trend $q_{CHF} \rightarrow 0$, when $\alpha \rightarrow 1$. When $\alpha > 0.9$, the Biasi critical heat flux is multiplied by factor $0.1(1 - \alpha)$.

To obtain the critical flux temperature,

$$q_{CHF} = h_{chen} (T_{CHF} - T_{sat})$$

is solved for T_{CHF} where $h_{chen} = h_{mic} + h_{mac}$.

If options 2-4 are used, boiling transition is realized when two conditions are satisfied: $x > x_c$ and $T_w > T_{CHF}^{Zuber, G=0}$, where $T_{CHF}^{Zuber, G=0}$ is the critical heat flux temperature calculated based on the Zuber correlation for the pool conditions ($G = 0$).

6.6.6.3 Applicability

The form of the modified Zuber equation for critical heat flux in pool boiling was developed analytically in a number of different ways (with different constants) [6.6-37]. The Zuber equation becomes the modified Zuber equation by multiplying by 0.9. The factor 0.9 was recommended by Walkush [6.6-19] after he compared his counter-current critical heat flux data with pool boiling critical heat flux data.

The constant in the similar equation developed in Reference 6.6-37 is 0.149, whereas Zuber's constant was 0.131. Whalley reports that the equation works well for predicting critical heat flux from long horizontal plates as long as two conditions are satisfied:

- (1) Liquid is prevented from entering around the sides of the plate. This can be ensured by adding sides to the flat plate.
- (2) The test section should be reasonably large. If the test section dimensions become small, then the number of vapor jets to be fitted in becomes important. The predicted critical heat flux varies significantly when the length is less than three times the distance between vapor jets. If the test section is reasonably large, then the impact of liquid entering around the sides of the plate is small.

The Biasi correlation was developed for vertical upflow boiling of water in uniformly heated tubes. The equations were developed from a database with the following ranges of parameters [6.6-11]:

Data points:	over 4500
Mass flow rate:	100 to 6000 kg/m ² -s
Pressure:	0.27 to 14.0 MPa
Diameter:	0.003 to 0.0375 m
Quality at CHF:	$\rho_v / (\rho_l - \rho_v)$ to 1
Axial power	uniform distribution

The RMS error of this correlation against the database was reported to be 7.3%. The Biasi correlation has been compared to other data banks [6.6-22]. Table 6.6-5 shows data which fall into different error bounds for the data which is in the range of the experimental conditions listed above. As explained previously, the correlation is only used for non-channel components for mass flow rates greater than 300 or 440 kg/m²-s, depending on the flow direction.

Table 6.6-5
Biasi Correlation Compared to Chalk River Data Bank

	Data Within the Error Bound (%)						No. of Data Points
	Constant Dryout Quality			Constant Inlet Subcooling			
	+10%	+20%	+30%	+10%	+20%	+30%	
Valid data	21.32	41.12	73.04	77.60	96.60	99.91	9936

According to Reference 6.6-23, the correlation has also been compared to 1928 data points from a Harwell round-tube data bank. All the data essentially fell within +40% and -50% of the correlation. On average, the correlation was 8% below the data and the standard deviation was 17%.

6.6.7 Minimum Stable Film Boiling Temperature

The boundary between the transition boiling regime and the film boiling regime corresponds to a minimum in the boiling curve. The boundary point is defined by the minimum stable film boiling temperature.

6.6.7.1 Technical Basis and Assumptions

The transition point from film boiling to transition boiling will occur only after the wall temperature drops below the minimum stable film boiling temperature, T_{\min} . If Option 1 from Section 6.6.6 is chosen, then transition boiling is defined to begin when the wall temperature drops below T_{\min} . For Options 2, 3 or 4, an additional condition has to be met before the wall rewets. This condition requires that the local equilibrium quality has to be lower than 97% of the critical quality described in Section 6.6.6. This ensures that there is sufficient liquid at the wall to keep the wall covered by a liquid film, which helps to minimize oscillations. Qualification against ATLAS test data [6.6-38] has shown that a factor of 0.97 fits the data.

Two options for calculating T_{\min} are incorporated in TRACG: (1) the Iloeje correlation option and (2) the homogeneous nucleation correlation option.

The Iloeje correlation [6.6-39] option is the recommended option. For this option, T_{\min} is given by:

$$T_{\min} = \max(T_{\min, \text{Iloeje}}, T_{\min, \text{homogeneous nucleation}}) \quad (6.6-32)$$

where $T_{\min, \text{Iloeje}}$ is given by Equation. 6.6-34 and $T_{\min, \text{homogeneous nucleation}}$ is given by Equation 6.6-36. For the homogeneous nucleation option, T_{\min} is given by:

$$T_{\min} = T_{\min, \text{homogeneous nucleation}} \quad (6.6-33)$$

The Iloeje correlation is based on Berenson's minimum pool film boiling temperature correlation and extended to provide the effects of mass flux and equilibrium quality. The correlation is given by:

$$\begin{aligned} \Delta T_{\min} &= T_{\min} - T_{\text{sat}} \\ &= 0.29 \Delta T_{\text{BER}} \left(1 - 0.295 x_e^{2.45}\right) \left[1 + (7.37 \cdot 10^{-2} G)^{0.49}\right] \end{aligned} \quad (6.6-34)$$

where:

$$\Delta T_{\text{BER}} = 0.127 \frac{\rho_g h_{fg}}{k_g} \left[\frac{g \Delta \rho}{\rho_\ell + \rho_g}\right]^{2/3} \left[\frac{\sigma}{g \Delta \rho}\right]^{1/2} \left[\frac{\mu_g}{g \Delta \rho}\right]^{1/3} \quad (6.6-35)$$

The mass flow rate, G , is limited to the range $54.4 \leq G \leq 135.9 \text{ kg/s-m}^2$. The equilibrium quality is limited to the range of $0.3 \leq x_e \leq 0.8$.

For the homogeneous nucleation correlation [6.6-40], the minimum stable film temperature, T_{\min} , is given by

$$T_{\min} = T_c + (T_c - T_\ell) \left(\frac{\rho_\ell k_\ell C_{p, \ell}}{\rho_w k_w C_{p, w}}\right)^{1/2} \quad (6.6-36)$$

where T_c is the critical temperature for water.

6.6.7.2 Model as Coded

Calculations of the minimum stable film boiling temperature are based on equations described in Section 6.6.7.1 with the following limitations for the mass flux G and equilibrium flow quality x_e :

$$\begin{aligned} 54.25 \text{ kg/m}^2\text{s} &< G < 135.63 \text{ kg/m}^2\text{s} \\ 0.3 &< x_e < 0.8 \end{aligned}$$

6.6.8 Transition Boiling

Transition boiling is characterized by a wall heat flux that decreases with increasing wall superheat. Physically, this is caused by dryout of the liquid film over portions of the surface, which adds to the thermal resistance.

6.6.8.1 Technical Basis and Assumptions

The heat transfer coefficient in the transition boiling mode is obtained by interpolating the values of the heat transfer coefficient in the nucleate and film boiling mode as follows [6.6-36]:

$$h_{TB} = \gamma h_{NB}(T_{CHF}) + (1 - \gamma)h_{FB}(T_{min}) \quad (6.6-37)$$

where [6.6-35]

$$\gamma = \left(\frac{T_w - T_{min}}{T_{CHF} - T_{min}} \right)^2 \quad (6.6-38)$$

and:

$h_{NB}(T_{CHF})$ = Nucleate boiling heat transfer coefficient evaluated at T_{CHF}

$h_{FB}(T_{min})$ = Film boiling heat transfer coefficient evaluated at T_{min} .

6.6.8.2 Model as Coded

Calculations of the heat transfer coefficients in the transition boiling region are based on equations described in Section 6.6.8.1 and include several interpolation procedures to provide smooth flow regime transition and smooth transition from wetted to unwetted wall. Calculations of the heat transfer coefficients at the critical heat flux temperature are based on the nucleate boiling correlation as described in Section 6.6.4. Calculation of the heat transfer coefficient at T_{min} is based on the film boiling heat transfer correlations as described in Sections 6.6.9 to 6.6.10.

6.6.8.3 Applicability

In order to operate in the transition boiling regime, the wall temperature of the passage must be controlled in the physical system so that it remains in the transition boiling regime. This may occur during reflood following a loss-of-coolant accident (LOCA) scenario. Compared with nucleate boiling and film boiling, relatively fewer investigations of transition boiling have been conducted. The data that do exist are relatively scarce and generally cover only narrow ranges of conditions. The few correlations that have been developed for transition boiling are not well established or accepted. Also, no steady-state transition boiling data for rod bundles are available.

Transition boiling has traditionally been interpreted as a combination of nucleate and film boiling occurring alternately over the heated surface. The variation in the heat flux in the regime is due to the varying fractions of time that the two boiling regimes exist at a given location. This interpretation led to the assumption made that transition boiling could be represented by an interpolation between nucleate boiling at the critical heat flux and film boiling at the minimum stable film boiling temperature. Since transition boiling occurs for a relatively short transient period on a fuel rod, such an interpolation is deemed to be acceptable and the model will be insensitive to the value of the heat transfer coefficient.

The form of the interpolation in Equation 6.6-38 was selected for its simplicity and physical basis. The exponent of 2 gave the best agreement with data [6.6-35].

The interpolation endpoints (CHF and the minimum film-boiling heat flux) and the associated uncertainties have been discussed in detail in Sections 6.6.6 and 6.6.7. The CHF is particularly well defined for fuel bundles. An appropriate and conservative uncertainty for sensitivity studies in this short duration transient heat transfer regime is to add the uncertainties of 11% (Chen) and 35% (Tien-Gonzalez, Section 6.6.10.3).

6.6.9 Film Boiling - Low Void Fraction

The assumption is made that film boiling can be adequately described as being in one of three forms. At low void fractions, the flow will take on the so-called inverted annular flow configuration where a thin vapor film covers the tube wall and a two phase mixture flows in the center of the tube or channel. At high void fractions, the liquid is in the form of dispersed drops in a vapor. The third form is a transition between the two regimes where the liquid is in the form of slugs and drops. The convective heat transfer correlations are presented in this section for inverted annular flow and in Section 6.6.10 for dispersed droplet flow.

6.6.9.1 Technical Basis and Assumptions

In the liquid continuous flow regime the heat transfer from the wall surface to the vapor-liquid interface is largely by thermal radiation, depending on the wall temperature. The heat transfer coefficient to liquid is based on radiation heat exchange between two parallel planes, one at wall temperature and the other at saturation temperature:

$$h_{w\ell} = \epsilon_w \frac{\sigma (T_w^4 - T_s^4)}{T_w - T_\ell} \quad (6.6-39)$$

where ϵ_w is the wall emissivity and σ is the Stefan-Boltzmann constant.

The heat transfer to vapor and from the vapor to the liquid is by convection and is given by the modified Bromley correlation. In this flow regime, TRACG applies a large value for the interfacial heat transfer from the vapor to the interface, such that the net resistance for convective heat transfer between the wall and the liquid is:

$$\frac{1}{h_{wv}} + \frac{1}{h_{iv}} \approx \frac{1}{h_{wv}} \quad (6.6-40)$$

where h_{wv} or h_v is given by Equation 6.6-41.

The (unmodified) Bromley correlation [6.6-24] is:

$$h_v = 0.62 \left(\frac{k_v^3 h_{fg} \rho_v (\rho_\ell - \rho_v) g}{\mu_v (T_w - T_s) L_H} \right)^{1/4} \quad (6.6-41)$$

where L_H is the characteristic length. This length is determined using the Helmholtz instability criteria [6.6-24]. The effect of the liquid velocity is thereby included in this derivation, and the modified Bromley correlation is:

$$h_v = C \left(\frac{k_v^9 h_{fg}^2 \rho_v^3 (\rho_\ell - \rho_v)^4 g^4}{\mu_v^4 (T_w - T_s)^2 \sigma} \right)^{1/11} \quad (6.6-42)$$

where σ in this equation is surface tension and:

$$C = \frac{4}{3} \left\{ \frac{\left(\frac{3n-1}{8} \right)^4}{\left(\frac{3\pi\sqrt{3}}{2} \right)^2} \right\}^{1/11} \quad (6.6-43)$$

and n is determined from $\frac{v_\ell}{v_m} = \frac{2n-1}{(3n-1)^{8/11}}$ (6.6-44)

$$v_m = \frac{8}{2^{8/11}} \left(\frac{3\pi\sqrt{2}}{2} \right)^{4/11} \left(\frac{(\rho_\ell - \rho_v)^3 k_v^4 (T_w - T_s)^4 \sigma^2}{\mu_v^3 h_{fg}^4 \rho_v^6} \right)^{1/11} \quad (6.6-45)$$

6.6.9.2 Model as Coded

Calculations of the heat transfer coefficients for the film boiling at low void fraction conditions are based on equations described in Section 6.6.9.1. For low void fractions, the modified Bromley correlation determines the net conductive resistance across the thin vapor film and the modified Bromley heat transfer coefficient is applied to the wall to liquid heat transfer coefficient. For high void fractions close to the transition to annular flow, the modified Bromley heat transfer coefficient is applied to the wall to vapor heat transfer coefficient. This is done to allow a continuous transition to annular flow film boiling. This interpolation is done linearly from a void fraction of 0.1 to 0.5. It should be noted that the impact of this implementation is small, since $T_v \approx T_{sat}$ for this condition.

6.6.9.3 Applicability

Equation 6.6-39 represents the heat transfer from the wall surface to the vapor-liquid interface and is a straightforward application of the Stefan-Boltzmann law. It is applicable for situations where the optically thin assumption is valid.

The Bromley correlation is widely used for inverted annular-flow film boiling and was developed from data for boiling in a horizontal tube. The modified Bromley correlation was developed for vertical geometries and is derived from theoretical considerations and compared to experimental data over a sufficiently wide range to verify the correlation. The range of applicability as reported in NEDO-20566-1 [6.6-24] is for wall temperatures less than 1260°C and pressures less than 8.3 MPa. Figure 6.6-12 [6.6-24] shows a plot of KWU reflood data compared to the modified Bromley. The agreement is excellent in the film boiling regime. Further comparison to data can be found in Reference 6.6-24. This methodology was successfully applied in the approved code SAFER.

6.6.10 Film Boiling - High Void Fraction

In this flow regime, both radiation and convection play important roles in the heat transfer. Radiation is treated in Section 6.6.12. This section covers convection heat transfer in the dispersed droplet flow regime.

6.6.10.1 Technical Basis and Assumptions

Due to steam superheat, there will be a temperature difference between steam and the interface between the steam and the droplets and, thus, a net heat transfer. A good correlation [6.6-25] for convection heat transfer coefficient from the steam to droplets is:

$$\beta = Nu_d k_v N_d \pi d_d \quad (6.6-46)$$

where N_d is the droplet number density given by:

$$N_d = \frac{6(1 - \alpha)}{\pi d_d^3} \quad (6.6-47)$$

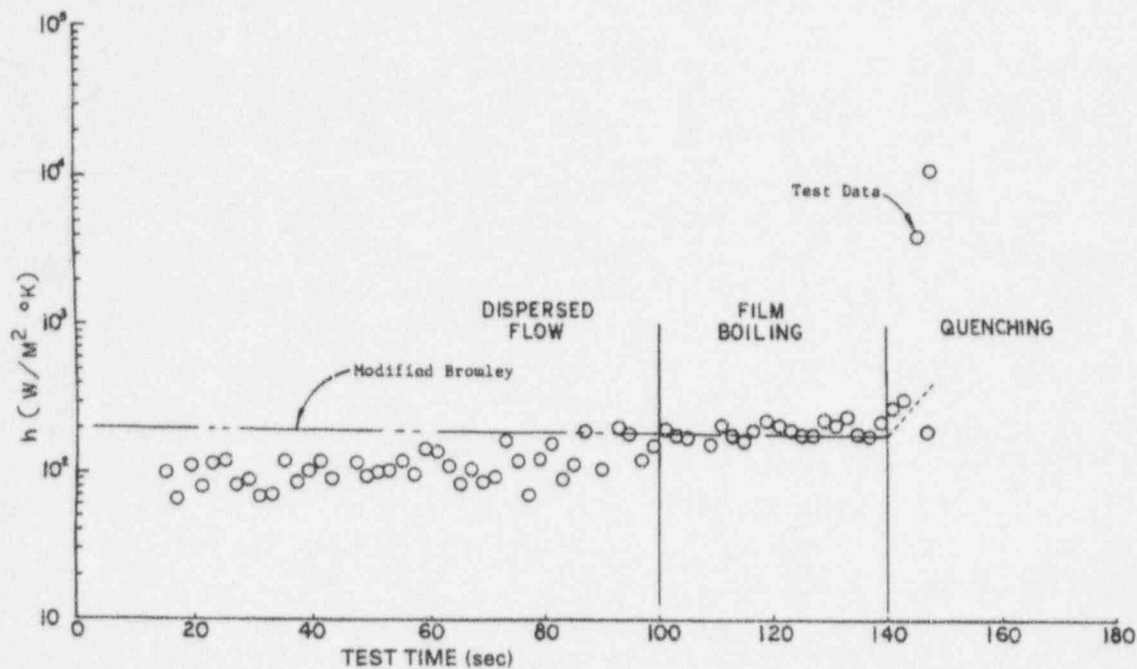


Figure 6.6-12. Comparison of Modified Bromley with Data During Reflood Test

and the droplet Nusselt number is given by (Section 6.5.5)

$$Nu_d = 2 + 0.74 \left(\frac{d_d \rho_v v_R}{\mu_v} \right)^{0.5} Pr_v^{1/3} \tag{6.6-48}$$

The presence of droplets in a steam atmosphere has two effects on the convection wall-to-steam heat transfer: (1) the bulk steam temperature will be lowered toward the saturation temperature, thus increasing the heat transfer, and (2) the temperature profile of the steam will be changed, causing a steeper temperature gradient close to the wall. This effect will also enhance the heat transfer. Sun, Gonzalez and Tien [6.6-26] solved the continuity and energy equation for the temperature profile of the steam. If a parabolic velocity profile for the steam is assumed, the Nusselt number is given by:

$$Nu_v = \frac{2 X I_1(X)}{I_0(X) - \frac{8}{X^2} I_2(X)} \tag{6.6-49}$$

where:

$$X = \frac{D_h}{2} \sqrt{\frac{\beta h_v}{k_v h_{fg}}} \tag{6.6-50}$$

However, Equation 6.6-49 was derived from the assumption that the temperature profile of the steam is determined from a balance between heat transfer from the wall and heat transfer to the droplets. Hence, the terms $\partial/\partial z$ were neglected in the continuity and energy equations. This is valid only for large droplet concentrations. For zero droplet concentration, the single-phase Nusselt number for a tube is calculated as described in Section 6.6.5. For laminar flow a value of 4.0 is obtained, whereas the limiting value of Equation 6.6-49 is 6.0.

For large droplet concentrations, an asymptotic approximation to Equation 6.6-49 is:

$$\text{Nu}_v \approx 2X - 1 \text{ for } x \rightarrow \infty \quad (6.6-51)$$

An expression having this behavior and having the appropriate limit for $x \rightarrow 0$ ($\alpha = 1$) is given by:

$$h_v = \frac{k_v}{D_h} \left(2X - 1 + \frac{(\text{Nu}_s + 1)^2}{\text{Nu}_s + 1 + 2X} \right) \quad (6.6-52)$$

where

$$\text{Nu}_s = \frac{D_h}{k_v} h_{g, \text{ single phase}} \quad (6.6-53)$$

Equation 6.6-52 is known as the modified Tien-Gonzalez correlation.

6.6.10.2 Model as Coded

Calculations of the heat transfer coefficients for the film boiling at high void fraction conditions are based on equations described in Section 6.6.10.1. Droplet diameter and number of droplets are input parameters and have been defined during interfacial heat transfer calculations (see Section 6.5.5) for the heat transfer coefficients. A interpolation procedure is included to provide smooth changes to the modified Bromley correlation:

$$h_v = (1 - x_2) h_{\text{MB}} + x_2 h_{\text{SGT}}$$

where MB designates modified Bromley and SGT designates Sun-Gonzalez-Tien. Values for x_2 are zero for low void fractions and one for dispersed flow. x_2 is interpolated linearly from 0 to 1 over the transition region to dispersed annular flow.

6.6.10.3 Applicability

The Tien-Gonzalez correlation was developed especially for convection heat transfer in rod bundles under emergency cooling conditions. The modified Tien-Gonzalez correlation was developed to yield correct heat transfer behavior as the droplet concentration approached zero. This correlation was successfully used in the CORECOOL code [6.6-28]. Figure 6.6-13 shows peak cladding temperatures as predicted by CORECOOL of ECCS experiments for full-scale fuel

elements in the BWR-FLECHT tests [6.6-29]. The agreement of the CORECOOL prediction with the measured peak cooling temperature is very good. Since in this flow regime the heat transfer is by both radiation and convection, it is important to isolate one effect so that "compensating errors" can be ruled out as the reason for good prediction. Figure 6.6-14 shows the CORECOOL prediction of the same experiment with no water droplets. The symbols indicate different rod locations, moving inward from the corner position. Except for the peripheral rods, where a considerable amount of conduction/convection existed across the narrow gap to the cold channel, the cooling of the rods was primarily by thermal radiation. The agreement is good.

CORECOOL has a bias and standard deviation of:

$$\mu = 28 \text{ K}$$

$$\sigma = 63 \text{ K}$$

when compared to peak cladding temperature (PCT) data from GE and AB Atomenergi CSHT (Core Spray Heat Transfer) experiments. Approximately half of the heat transfer is from convection and half is from radiation. Conservatively assuming that all of the uncertainty can be attributed to the convection model, then the error in the heat transfer coefficient (Equation 6.6-52) is approximately 35%, based on a temperature difference of 900 K.

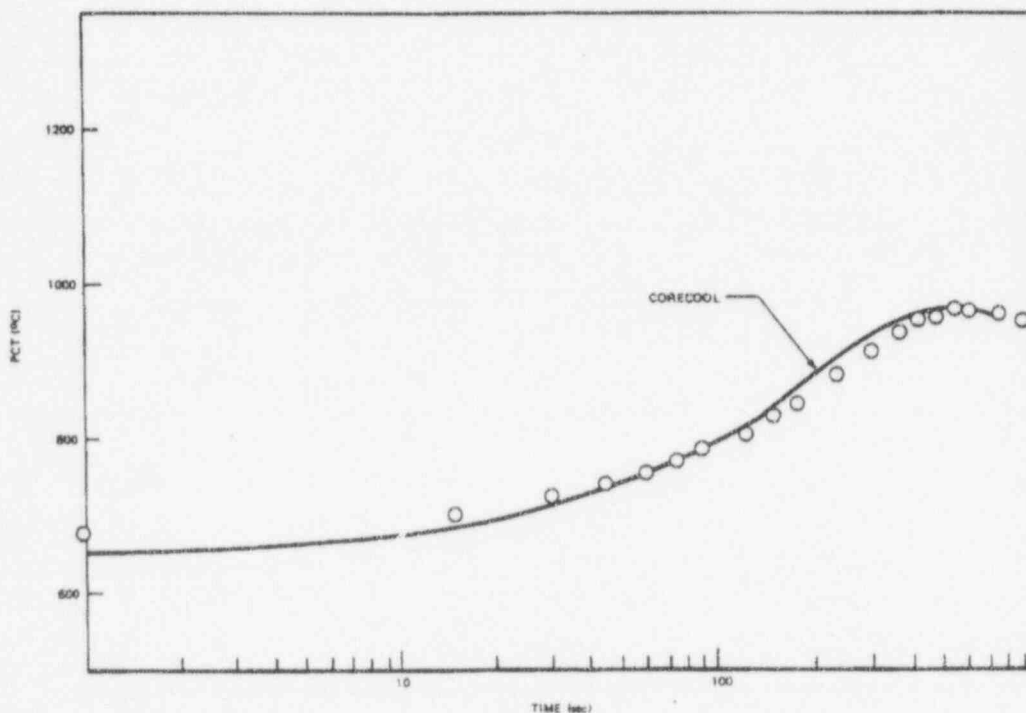


Figure 6.6-13. Peak Cladding Temperature for a BWR Fuel Element

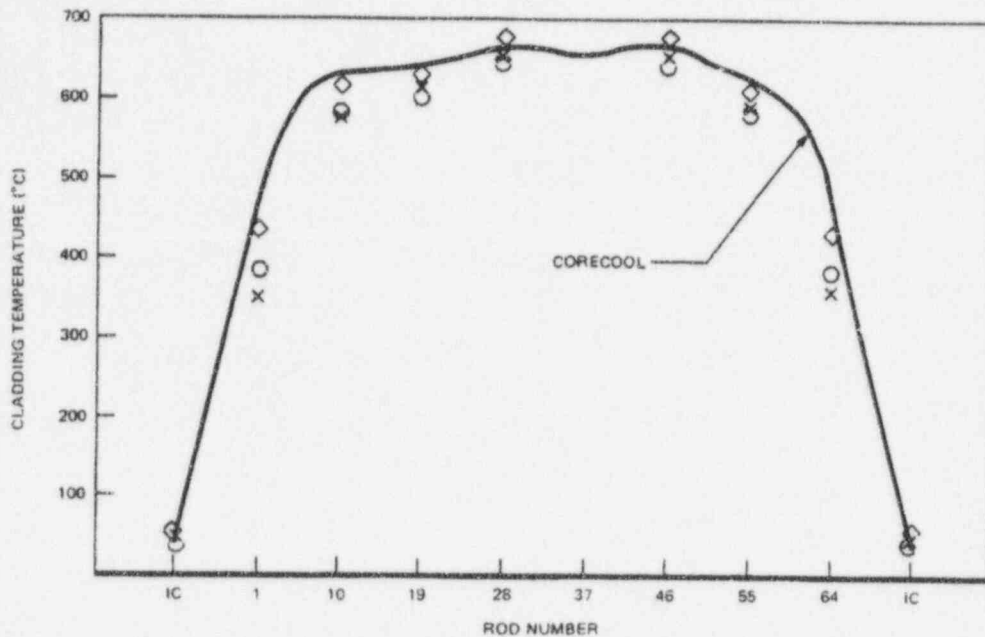


Figure 6.6-14. "Radiation Only" Experiment

6.6.11 Condensation Heat Transfer in the Presence of Noncondensible Gases

Condensation heat transfer will occur when the wall temperature is less than the saturation temperature and the flow regime is vapor continuous.

6.6.11.1 Technical Basis and Assumptions

Steam Condensation in Tubes

A modified version of the Vierow-Schrock (V-S) condensation correlation [6.6-30] has been used in TRACG. The correlation is based on a two-part correction to a reference local heat transfer coefficient termed the "Nusselt" heat transfer coefficient. This reference value is calculated by dividing the condensate thermal conductivity by the local liquid film thickness:

$$h_{\text{condensation}} = f_1 f_2 h_{\text{ref}} \tag{6.6-54}$$

$$h_{\text{ref}} = k_l / \delta$$

The local condensate film thickness is defined as [6.6-31]:

$$\delta = \left(\frac{3\mu_l \Gamma}{g\rho_l(\rho_l - \rho_v)} \right)^{1/3} \quad \text{or} \quad \delta = \left(\frac{3\mu_l^2 \text{Re}_l}{4g\rho_l \Delta\rho} \right)^{1/3} \tag{6.6-55}$$

for laminar condensate film flow ($Re_\ell < 1000$) where

$$Re_\ell = \frac{4\Gamma}{\mu_\ell} \quad (6.6-56)$$

For turbulent condensate film flow, Burmeister [6.6-32] presents

$$\frac{Re_\ell}{4} = 0.003 \left[\frac{g^{1/3} \rho_\ell^{2/3} k_\ell (T_s - T_w) z}{h_{fg} \mu_\ell^{5/3}} \right]^{3/2} \quad (6.6-57)$$

Re-arranging and differentiating yields:

$$d(Re_\ell^{2/3}) = 0.052 \left[\frac{g^{1/3} \rho_\ell^{2/3} k_\ell (T_s - T_w)}{h_{fg} \mu_\ell^{5/3}} \right] dz \quad (6.6-58)$$

A simple energy balance yields:

$$\Gamma(z) = \frac{\bar{h}(z)}{h_{fg}} (T_s - T_w) z \quad (6.6-59)$$

Combining Equations 6.6-56 and 6.6-59 and differentiating

$$d(Re_\ell) = \frac{4h}{\mu_\ell h_{fg}} (T_s - T_w) dz \quad (6.6-60)$$

Now, combining Equations 6.6-58 and 6.6-60

$$\frac{2}{3} Re_\ell^{-1/3} = 0.052 \frac{g^{1/3} \rho_\ell^{2/3} k_\ell}{\mu_\ell h_{fg}} \cdot \frac{1}{4h} \quad (6.6-61)$$

Using Equations 6.6-54 and 6.6-61 and solving for δ gives the turbulent film thickness

$$\delta = 51.3 \left(\frac{\mu_\ell^2}{\rho_\ell^2 g Re_\ell} \right)^{1/3} \quad \text{or} \quad \delta = 32.3 \left(\frac{\mu_\ell^3}{\rho_\ell g \Gamma} \right)^{1/3} \quad (6.6-62)$$

for $Re_\ell > 2000$.

As stated above, the two-part correction takes the form:

$$h_{\text{condensation}} = f_1 f_2 h_{\text{ref}} \quad (6.6-63)$$

where f_1 is a factor greater than unity, which accounts for increased heat transfer due to shearing (thinning) of the condensate film layer. The factor, f_2 , is less than unity and accounts for the decrease in heat transfer resulting from the presence of noncondensibles.

The factor f_1 is given by:

$$f_1 = 1 + 2.88 \times 10^{-5} Re_m^{1.18} \quad \text{for } Re_\ell \leq 1000 \quad (6.6-64)$$

with the limit of $f_1 \leq 3$ and

$$f_1 = 1 \quad \text{for } Re_\ell > 2000$$

The factor f_2 is correlated in terms of the density ratio for air by:

$$f_2 = \begin{cases} 1.0 - 10.0 x_{\text{air}} & \text{for } x_{\text{air}} < 0.066 \\ 1.0 - 0.938 x_{\text{air}}^{0.13} & 0.066 < x_{\text{air}} < 0.49 \\ 1.0 - x_{\text{air}}^{0.22} & 0.49 < x_{\text{air}} < 1.0 \end{cases} \quad (6.6-65)$$

$$x_{\text{air}} = \frac{\rho_{\text{air}}}{\rho_m}$$

Incorporating the film thickness into Equation 6.6-54, the reference (or Nusselt) condensation heat transfer coefficient becomes:

$$h_{\text{Nusselt}} = 1.1 k_\ell \left(\frac{\rho_\ell \Delta \rho g}{\mu_\ell^2 Re_\ell} \right)^{1/3} \quad \text{for } Re_\ell < 1000 \quad (6.6-66)$$

$$h_{\text{Nusselt}} = 0.0195 k_\ell \left(\frac{\rho_\ell^2 g Re_\ell}{\mu_\ell^2} \right)^{1/3} \quad \text{for } Re_\ell > 2000 \quad (6.6-67)$$

A cubic spline interpolation is used for $1000 < Re_\ell < 2000$.

The Vierow-Schrock correlation has been included in this description for historical reasons. It has been supplanted by a more recent correlation which has a wider data base and is recommended by the developers at U.C. Berkeley. This correlation, referred to as the K-S-P (Kuhn-Schrock-Peterson) correlation [6.6-33, 6.6-30], is the default and recommended correlation and was also developed at UC Berkeley for condensation in the presence of noncondensibles inside tubes. The correlation takes the same form as Equations 6.6-54 and 6.6-63. However, f_1 is split up into two parts:

$$f_1 = f_{1 \text{ shear}} \cdot f_{1 \text{ other}} \quad (6.6-68)$$

where

$$f_{1 \text{ other}} = 1 + 1.83 \times 10^{-4} \text{Re}_\ell \quad \text{where again} \quad \left(\text{Re}_\ell = \frac{4\Gamma}{\mu} \right) \quad (6.6-69)$$

and $f_{1 \text{ shear}}$ is:

$$f_{1 \text{ shear}} = \frac{\delta_1}{\delta_2} \quad (6.6-70)$$

δ_1 is equivalent to δ from Equation 6.6-55 and is the film thickness without shear. δ_2 is the film thickness with shear [6.6-33]. With interfacial shear the predicted film thickness, δ_2 is given implicitly by:

$$\Gamma = \frac{g}{\mu_f} \rho_f (\rho_f - \rho_g) \frac{\delta_2^3}{3} + \frac{\rho_f \tau_i \delta_2^2}{2\mu_f} \quad (6.6-71)$$

where
$$\tau_i = \frac{1}{2} f_R \rho_g V_g^2 \quad (6.6-72)$$

$$f_R = 0.046 \text{Re}_m^{-0.2} \quad (6.6-73)$$

leading to the interfacial shear prediction

$$\tau_i = \frac{0.023 \left(\frac{\mu_m}{D_i} \right)^2 \text{Re}_g^{1.8}}{\rho_g} \quad (6.6-74)$$

The f_2 degradation function has been correlated in the form

$$f_2 = (1 - cx^b)$$

for both air and helium. For air x becomes x_{air} where

$$x_{\text{air}} = \frac{\rho_{\text{air}}}{\rho_m} \quad (6.6-75)$$

and

$$f_{2, \text{air}} = \begin{cases} 1.0 - 2.601 x_{\text{air}}^{0.708}, & x_{\text{air}} < 0.1005 \\ 1.0 - x_{\text{air}}^{0.292}, & x_{\text{air}} \geq 0.1005 \end{cases} \quad (6.6-76)$$

For helium x becomes x_{He} where

$$x_{\text{He}} = \frac{\rho_{\text{He}}}{\rho_m} \quad (6.6-77)$$

and

$$f_{2,\text{He}} = \begin{cases} 1.0 - 35.81 x_{\text{He}}^{1.074}, & x_{\text{He}} < 0.010005 \\ 1.0 - 2.09 x_{\text{He}}^{0.457}, & 0.010005 \leq x_{\text{He}} < 0.099895 \\ 1.0 - x_{\text{He}}^{0.137}, & 0.099895 \leq x_{\text{He}} \leq 1.0 \end{cases} \quad (6.6-78)$$

Given the appropriate value for f_2 (see Section 6.6.11.2) the Kuhn-Schrock-Petersen correlation is formulated as

$$h = f_1 f_2 h_{\text{Nusselt}} = f_{1_{\text{shear}}} \cdot f_{1_{\text{other}}} \cdot f_2 \cdot h_{\text{Nusselt}}$$

or

$$h = f_2 \left(1 + 183 \times 10^{-4} \text{Re}_\ell \right) \frac{k_\ell}{\delta_2} \quad (6.6-79)$$

Steam Condensation in Containment

The formulation of the local condensate film thickness in Equation 6.6-55 was derived for flat plates and is therefore suitable for use for steam condensation in the containment. The default application for condensation is to use the K-S-P correlation (Equation 6.6-79) with the $f_{1_{\text{shear}}}$ factor set equal to 1, or $\delta_2 = \delta_1$. This is appropriate, since velocities in the containment will be small compared to the tubes and the $f_{1_{\text{shear}}}$ factor was developed specifically for tubes. The f_2 factors will remain the same.

Another option is to use the "Uchida" correlation for condensation in the containment. The "Uchida" correlation is:

$$\bar{h} = 380 \left(\frac{1 - x_{\text{air}}}{x_{\text{air}}} \right)^{0.7} \frac{\text{Watts}}{\text{m}^2 \text{K}} \quad (6.6-81)$$

At $x_{\text{air}} = 0$ Equation 6.6-81 is undefined. As a result, TRACG takes the minimum of the heat transfer coefficients predicted by Equation 6.6-81 and the K-S-P correlation with $f_{1_{\text{shear}}} = 1$.

An option to use the Vierow-Schrock correlation with the f_1 factor set equal to 1 is also available.

6.6.11.2 Model as Coded

The f_2 degradation functions for both the V-S and K-S-P correlations are correlated by piecewise functions where the independent variable x is a density ratio. Only air and helium have been considered in developing these correlations.

6.6.11.3 Applicability

Steam Condensation in Tubes

The Vierow-Schrock correlation was developed for condensation of steam inside a tube in the presence of noncondensable gas. Subsequent experiments have shown that the Vierow-Schrock correlation is accurate over the range of conditions of the Vierow experiment, but needs some care in extrapolation beyond that range. The standard deviation of the correlation with the data is approximately 30% [6.6-33]. The ranges and physical dimensions of the experiment were:

Inlet pressure:	0.03 - 0.45 MPa
Inlet temperature	343 - 419 K
Inlet steam flow rate	0.0022 - 0.0083 kg/s
Inlet air mass fraction	0 - 0.14
Local air mass fraction	0 - ~1
Tube dimensions	
Length	1.8 m
Outside diameter	25.4 mm
Tube thickness	1.65 mm

The limit of $f_1 \leq 3$ was added to the model due to the rapid increase in f_1 that occurs when the mixture Re exceeds the conditions of the Vierow experiment. Even with this limit, the V-S correlation still overpredicts the Kuhn heat transfer data by more than 100% at high mixture Re inside of tubes. However, as shown in Figure 6.6-16, the K-S-P correlation agrees well with the (unmodified) Vierow-Schrock correlation over the range of data in the Vierow experiment.

Although the V-S correlation overpredicts the heat transfer coefficients overall, it predicts more degradation from noncondensable gases (lower heat transfer coefficients) than does the K-S-P correlation, as shown in Figure 6.6-17. It is the f_1 factor which causes the overprediction of the modified Vierow-Schrock correlation.

The K-S-P correlation has a standard deviation of 7.4% when compared to the pure steam data and a standard deviation of 17.6% when compared to the 70 steam-air tests of Kuhn. The Kuhn experiment benefited from the experience of previous researchers and, as a result, provided the best set of data.

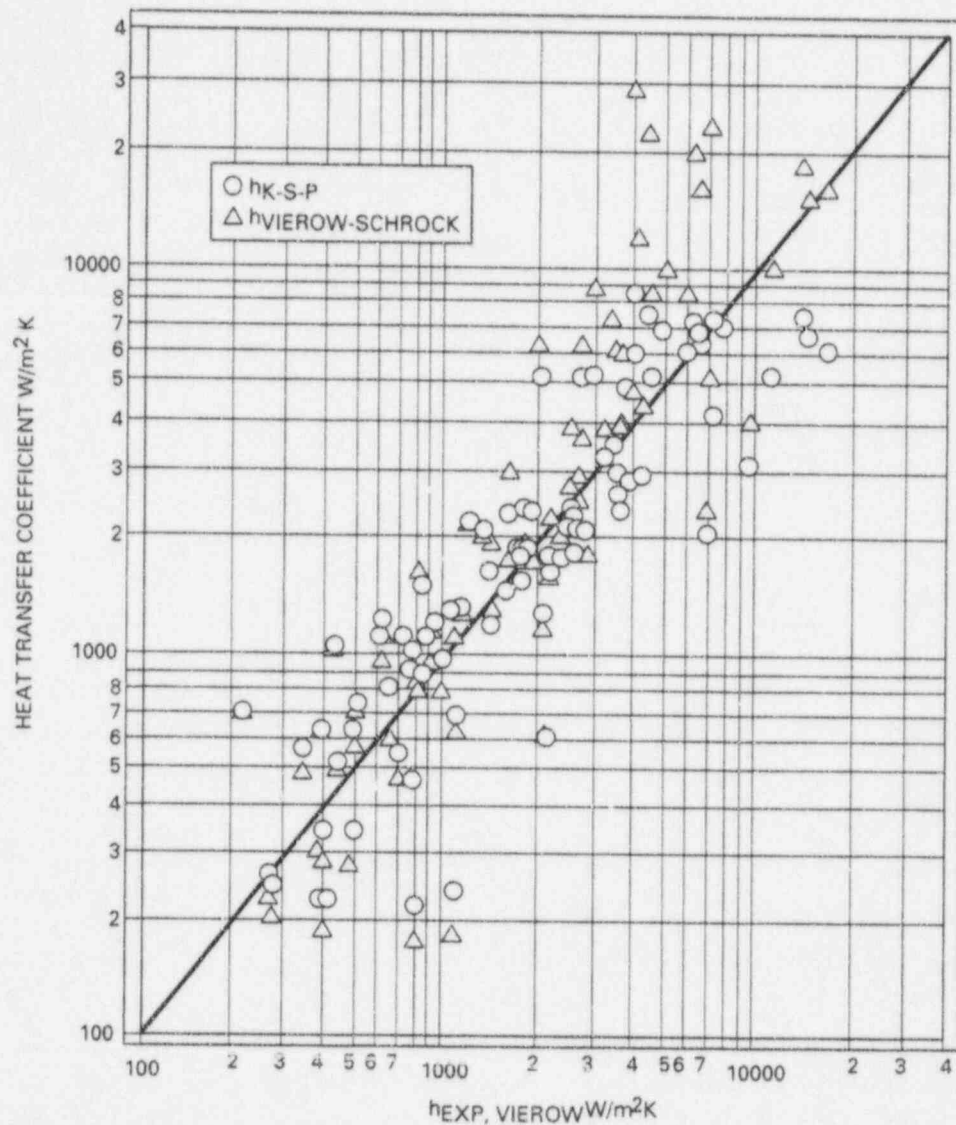


Figure 6.6-16. Heat Transfer Coefficients Predicted by K-S-P and Vierow-Schrock Correlations versus Vierow's Experimental Data

Steam Condensation in Containment

The TRACG correlation is in good agreement with correlations designed for vertical plate condensation. Most of the condensation in the containment will be similar to this situation. Thus TRACG should provide a good estimate of the condensation heat transfer coefficient. If the containment contains significant amounts of horizontal surface area, care should be taken to model this area with a nonhorizontal equivalent area since no condensation heat transfer will be predicted using $g \cos(0^\circ) = 0$.

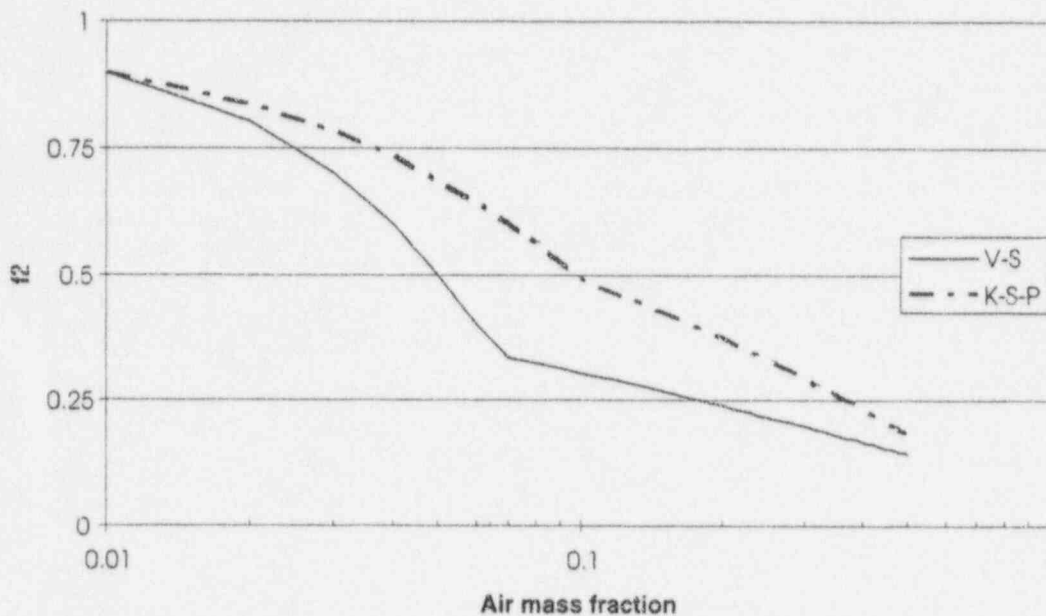


Figure 6.6-17. Comparison of the V-S and K-S-P Predictions of Heat Transfer Degradation Due to the Presence of Air

6.6.12 Thermal Radiation

During a BWR loss-of-coolant accident (LOCA), radiation heat transfer may account for a significant amount of the total heat transfer in the fuel bundle. An analytical model for calculating radiation heat transfer in a BWR fuel bundle was established and implemented into TRACG. The model considers surface-to-surface radiation and the interaction between radiation and the two-phase mixture in the bundle. The surface-to-surface radiation model contains a first-order anisotropic transport correction, and the interaction with the two-phase mixture consists of absorption and emission.

6.6.12.1 Radiation Heat Transfer Model - Technical Basis and Assumptions

The radiation heat transfer model [6.6-44] is based on the following assumptions:

- All surfaces are gray.
- All surfaces have uniform temperatures.
- All surfaces emit radiation diffusely.
- The two-phase fluid between surfaces has uniform temperature, and it absorbs and emits radiation.

- The semi-gray radiation model is applied for the two-phase mixture (i.e., absorption is based on the wall temperature, while emission is based on the temperature of the two-phase mixture).
- A first-order anisotropic transport correction is applied for surface reflections. For large and/or curved surfaces, there is generally a tendency for radiation to be reflected backwards towards the origin of the incident radiation. Hence, the assumption that a fraction, μ , of the incident radiation is reflected backwards toward the origin, whereas the rest, $1-\mu$, is reflected uniformly in all directions, is a significant improvement over the assumption of isotropic reflection.

The radiosity of surface i , B_i can be expressed as the sum of the emitted and reflected radiation (Figure 6.6-20):

$$B_i = \epsilon_i S_i + (1 - \epsilon_i) H_i \tag{6.6-93}$$

where:

$$S_i = \sigma T_i^4 \tag{6.6-94}$$

$$H_i = \sum_j H_{ji} \tag{6.6-95}$$

and H_{ji} is the incident radiation of surface i coming from surface j .

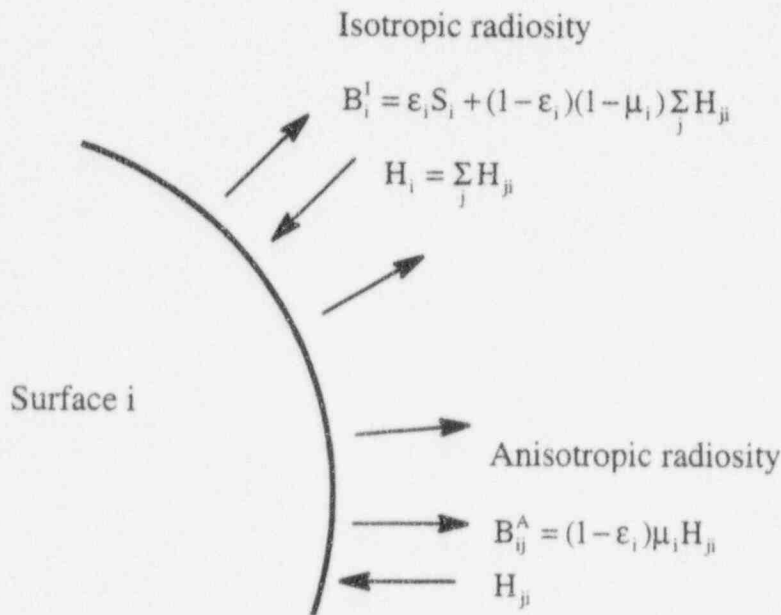


Figure 6.6-20. Radiation Heat Transfer at a Surface

The isotropic part of the radiosity of surface i , B_i^I , is given by:

$$B_i^I = \epsilon_i S_i + (1 - \epsilon_i)(1 - \mu_i) H_i \quad (6.6-96)$$

and the anisotropic part, B_{ij}^A , which is reflected back to surface j , is:

$$B_{ij}^A = \mu_i (1 - \epsilon_i) H_{ji} \quad (6.6-97)$$

The incident radiation from the direction of surface j is the sum of the radiation leaving surface j in the direction of surface i reduced by the transmissivity of the medium plus what is emitted by the medium:

$$H_{ji} = \frac{1}{A_i} (A_j B_j^I F_{ji} + A_j B_{ji}^A) \tau_{ji} + \epsilon_{mij} F_{ij} S_{mij} \quad (6.6-98)$$

After simple algebraic manipulations, the following expression is obtained:

$$B_{ij}^A = (a_{ij} B_i^I + b_{ij} B_j^I + c_{ij}) F_{ij} \quad (6.6-99)$$

where:

$$a_{ij} = \frac{X_i X_i \tau_{ij} \tau_{ji}}{1 - X_i X_j \tau_{ij} \tau_{ji}} \quad (6.6-100)$$

$$b_{ij} = \frac{X_i \tau_{ji}}{1 - X_i X_j \tau_{ij} \tau_{ji}} \quad (6.6-101)$$

$$c_{ij} = \frac{X_i (\epsilon_{mij} S_{mij} + X_j \tau_{ji} \epsilon_{mji} S_{mji})}{1 - X_i X_j \tau_{ij} \tau_{ji}} \quad (6.6-102)$$

$$X_i = \mu_i (1 - \epsilon_i) \quad (6.6-103)$$

$$\tau_{ij} = e^{-(a_{lij} + a_{vij}) R_{ij}} \quad (6.6-104)$$

$$\epsilon_{mij} = \epsilon_{lij} + \epsilon_{vij} \quad (6.6-105)$$

$$S_{mij} = \frac{\epsilon_{lig} S_\ell + \epsilon_{vij} S_v}{\epsilon_{lij} + \epsilon_{vij}} \quad (6.6-106)$$

$$S_\ell = \sigma T_\ell^4 \quad (6.6-107)$$

$$S_v = \sigma T_v^4 \quad (6.6-108)$$

$$\epsilon_{\ell ij} = \frac{a_{\ell}}{a_{\ell} + a_v} \left[1 - e^{-(a_{\ell} + a_v)R_{ij}} \right] \quad (6.6-109)$$

$$\epsilon_{vij} = \frac{a_v}{a_{\ell} + a_v} \left[1 - e^{-(a_{\ell} + a_v)R_{ij}} \right] \quad (6.6-110)$$

$$a_{\ell ij} = \frac{a_{\ell,i} S_i + a_{\ell,j} S_j}{S_i + S_j} \quad (6.6-111)$$

$$a_{vij} = \frac{a_{v,i} S_i + a_{v,j} S_j}{S_i + S_j} \quad (6.6-112)$$

a_{vi} and $a_{\ell i}$ are the vapor and liquid absorption coefficients, respectively. For absorption, these coefficients are evaluated at the temperature of the surface, while the temperature of the vapor is used for emission from the vapor.

Combining Equations 6.6-94, 6.6-96, 6.6-97 and 6.6-99, the following expression is obtained:

$$B_i^I = \epsilon_i S_i + \frac{1 - \mu_i}{\mu_i} \sum_j (a_{ij} B_i^I + b_{ij} B_j^I + c_{ij}) F_{ij} \quad (6.6-113)$$

This is a system of linear equations, which can be solved for B_i^I .

The heat flux of surface i , is the difference between the radiosity and incident radiation:

$$q_i = B_i - H_i \quad (6.6-114)$$

Combining Equations 6.6-93, 6.6-96 and 6.6-114 yields:

$$q_i = \frac{\epsilon_i}{1 - \epsilon_i} \frac{S_i [1 - \mu_i (1 - \epsilon_i)] - B_i^I}{1 - \mu_i} \quad (6.6-115)$$

The energy absorbed and emitted by vapor is given by the following equations:

$$Q_{abs,v} = \sum_i \sum_j A_i \left(F_{ij} B_i^I + B_{ij}^A \right) (1 - \tau_{ij}) \frac{a_{vij}}{a_{vij} + a_{\ell ij}} \quad (6.6-116)$$

and:

$$Q_{\text{emit},v} = \sum_i \sum_j A_i \epsilon_{\text{inj}} \frac{\epsilon_{\text{vij}} S_v}{\epsilon_{\text{vij}} + \epsilon_{\ell ij}} F_{ij} \quad (6.6-117)$$

Similar expressions can be written for the absorption and emission for the liquid. Energy conservation can be shown by:

$$\sum_i Q_i = Q_{\text{abs},\ell} + Q_{\text{abs},v} - Q_{\text{emit},v} - Q_{\text{emit},\ell} \quad (6.6-118)$$

after simple algebraic manipulations.

Net heat fluxes for surface i to either vapor or liquid can be derived from Equations 6.6-116 and 6.6-117, as follows:

$$q_{i,v} = \sum_j \left\{ \left(F_{ij} B_i^I + B_{ij}^A \right) \left(1 - \tau_{ij} \right) \frac{a_{\text{vij}}}{a_{\ell ij} + a_{\text{vij}}} - F_{ij} \epsilon_{\text{vij}} S_v \right\} \quad (6.6-119)$$

$$q_{i,\ell} = \sum_j \left\{ \left(F_{ij} B_i^I + B_{ij}^A \right) \left(1 - \tau_{ij} \right) \frac{a_{\ell ij}}{a_{\ell ij} + a_{\text{vij}}} - F_{ij} \epsilon_{\ell ij} S_\ell \right\} \quad (6.6-120)$$

6.6.12.2 Model as Coded

The equations for the isotropic radiosities as given by Equation 6.6-113 constitute a system of linear equations and are solved by direct inversion.

The view factors and the beam lengths are dependent on the geometry only and are given by the general expressions [6.6-48]:

$$F_{ij} = \frac{\int_{A_i} \int_{A_j} \frac{\cos \beta_i \cos \beta_j}{\pi R^2} dA_j dA_i}{A_i} \quad (6.6-121)$$

and

$$R_{ij} = \frac{\int_{A_i} \int_{A_j} \frac{\cos \beta_i \cos \beta_j}{\pi R} dA_j dA_i}{A_i} \quad (6.6-122)$$

where R is the distance between two points on surface i and j , and β_i and β_j are the angles between the line R and the normals to surface i and j respectively. For elongated surfaces, as radiation in the axial direction is neglected, Equations 6.6-121 and 6.6-122 reduce to [6.6-47]:

$$F_{ij} = \frac{\int_{S_i} \int_{S_j} \frac{\cos \beta_i \cos \beta_j}{2R} dS_j dS_i}{S_i} \quad (6.6-123)$$

and

$$R_{ij} = \frac{\int_{S_i} \int_{S_j} \frac{\cos \beta_i \cos \beta_j}{2} dS_j dS_i}{S_i} \quad (6.6-124)$$

where R is the distance between two points along the perimeter of surface i and j , and β_i and β_j are the angles between the line R and the normals to perimeter i and j , respectively. Equations 6.6-111 and 6.6-112 are integrated directly by numerical integration.

The interaction of the thermal radiation with steam and droplets is based on the semi-grey radiation model, and the assumption that the medium is optically thin. For the droplets it can be shown [6.6-26] that, when the medium is optically thin, scattering can be neglected and the absorption coefficient will be given by [6.6-26]:

$$a_\ell = 1.11 \frac{\alpha_d}{d_d} \quad (6.6-125)$$

The absorption coefficient for the steam is a function of the temperature and pressure [6.6-47]. A good polynomial fit is given by:

$$a_v = P \cdot 10^{-5} (5.2 \cdot 10^4 - 9 \cdot 10^{-7} T + 5.6 \cdot 10^{-10} T^2 - 1.2 \cdot 10^{-13} T^3) \quad (6.6-126)$$

6.6.12.3 Applicability

The range of parameters in which the assumptions are valid include low pressures and high temperatures. This is the range where core spray heat transfer apply for BWR LOCA conditions. The radiation heat transfer model is identical to the radiation heat transfer model in CORECOOL [6.6-26], and has been extensively tested as part of the SAFER/CORECOOL models. CORECOOL was found to accurately predict core spray heat transfer and peak cladding temperatures for the following ranges:

$$0.1 < P < 7.0 \text{ MPa}$$

$$T_{\text{sat}} < T < 1420 \text{ K}$$

Peak cladding temperatures were predicted with an average error of $\mu = 28\text{K}$ and standard deviation of $s_{n-1} = 63\text{K}$.

6.6.13 Quenching Heat Transfer

Experimental studies simulating the reflood stage of a postulated loss-of-coolant accident for a BWR indicate that cladding temperature history can reasonably be characterized by the boiling curve with rewet being controlled by the transition boiling model (Sections 6.6.6-6.6.8). However, an optional model for conduction controlled quenching exists in TRACG, although it is currently not active. For completeness, a brief description of the model is given below.

6.6.13.1 Technical Basis and Assumptions

The reflood initialization consists of a search to locate quench fronts. Rather than assume that the core is dry at the beginning of reflood, which may not be the case, a pattern search of each average rod is made for the combined condition of clad surface temperature less than the quench front temperature and sufficient liquid available to form a film on the rod. Two quench fronts per rod are accounted for: (1) a falling film from the top and (2) a bottom quench front.

The motion of a quench front on a hot surface is a complex function of axial conduction, radial convection both ahead and behind the front, internal heat generation, and heat transfer. Since axial conduction of heat from ahead of the front to the quenched side occurs on a length scale of a centimeter or less, and typical fuel rods are several meters long, analytical methods have been developed to approximate quench front motion without resorting to costly two-dimensional conduction solutions [6.6-48, 6.6-49]. A correlation is used for the quench front velocity v_q :

$$v_q = \frac{k_w}{\rho_w C_{pw} d_w} (\overline{\text{Bi}} (1 + 0.40\overline{\text{Bi}}))^{0.5} \quad (6.6-127)$$

where:

$$\overline{\text{Bi}} = \frac{\text{Bi}}{\overline{T}^2} \quad (6.6-128)$$

$$\text{Bi} = \frac{h_q d_w}{k_w} \quad (6.6-129)$$

$$\overline{T} = \frac{\sqrt{\Theta}}{1 - \Theta} \quad (6.6-130)$$

$$\Theta = \frac{T_w^+ - T_o}{T_w^+ - T_{\text{sat}}} \quad (6.6-131)$$

and:

h_q	= Heat transfer coefficient just behind the quench front
T_o	= Quench front temperature
T_w^+	= Wall temperature just ahead of the quench front
d_w	= Wall thickness

There is considerable ambiguity as to the proper definition of the quench front temperature [6.6-45]. The value used in TRACG is:

$$T_o = T_s + 100 \text{ K} \quad (6.6-132)$$

The value of the heat transfer coefficient behind the quench front is the maximum of either the heat transfer coefficient just behind the quench front, h_ℓ^- , or $6000 \text{ W/m}^2\text{K}$. The latter value is based on an order of magnitude analysis of the FLECHT results [6.6-50]:

$$h_q = \max(h_\ell^-, 6000) \quad (6.6-133)$$

The volumetric heat removal rate due to the advancement of the quench front is:

$$\dot{q}_w''' = \rho_w C_{pw} v_q (T_w^+ - T_{sat}) \quad (6.6-134)$$

6.6.13.2 Model as Coded

The model has been encoded as described by Equations 6.6-127 - 6.6-134 with the following limitations:

- An upper limit on the quench front velocity of 0.1 m/sec. is applied.
- For reflooding, if the downstream heat transfer coefficient is larger than the quench front heat transfer coefficient (Equation 6.6-133), then the larger of the two is used for the quench front heat transfer coefficient.
- For reflooding, a multiplier is applied to the quench front velocity for high void fractions forcing the quench front velocity to 0.0 as the void fraction approaches 1.0. The multiplier is given by: 1.0 for $\alpha < 0.7$ and $\frac{1-\alpha}{0.3}$ for $0.7 < \alpha < 1.0$.

6.6.13.3 Applicability

The quench front model is primarily applicable to film front quenching and reflood quenching for conditions, where the heat transfer coefficient ahead of the quench front is small compared to the quench front heat transfer coefficient. For conditions where a significant precursory cooling exists, the quench front model will underpredict the quench front velocity.

6.6.14 Metal-Water Reaction

At high temperatures, the zirconium used for the fuel rod cladding and the fuel channel box will react chemically with the steam:



6.6.14.1 Technical Basis and Assumptions

The reaction rate is a function of the temperature and is given by Cathcart [6.6-51]:

$$\frac{ds}{dt} = \frac{3.217 \cdot 10^{-6}}{s} \exp\left(-\frac{2.007 \cdot 10^4}{T}\right) \quad (6.6-136)$$

where s is the thickness of the oxide layer.

The heat generation rate is given by:

$$Q = 6.45 \text{ MJ} / \text{kg}_{\text{Zr}} \quad (6.6-137)$$

6.6.14.2 Model as Coded

The metal-water reaction is calculated by direct integration of Equation 6.6-136.

6.6.14.3 Applicability

The metal-water reaction rate is calculated by the Cathcart correlation [6.6-51] assuming that the reaction rate is limited by diffusion through the Zirconium-oxide layer. For severe conditions with large hydrogen generation, the reaction rate can be limited by vapor diffusion through a hydrogen film at the surface. This process is not modeled and will lead to an overprediction of the reaction rate for this condition.

6.6.15 Assessment and Application to BWR

The technical basis for the wall heat transfer correlations and their applicability for use in TRACG was discussed in Subsections 6.6.3 through 6.6.11. Those subsections discussed the ranges of applicability of the specific correlations and also compared the correlations to other data or other correlations. This section (6.6.15) discusses the performance of TRACG in situations where the wall heat transfer correlations are used.

A comparison has been made of heat transfer coefficients directly evaluated from the specific correlations to those calculated by TRACG for single-phase water flow in a pipe. From low to high flow the correlation changes from natural convection to turbulent flow. In both regimes the calculated heat transfer agrees well with the heat transfer coefficient calculated by TRACG. This provides assurance that the correlations have been correctly implemented into TRACG.

Comparisons of TRACG predictions of nucleate boiling have been made. Comparisons of the void fraction predicted by TRACG to the data are in good agreement with the data. This

provides an assessment of the split of energy from the wall that goes into vapor generation versus heating up the bulk subcooled liquid. A comparison of heat transfer coefficients evaluated directly from the correlations has been made with those made by TRACG for a heated pipe. At the bottom of the pipe, the heat transfer is by turbulent single phase heat transfer. As more heat is added to the liquid, it transitions into subcooled and then saturated nucleate boiling. The independent calculations of the correlations (based on ASME physical properties) agree well with the TRACG generated coefficients.

The ability of TRACG to predict boiling transition in a BWR fuel bundle has been shown. The flow rates for the tests were selected such that the bundle had dryout-rewet behavior. The tests show that TRACG accurately predicts transient critical power behavior. The calculated Δ CPR values compare well with the experimental values as do the calculated time to the onset of boiling transition for transient tests.

The ability of TRACG to predict correct heat transfer for conditions of low void fraction film boiling has been shown. TRACG was used to predict the system response of a test facility during refill-reflood transients of a large break LOCA. TRACG predicts the overall system performance well.

TRACG was also used to predict film boiling at high void fraction in another test facility.

TRACG's ability to predict the thermal hydraulic response of the GIRAFFE test facility has been investigated. The GIRAFFE test facility is an integral system effects test for the SBWR design and the pressure response is dominated by condensation in tubes and, to a lesser extent, the containment. Results obtained from TRACG analyses of the GIRAFFE system response tests compare favorably with the test results. Steady-state performance tests for the PCC heat exchanger unit were also conducted at GIRAFFE. The primary result obtained was information on the degradation in heat transfer due to the presence of noncondensable gases. TRACG predictions of the results were in reasonable agreement with the data. TRACG generally predicted less heat transfer than the results showed.

Applicability of the wall heat transfer correlations for BWRs has been investigated for various reactor and containment regions.

Wall Heat Transfer Regimes: There are specific correlations for all wall heat transfer regimes encountered in the core, the drywell, and the wetwell air space.

Hydraulic Diameter: The correlations are valid for the desired range of hydraulic diameter for the core region. For containment volumes, the correlations are valid with the use of the equivalent hydraulic diameter concept, but with larger uncertainty.

Mass Flux/Reynolds Number: The wall heat transfer correlations are validated over the range of mass flux and Re data encountered in the core. In the wetwell airspace and drywell, the range of mass fluxes and Re are well covered.

Pressure: The correlations applicable for the drywell and wetwell air space were developed within the pressure ranges of these compartments.

Void Fraction: The void fraction ranges are covered in all the regions.

6.6.16 References

- 6.6-1 W.M. Rohsenow and H.Y. Choe, *Heat, Mass and Momentum Transfer*, Prentice-Hall, Englewood Cliffs, New Jersey, 1961.
- 6.6-2 F.W. Dittus and L.M.K. Boelter, University of California (Berkeley), Publication Engineering, 2, p. 443, 1930.
- 6.6-3 M. Fishenden and O.A. Saunders, *An Introduction to Heat Transfer*, Oxford University Press, London, 1950.
- 6.6-4 J.P. Holman, *Heat Transfer*, 5th ed., McGraw-Hill, New York, 1981.
- 6.6-5 F. Kreith, *Principles of Heat Transfer*, 3rd ed., Harper and Row, New York, 1973.
- 6.6-6 M.T. Farmer, B.G. Jones and R.W. Spencer, *Analysis of Transient Contacting in the Low Temperature Film Boiling Regime. Part II: Comparison with Experiment, Nonequilibrium Transport Phenomena*, ASME HTD, 77, pp. 39-45, 1987.
- 6.6-7 W.M. Kays, *Convective Heat and Mass Transfer*, McGraw-Hill, New York, 1966.
- 6.6-8 R.T. Lahey and F.J. Moody, *The Thermal-Hydraulics of a Boiling Water Nuclear Reactor*, American Nuclear Society, 1977.
- 6.6-9 R. Viskanta and A.K. Mohanty, *TMI-2 Accident: Postulated Heat Transfer Mechanisms and Available Data Base*, NUREG/CR-2121, ANL-81-26, April 1981.
- 6.6-10 B. Gebhart, *Heat Transfer*, 2nd ed., chap. 8, McGraw-Hill, New York, 1970.
- 6.6-11 V.P. Carey, *Liquid-Vapor Phase-Change Phenomena*, Hemisphere Publishing, 1992.
- 6.6-12 F.J. Bailey, *An Analysis of Turbulent Free Convection Heat Transfer*, *Proc. Inst. Mech. Eng.*, 169, no. 20, p. 361, 1955.
- 6.6-13 H.K. Forster, and N. Zuber, *Dynamics of Vapor Bubbles and Boiling Heat Transfer*, *AIChE J.*, pp. 531-535, 1955.
- 6.6-14 R.J. Pryor, et al., *TRAC-PIA, An Advanced Best Estimate Computer Program for PWR LOCA Analysis*, Los Alamos Scientific Laboratory, NUREG/CRA-0665, LA-777-7S, May 1979.
- 6.6-15 R.T. Lahey, *Two-Phase Flow in Boiling Water Reactors*, NEDO-13888, July 1974.
- 6.6-16 F. Saha, and N. Zuber, "Point of Net Vapor Generation and Vapor Void Fraction in Subcooled Boiling," *Proceedings of the 5th International Heat and Mass Transfer Conference*, Tokyo, Japan, 1974.

- 6.6-17 D.R. Liles, et al., "TRAC-PF1/MOD1 Correlations and Models," NUREG/CR-5069, LA-11208-MS, December 1988.
- 6.6-18 W.H. McAdams, *Heat Transmission*, 3rd ed., McGraw-Hill, New York, 1954.
- 6.6-19 J.F. Walkush, "High Pressure Counterflow CHF", MIT, September 1974. EPRI Report 292-2, January 1975.
- 6.6-20 N. Zuber, M. Tribus and J.W. Westwater, "The Hydrodynamic Crisis in Pool Boiling of Saturated and Subcooled Liquids," *International Developments in Heat Transfer*, Part II, pp. 230-236, 1961.
- 6.6-21 "General Electric Thermal Analysis Basis (GETAB): Data Correlation and Design Application," General Electric Company, NEDO-10958, December 1973.
- 6.6-22 D.C. Groeneveld, S.C. Cheng, and T. Doan, "1986 AECL-UO Critical Heat Flux Lookup Table," *Heat Transfer Engineering*, **7**, pp. 46-62, 1986.
- 6.6-23 R.A. Dimenna, et al., "RELAP5/MOD2 Models and Correlations," NUREG/CR-5194, EGG-2531, August 1988.
- 6.6-24 J.E. Leonard, K.H. Sun, J.G.M. Andersen and G.E. Dix, "Calculation of Low Flow Film Boiling Heat Transfer for BWR LOCA Analysis," NEDO-20566-1, January 1977.
- 6.6-25 P.N. Rowe, K.T. Claxton, and J.B. Lewis, "Heat and Mass Transfer from a Single Sphere in an Extensive Flowing Fluid," *Trans. Inst. Chem. Eng.*, **43**, T14-T31 (1965).
- 6.6-26 K.H. Sun, J.M. Gonzalez and C.L. Tien, "Calculation of Combined Radiation and Convection Heat Transfer in Rod Bundles Under Emergency Cooling Conditions," ASME paper, August 1975.
- 6.6-27 L. Biasi, et al., "Studies on Burnout: Part 3," *Energia Nucleare*, **14**, pp. 530-536, 1967.
- 6.6-28 J.G.M. Andersen, "CORECOOL: A Model for the Temperature Distribution and Two-Phase Flow in a Fuel Element Under LOCA Conditions," General Electric, NEDO-21325, 76NED24, July 1976.
- 6.6-29 J.D. Duncan, and J.E. Leonard, "Emergency Cooling in Boiling Water Reactors Under Simulated Loss-of-Coolant Conditions," BWR-FLECHT Final Report, GEAP-13197, 86, 1971.
- 6.6-30 W.R. Usry, "Single Tube Condensation Test Program," NEDC-32301, March 1994.
- 6.6-31 J.G. Collier, *Convective Boiling and Condensation*, 2nd ed., McGraw-Hill, 1972.
- 6.6-32 L.C. Burmeister, *Convective Heat Transfer*, p. 657, Wiley, 1983.
- 6.6-33 S.Z. Kuhn, V.E. Schrock and P.F. Peterson, *Final Report on U. C. Berkeley Single Tube Condensation Studies*, UCB-NE-4201 Rev. 2, August 1994.

- 6.6-34 A.A. Dehbi, M.W. Golay and M.S. Kazimi, "The Effects of Noncondensable Gases on Steam Condensation under Turbulent Natural Conditions," MIT Report No. MIT-ANP-TR-004, June 1991.
- 6.6-35 O.C. Jones, Jr. and S.G. Bankoff, editors, *Thermal and Hydraulic Aspects of Nuclear Reactor Safety, Volume 1: Light Water Reactors*, p. 27, ASME, New York, 1977.
- 6.6-36 R.J. Pryor, et al., "TRAC-P1A, An Advanced Best Estimate Computer Program for PWR LOCA Analysis," Los Alamos Scientific Laboratory, NUREG/CRA-0665, LA-777-7S, May, 1979.
- 6.6-37 P.B. Whalley, *Boiling Condensation and Gas-Liquid Flow*, Clarendon Press, 1987.
- 6.6-39 O.C. Iloeje, and P. Griffith, "An Investigation of the Collapse and Surface Rewet in Film Boiling in Forced Vertical Flow," Transactions of ASME, pp. 166-172, May 1975.
- 6.6-40 R.E. Henry, "A Correlation for the Minimum Film Boiling Temperature," AIChE Symposium Series, 138, pp. 81-90, 1974.
- 6.6-42 S.C. Cheng, P.W.K. Law, and K.T. Poon, "Measurements of True Quench Temperature of Subcooled Water Under Forced Convection Conditions," Int. J. Heat Mass Transfer, 20, pp. 235-243, 1985.
- 6.6-43 D.C. Groeneveld, and J.C. Stewart, "The Minimum Film Boiling Temperature for Water During Film Boiling Collapse," Proc. 7th Int. Heat Transfer Conv., 4, pp. 393-398, Munich, 1982.
- 6.6-44 J.G.M. Andersen and H. Abel-Larsen, *CORECOOL—Model Description of the Programme*, Department of Reactor Technology, Risø National Laboratory, Denmark, RISØ-M-21380, November 1980.
- 6.6-46 M.M. Abu-Romia and C.L. Tien, *Appropriate Mean Absorption Coefficients for Infrared Radiation of Gases*, Journal of Heat Transfer, 89C, p321-327, 1967.
- 6.6-47 R. Siegel and J. Howel, *Thermal Radiation Heat Transfer*, McGraw-Hill, New York, 1972.
- 6.6-48 R. Semeria and B. Martinet, *Calefaction Spots on a Heating Wall: Temperature Distribution and Resorption*, Proceedings of the Institution of Mechanical Engineers, 180, 192-205, 1966.
- 6.6-49 A. Yamanouchi, *Effect of Core Spray Cooling in Transient State After Loss-of-Coolant Accident*, J. of Nucl. Sc. and Techn., 5, 547-558, November 1968.
- 6.6-50 J.O. Cermak et. al., *PWR Full Length Emergency Cooling Heat Transfer (FLECHT) Group I Test Report*, Westinghouse Electric Company, WCAP-7435, January 1970.
- 6.6-51 J.V. Cathcart, *Quarterly Progress Report on the Zirconium Metal-Water Oxidation Kinetics Program*, ORNL/NUREG/TM-41, August 1976.

- 6.6-52 Letter from P.W. Marriott (GE) to Richard W. Borchardt (NRC), *NRC Requests for Additional Information (RAIs) on the Simplified Boiling Water Reactor (SBWR) Design*, MFN No. 128-94, Docket No. STN 52-004, October 5, 1994.
- 6.6-53 K.H. Chu and B.S. Shiralkar, *Prediction of Critical Power Based on a Two Fluid and Multi-Field Model*, Fourth International Meeting on Nuclear Thermal Hydraulics, Operation and Safety, 1993.

6.7 Turbulent and Molecular Mixing Models

Single- and two-phase fluid mixing models have been formulated to account for mixing due to molecular and turbulent diffusion. The formulation focuses on describing the local mixing velocity j^* separately, first for turbulent diffusion and then for molecular diffusion.

During turbulent flow, volumes of fluids are exchanged laterally among adjacent locations leading to transport of mass, momentum and energy. These mixing effects alter local axial mass flux, quality, void fraction and enthalpy distributions.

A mixing model has been incorporated to account for this turbulent flow behavior. The model accounts for exchange of mass, momentum, and energy laterally. This exchange is caused by turbulent shear and eddy interchange. It is able to account for the void profile, pressure drop characteristics, and enthalpy distribution more accurately than a model which ignores these phenomena.

Typical applications may include turbulent mixing phenomena in the upper plenum, containment, and molecular diffusion/convection for boron mixing.

6.7.1 Technical Basis and Assumptions

As a part of the two-phase turbulent mixing model development, an extensive study of existing literature has been made. The study identified fundamental measurements for phenomena such as jet and plume mixing, two-phase recirculation flow, and subchannel mixing. From these measurements, information has been obtained on local mixing velocities dependent on local thermodynamic and flow conditions [6.7-1,6.7-2].

6.7.2 Applicability

The mixing model described in the previous section is relatively simple, but has produced good results for a number of applications. The predictions were generally within 0.1 of the measurements. Calculations made without the mixing term showed a larger variation between the central and peripheral regions, with less favorable agreement with the data. In both cases, the geometry was cylindrical with diameters from 1 to 2m. The pressure ranged from 4.6 to 6.4 MPa.

The model is based on data that includes low pressure conditions, and has been assessed against subchannel and plume mixing data over a range of pressures. The main limitation in the model is the use of a length scale which is not well defined. Because the length scale is typically the cell size, the results will be dependent on the nodalization, and empirical confirmation is needed at different scales.

The main applications where a mixing model is needed is for ECCS mixing in the upper plenum, for the distribution of noncondensable gases in the drywell, and for thermal stratification in the suppression pool.

For the upper plenum, a specific model has been developed based on the tracking of spray trajectories and submerged jet mixing. This model is described in Section 7.8.2.

The mixing model described in this section is not currently being used for containment applications. In the drywell, flows are calculated by application of the momentum equation (Section 3.1), with the mixing terms set to zero. Thus, the flows are dependent only on wall friction and buoyancy. The calculated noncondensable distributions provide a measure of the adequacy of the model. Comparisons with the data obtained in the PANDA facility at the Paul Scherrer Institute show that the trends are reasonably predicted. In this context, the mixing model is only being used for sensitivity studies. An alternate bounding approach will address the effects of the noncondensable distribution on containment performance.

Stratification in the suppression pool is being modeled empirically with TRACG. In this model, the portion of the pool below the lowest source of thermal energy is assumed to be stratified. The portion above the source will be well mixed. These phenomena are not sensitive to the mixing model used. The validity of the TRACG model has been demonstrated by comparison against a variety of large-scale data.

6.7.3 References

- 6.7-1 J.T. Rogers and R.G. Rosehart, *Mixing by Turbulent Interchange in Fuel Bundles, Correlations and Interfaces*, ASME, 72-HT-53, 1972.
- 6.7-2 R.D. Blevins, *Applied Fluids Dynamica Handbook*, van Nostrand Reinhold Company, New York, 1984.
- 6.7-3 M.S. Kazimi and J.E. Kelley, *Formulation of Two-Fluid Model for Mixing in LWR Bundles*, Thermal Hydraulics of Nuclear Reactors (Edited by Mati Merilo, EPRI), Volume I, pp. 433-439, American Nuclear Society, 1983.

7.0 Component Models

Descriptions of the various component models included in TRACG are given in this section. A physical description of each component is presented with a typical noding diagram showing the conventions used to model the component. Mathematical models, including finite-difference approximations, are given only for those aspects of the component that are not covered in the basic hydrodynamics and heat-transfer descriptions. User options, restrictions on the use of the component, and input/output information are also given. Specialized models for pumps, jet pumps, fuel channels, steam separators, and heat exchangers are described. Models for the steam dryer and the upper plenum regions of the vessel are also described. The terminology in Section 7 is consistent with the nomenclature defined in Sections 3 and 6. Symbols specific to a particular model are defined in the individual subsections.

7.1 Pipe

The pipe (PIPE) component models the flow in a one-dimensional (1-D) duct or pipe. The pipe component can be used alone in a simulation or it can be used as a connector between components to model a reactor system. Capability is provided to model area changes, wall heat sources, and heat transfer across the inner and outer wall surfaces. A wide selection of pipe materials is available to represent the wall material in the wall conduction calculation.

Figure 7.1-1 shows a typical noding diagram for a pipe containing a Venturi tube and an abrupt area change. The numbers within the pipe indicate cell numbers, and those above indicate cell boundary numbers. The geometry is specified by providing a volume and length for each cell and a flow area, hydraulic diameter and loss coefficient at each cell boundary. The junction variables, JUN1 and JUN2, provide reference numbers for connecting a pipe to other components. The numerical methods used to treat the thermal-hydraulics in the pipe are described in Section 8.

Input options are available to allow for wall heat transfer and to select correlations for CHF. Wall heat transfer can be omitted by setting the number of heat-transfer nodes (NODES) to zero. Generalized heat-transfer capability allows the user to specify heat exchange between any pipe cell and any other component fluid cell or wall node in the model. The generalized heat-transfer option is activated through the IHTS and IWT input parameters. The CHF calculation can be bypassed by setting the input parameter, ICHF, to a negative value.

Calculation of pressure drop due to wall friction losses for the pipe component described in Section 6.2.1 requires a wall roughness input by the user. An abrupt area change can be modeled by input of additional pressure loss factors. Because of central differencing, any irreversible losses must be modeled with an appropriate pressure loss factor.

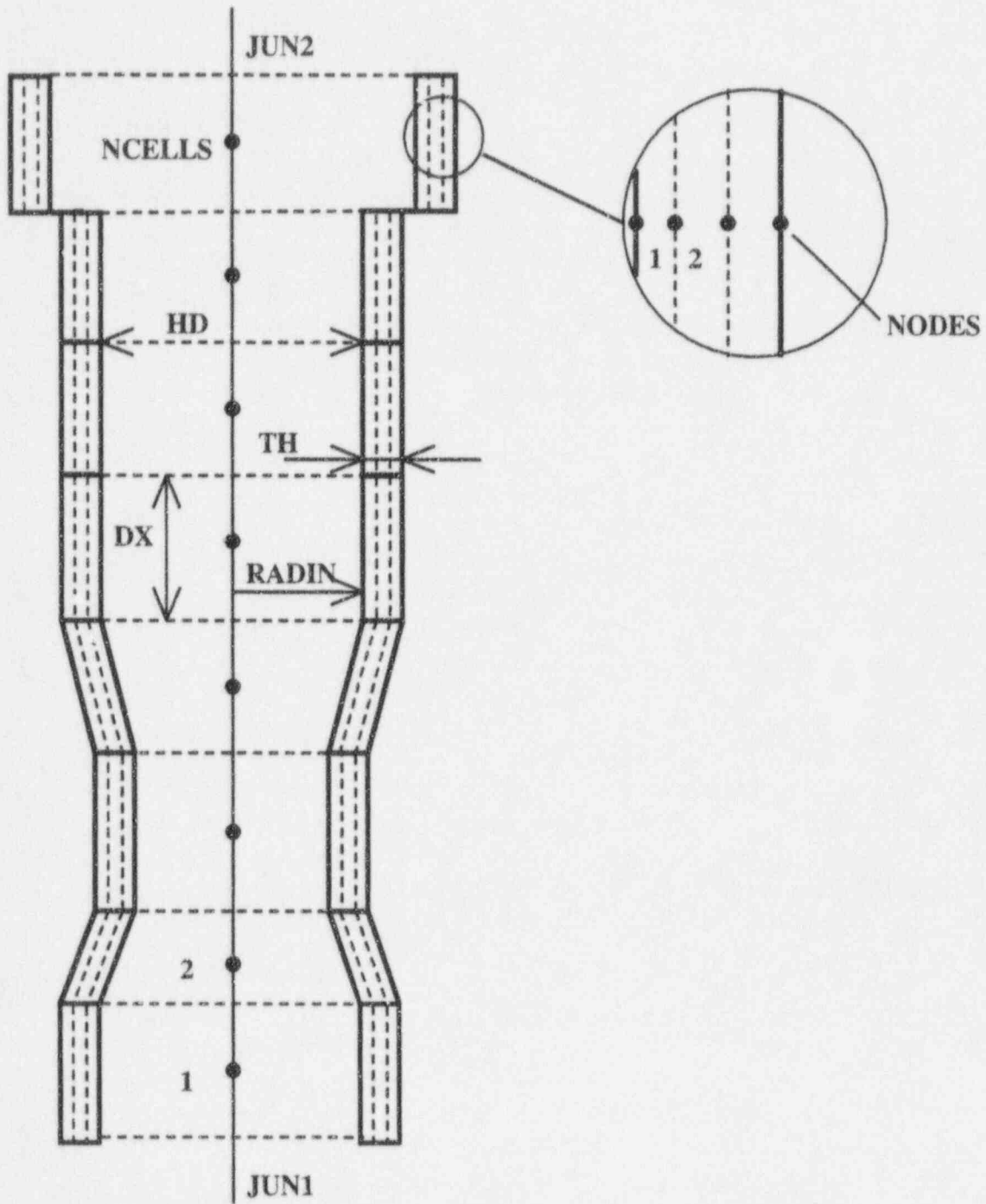


Figure 7.1-1. PIPE Noding Diagram

Pipe components may be connected to any other component. However, computational expense increases rapidly with the number of component junctions and the users are cautioned to minimize the number of components used in their models. In addition, 1-D cells of grossly different length should not be placed together, as this can cause computational difficulties, particularly when area changes also occur.

Output for a pipe consists of mass flow rate in and out of the pipe, mass flux in and out of the pipe, and nodal values of pressure, void fraction, liquid and vapor velocities, saturation temperature, liquid and vapor temperatures, liquid and vapor density, cell-to-cell pressure drop, choking, and CCFL indicators. If wall heat transfer is included, information on the heat-transfer regime, liquid and vapor HTC on inner and outer surfaces, surface heat fluxes to liquid and vapor on the inner wall surface, heat sources and wall temperatures for each radial node are printed for each axial cell.

7.2 Pump

The pump (PUMP) component is represented by a 1-D component with N cells ($N > 1$). Figure 7.2-1 shows a typical noding diagram for the pump component. The pump momentum is modeled as a source, called SMOM. SMOM is required to act between Cells 1 and 2; therefore, it is necessary to construct the cell noding such that the cell numbers increase in the normal flow direction.

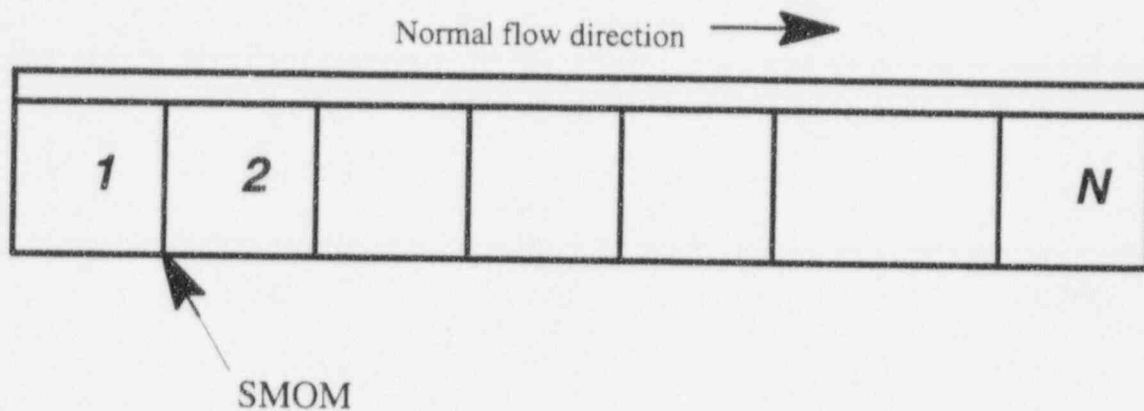


Figure 7.2-1. PUMP Noding

7.2.1 Pump Governing Equations

The pump component combines the PIPE component with pump correlations. The pump model is identical to the 1-D pipe model except that the momentum equations at the SMOM face are rewritten as:

$$\frac{v_{\ell}^{n+1} - v_{\ell}^n}{\Delta t} = \frac{P_1^{n+1} - P_2^{n+1} + \Delta P_p^{n+1}}{\rho_m \Delta x} - g \cos \theta \quad (7.2-1)$$

where

$$\Delta P_p^{n+1} = \Delta P_p^n + \left(\frac{\partial \Delta P_p}{\partial v} \right)^n (v_{\ell}^{n+1} - v_{\ell}^n) + \left(\frac{\partial \Delta P_p}{\partial \Omega} \right)^n (\Omega^{n+1} - \Omega^n) \quad (7.2-2)$$

and

$$v_v = v_{\ell} \quad (7.2-3)$$

ΔP_p is the pressure rise through the pump evaluated from the pump correlation. The steady-state solution of Equation 7.2-1 is:

$$\Delta P_p = P_2 - P_1 + g \cos \theta \rho_m \Delta x \quad (7.2-4)$$

which is the desired result. Friction does not enter explicitly into the pump motion equation. Therefore, additive friction is not allowed at the SMOM face.

The pump model describes the interaction of the system fluid with a centrifugal pump. The model calculates the pressure differential across the pump and its angular velocity as a function of the fluid flow rate and the fluid properties. The model can treat any centrifugal pump and allows for inclusion of head degradation caused by two-phase effects.

Pump characteristic curves describe the pump head and torque response as a function of fluid volumetric flow rate and pump speed. Homologous curves (one curve segment represents a family of curves) are used for this description because of their simplicity. These curves describe, in a compact manner, all operating states of the pump obtained by combining positive or negative impeller velocities with positive or negative flow rates.

To account for two-phase effects on pump performance, the pump curves are divided into two separate regimes. Data indicate that two-phase pump performance in the vapor fraction range of 20 to 80% is degraded significantly in comparison with its performance at vapor fractions outside of this range. One set of curves describes the pump performance for single-phase fluid (void fraction 0.0 or 1.0), and another set describes it for two-phase fluid. The pump head at any vapor fraction is calculated from the relationship:

$$H = H_1 - m(\alpha) (H_1 - H_2) \quad (7.2-5)$$

where

- H = Total pump head
- H_1 = Pump head from the single-phase homologous curves
- H_2 = Pump head from the fully degraded homologous curves
- m = Pump degradation multiplier
- α = Vapor fraction

The two-phase hydraulic torque is treated similarly. The following definitions are used in the subsequent development:

- H = Pump head = $\Delta P_p / \rho$
- Q = Pump volumetric flow rate
- Ω = Pump impeller angular velocity

where ΔP_p is the pump differential pressure and ρ is the pump inlet density. To allow one set of curves to be used for a variety of pumps, the following normalized quantities are used:

$$h = \frac{H}{H_r} \quad (7.2-6)$$

$$q = \frac{Q}{Q_r} \quad (7.2-7)$$

$$w = \frac{\Omega}{\Omega_r} \quad (7.2-8)$$

where the subscript, r, denotes the rated condition. The pump similarity relations [7.2-1] show:

$$\frac{h}{w^2} = f\left(\frac{q}{w}\right) \quad (7.2-9)$$

For small w, this correlation is not satisfactory and the following combination of variables is used:

$$\frac{h}{q^2} = f\left(\frac{w}{q}\right) \quad (7.2-10)$$

The first correlation is used in the range $0 \leq |q/w| \leq 1$ and the second is used in the range of $0 \leq |w/q| \leq 1$. The four resulting curve segments, as well as the curve selection logic used in TRACG, are shown in Table 7.2-1.

The dimensionless hydraulic torque is defined by:

$$\beta = \frac{T/\rho}{T_r/\rho_r} \quad (7.2-11)$$

where

- T = Hydraulic torque
- T_r = Rated torque
- ρ = Pump inlet density
- ρ_r = Rated density

The single-phase torque, T , is dependent on the fluid density and is calculated from:

$$T = \beta T_r \left(\frac{\rho}{\rho_r} \right) \quad (7.2-12)$$

The density ratio multiplier is needed to correct for the density difference between the pumped fluid and the rated condition. For two-phase conditions, the impeller torque is calculated from:

$$T = T_1 - N(\alpha) (T_1 - T_2) \quad (7.2-13)$$

where

- T = Total impeller torque
- T_1 = Impeller torque from the single-phase homologous curves
- T_2 = Impeller torque from the fully degraded homologous curves
- $N(\alpha)$ = Torque degradation multiplier

The homologous, normalized, torque curve segments for β are correlated in the same manner as the head curve segments shown in Table 7.2-1.

In addition to the homologous head and torque curves, the head and torque degradation multipliers defined in Equations 7.2-5 and 7.2-13 are needed. These functions are usually nonzero only in the vapor fraction range where the pump head and torque are either partially or fully degraded.

The pump model can either specify the pump angular velocity or the motor torque while its motor is energized. When the torque is specified, the time rate of change for the pump motor assembly is proportional to the sum of the moments acting on it, and is calculated from:

$$I \frac{d\Omega}{dt} = \sum_i T_i = T_m - (T + T_f + T_b) \quad (7.2-14)$$

where

- I = Pump motor assembly moment of inertia
- T = Impeller torque
- T_f = Torque caused by friction (constant)
- T_b = Bearing and windage torque
- T_m = Applied motor torque

We assume that T_b is:

$$T_b = C \frac{\Omega_i \Omega_i}{\Omega_r^2} \quad (7.2-15)$$

where C is an input constant and Ω_r is the rated impeller angular velocity. T_f is multiplied by $\Omega/|\Omega|$ so that it also changes sign if the speed reverses. The impeller torque is evaluated using the homologous torque curves and Equation 7.2-13; it is a function of the fluid density and flow rate as well as the pump angular velocity. T_m is defined through the control system. It is initially set to zero and retains that value unless the control system changes it to a nonzero value. For time step $(n+1)$, Equation 7.2-14 is calculated implicitly and is substituted into Equations 7.2-1 and 7.2-2, which are solved together with the thermal-hydraulic equations as described in Section 3 for the new fluid velocities. The new pump speed is then obtained by backsubstitution.

The pump work, which is added to the fluid energy equation, is calculated as:

$$E_p = \Omega T \quad (7.2-17)$$

The wall heat transfer, wall friction, CHF calculation, and implicit hydrodynamics options are the same for the pump component as for the pipe component. In addition, the following options are specified: pump type, motor action, reverse speed, two-phase, and pump curve. The input variables, IPMPTR and NPMPTX, specify the trip identifier for the pump trip initiation and the number of pairs of points in the pump-speed table (SPTBL), respectively. If IPMPTR = 0, no pump trip action occurs (a constant speed pump).

If the pump motor is energized, its angular velocity is assumed to be the constant value specified. If the motor is not energized, a pump coastdown calculation is performed using the specified initial pump speed.

There are three pump options available (IPMPTY = 1, 2, or 3). For pump option 1 (IPMPTY = 1), the pump speed variation is specified by input. Pump option 2 (IPMPTY = 2) is similar to option 1 except the pump speed is calculated after a trip has occurred. Pump option 3 (IPMPTY = 3) allows the motor torque to be calculated by the control system and the pump speed.

If the reverse speed option is turned off (IRP = 0), the pump is allowed to rotate in the forward direction only. For this case, if negative rotation is calculated (after trip with pump Option 2), its speed will be set to zero.

If the two-phase option is turned on (IPM = 1), the degraded pump head and torque are calculated from Equations 7.2-5 and 7.2-13. If the two-phase option is turned off (IPM = 0), only the single-phase head and torque homologous curves are used.

There are several restrictions and limitations in the pump component. Because there is no pump motor torque-versus-speed model, the pump speed is assumed to be input if the motor is

energized. Pump noding is restricted such that the pump momentum source is located between Cells 1 and 2 of the pump model. Finally, the head degradation multiplier, $M(\alpha)$, and the torque degradation multiplier, $N(\alpha)$, are assumed to apply to all operating states of the pump.

7.2.2 Pump Head and Torque Homologous Curves

The user may specify pump homologous curves in the input or alternatively use the built-in pump curves. The built-in pump curves are based on the MOD-1 Semiscale system pump [7.2-2 - 7.2-4]. The single-phase head (HSP), fully degraded two-phase head (HTP), head degradation multiplier (M), single-phase torque (TSP), fully degraded two-phase torque (TTP), and torque degradation multiplier (N) curves are provided in Figures 7.2-2 through 7.2-7, respectively. Where applicable, the curves are numbered corresponding to the conditions provided in Table 7.2-1. Because these homologous curves are dimensionless, they can describe a variety of pumps by specifying the desired rated density, head, torque, flow, and angular velocities as input.

7.2.3 References

- 7.2-1 V.L. Streeter and E.B. Wylie, *Hydraulic Transients*, New York: McGraw-Hill Book Company, Inc., pp. 151-160, 1967.
- 7.2-2 D.J. Olsen, *Experiment Data Report for Single- and Two-Phase Steady State Tests of the 1-1/2-Loop MOD-1 Semiscale System Pump*, ANCR-1150, May 1974.
- 7.2-3 G.G. Loomis, *Intact Loop Pump Performance During the Semiscale MOD-1 Isothermal Test Series*, ANCR-1240, October 1975.
- 7.2-4 D.J. Olsen, *Single- and Two-Phase Performance Characteristics of the MOD-1 Semiscale Pump Under Steady State and Transient Fluid Conditions*, ANCR-1165, October 1974.

Table 7.2-1

**Definitions of the Four Curve Segments that Describe
the Homologous Pump Curves**

Curve Segment	Selection Criteria	Correlation
1	$ q/w \leq 1$ and $w > 0$	$\frac{h}{w^2} = f_1\left(\frac{q}{w}\right)$
4	$ q/w \leq 1$ and $w < 0$	$\frac{h}{w^2} = f_4\left(\frac{q}{w}\right)$
3	$ w/q \leq 1$ and $q < 0$	$\frac{h}{q^2} = f_3\left(\frac{w}{q}\right)$
2	$ w/q \leq 1$ and $q > 0$	$\frac{h}{q^2} = f_2\left(\frac{w}{q}\right)$
Static State	$w = 0$ and $q = 0$	$h = 0$

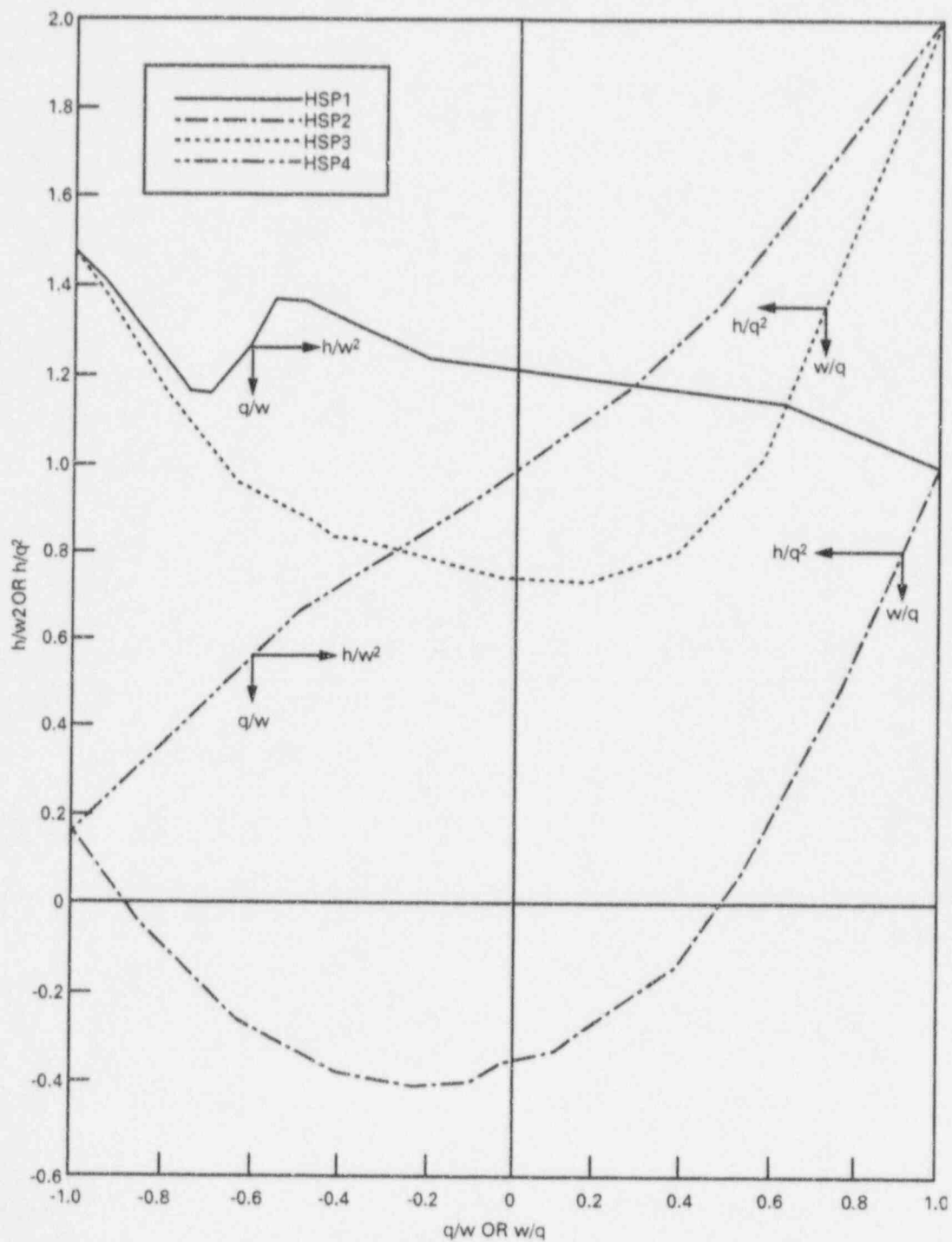


Figure 7.2-2. Single-Phase Homologous Head

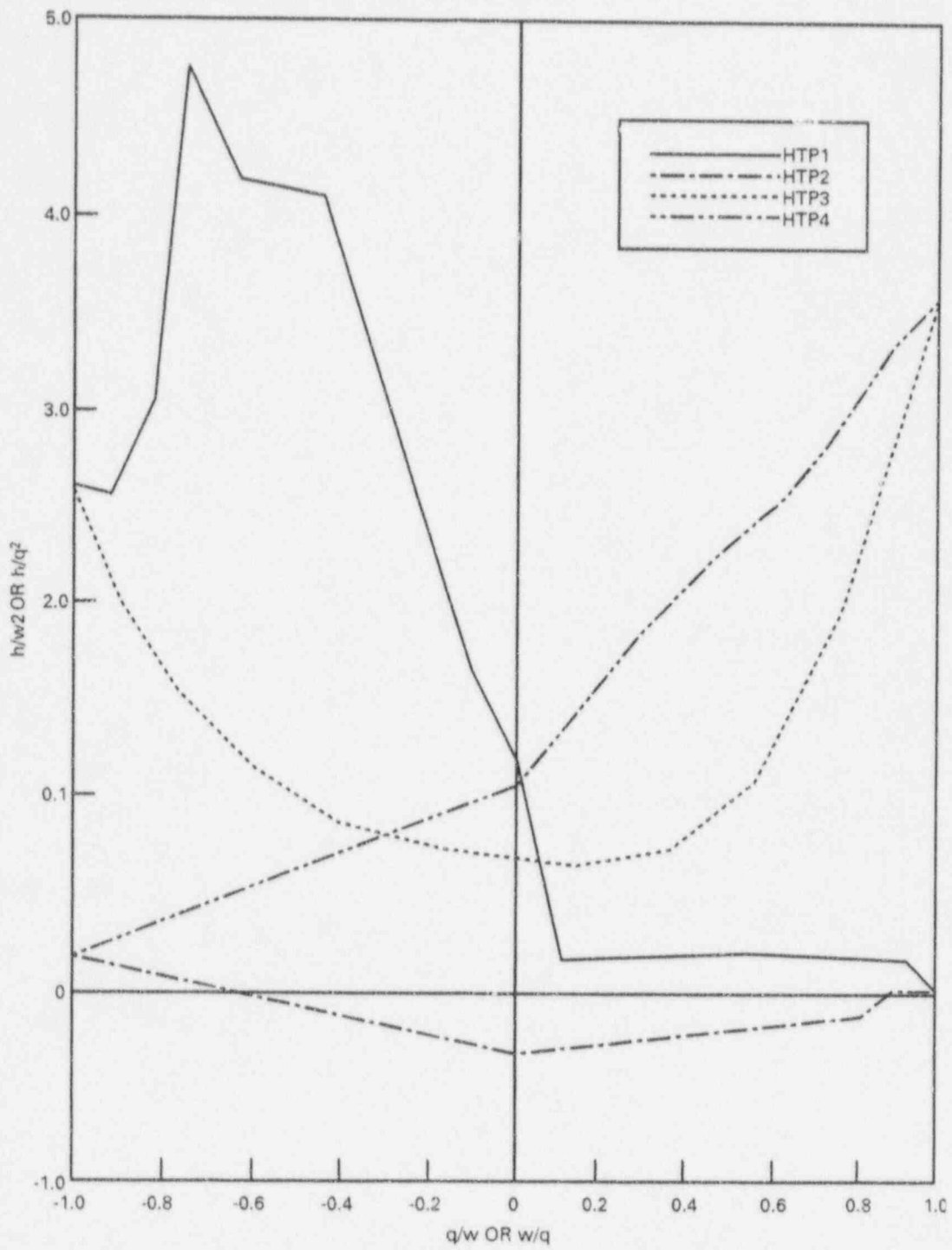


Figure 7.2-3. Fully Degraded Homologous Head Curves

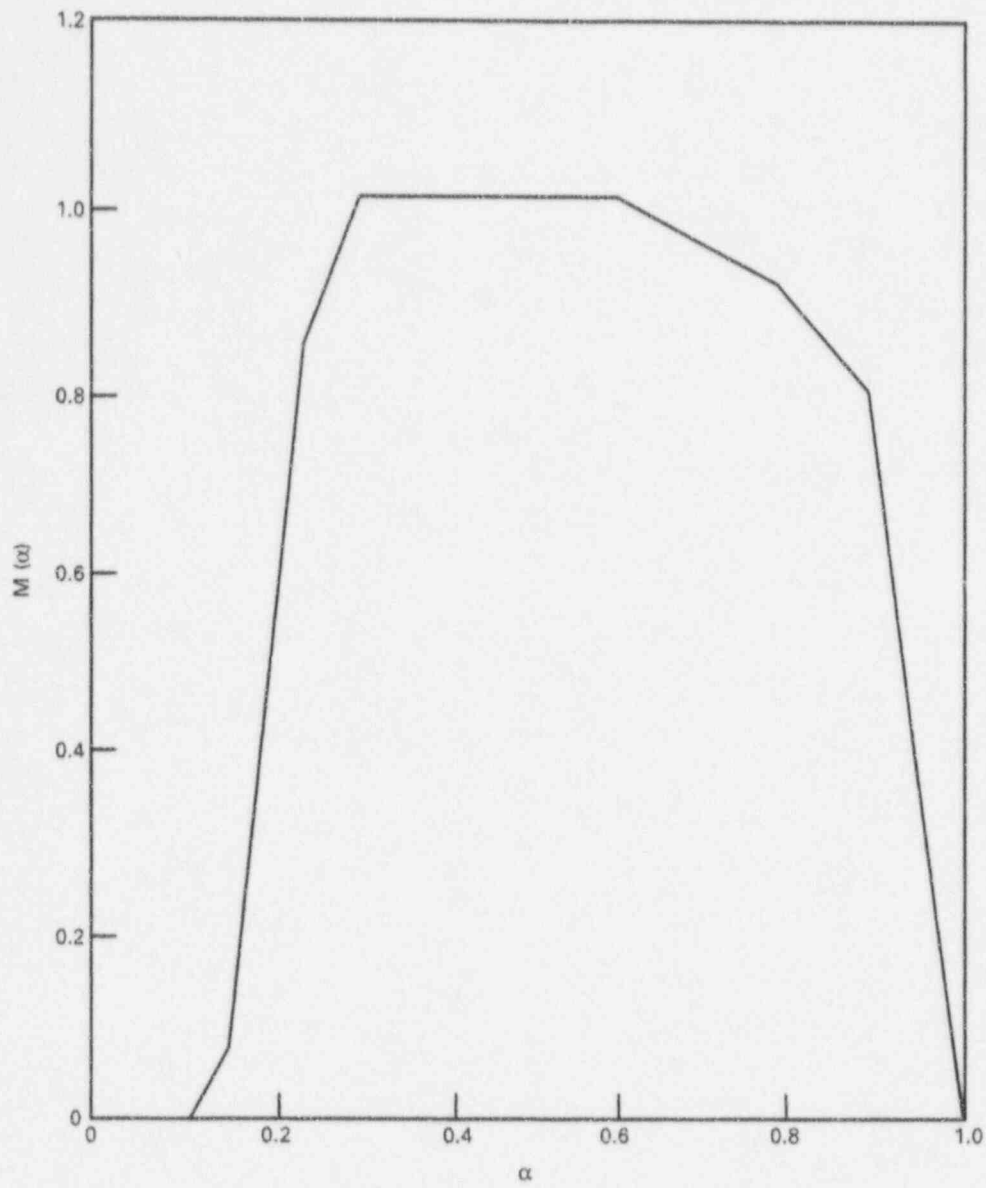


Figure 7.2-4. Head Degradation Multiplier

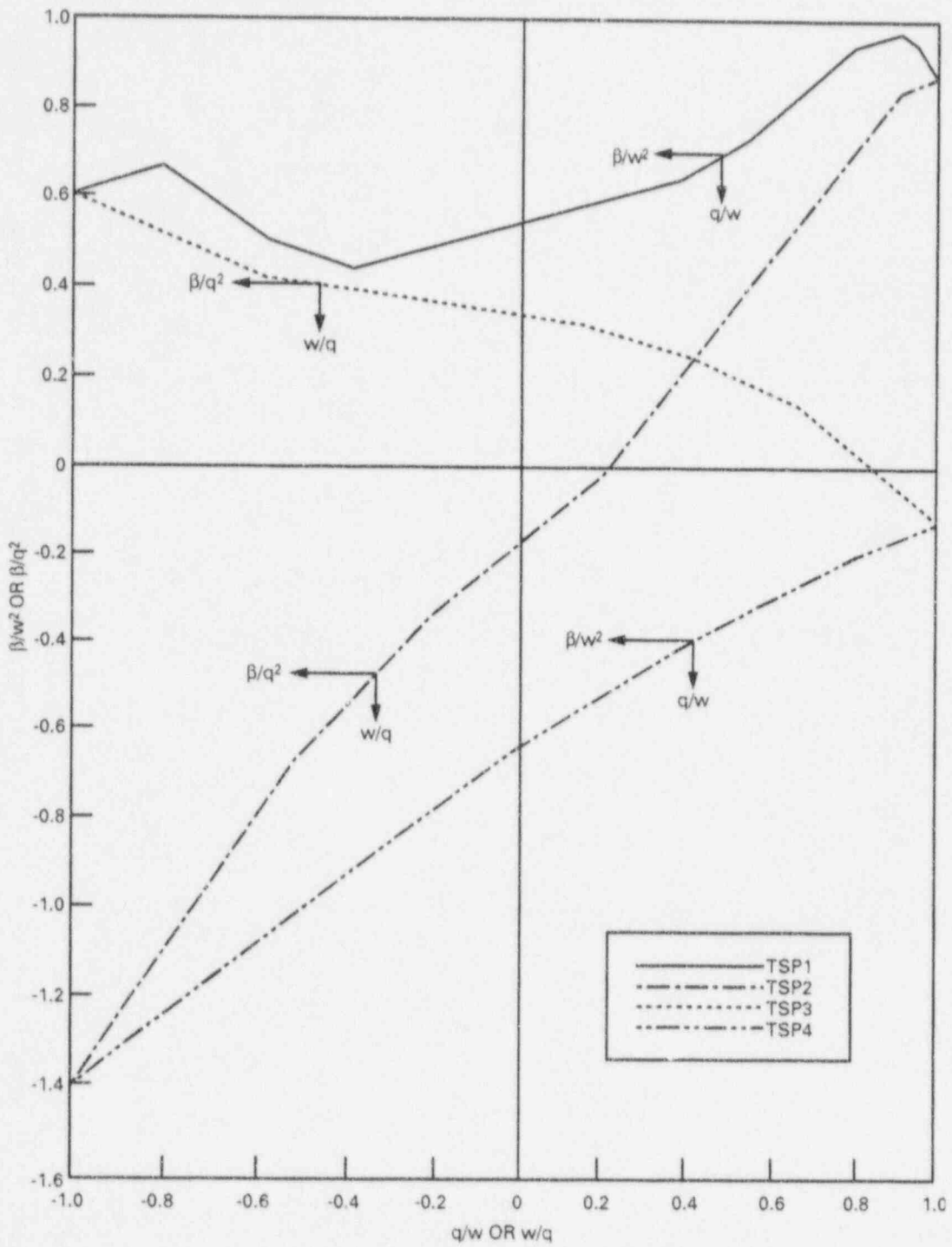


Figure 7.2-5. Single-Phase Homologous Torque Curves

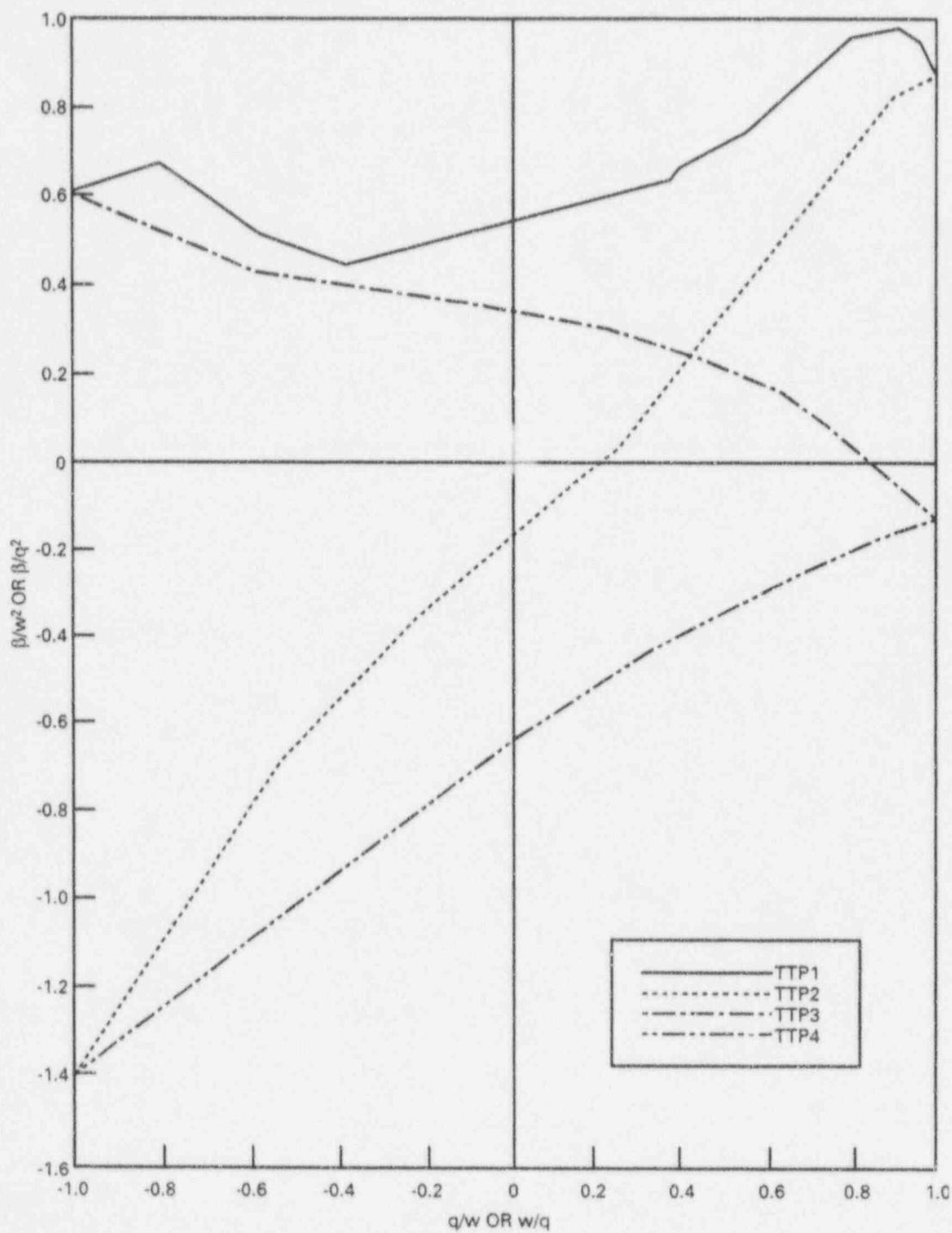


Figure 7.2-6. Fully Degraded Homologous Torque Curves

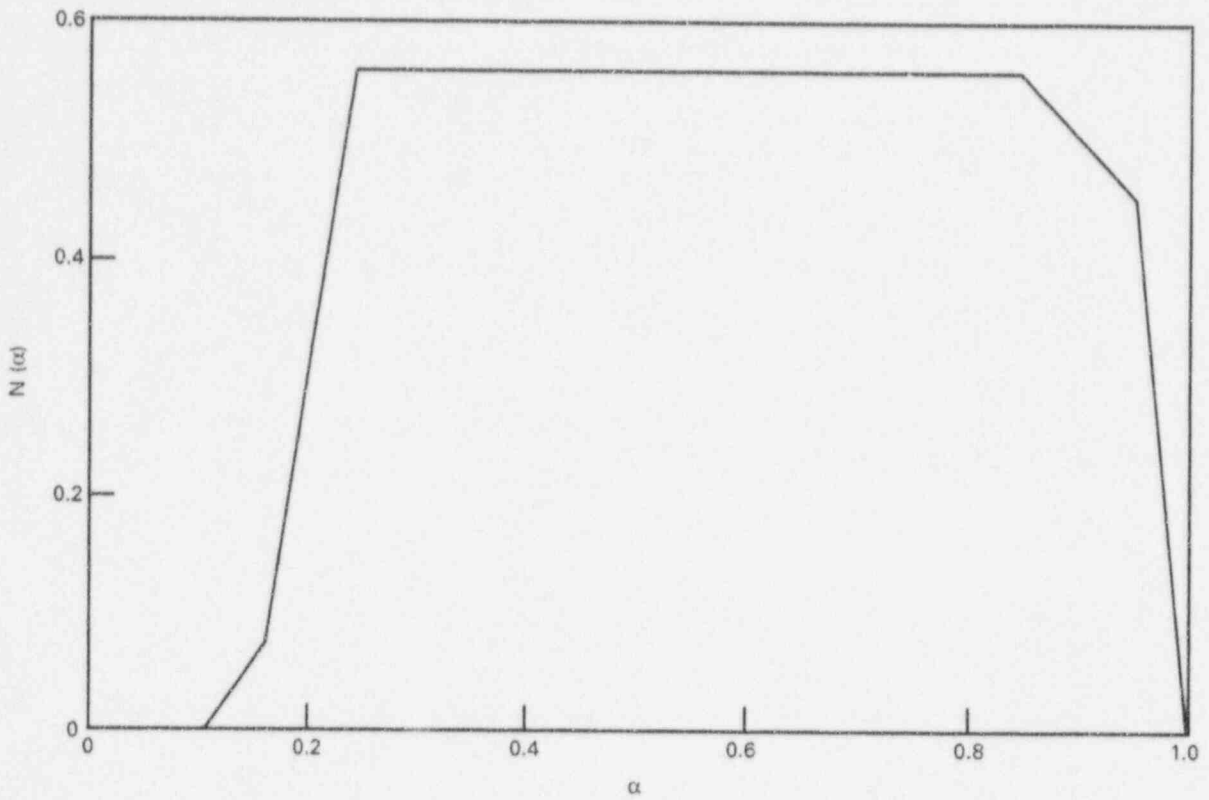


Figure 7.2-7. Torque Degradation Multiplier

$$Fr = \frac{v_v^2}{gD_t} \quad (7.9-9)$$

In the above equations, the heat exchanger geometry is specified by the following parameters:

- D_h = Shell hydraulic diameter
- D_t = Individual tube outer diameter
- D_B = Distance between tube bank baffles

The method for handling condensation requires that all the energy be taken out of the liquid phase; condensation then occurs due to interfacial heat transfer. This being the case, the liquid and vapor coefficients must be adjusted accordingly:

$$h_\ell = \text{FRACL } h_{\ell} + (1 - \text{FRACL}) h_v \left(\frac{T_{\text{sat}} - T_w}{T_\ell - T_w} \right) \quad (7.9-10)$$

$$h_v = 0.0 \quad (7.9-11)$$

where h_ℓ and h_v are the heat transfer coefficients. FRACL is the fraction of the heat transfer tubes that is covered by liquid. This is determined by user input of two tables: (1) shell liquid level versus shell void fraction and (2) FRACL versus liquid level.

7.9.3 References

- 7.9-1 T. Fujii, H. Vehara, and C. Kurato, *Laminar Filmwise Condensation of Flowing Vapour on a Horizontal Cylinder*, International Journal of Heat and Mass Transactions, 15, pp. 235-246, 1972.
- 7.9-2 D.Q. Kern, *Process Heat Transfer*, New York: McGraw-Hill Book Company, 1950.

7.9.2 Heat Transfer Correlations

Correlations appropriate to flow condensation on horizontal and vertical tube banks [7.9-1] have been introduced. In addition, a correlation for single-phase (liquid) convection across tube banks [7.9-2] has been implemented in order to better describe the behavior in the liquid-filled regions of the heat exchanger. These correlations are presently available in the code for heat exchangers only--models for convection and condensation described in Section 6.6 are used for other components. The correlations used are:

For condensing flow on horizontal tube banks,

$$h_v = X_f \frac{k_\ell}{D_t} \text{Re}_\ell^{1/2} \left(1 + \frac{0.276}{X_f^4 \text{Fr} H_f} \right)^{1/4} \quad (7.9-2)$$

For condensing flow on vertical tube banks,

$$h_v = X_f \frac{k_\ell \text{Re}_\ell^{1/2}}{D_t} + 0.943 \left[\frac{h_{fg} k_\ell^3 \rho_\ell^2 g}{\mu_\ell D_B (T_{\text{sat}} - T_w)} \right]^{1/4} \quad (7.9-3)$$

For liquid crossflow across tube banks,

$$h_\ell = 0.36 \frac{k_\ell}{D_t} \left(\frac{D_h \rho_\ell v_\ell}{\mu_\ell} \right)^{0.55} \left(\frac{C_{P_\ell} \mu_\ell}{k_\ell} \right)^{1/3} \quad (7.9-4)$$

X_f , H_f , R_f , Re_ℓ (liquid film Reynolds number) and Fr (Froude number) are dimensionless parameters defined as:

$$X_f = 0.9 \left(1 + \frac{1}{R_f H_f} \right)^{1/3} \quad (7.9-5)$$

$$H_f = \frac{k_\ell (T_{\text{sat}} - T_w)}{\mu_\ell h_{fg}} \quad (7.9-6)$$

$$R_f = \left(\frac{\rho_\ell \mu_\ell}{\rho_g \mu_g} \right)^{1/2} \quad (7.9-7)$$

$$\text{Re}_\ell = \frac{\rho_\ell v_\ell D_t}{\mu_\ell} \quad (7.9-8)$$

$$\alpha_{DC} = \begin{cases} 0.0 & \text{if liquid level} \geq \text{drain cooler height} \\ 1.0 & \text{if liquid level} \leq \text{drain cooler height} - 0.05\text{m} \\ 20.0 \times (\text{drain cooler height} - \text{liquid level}) & \text{otherwise} \end{cases} \quad (7.9-1)$$

The 5 cm for linear interpolation of the donor celled void fraction provides a gradual change in α_{DC} as the drain cooler inlet is uncovered.

The validity of the α_{DC} modeling is dependent on an accurate user specification of the shell liquid level versus void fraction and the applicability of the above and below void fraction assumptions. If the assumptions or input requirements are not appropriate for a particular application, the user has the option to use other components to model the shell side of the heat exchanger in more detail. The generalized component-to-component heat transfer is then used to model the heat transfer between the tubes and shell.

Another change to the hydrodynamic equations was forced by the normally high inlet steam velocities found in the main condenser. Momentum flux was eliminated at the drain cooler inlet interface. This was done to prevent $V \cdot \nabla V$ induced pressurization of the first cell in the drain cooler.

Some special features of tees that are used as heat exchangers are:

- Side arm input is simplified--the pipe arrays do not have to be input for the side arm.
- Heat transfer from the walls of the shell is not modeled (NODES = 0).
- The shell must consist of only one cell, but the drain cooler may contain as many cells as required. The side-arm always connects to the first cell (shell).
- The heat transfer pipe may contain as many cells as needed. U-tubes may be represented by appropriate assignment of the heat transfer connections.

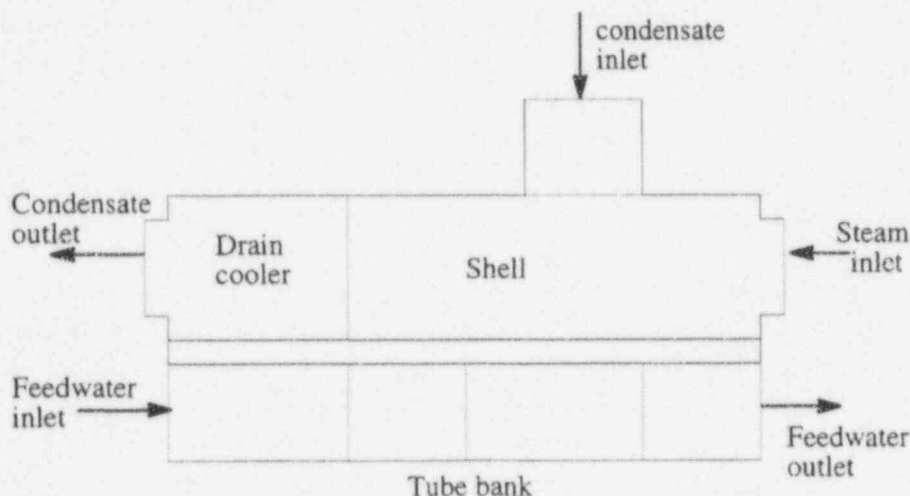


Figure 7.9-1. Model of Feedwater Heater Using a HEAT Component (modified TEE) and PIPE Component for the Tube Bank

7.9 Heat Exchanger

The modeling of heat exchangers (heaters or condensers) can be accomplished using a combination of standard TRACG components without the use of the specialized heat exchanger component. A pipe component is typically used to simulate the tube bank. Multiple pipes with the associated manifold tees can also be used to represent the tubes if additional detail is required. The nodalization within the simulated tube(s) is flexible and as such can be customized for a particular application. The shell side of the heat exchanger can be simulated using either the vessel component, which allows multi-dimensional flow or the one-dimensional tee component. In either case, the level of modeling detail can be specified to match the individual application. The heat transfer between the tube and shell utilizes the generalized component-to-component heat transfer capability of TRACG. This feature allows for heat transfer from the wall of any one-dimensional component cell to the fluid in any other component cell, including the vessel component. The correlations used to evaluate the wall heat transfer are described in Section 6.6.

The modeling flexibility using a combination of standard TRACG components makes this the recommended approach for most applications. However, for some applications, the use of a simplified heat exchanger component may be desirable. The heat exchanger component allows the user to simulate typical heat exchangers with a minimum number of cells. To accomplish this, the model requires that the details of the shell side geometry be provided as a function of shell average void fraction. The user-supplied tables of shell liquid level versus void fraction and fraction of tubes covered by liquid versus liquid level provide the basis for determining the detailed shell internal conditions. The heat exchanger component is recommended only if the assumptions and input requirements of the component are appropriate for a particular application.

7.9.1 Model Assumptions

The heat exchanger is based on the tee component and includes changes to the heat transfer correlation package and special treatment of the momentum and mass flow in the primary tube. A typical heat exchanger component is shown in Figure 7.9-1. Included in the figure is a pipe component that represents the heat transfer tubes within the heater. The combination of the heat exchanger and pipe represents a typical tube-in-shell heat exchanger, with attached drain-cooler region. The steam enters the shell (Cell 1), condenses, enters the drain cooler (Cell 2) as single-phase liquid (normally), undergoes further cooling and, finally, exits the heat exchanger. The side arm is included and attached to the steam shell cell, since high-pressure saturated liquid (from turbine separators or higher-pressure feedwater heaters) is frequently input to the heater shells in a separate flow path. Typical shell void fractions are about 0.5, while the drain cooler normally receives only liquid from the cell. The user must specify the drain cooler inlet height and a table of shell liquid level versus void fraction. The assumption is made that only liquid is present below the position of the liquid level and only vapor is present above the level. With this assumption, the donor cell void fraction α_{DC} for flow from the shell to the drain cooler is:

nodal enthalpy and w_{ent} is the entrainment by the jet within a given node. The energy source at the upper tie plate is obtained by calculating $W_o h_o + \Sigma W_{ent} h_{node}$, which is the sum of the energy of the injected fluid and the entrained fluid, and distributing it according to the assumed function.

In case the jet overshoots the centerline, the amount of liquid overshooting the central line is added to the central node.

7.8.3 References

- 7.8-1 M. Van Dyke, *Perturbation Method in Fluid Mechanics*, Academic Press, 1964.
- 7.8-2 W. Schneider, *Flow Induced by Jets and Plumes*, Journal of Fluid Mechanics, Volume 108, pp. 55-65.
- 7.8-3 S.A. Sandoz and W.A. Sutherland, *Core Spray Performance*, HTD-Vol. 7, pp. 107-114, the 19th National Heat Transfer Conference, Orlando, Florida, July 1980.
- 7.8-4 G.N. Abramovich, *Theory of Turbulent Jets*, MIT Press, 1967.
- 7.8-5 *Single Nozzle Spray Analysis*, NP 1344, EPRI Research Project, 1377-3.
- 7.8-6 J.B. Riestler, R.A. Bajura and S.H. Schwatz, *Effects of Water Temperature and Salt Concentration on the Characteristics of Horizontal Buoyant Submerged Jets*, Journal of Heat Transfer, Volume 102, p. 557, August 1980.

7.8.2.2.4 Jet Trajectory

The jet trajectory is now determined by the transformation of s, ψ coordinates to β, z , coordinates, where β and y are measured from the nozzle plane:

$$\frac{d\beta}{ds} = \cos\psi \quad (7.8-38)$$

$$\frac{dz}{ds} = \sin\psi \quad (7.8-39)$$

with the initial condition $s=0$, $\beta=0$, and $z=z_N$, the nozzle elevation.

Integration of the conservation equations is carried out until the jet hits the upper tie plate ($y=0$). At that location, the mass and energy source for TRACG are calculated. The β coordinates of the outer and inner edge of the jet are calculated to give the jet width.

$$b_x = \frac{b}{\sin\psi} \quad (7.8-40)$$

where b is the normal jet width given by

$$\frac{db}{ds} = k \quad (7.8-41)$$

and k is the assumed spread rate. Within this jet width, the assumed profiles for velocity and enthalpy now give the mass distribution at the upper tie plate.

7.8.2.2.5 Jet Distribution

The jet formed by several nozzles all aimed at a particular angle are assumed to form a ring jet enveloped between the extreme trajectories. The assumed velocity distribution now gives the mass distribution at the upper tie plate.

7.8.2.2.6 Ambient Fluid Interaction

The submerged jet interacts with the ambient fluid in which it is discharged. The interaction can be obtained if one writes the jet conservation equations along and normal to the jet trajectory. For the purposes of calculation, the jet is assumed to be in a stagnant environment. The ambient fluid, however, is treated with a line sink along the jet trajectory.

7.8.2.2.7 Source Calculation

For the ambient fluid, the jet forms a line sink. Thus, the jet entrainment is calculated for a TRACG node and used as a mass sink. At the upper tie plate, the assumed distribution is applied to the total mass flow rate $W_o + \Sigma W_{ent}$, where W_o is the injected mass and ΣW_{ent} is the entrained mass. The energy sink and source are calculated as $w_{ent} h_{node}$, where h_{node} is the

Energy:

$$\frac{d}{ds} [v_m (\rho_m - \rho_\infty) (h_m - h_\infty) b A_4 + v_m h_\infty (\rho_m - \rho_\infty) b A_5] \quad (7.8-35)$$

$$+ \frac{d}{ds} [v_m \rho_\infty (h_m - h_\infty) b A_7 + v_m h_\infty \rho_\infty b A_6] = dQ h_\infty$$

The above set of non-linear ordinary differential equations in ψ_m , h_m , b , ψ can be solved by numerical integration.

7.8.2.2.3 Initial Region

At the nozzle exit, the velocity and enthalpy profiles are uniform. Shear layers originating at the edges of the nozzle consume the inner core of uniform properties. These regions are difficult to evaluate because, to some extent, pressure gradients also exist in them. In the traditional analysis, assumptions are made regarding the growth of boundary layer in the initial region that gives the location at which the initial region terminates. Beyond the initial region, there is a transition region after which the fully developed region prevails. In the fully developed region, self-similar profiles for velocity and enthalpy are obtained given by the profiles of the previous section. It is a common observation in heated jets [7.8-4] that the constant velocity core vanishes first and then the constant enthalpy core. This is due to the turbulent mixing length for momentum exchange being larger than the energy exchange. The mixing length for energy exchange is roughly the square root of the Prandtl number times that of momentum exchange. The initial region is thus defined as the point where the constant enthalpy core disappears. This can be determined from the above set of equations by setting $h_m = h_o$, the initial subcooled enthalpy. For the purposes of computation, the buoyancy terms are ignored in the initial region. Thus, the y momentum is ignored completely giving the conservation equations in the form:

Momentum:

$$\rho_o v_o^2 b = v_m^2 (\rho_o - \rho_\infty) b A_1 + v_m^2 \rho_\infty b A_2 \quad (7.8-36)$$

Energy:

$$\rho_o v_o h_o b = v_m (\rho_o - \rho_\infty) b (h_o - h_\infty) A_4 \quad (7.8-37)$$

$$+ v_m h_\infty (\rho_o - \rho_\infty) b A_5 + v_m \rho_\infty (h_o - h_\infty) b A_7$$

$$+ v_m h_\infty \rho_\infty b A_6$$

These sets of equations give the value v_m and b at the location where the constant enthalpy core disappears. Assuming a spread rate of $b=k\beta$, then the length of the initial region can be determined when b is calculated.

Energy:

$$\begin{aligned}
 & \frac{d}{ds} \left[v_m (\rho_m - \rho_\infty)(h_m - h_\infty) b \int_0^1 \eta f \phi dy^* \right] \\
 & + \frac{d}{ds} \left[v_m (\rho_m - \rho_\infty) h_\infty b \int_0^1 \eta f dy^* \right] \\
 & + \frac{d}{ds} \left[v_m (h_m - h_\infty) \rho_\infty b \int_0^1 \phi f dy^* \right] \\
 & + \frac{d}{ds} \left[v_m \rho_\infty h_\infty b \int_0^1 f dy^* \right] = dQ h_\infty
 \end{aligned} \tag{7.8-30}$$

where

$$y^* = \frac{y}{b} \tag{7.8-31}$$

Denoting these integrals as $A_1, A_2, A_3, A_4, A_5, A_6,$ and $A_7,$ one gets:

Mass:

$$\frac{d}{ds} [v_m (\rho_m - \rho_\infty) b A_5 + v_m \rho_\infty b A_6] = dQ \tag{7.8-32}$$

Momentum s :

$$\frac{d}{ds} [v_m^2 (\rho_m - \rho_\infty) b A_1 + v_m^2 \rho_\infty b A_2] = (\rho_m - \rho_\infty) g \sin \psi A_3 \tag{7.8-33}$$

Momentum ψ :

$$\frac{d\psi}{ds} [v_m^2 (\rho_m - \rho_\infty) b A_1 + v_m^2 \rho_\infty b A_2] = (\rho_m - \rho_\infty) g \cos \psi A_3 \tag{7.8-34}$$

7.8.2.2.2 Solution Procedure

The solution to the above set is sought by assuming known velocity, density and enthalpy profiles of the form:

$$\frac{\rho - \rho_\infty}{\rho_m - \rho_\infty} = \eta \left(\frac{y}{b} \right) \tag{7.8-24}$$

$$\frac{v}{v_m} = f \left(\frac{y}{b} \right) \tag{7.8-25}$$

$$\frac{h - h_\infty}{h_m - h_\infty} = \phi \left(\frac{y}{b} \right) \tag{7.8-26}$$

Substituting these in the above momentum equations gives

Mass:

$$\frac{d}{ds} \left[v_m (\rho_m - \rho_\infty) b \int_0^1 \eta f dy^* + v_m \rho_\infty b \int_0^1 f dy^* \right] = dQ \tag{7.8-27}$$

Momentum s:

$$\begin{aligned} \frac{d}{ds} \left[v_m^2 (\rho_m - \rho_\infty) b \int_0^1 \eta f^2 dy^* + v_m^2 \rho_\infty b \int_0^1 f^2 dy^* \right] \\ = (\rho_m - \rho_\infty) g \sin \psi \int_0^1 \eta dy^* \end{aligned} \tag{7.8-28}$$

Momentum ψ :

$$\begin{aligned} \frac{d\psi}{ds} \left[v_m^2 (\rho_m - \rho_\infty) b \int_0^1 \eta f^2 dy^* + v_m^2 \rho_\infty b \int_0^1 f^2 dy^* \right] \\ = (\rho_m - \rho_\infty) g \cos \psi \int_0^1 \eta dy^* \end{aligned} \tag{7.8-29}$$

Momentum:

$$\frac{d}{dx} \left[\int_0^b \rho v^2 dy \right] = \int_0^b (\rho - \rho_\infty) g dy \quad (7.8-18)$$

Energy:

$$\frac{d}{dx} \left[\int_0^b \rho v h dy \right] = h_\infty \frac{d}{dx} \left[\int_0^b \rho v dy \right] \quad (7.8-19)$$

Writing this in a system of coordinates along and normal to the trajectory we have

Mass:

$$\frac{d}{ds} \left[\int_0^b \rho v dy \right] = dQ \quad (7.8-20)$$

Momentum s:

$$\frac{d}{ds} \left[\int_0^b \rho v^2 dy \right] = \int_0^b (\rho - \rho_\infty) g \sin\psi dy \quad (7.8-21)$$

Momentum ψ :

$$\frac{d\psi}{ds} \left[\int_0^b \rho v^2 dy \right] = \int_0^b (\rho - \rho_\infty) g \cos\psi dy \quad (7.8-22)$$

Energy:

$$\frac{d}{ds} \left[\int_0^b \rho v h dy \right] = h_\infty \frac{d}{ds} \left[\int_0^b \rho v dy \right] \quad (7.8-23)$$

If the level of the liquid rises above the nozzles, the injected liquid forms a submerged jet. The transition between submerged jet and spray is modeled as a linear interpolation in the model. This is done to avoid discontinuities.

$$z_L < z_N - 1.1d_N \quad \text{Spray Distribution}$$

$$z_L > z_N + 1.1d_N \quad \text{Jet Distribution}$$

Here z_L is the two-phase mixture level, z_N is the nozzle elevation, and d_N is the nozzle diameter. In between these two, a linear interpolation in distribution is obtained. Thus:

$$S = S_{\text{jet}} \frac{z_L - z_N + 1.1d_N}{2.2 d_N} + S_{\text{spray}} \frac{z_N - z_L + 1.1d_N}{2.2 d_N} \quad (7.8-16)$$

If a two-phase level is not calculated, a similar criterion is arrived at using the void fraction. The transition is fixed at $\alpha = 0.75$ at the sparger elevation.

7.8.2.2 Submerged Jet Model

If the liquid level in the upper plenum rises above the sparger level, the injected liquid from the nozzles forms a submerged jet. The submerged jet model is analyzed by utilizing the basic conservation equations of motion written in an orthogonal system of coordinates along and normal to the trajectory. These are integrated over the jet width using an assumed velocity profile. A jet spread rate is also assumed. The location at which the jet from a set of nozzles terminates on the upper tie plate is then calculated. Knowing the jet width, the angle at which it hits the tie plate and the profiles of velocity and enthalpy, one can calculate the distribution due to a set of spray nozzles. The source S due to different sets is then linearly superimposed.

The method of analysis closely follows that outlined by Abromovich [7.8-4]. The integral methods are reasonably accurate and very fast compared to the differential methods, and are deemed to be sufficiently accurate for this analysis.

7.8.2.2.1 Basic Conservation Equations

The basic conservation equations of mass continuity, momentum and energy for a submerged jet are in (steady-state) integral form [7.8-6].

Mass:

$$\frac{d}{dx} \left[\int_0^b \rho v dy \right] = dQ \quad (7.8-17)$$

7.8.2.1.3 Spray Distribution

The above distribution (Equation 7.8-10) has to satisfy the total spray rate plus the condensed liquid. Thus:

$$\int \frac{q_m}{2} \left(1 + \cos\left(\frac{\pi y}{b}\right) \right) \frac{dy}{b} = W + W_c \quad (7.8-11)$$

7.8.2.1.4 Heat Transfer

Tests indicate that spray drops reach saturation temperature within five to six nozzle diameters. Thus, in the analysis spray drops are assumed to reach saturation temperature in the first node, since the TRACG node is generally much larger than the nozzle diameter. It is also assumed that sufficient steam is available for the droplets to reach saturation temperature.

7.8.2.1.5 Source Calculation

The steam condensed can be calculated by bringing the total injected liquid from inlet enthalpy to saturation. Thus:

$$W_c = \frac{W (h_f - h_{fo})}{h_{fg}} \quad (7.8-12)$$

This is treated as a vapor sink at the node where spray is injected. The total mass of injected liquid plus the condensed mass is now distributed at the upper tie plate by Equation 7.8-10. Then the source for a particular TRACG node i from a set of spray nozzles j above the tie plate or a two-phase level between r coordinate given by r_i and r_{i+1} is:

$$S_{ij} = \int_{r_i}^{r_{i+1}} q_m \left(1 + \cos\left(\frac{\pi y}{b}\right) \right) dr \quad (7.8-13)$$

The sources from various ring jets are now combined:

$$S_i = \sum_j S_{ij} \quad (7.8-14)$$

In case the spray overshoots the centerline, a reflection with respect to the central plane gives the distribution. Mathematically,

$$S_i' = S_i + S_{-i} \quad (7.8-15)$$

The distribution of spray beyond the centerline is symmetrically reflected and added. In case of a solid wall, like in the sector test hardware, the distributions beyond the centerline are added and input in the central node.

The initial conditions are:

$$\begin{aligned}
 v &= v_0 && \text{for } s = 0 \\
 \psi &= \theta_0 - \phi_0 / 2 && \text{for the outer trajectory} \\
 \psi &= \phi_0 && \text{for the middle trajectory} \\
 \psi &= \theta_0 + \phi_0 / 2 && \text{for the inner trajectory}
 \end{aligned}$$

It is assumed implicitly here that the injected liquid shatters in the form of uniform sized droplets at a short distant from the nozzle exit.

The above ordinary differential equations are integrated along the trajectory to give the velocity and trajectory angle at every spatial location. However, in order to determine the location at which the trajectory terminates on the upper tie plate, the following equations are solved:

$$\frac{dz}{ds} = \sin\psi \tag{7.8-8}$$

$$\frac{dx}{ds} = \cos\psi \tag{7.8-9}$$

with the initial condition that

$$\begin{aligned}
 z &= z_N \quad \text{for } s = 0, \text{ and } z_N \text{ is the elevation of the nozzle.} \\
 \beta &= 0 \quad \text{for } s = 0
 \end{aligned}$$

The trajectory is thus started at the nozzle exit. A combined solution of the equations defined by Equations 7.8-6 to 7.8-9 gives the location of the trajectory above the tie plate. Each trajectory is terminated when $y=0$. The β coordinate at the upper tie plate or two-phase level determines the spray width. Between the spray extremities, the mass flux is assumed to be Gaussian distributed. Since Gaussian distribution extends to infinity, for the purpose of calculation this was replaced with a cosine fit given by:

$$\frac{q}{q_m} = \frac{1}{2} \left(1 + \cos\left(\frac{\pi y}{b}\right) \right) \tag{7.8-10}$$

where y is the location along the mid trajectory and b the corresponding spray width, q is the spray flow rate at a location. The boundary conditions of $q=q_m$ at $y=0$ and $q=0$ at $y=b$ are automatically satisfied.

distributed sources and sinks, which, when summed together, gives the total mass of the injected liquid. Turbulence can be modeled by a simple mixing length hypothesis. This is appropriate due to the uncertainty of the more sophisticated models in two-phase flows, and the coarse nodalization. Descriptions of the spray, jet and the gross motion of the upper plenum pool are described in the following section.

7.8.2.1 Spray Model

If the liquid level in the upper plenum falls below the spray level, the injected liquid from the nozzles form a spray. Spray systems are complex to analyze, but single sprays have been studied extensively in the literature both by experimental and analytical techniques. Most analytical studies confine themselves to the study of individual spray drops of a uniform size. In a real spray, particles vary in size and either an average diameter or Sauter Mean Diameter (SMD) are used to describe the spray characteristics [7.8-5]. Heat transfer to spray drops is analyzed based on conduction heat transfer. There are also some studies following a field approach where droplets are assumed to form a continuum with the ambient liquid. Preliminary work undertaken with this approach proved to be very inconvenient because of a need to describe the jet growth and the prediction of a distorted trajectory. Consequently, this approach was abandoned in favor of the droplet approach.

7.8.2.1.1 Droplet Size

In the referenced literature, several empirical correlations are available for describing the mean droplet size [7.8-5]. Since these empirical correlations are fitted to specific nozzle geometries, a more general correlation based on the critical Weber Number criterion is used in TRACG:

$$We = \frac{\rho_v v_r^2 d}{s} \quad (7.8-5)$$

7.8.2.1.2 Spray Trajectory

The spray trajectory is determined by the paths of droplets emanating at the extremities of the distribution. If the nozzle inclination to the horizontal is θ_0 , and the initial spray cone angle, ϕ_0 , then the outer, middle and inner extremity droplets are aimed at $\theta_0 - \phi_0 / 2$, θ_0 , and $\theta_0 + \phi_0 / 2$, respectively, to the horizontal. The spray emanating from all nozzles aimed at a particular angle θ_0 is combined to form a ring spray source.

The relevant equations of motion of a droplet in terms of coordinates parallel to the trajectory and normal to it are:

$$v \frac{dv}{ds} = -g \sin \psi - C_D \frac{3}{4} \frac{|v| v}{d} \frac{\rho_v}{\rho_l} \quad (7.8-6)$$

$$v^2 \frac{d\psi}{ds} = -g \cos \psi \quad (7.8-7)$$

coordinates. The jets and sprays cannot be described adequately by this system of coordinates. In this sense, the analysis carried out in this work resembles that of singular perturbation analysis in Boundary Layer theory [7.8-1] that is so well developed. In that analysis, a fine grid is adopted for the boundary layer scaled by the local boundary layer thickness, and a coarse grid is adopted for the external flow scaled by the main geometric dimensions. The two flows are then matched asymptotically at their boundaries. In the present analysis, a similar approach is undertaken.

In the present model, the entrainment of vapor by the spray is neglected. The effect of this may be an underprediction of the spray penetration for high pressure. In the submerged regime where the liquid phase is continuous, the gross motion of the liquid in the upper plenum is modeled taking into account turbulence mixing (Section 6.7) and jet entrainment [7.8-2]. After calculating the submerged jet regime, the entrainment of the ambient liquid due to the injected jet is calculated for each TRACG node. The upper plenum liquid motion is then calculated with the jet entrainment treated as a line sink.

The spray nozzles are mounted on a sparger pipe, located at the periphery of the upper plenum, usually in two or three sets each aimed at a particular angle so as to more evenly distribute the liquid spray over the core. It is assumed in the model that the injected liquid from any one set of nozzles will coalesce downstream of the nozzles and form a sheet or ring jet. Any interaction between the different ring jets formed by nozzle sets aimed at different angles is assumed to be negligible in the present model.

In the spray regime, the motion of droplets in the upper plenum is predicted. An empirical correlation for the mean droplet size is utilized. Depending on the initial spray velocity, the trajectories of mean, outer and innermost droplets are calculated for each nozzle. Between the outer and inner extremities of the spray, Gaussian distribution for the flux profile is utilized. With this profile and the calculated spray width, the source distribution at the upper tie plate or the two-phase level is calculated as a function of radius from the center. From this distribution, the mass source for each TRACG node at the upper tie plate or the two-phase level is calculated. The spray reaches saturation temperature in a short distance from the nozzle exit, usually a few nozzle diameters [7.8-3]; therefore, the spray is assumed to be saturated at the time it reaches the upper tie plate or the two-phase level.

In the submerged jet regime, the basic conservation equations of mass, momentum and energy are written in an integral form [7.8-4] in an orthogonal system of coordinates coinciding with the jet trajectory and normal to it. The jet spread rate is assumed to be the same as an undeflected jet. The properties of the jet such as entrainment, velocity and enthalpy distribution and the jet trajectory are also simultaneously calculated. The location at which the jet terminates at the upper tie plate and the mass source distribution at the tie plate is calculated.

The motion generated in the ambient fluid is mainly due to the entrainment effects of the injected liquid. As described, the ambient upper plenum is analyzed using the entrainment as a line sink. Where the jet terminates on the upper tie plate, the calculated jet mass distribution is added as a source distribution. Thus, the effects of the injected jet are treated by a system of

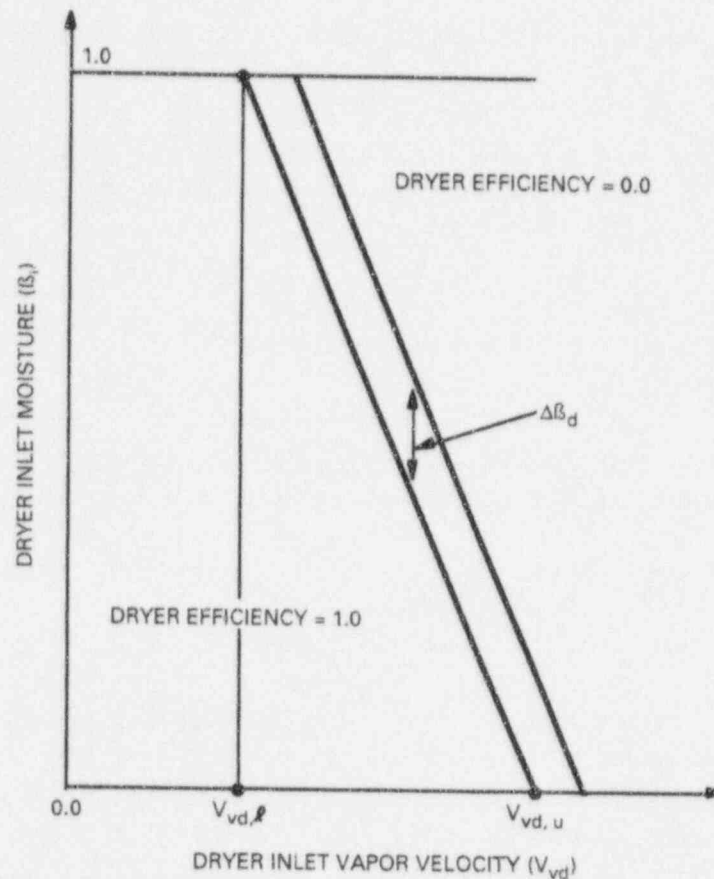


Figure 7.8-5. Dryer Efficiency Summary

7.8.2 Upper Plenum Model

One of the means of mitigating the severity of a postulated LOCA in a BWR is to inject subcooled water through the Emergency Core Cooling System (ECCS). Depending on the design, the emergency core cooling systems can include both the High Pressure Core Spray System (HPCS) and the Low Pressure Core Spray System (LPCS). This section describes a model for the HPCS and the LPCS, which are injected into the upper plenum.

At the time of core spray initiation, the core spray nozzles could be submerged in a two-phase mixture, in which case the injected liquid forms a submerged jet. If the two-phase mixture is below the nozzle elevation, then a spray forms downstream of the nozzles. The physical processes underlying spray and jet formation are different and are thus formulated separately.

For a realistic system transient calculation by TRACG, there is a practical upper limit for the system nodalization. The upper plenum, being a three-dimensional component in the system, would be nodalized rather coarsely in comparison with the size of the nozzles. For an accurate calculation of the jets and sprays, one needs a fine mesh size along the trajectory of the jet and normal to it. Prediction of the gross motion in the plenum requires cylindrical noding

The range of dryer inlet moisture over which the dryer efficiency degrades is a user input constant. The default value of $\Delta\beta_d$ is 0.05 in TRACG.

The dryer inlet moisture is determined from the donor void fraction assuming homogeneous flow at the dryer face and is given by:

$$\beta_i = 1 - \frac{\alpha}{\alpha + (1 - \alpha) \left[\frac{\rho_\ell}{\rho_v} \right]} \quad (7.8-3)$$

where ρ_l and ρ_v are the donor liquid and vapor densities, respectively.

Finally, the critical dryer inlet moisture is given as a linear function of the vapor velocity at the dryer face and is given by:

$$\begin{aligned} \beta_{i,crit} &= 1.0 \quad \left[\text{for } v_{vd} < v_{vd,\ell} \right] \\ \beta_{i,crit} &= 1.0 - \frac{v_{vd} - v_{vd,\ell}}{v_{vd,u} - v_{vd,\ell}} \quad \left[\text{for } v_{vd,\ell} < v_{vd} < v_{vd,u} \right] \\ \beta_{i,crit} &= 0.0 \quad \left[\text{for } v_{vd,u} < v_{vd} \right] \end{aligned} \quad (7.8-4)$$

where

- v_{vd} = Vapor velocity at dryer face
- $v_{vd,\ell}$ = Lower dryer vapor velocity (Figure 7.8-5)
- $v_{vd,u}$ = Upper dryer vapor velocity (Figure 7.8-5)

The lower dryer vapor velocity is the dryer inlet vapor velocity below which the dryer efficiency is 100% regardless of dryer inlet moisture. The upper dryer vapor velocity is the dryer inlet vapor velocity above which the dryer efficiency is less than 100% regardless of dryer inlet moisture. The dryer efficiency relationships are summarized in Figure 7.8-5.

The lower and upper dryer velocity are estimated from data [7.7-3] as 0.25 and 1.2 m/s, respectively. Dryer performance tests were performed at normal operating pressure with flow rates covering from 25 kg/sec to 51 kg/sec per separator.

$$K_{SD} = \frac{2\rho_v \Delta P_{SD}}{\left(\frac{W_v}{A_{SD}}\right)^2} \quad (7.8-1)$$

where

- ρ_v = Vapor density
- W_v = Steam flow through the dryer
- A_{SD} = Dryer flow area
- ΔP_{SD} = Pressure drop in the dryer

The separation of moisture from the steam flow in the dryer is simulated by imposing a large liquid resistance in the axial direction at the cell boundary between the steam dome and the dryer.

The separation efficiency of the dryer depends on the vapor velocity and the moisture content of the steam flow entering the dryer (Figure 7.8-5). For a given inlet vapor velocity, there corresponds a critical dryer inlet quality. Good moisture separation is achieved if the dryer inlet quality is below the critical value. If the inlet moisture is above the critical value, the dryer capacity is exceeded and the moisture would pass through the dryer.

The dryer efficiency is computed by comparing the dryer inlet moisture to a critical dryer inlet moisture. The dryer efficiency is 100% if the dryer inlet moisture is below the critical dryer inlet moisture and is zero if the dryer inlet moisture exceeds the critical inlet moisture by a user-defined amount, $\Delta\beta_d$. The dryer efficiency is linearly interpolated between these two extremes based on the dryer inlet moisture. The dryer efficiency is given by:

$$\begin{aligned} \eta_D &= 1.0 && \text{for } \beta_i < \beta_{i,crit} \\ \eta_D &= 1.0 + \frac{\beta_{i,crit} - \beta_i}{\Delta\beta_d} && \text{for } \beta_{i,crit} < \beta_i < \beta_{i,crit} + \Delta\beta_d \\ \eta_D &= 0.0 && \text{for } \beta_i > \beta_{i,crit} + \Delta\beta_d \end{aligned} \quad (7.8-2)$$

where

- η_D = Dryer efficiency
- β_i = Dryer inlet moisture
- $\beta_{i,crit}$ = Critical dryer inlet moisture
- $\Delta\beta_d$ = Range of dryer inlet moisture over which efficiency degrades from 100% to 0%

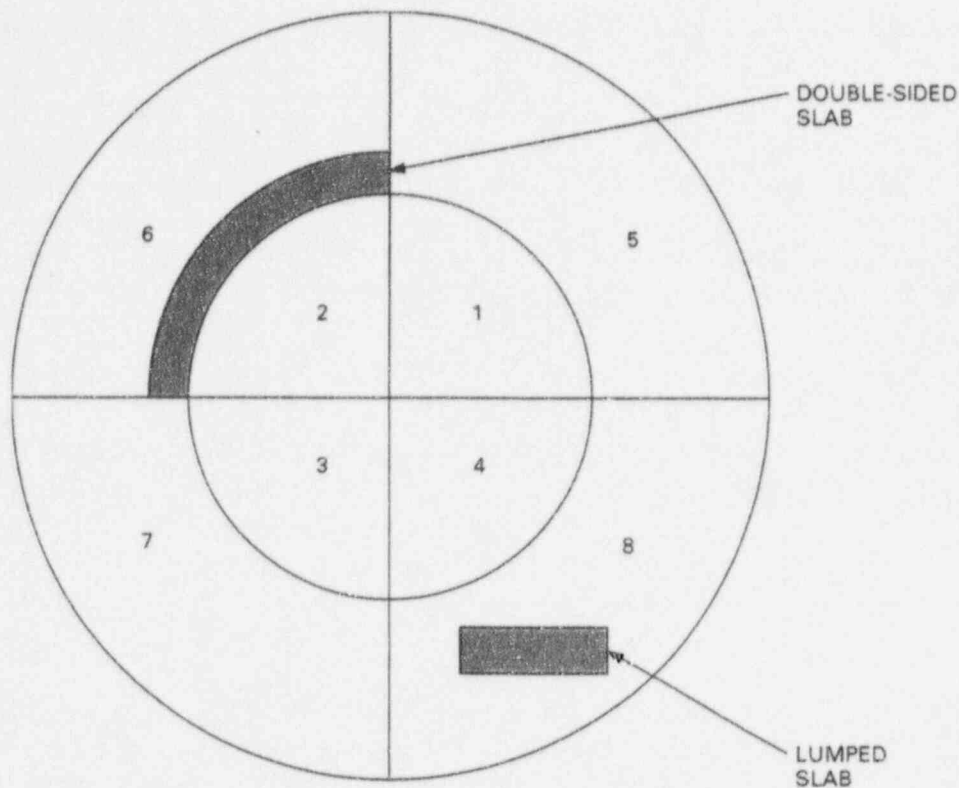


Figure 7.8-4. Sample Geometry for Double-Sided Heat Slab

The user specifies the inside surface area, thickness, and material type for the double slab associated with each vessel cell. If the double slab area for a particular cell is input as zero, no double slab is assumed to exist for that cell. The double slab material properties (density, specific heat, and thermal conductivity) are evaluated separately for each conduction heat transfer node within a double slab, these properties being evaluated at the mean temperature for each node. The number of conduction heat transfer nodes within the double slabs is specified by the user, and the same value is used for all double slabs.

7.8.1 Steam Dryer

The steam dryer is structured as an integral part of the pressure vessel. The characteristics of the steam dryer to be modeled are the dryer pressure drop and further separation of moisture in the steam flow from the steam separator.

The pressure drop is simulated by a flow resistance to the steam flow at the cell boundary between the steam dome and dryer. By imposing the appropriate loss factor on the vapor phase in the axial direction, the pressure drop in the dryer is correctly determined. The loss factor K_{SD} for the dryer is defined as:

The reactor core region in the vessel is specified by the upper, lower, and radial core positional parameters (ICRU, ICRL, and ICRR). These parameters define, respectively, the upper, lower, and radial boundaries of the cylindrical core region. The example provided in Figure 7.8-3 shows a possible configuration in which $ICRU = 4$, $ICRL = 2$, and $ICRR = 3$. Each mesh cell stack in the core region contains a channel component to simulate the fuel bundles in that core region. The flow into this core bypass region is calculated based on the leakage flow model described in Section 7.5.1. The bypass fluid properties associated with each channel are used in the kinetics calculations described in Section 9.

A very important aspect of this three-dimensional vessel component is that it results in a multidimensional hydraulic model of regions within a BWR vessel in which multidimensional effects may be important. For example, an important aspect of BWR LOCA analysis is the emergency core coolant spray (ECCS) into the upper plenum. The noding diagram in Figure 7.8-3 results in a model in which the radial distribution of ECCS water in the upper plenum is represented by three vessel radial rings. The solution to the conservation equations in that region plus the coupled solutions for the conservation equations in the core bypass, channels, separators, and in ECC spray connections results in a radial distribution of ECC water in the upper plenum.

Heat slabs of arbitrary masses and volumes can be defined in any mesh cell (including core regions) to model that heat capacity of structures within the vessel. A heat transfer coefficient is computed for each slab using the local fluid conditions. The temperature calculation is based on a lumped-parameter model (Section 4).

In addition to the lumped-parameter heat model, a double-sided heat slab model is available to permit accurate modeling of heat conduction through cylindrical structures found within a BWR vessel. The double-sided heat slab (double slab) model will allow the user to model heat conduction through a surface separating two different vessel radial or axial regions. Double slabs may also be used to model the release of stored energy from the reactor vessel wall. In this case, the outside surface of the double slab will not connect to a vessel region but will use boundary conditions specified by the user.

Two double-sided heat slabs may be associated with each fluid cell on each vessel axial level. These double slabs are considered to lie on the outside radial surface and upper axial surface of their associated fluid cell, as shown in Figure 7.8-4. In this figure, the outside surface of the double-sided heat slab associated with fluid Cell 2 is actually in contact with fluid Cell 6. A double-sided slab on the axial surface of Cell 2 would be in contact with fluid Cell 2 in the level above. Heat transfer coefficients for both sides of a double-sided heat slab are calculated, using the appropriate old-time fluid conditions from the fluid cells on each side of the heat slab. The liquid and vapor temperatures from the appropriate fluid cells are used in calculating the heat flux on each surface of the double slab. If the double slab lies on the outside surface of the vessel, the external heat transfer coefficients and fluid temperatures are set equal to values supplied by the user. Energy source terms are included in the energy equation for the fluid cells on each side of the double slab to account for energy transfer from the slab.

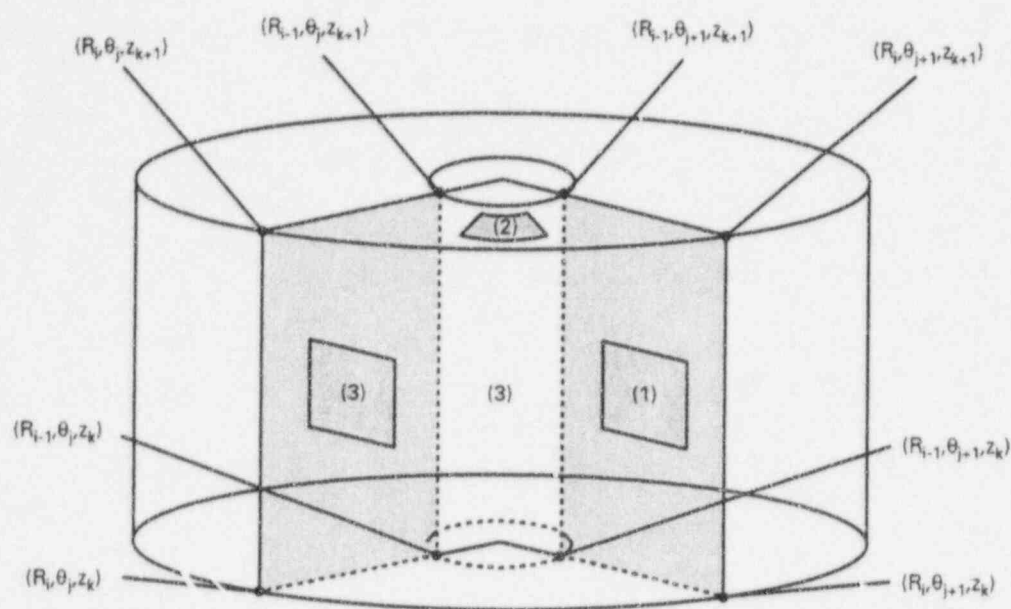


Figure 7.8-1 Boundaries of a Three-Dimensional Mesh Cell.
 (The face-numbering convention is also shown.
 Faces, 1, 2, and 3 are in the θ , z , and R directions,
 respectively.)

Plumbing connections from other components to the vessel are made on the faces of the mesh cells. Any number of connections may be made to the vessel; in fact, any mesh cell in the vessel can have one component or more connected to it. Five input parameters are used to describe a connection: ISRL, ISRC, ISRF, JUNS and ZJUN. The parameter ISRL defines the axial level in which the connection is made; ISRC is the mesh-cell number, as defined above; and ISRF is the face number, as defined in Figure 7.8-1. If ISRF is positive, the connection is made on the face shown in the figure with the direction of positive flow into the cell. The parameter JUNS is the system function number used to identify this function. The parameter ZJUN specifies the axial location of the connection expressed as a fraction of the level height. Internal and external connections are allowed. The user is cautioned against connecting to the vessel any component with a flow area that differs greatly from the flow area of the mesh-cell face to which it is connected because this can cause anomalous pressure gradients. Such a situation can be avoided by proper adjustment of the vessel geometry coordinate spacings and/or the use of taper or expansion sections on one-dimensional components prior to the vessel connections.

7.8 Vessel

The vessel (VSSL) component employs a three-dimensional, two-fluid, thermal-hydraulic model in cylindrical coordinates to describe the vessel flow. For modeling a BWR reactor vessel, a regular cylindrical mesh, with variable mesh spacings in all three directions, encompasses the downcomer, core bypass, and upper and lower plenums of the vessel. The user describes the mesh by specifying the radial, angular, and axial coordinate of the mesh-cell boundaries:

$$R_i \quad i = 1, \dots, \text{NRSX}$$

$$\theta_j \quad j = 1, \dots, \text{NTSX}$$

and

$$z_k \quad k = 1, \dots, \text{NASX}$$

where NRSX is the number of rings, NTSX is the number of angular segments, and NASX is the number of axial levels. The point (R_i, θ_j, z_k) is a vertex in the coordinate mesh. Mesh cells are constructed and identified by an axial level number and a cell number. For each axial level, the cell number is determined by counting the cells radially outward starting with the first angular segment and the innermost ring of cells (Figure 7.8-1). Figure 7.8-1 shows the relative face-numbering convention for an individual cell that is used in connecting other components to the vessel.

NOTE: Only three faces must be identified per mesh cell because the other faces will be defined by neighboring cells.

All fluid flow areas (on cell faces) and all fluid volumes are dimensioned so that the internal structure within the vessel can be modeled. Flow areas and fluid volumes are computed based on the geometric mesh spacings and scaled according to factors supplied as input. The scaled volumes and flow area are then used in the fluid-dynamics and heat-transfer calculations. Flow restrictions and the volume occupied by the structure within each mesh cell are modeled through use of these scale factors. For example, the downcomer walls are modeled by setting the appropriate flow area scale factors to zero. Flow restrictions such as the top and bottom core support plates require scale factors between zero and one.

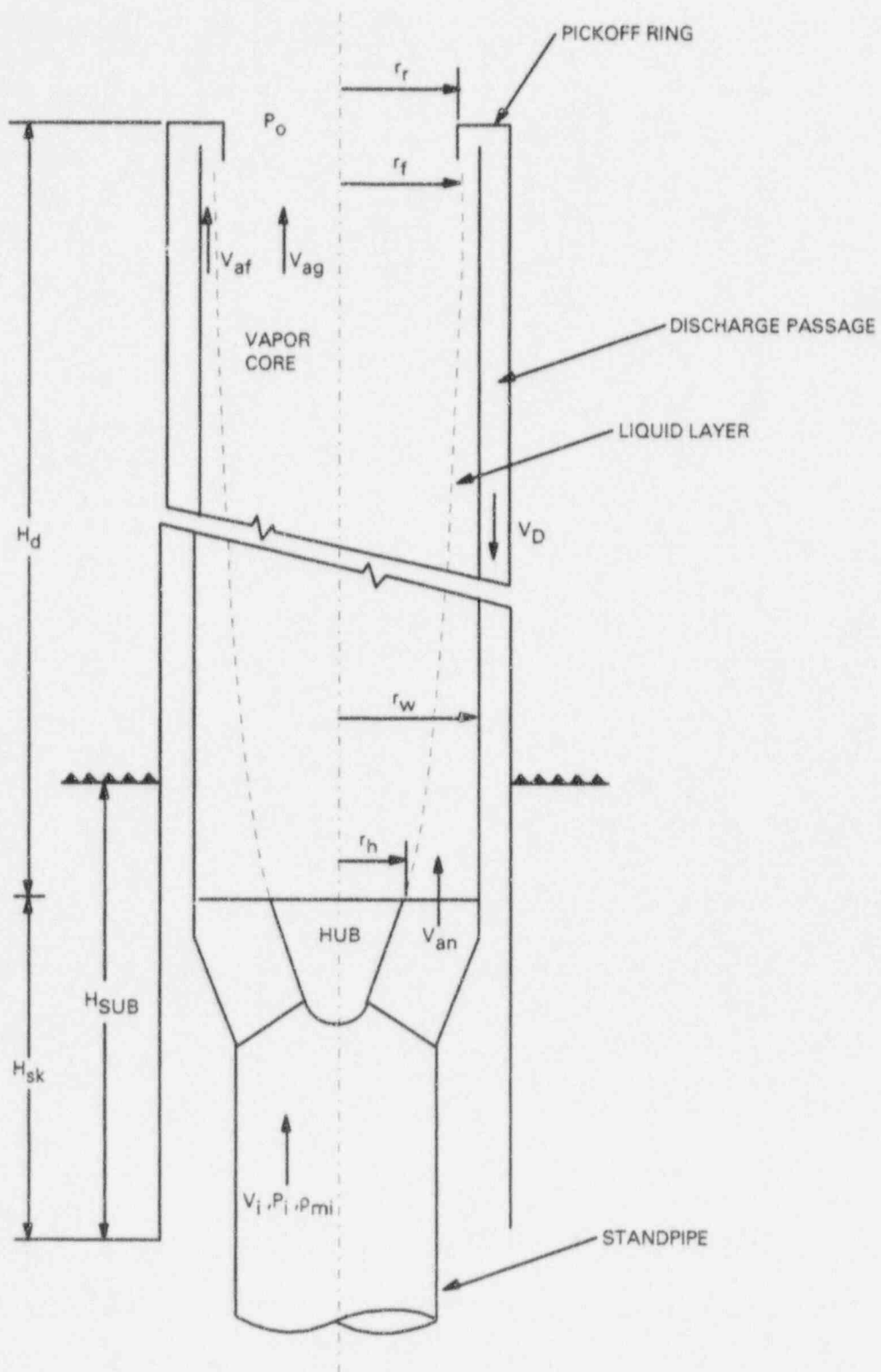


Figure 7.7-2. Schematic of the Separator Model

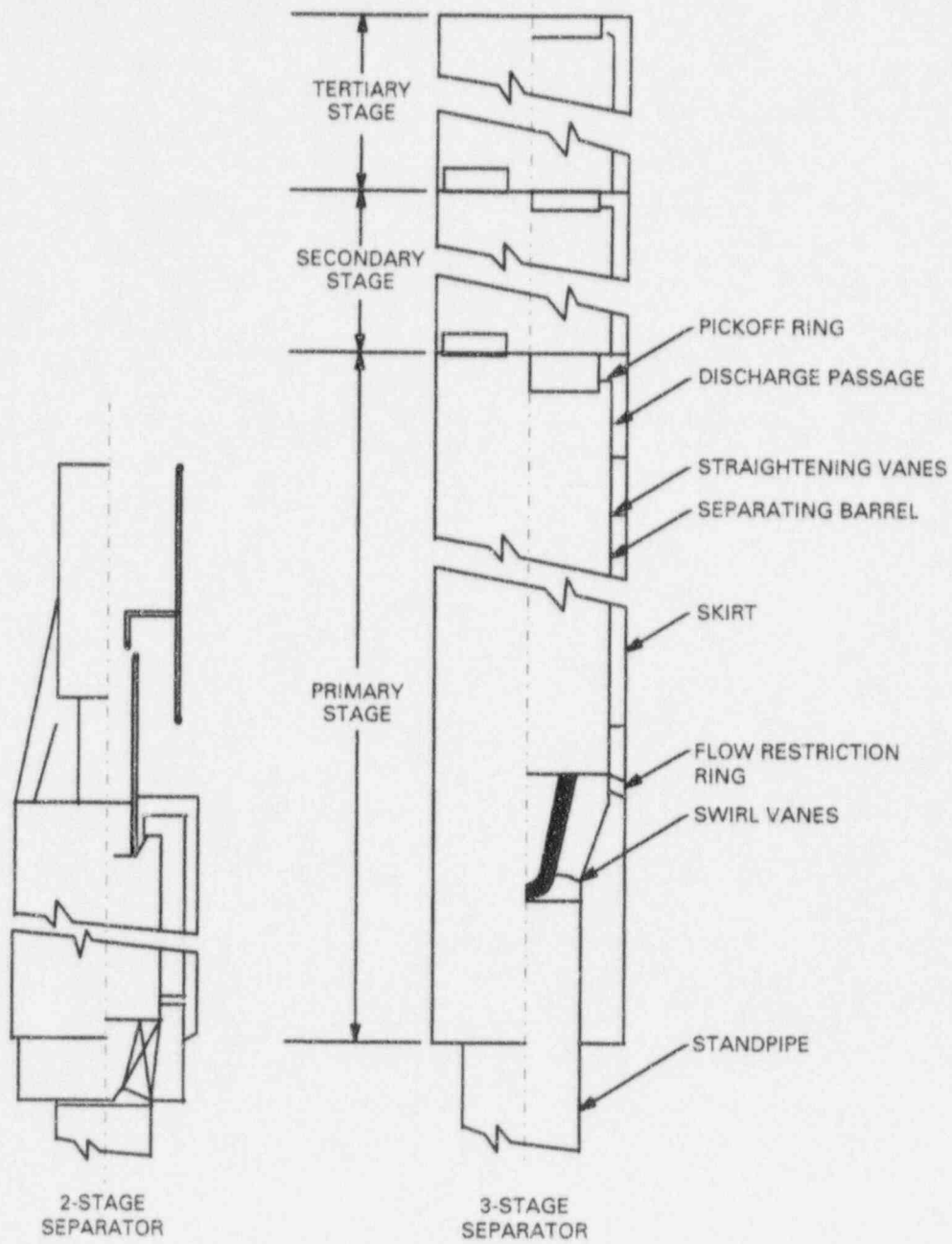


Figure 7.7-1. Typical Types of Steam Separators

7.7.4 Assessment

Full-scale performance test data for two-stage and three-stage steam separators are reported in References 7.7-3 through 7.7-5. These tests were performed at full scale conditions and provided carryunder, carryover and pressure drop data for a wide range of inlet conditions.

The steam separators are designed to have the best performance under normal operating conditions, in the range of 10% inlet quality for two-stage and 12% inlet quality for three-stage separators. Both carryunder and carryover are at their minimum values around the normal operating conditions for two-stage and three-stage separators.

**Table 7.7-1
Summary of Parameters Used in the Separator Model**

2-Stage Separator			3-Stage Separator		
Parameter	1st	2nd	1st	2nd	3rd
AA	110.	20.	110.	20.	20.
BB	0.5	0.25	0.5	0.25	0.55
CC	0.0004	Not used	0.0004	Not used	Not used
DD	0.009	Not used	0.11	Not used	Not used

7.7.5 References

- 7.7-1 Crane Company, *Flow of Fluids Through Valves, Fittings, and Pipe*, Technical Paper No. 410, Crane Company, New York.
- 7.7-2 H. Schlichting, *Boundary Layer Theory*, McGraw-Hill, New York.
- 7.7-3 R.H. Moen, et. al., *Advances in Boiling Water Reactor Steam Separator Systems*, ASME 69-WA/NE-5, November 1969.
- 7.7-4 E.L. Burley, *Performance of Internal Steam Separator System in Boiling Water Reactors*, ASME 69-WA/NE-24, November 1969.
- 7.7-5 S. Wolf, and R.H. Moen, *Advances in Steam-Water Separators for Boiling Water Reactors*, ASME 73-WA/PWR-4, November 1973.

pool surrounding the separators. The amount entrained is proportional to the drag force which is proportional to the square of the downward water velocity (or water flow). It is assumed that the second part is proportional to the square of the total water flow discharged from the second and higher stages, i.e.:

$$(W_{g,cu})_{total} = [W_{g,cu}]_1 + CC \left[\sum_{i=2}^N (W_{f,cu})_i \right]^2$$

where

$$\begin{aligned} N &= 2 \text{ for 2-stage separator} \\ &= 3 \text{ for 3-stage separator} \end{aligned}$$

and CC is a proportional constants to be determined from data.

The total water that is carried over consists of two parts. The first part is the water flow through the last stage. The second part is the water flow entrained by the upward steam flow discharged from the second and higher stages through the discharge passage. Similarly, the second part is assumed to be proportional to the square of the total steam flow discharged from higher stages, i.e.:

$$(W_{f,co})_{total} = [W_{f,co}]_N + DD \left[\sum_{i=2}^N (W_{g,co})_i \right]^2$$

where DD is a proportionality constant determined from data.

The carryunder and carryover are defined as follows:

$$CU = \frac{[W_{g,cu}]_{total}}{\text{Total Downward Water Flow}}$$

$$CO = \frac{[W_{f,co}]_{total}}{\text{Total Upward Steam Flow}}$$

Full scale performance test data for two-stage and three-stage steam separators are reported in References 7.7-3 to 7.7-5. In calculating these test conditions, it was determined that the parameters AA, BB, CC and DD with values summarized in Table 7.7-1 would yield good predictions.

Assuming homogeneous flow in the discharge passage, the mean void fraction is:

$$\alpha_{cu} = \frac{W_{g,cu}}{W_{g,cu} + W_{f,cu}(\rho_g / \rho_f)}$$

the mean discharge density is:

$$\rho_{m,D} = \alpha_{cu}\rho_g + (1 - \alpha_{cu})\rho_f$$

and the mean discharge velocity is:

$$v_D = \frac{W_D}{\rho_{m,D}A_D}$$

In summary, for given nozzle inlet conditions (P_i , x_i , and W_i) the unknowns (v_{ag} , v_{af} , C , r_f , P_o , and P_w) are calculated by solving Equations 7.7-5 to 7.7-10 simultaneously.

Similar equations can be written for the second and third stages. It is assumed that P_o is uniform axially (i.e., the vapor core pressure drop in the axial direction is small); therefore, the axial momentum equations can be neglected in the calculations. For these stages, the unknowns are reduced to v_{ag} , v_{af} , C , r_f , and P_w , and the equations are the conservation of liquid mass, vapor mass, and angular momentum, the pressure drop across the water layer, and the pressure drop in the discharge passage.

The right-hand sides of Equations 7.7-5, 7.7-6, and 7.7-7 represent the water flow, vapor flow, and angular momentum, respectively, entering the separating barrel. For the second and third stages, these terms are modified as follows:

$$(\text{Water flow})_{in} = [W_{f,co}]_{\text{previous stage}}$$

$$(\text{Steam flow})_{in} = [W_{g,co}]_{\text{previous stage}}$$

$$(\text{Angular momentum})_{in} = \left[\int_0^{r_f} v_i (2\pi r dr \rho v_a) \right]_{\text{previous stage}}$$

7.7.3 Carryunder and Carryover

The total vapor flow that is carried under consists of two parts. The first part is the steam flow through the first discharge passage with exit below the surface of the water pool surrounding the separators. The second part is the steam entrained by the total downward water flow which is discharged from second and higher stages with exit above the surface of the water

For the discharge passage [7.7-2],

$$C_F = \frac{0.079}{Re^{0.25}}$$

The steam and water flows discharged through the discharge passage are calculated as follows:

$$W_{g,cu} = \int_{r_r}^{r_w} \alpha \rho_g v_a 2\pi r dr$$

$$W_{f,cu} = \int_{r_r}^{r_w} (1 - \alpha) \rho_f v_a 2\pi r dr$$

for $r_f < r_r$

$$W_{g,cu} = \pi \rho_g v_{af} a (r_w - r_r)^2$$

$$W_{f,cu} = \pi \rho_f v_{af} \left[(r_w^2 - r_r^2) - a (r_w - r_r)^2 \right]$$

For $r_r < r_f$:

$$W_{g,cu} = x_i w_i - 2\pi \rho_g v_{ag} \left(\frac{1}{2} - \frac{1}{3} b \frac{r_r}{r_w} \right) r_r^2$$

$$W_{f,cu} = (1 - x_i) w_i - 2\pi \rho_f v_{ag} \left(\frac{1}{3} b \frac{r_r}{r_w} \right) r_r^2$$

The steam and water flows leaving the present stage and entering the next stage are:

$$W_{g,co} = (\text{steam flow})_{in} - W_{g,cu}$$

$$W_{f,co} = (\text{water flow})_{in} - W_{f,cu}$$

The total discharge flow is:

$$WD = W_{g,cu} + W_{f,cu}$$

The left-hand side of Equation 7.7-10 can be integrated as follows:

For $r_f < r_r$:

$$\int_{r_f}^{r_w} \left(\frac{\rho}{2} v_a^2 + P \right) dA \left[\int_{r_f}^{r_w} dA \right]^{-1} =$$

$$\frac{1}{(r_w^2 - r_f^2)} \left\{ \frac{1}{2} v_{af}^2 \left[(\rho_f + a(\rho_f - \rho_g))(r_w^2 - r_f^2) - 2a(\rho_f - \rho_g)r_w(r_w - r_f) \right] \right.$$

$$+ P_w (r_w^2 - r_f^2) - [\rho_f + a(\rho_f - \rho_g)] C^2 \frac{(r_w - r_f)^2}{r_w}$$

$$\left. + \frac{1}{2} a(\rho_f - \rho_g) C^2 \left[2r_w \log \left(\frac{r_w}{r_f} \right) - \frac{(r_w^2 - r_f^2)}{r_w} \right] \right\} \quad (7.7-11)$$

for $r_f \geq r_r$

$$\int_{r_f}^{r_w} \left(\frac{\rho}{2} v_a^2 + P \right) dA \left[\int_{r_f}^{r_w} dA \right]^{-1} =$$

$$\frac{1}{(r_w^2 - r_f^2)} \left\{ \left(\frac{1}{2} \rho_g v_{ag}^2 + P_o \right) (r_f^2 - r_r^2) + \frac{1}{3r_w} b(\rho_f - \rho_g) v_{ag}^2 (r_f^3 - r_r^3) \right\} + \quad (7.7-12)$$

$$\frac{1}{(r_w^2 - r_f^2)} \left\{ \frac{1}{2} v_{af}^2 \left[(\rho_f + a(\rho_f - \rho_g))(r_w^2 - r_f^2) - 2a(\rho_f - \rho_g)r_w(r_w - r_f) \right] \right.$$

$$+ P_w (r_w^2 - r_f^2) - [\rho_f + a(\rho_f - \rho_g)] C^2 \frac{(r_w - r_f)^2}{r_w}$$

$$\left. + \frac{1}{2} a(\rho_f - \rho_g) C^2 \left[2r_w \log \left(\frac{r_w}{r_f} \right) - \frac{(r_w^2 - r_f^2)}{r_w} \right] \right\}$$

For turbulent flow over a flat plate (Reference 7.7-2),

$$C_F = \frac{0.455}{(\log R_{eL})^{2.58}}$$

where R_{eL} is defined as:

$$R_{eL} = \frac{\rho v_w}{\mu} \left(\frac{H_D v_w}{v_{af}} \right)$$

The term $(H_D v_w/v_{af})$ represents the linear distance that a water particle will travel inside the separator barrel.

The radial pressure drop across the water layer due to centrifugal force is:

$$\int_{P_o}^{P_w} dP = \int_{r_f}^{r_w} \rho \frac{v_t^2}{r} dr$$

or

$$P_o = P_w - \left[\rho_f + a(\rho_f - \rho_g) \right] C^2 \left(\frac{1}{r_f} - \frac{1}{r_w} \right) + \frac{1}{2} a(\rho_f - \rho_g) C^2 \left(\frac{r_w}{r_f r_f} - \frac{1}{r_w} \right) \quad (7.7-9)$$

The pressure drop in the discharge passage is:

$$\begin{aligned} \int_{r_r}^{r_w} \left(\frac{\rho}{2} v_a^2 + P \right) dA \left[\int_{r_r}^{r_w} dA \right]^{-1} \\ = \frac{1}{2} \rho_{M,D} v_D^2 \left[1 + 4C_F \left(\frac{H_D}{D_D} + E_{LD} \right) + C_K \right] \\ + (P_o + \rho_f h_{sub} g - \rho_D h_{12} g) \end{aligned} \quad (7.7-10)$$

where $\rho_{M,D}$ and v_D are the mean discharge density and velocity to be defined. H_D and D_D are the length of the separator barrel and hydraulic diameter of the discharge passage, h_{12} is the distance from pickoff ring to discharge exit. E_{LD} is the equivalent L/D coefficient at the pickoff ring, and C_K is the total loss coefficient in the discharge passage.

Assuming that the flow through the swirl vane passage is homogeneous, the pressure and velocity entering the separating barrel are related to the conditions at the standpipe as follows:

$$W_i = \rho_{mi} v_i A_i = \rho_{mi} v_{an} A_n$$

$$P_i + \frac{1}{2} \rho_{mi} v_i^2 = P_n + \frac{1}{2} \rho_{mi} (v_{an}^2 + v_{tn}^2) (1 + C_{NOZ})$$

and

$$\frac{v_{an}}{v_{tn}} = \tan \theta$$

where θ is the angle between the swirl vane and a horizontal plane, and C_{NOZ} is the contraction loss coefficient (Reference 7.7-1) defined as:

$$C_{NOZ} = 0.5 \left(1 - \frac{A_N}{A_I} \right)$$

A_N is the exit flow area of the swirl vane passages and A_I is the standpipe flow area.

F_a and F_t in Equations 7.7-7 and 7.7-8 are the axial and tangential components of the frictional force on the swirling water layer:

$$F_a = F_f \frac{v_{af}}{v_w}$$

$$F_t = F_f \frac{v_{tw}}{v_w}$$

where v_{tw} is the tangential velocity on the wall,

$$v_{tw} = \frac{C}{\sqrt{r_w}}$$

and v_w is the resultant swirling velocity on the wall,

$$v_w = \sqrt{v_{tw}^2 + v_{af}^2}$$

F_f is the resultant frictional force,

$$F_f = \frac{1}{2} \rho_f C_F v_w^2 (2\pi r_w) H_D$$

The integrated equation is as follows:

$$\begin{aligned} & \frac{2}{3} \pi \rho_{mi} v_{tn} v_{an} (r_w^3 - r_h^3) \\ &= 2\pi v_{ag} C \left[\frac{1}{4} \rho_g r_f^{5/2} + \frac{1}{5} \frac{b}{r_w} (\rho_f - \rho_g) r_f^{7/2} \right] \\ &+ 2\pi v_{af} C \left[\rho_f + a(\rho_f - \rho_g) \right] \frac{2}{5} (r_w^{5/2} - r_f^{5/2}) \\ &- 2\pi v_{af} C r_w a (\rho_f - \rho_g) \frac{2}{3} (r_w^{3/2} - r_f^{3/2}) + F_t r_w \end{aligned}$$

Axial Momentum

$$\pi r_h^2 P_o + \int_{r_h}^{r_w} (\rho_{mi} v_{an}^2 + P_n) 2\pi r dr = \int_0^{r_w} (\rho v_a^2 + P) 2\pi r dr + F_a \tag{7.7-8}$$

The integrated equation is as follows:

$$\begin{aligned} & \pi r_h^2 P_o (\rho_{mi} v_{an}^2 + P_n) \pi (r_w^2 - r_h^2) \\ &= (\rho_g v_{ag}^2 + P_o) \pi r_f^2 + \frac{2}{3} \pi b (\rho_f - \rho_g) v_{ag}^2 \frac{r_f^3}{r_w} \\ &+ 2\pi v_{af}^2 \left[(\rho_f + a(\rho_f - \rho_g)) \left(\frac{r_w^2}{2} - r_f^2 \right) \right. \\ &\quad \left. - a(\rho_f - \rho_g) r_w (r_w - r_f) \right] + F_a \\ &+ 2\pi \left[\frac{1}{2} P_w (r_w^2 - r_f^2) - \frac{1}{2r_w} (\rho_f + a(\rho_f - \rho_g)) C^2 (r_w - r_f)^2 \right. \\ &\quad \left. + \frac{1}{4} a(\rho_f - \rho_g) C^2 \left(2r_w \log \left(\frac{r_w}{r_f} \right) - \frac{1}{r_w} (r_w^2 - r_f^2) \right) \right] \end{aligned}$$

assumed to be uniform radially and axially. The pressure at the separator wall (P_w) is related to P_o by centrifugal force across the water layer.

7.7.2 Model Formulations

For the first stage of the separator, a total of six unknowns are introduced in this model: v_{ag} , v_{af} , C , r_f , P_o , and P_w . The required equations are formulated from conservation of water mass, vapor mass, axial momentum, and angular momentum for the fluid entering and leaving the separating barrel, from centrifugal pressure drop across the water layer, and from pressure drop in the discharge passage. The above unknowns can then be solved for given conditions of pressure P_i , total flow rate W_i , and quality x_i at the nozzle inlet.

The mass and momentum conservation equations for flows entering the separating barrel at the swirl vane exit and leaving the separating barrel at the pickoff ring are as follows:

Water Mass

$$\begin{aligned}
 (1 - x_i) W_i &= \int_0^{r_w} \rho_f v_a (1 - \alpha) 2\pi r dr & (7.7-5) \\
 &= 2\pi \rho_f v_{ag} \left(\frac{1}{3} \frac{r_f}{r_w} b \right) r_f^2 \\
 &\quad + 2\pi \rho_f v_{af} \left[\left(\frac{1+a}{2} \right) (r_w^2 - r_f^2) - a r_w (r_w - r_f) \right]
 \end{aligned}$$

Vapor Mass

$$\begin{aligned}
 x_i W_i &= \int_0^{r_w} \rho_g v_a \alpha 2\pi r dr & (7.7-6) \\
 &= 2\pi \rho_g v_{ag} \left(\frac{1}{2} - \frac{1}{3} \frac{r_f}{r_w} b \right) r_f^2 \\
 &\quad + \pi \rho_g v_{af} a (r_w - r_f)^2
 \end{aligned}$$

Angular Momentum

$$\int_{r_h}^{r_w} v_{tn} r (2\pi r dr \rho_{mi} v_{an}) = \int_0^{r_w} v_t r (2\pi r dr \rho v_a) + F_t r_w \quad (7.7-7)$$

- It is assumed that the tangential velocity in each region is proportional to a quantity C which is related to the vortex strength or angular momentum. For the radial distribution of tangential velocity, it would be reasonable to expect a tangential velocity profile with zero at the vapor core center, a peak value at the interface between the two regions, and a somewhat lower velocity in the water layer region due to wall effects. In the following, it is assumed that there is solid rotation in the vapor core region and the tangential velocity decays with $1/\sqrt{r}$ in the water layer region, as follows:

$$0 < r < r_f : v_t = \frac{rC}{r_f^{3/2}} \text{ in vapor core} \quad (7.7-1)$$

$$r_f < r < r_w : v_t = \frac{C}{\sqrt{r}} \text{ in water layer} \quad (7.7-2)$$

At the interface where $r = r_f$, the tangential velocity is $C/\sqrt{r_f}$.

- The radial distributions of void fraction in each region are affected mainly by the vortex strength and the inlet quality. For higher vortex strength and inlet quality, it is expected that the void fraction profile in the vapor core region would get closer to 1.0. For higher vortex strength and lower inlet quality, it is expected that the void fraction profile in the water layer region would get closer to 0.0. With these expected characteristics, the void fraction profiles in each region are assumed to have the following functional forms:

$$0 < r < r_f : \alpha = 1 - b \frac{r}{r_w} \text{ in vapor core} \quad (7.7-3)$$

$$r_f < r < r_w : \alpha = a \left[\frac{r_w}{r} - 1 \right] \text{ in water layer} \quad (7.7-4)$$

and

$$a = AA \left[\frac{\sqrt{gr_w^2}}{C} \right]^{0.5} x_i^2$$

$$b = BB \left[\frac{\sqrt{gr_w^2}}{C} \right]^{0.5} (1 - x_i)^3$$

where x_i is the inlet quality, AA and BB are parameters to be determined from data.

- Since the vapor density is relatively small, it is reasonable to expect the pressure variation in the vapor core to be small. In the model, the vapor core pressure (P_o) is

W	flow rate
x	quality

Greek Symbols

α	void fraction
ρ	density
$\rho_{M,D}$	mean discharge density
π	constant=3.14159...
μ	viscosity
θ	swirl vane angle

Subscripts

a	axial
cu	carryunder
co	carryover
D	discharge
f	water layer
g	vapor
i	inlet
m	mixture
n	swirl vane exit
t	tangential
w	separator barrel

7.7.1 Technical Basis and Assumptions

Under normal operating conditions, the steam-water mixture enters the separator from the standpipe, and passes through a set of stationary swirl vanes into the separating barrel. The swirl vanes are physically similar to a set of stationary turbine blades with blade tip angle of θ to the horizontal at the blade channel exit. These vanes produce a high rotational velocity component in the fluid flowing through the separating barrel. The resultant centrifugal force separates the steam-water mixture into a water layer on the wall and a steam vortex core. Figure 7.7-1 shows two typical types of steam separators used in General Electric BWRs. Figure 7.7-2 depicts the geometries and flows in the separator model. In this model, consideration is focused on the conservation of mass and momentum in the water layer region and vapor core region. Integral formulations are used for the conservation equations. The following assumptions are made at the axial locations near the pickoff ring:

- A mean (or uniform) axial velocity is assumed in each flow region, i.e.:

$$0 < r < r_f : v_a = v_{ag}, \text{ Uniform in vapor core}$$

$$r_f < r < r_w : v_a = v_{af}, \text{ Uniform in water layer}$$

where r_f is the inner radius of the water layer. Velocity slip conditions exist at the interface and at the wall.

7.7 Steam Separator

The performance characteristics of the steam separator are measured in terms of the pressure drop across the separator, carryover, which is the amount of liquid entrained in the steam leaving the separator, and carryunder, which is the amount of steam entrained into the liquid leaving the separator. These quantities have important effects on plant transient performance. The separator pressure drop is one of the resistances for the flow circulating through the reactor core. The carryover affects the steam dryer pressure drop and dryer efficiency. The carryunder affects the water subcooling in the downcomer and at the reactor core inlet. Core inlet subcooling, in turn, affects the thermal-hydraulic performance of the fuel bundles, and the moderator-to-fuel ratio in the core. The following sections describe the assumptions and formulation of a mechanistic based model for internal steam separators in BWRs.

Nomenclature

a	void profile function in water layer (Equation 7.7-4)
A	area
AA	constant parameter used in void profile function "a"
A_I	standpipe flow area
A_N	exit flow area of the swirl vane passage
b	void profile function in vapor core (Equation 7.7-3)
BB	constant parameter used in void profile function "b"
C	proportional constant used in Equation 7.7-1
CC	proportional constant
C_F	frictional coefficient
C_{NOZ}	contraction loss coefficient
DD	proportional constant
D_D	hydraulic diameter of the discharge passage
E_{LD}	equivalent L/D coefficient at the pickoff ring
F	frictional force
F_f	resultant frictional force
g	acceleration of gravity
h_{12}	distance from pickoff ring to discharge exit
H_D	barrel length
P_0	vapor core pressure
P	pressure
r	radius
r_f	inner radius of the water layer (Figure 7.7-2)
r_w	inner radius of the separator barrel (Figure 7.7-2)
Re	Reynolds number
v	velocity

The agreement between TRACG and the data has been determined to be very good for both positive and negative drive flow. Only for negative drive flow and large M-ratios, where the suction velocity exceeds the drive velocity, is some deviation from the data observed. Except for negative drive flow and large M-ratios, which is not a typical operating condition, the N-ratio is predicted with a typical accuracy of 0.1.

7.6.5 References

- 7.6-1 I.E. Idelchik, *Handbook of Hydraulic Resistance Coefficient of Local Resistance and Friction*, AEC-TR-6630, 1966.
- 7.6-2 G.E. Wilson, *INEL One-Sixth Scale Jet Pump Data Analysis*, EGG-CAAD-5357, February 1981.
- 7.6-3 Crane Company, *Flow of Fluids Through Valves, Fittings, and Pipe*, Technical Paper No. 410, Crane Company, New York.
- 7.6-4 H. Schlichting, *Boundary Layer Theory*, McGraw-Hill, New York.
- 7.6-5 H.S. Capro, *One-Sixth Scale Model BWR Jet Pump Test*, Idaho National Engineering Laboratory, LTR 20-105, November 1979.

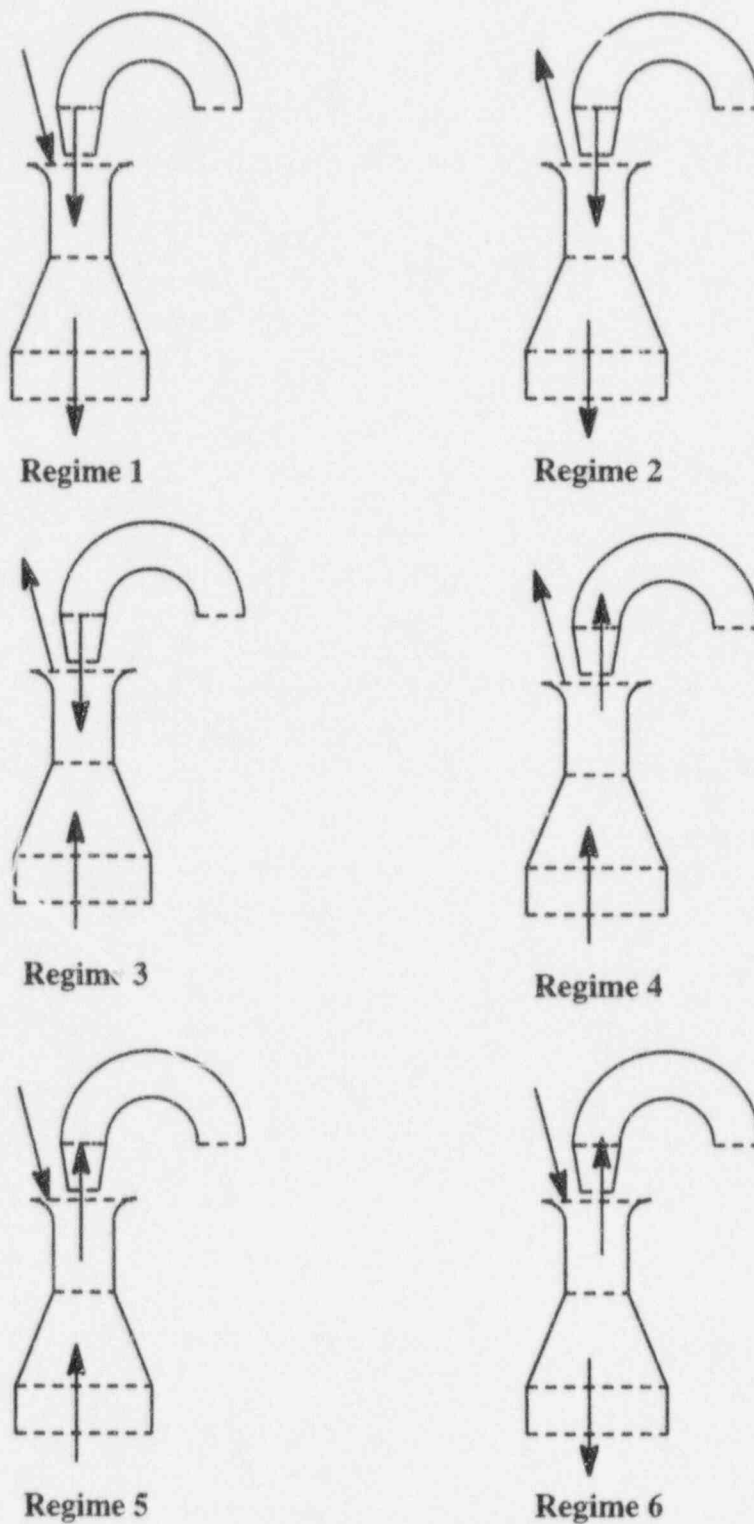


Figure 7.6-3. Jet Pump Flow Regimes

where

β = Contraction angle

A^* = Area ratio of outlet to inlet of contraction

C_o = Constant

The default value of C_o is 0.38 in TRACG. The user can optionally input their own value of C_o . This pressure loss coefficient is used at every face in the jet pump where the flow area at the cell centers on either side of the face decrease in the direction of flow.

7.6.2.3 Inlet Losses

There is an irreversible pressure loss at the jet pump suction inlet due to the contraction of the suction flow from the downcomer to the jet pump. The loss coefficient for this loss has been estimated to be 0.02 from data obtained at INEL using 1/6 scale jet pumps [7.6-2]. When flow at the jet pump diffuser outlet reverses, there is a contraction loss from the lower plenum into the jet pump diffuser. The loss coefficient for this loss has been estimated from data to be 0.38. These values are in TRACG as default values, but the user may change them.

7.6.2.4 Outlet Losses

There is a loss at the diffuser outlet due to the flow expansion from the diffuser outlet into the lower plenum for normal operating conditions in the jet pump. The loss coefficient for this loss is estimated to be 1.0 and is implemented into TRACG at the diffuser outlet for forward flow in the diffuser.

7.6.3 Applicability

The jet pump model was developed based on 1/6 scale jet pump data from Idaho National Engineering Laboratory [7.6-1, 7.6-5]. The test data included a range of drive flow $-4.2 \cdot 10^{-3} - 4.2 \cdot 10^{-3} \text{ m}^3 / \text{sec}$ covering typical operating conditions of a BWR jet pump and covering all six flow regimes indicated in Figure 7.6-3.

7.6.4 Assessment

Assessments against the 1/6 scale jet pump data have been made. M and N ratios are defined as follows:

$$M = \frac{W_{\text{Suction}}}{W_{\text{Drive}}}$$

$$N = \frac{P_{\text{Discharge}} - P_{\text{Suction}}}{P_{\text{Drive}} - P_{\text{Discharge}}}$$

where

$$M = \frac{W_1}{-W_3} = \frac{A_1 v_1}{-A_3 v_3} \quad (7.6-6)$$

$$M_0 = \frac{A_2 - A_3}{A_3} \quad (7.6-7)$$

$$c^* = \max \left[1, \left(\frac{A_1}{A_2 - A_3} \right)^2 \right] \quad (7.6-8)$$

7.6.2 Jet Pump Form Loss Coefficients

Additional losses are included in the jet pump model. These losses account for inlet and exit losses as well as form losses in converging or diverging flow areas.

7.6.2.1 Diffuser (Expansion) Losses

The irreversible pressure loss coefficient through a diffuser is given by Idelchik [7.6-1] as:

$$K = C_e (\tan \beta)^{1.5} (1 - A^*)^2 \quad (7.6-9)$$

where

- β = Diffuser angle
- A^* = Area ratio of outlet to inlet
- C_e = Constant

The recommended value of C_e is 0.0 and is the default value in TRACG. Users may input the value of C_e if they so desire.

This pressure loss coefficient is used at every cell face of the jet pump where the flow areas at the cell centers on either side of the face increase in the direction of flow.

7.6.2.2 Nozzle (Contraction) Losses

The irreversible pressure loss coefficient through a nozzle is due to the contraction is given by Idelchik [7.6-1] as:

$$K = C_o \sin \beta (1 - A^*) \quad (7.6-10)$$

Two loss coefficients have been implemented into TRACG to account for incomplete mixing of the fluid stream. The losses are the nozzle loss applied at face 3 in Figure 7.6-2, and the mixing loss applied at face 2 in Figure 7.6-2. These losses have been correlated against data from the 1/6 scale jet pump test performed at INEL. The losses depend on the flow regime, and are given in Tables 7.6-1 and 7.6-2.

Table 7.6-1
Mixing Losses

Regime	Drive flow	M	$\frac{\Delta P}{\rho_l}$
1	$v > 0$	$0 < M$	$\max \left[0, 0.065 \left(\frac{M}{M_o} - 1 \right) \frac{M}{M_o} \right] c^* v_1^2$
2	$v > 0$	$-1 < M < 0$	0.0
3	$v > 0$	$M < -1$	0.0
4	$v < 0$	$0 < M$	0.0
5	$v < 0$	$-1 < M < 0$	$0.065 c^* v_1^2$
6	$v < 0$	$M < -1$	$0.065 c^* v_1^2$

Table 7.6-2
Nozzle Losses

Regime	Drive flow	M	$\frac{\Delta P}{\rho_l}$
1	$v > 0$	$0 < M$	0
2	$v > 0$	$-1 < M < 0$	$\min [2.5, M (0.08M - 0.06)] v_3^2$
3	$v > 0$	$M < -1$	$\min [2.5, M (0.08M - 0.06)] v_3^2$
4	$v < 0$	$0 < M$	$\max [0, 0.48 (1 - M)] v_3^2$
5	$v < 0$	$-1 < M < 0$	$0.84 - M(0.33 - 1.74M) v_3^2$
6	$v < 0$	$M < -1$	$2.55 v_3^2$

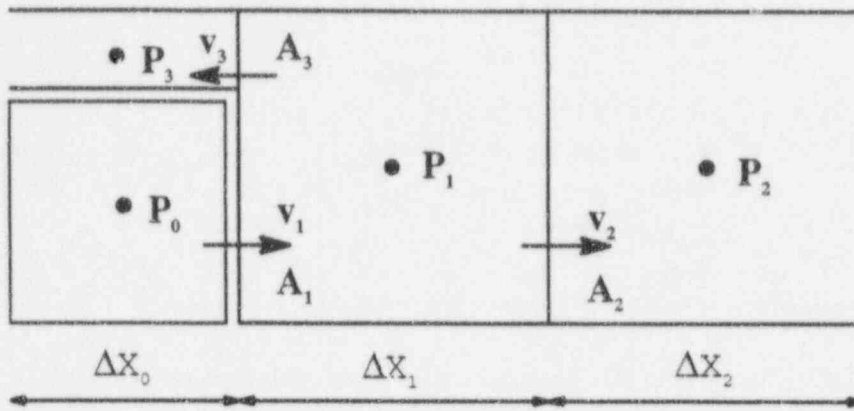


Figure 7.6-2. Simple Noding Scheme for Jet Pump Component

The momentum equation in the TRACG solution scheme depends on noding and flow direction. The calculated pressure change for a single-phase steady-state flow without sources, friction loss, and gravity from the suction inlet to Cell 1 is given by:

$$\begin{aligned} \frac{P_1 - P_0}{\rho_\ell} &= -\frac{1}{2} (v_1 + v_1 \frac{A_1}{A_2})(v_1 \frac{A_1}{A_2} - v_1) & (7.6-3) \\ &= \frac{1}{2} v_1^2 (1 + \frac{A_1}{A_2}) \frac{A_3}{A_2} \end{aligned}$$

This pressure increase is the pressure recovery given by Bernoulli's equation for a stream expanding from an area of A_1 to A_2 . This pressure gain will not occur in the jet pump and is compensated for by a simple loss coefficient.

From Cell 1 to Cell 2, the pressure change is given by:

$$\frac{P_2 - P_1}{\rho_\ell} = -v_2 (v_2 - v_1 \frac{A_1}{A_2}) + B \quad (7.6-4)$$

By combining Equations 7.6-2 and 7.6-4, the momentum source term is calculated to be:

$$B = \frac{A_3}{A_2} v_3 (v_3 + v_1) + \frac{A_3}{A_2} v_1 v_2 \quad (7.6-5)$$

This source term is applied in TRACG for positive drive flow. In the case of negative source flow (positive side tube velocity), the flow in the primary tube may not be accelerated by the source flow. Therefore, the momentum source term is set to zero. But there is an irreversible loss due to the flow splitting similar to the flow with sudden expansion.

7.6 Jet Pump

This model is based on the tee component; however, modifications have been made to include the momentum source term for the junction in order to conserve momentum for the mixing process. Furthermore, losses have been included to account for inefficient mixing and for smooth and abrupt flow area changes.

7.6.1 Jet Pump Momentum Source

The momentum source term to be applied to the momentum equation for primary tube flow (Figure 7.6-1) is obtained by considering the momentum balance for the different flow configurations that can occur in the jet pump (Figure 7.6-3).

Considering the simple nodalization shown in Figure 7.6-2, the momentum source is derived for the liquid phase momentum equations. The results will also be applicable to the vapor momentum equation. The steady-state pressure changes due to the merging of two liquid flows (Figure 7.6-2) are for normal operating conditions ($V_1 > 0$, $V_2 > 0$, $V_3 < 0$):

$$\frac{P_1 - P_o}{\rho_l} = 0 \quad (7.6-1)$$

$$\frac{P_2 - P_1}{\rho_l} = v_2(v_1 - v_2) + v_3(v_1 + v_3) \frac{A_3}{A_2} \quad (7.6-2)$$

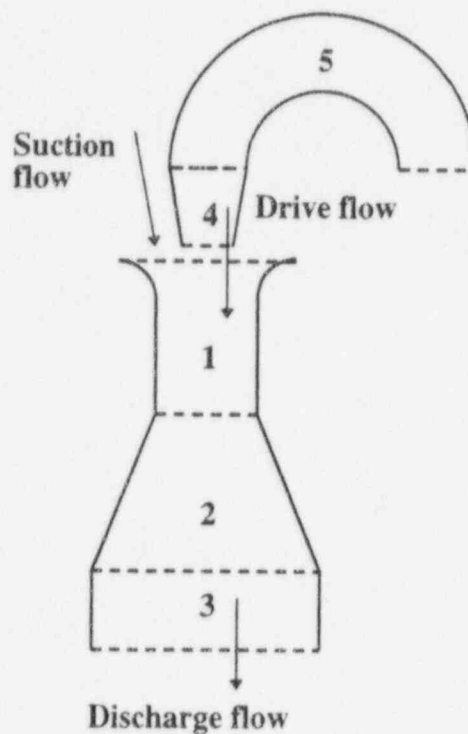


Figure 7.6-1. Jet Pump Nodalization

- 7.5-6 *General Electric Company Analytical Model for Loss-of-Coolant Analysis in Accordance with 10CFR50 Appendix K, Licensing Topical Report NEDO-20566, January 1976.*
- 7.5-7 *D.S. Rowe and C.W. Angle, Crossflow Mixing Between Parallel Flow Channel During Boiling, Part II, BNWL-371, pt. 2, Pacific Northwest Laboratory, 1967.*

The assessment of the critical power calculation can be found in Section 3.6 of the TRACG Qualification Report.

7.5.6 Upper Bound Temperature Estimate

The TRACG hot rod model allows a simulation of the local variation in channel hydraulic conditions to provide an estimate of the upper bound peak cladding temperature. The hot rod model is based on the assumption that the hot rod is exposed to a slightly higher void fraction than the cell average void fraction "seen" by the other rods. The corresponding lower interfacial heat transfer gives a higher vapor temperature surrounding the hot rod.

The assessment of the upper bound temperature estimate can be found in Sections 5.1 and 5.2 of the TRACG Qualification Report.

7.5.7 Water Rod Model

An option to model water rod flow is available for the channel component. The water rod model allows the modeling of a flow path between any two channel cells. The geometry of this internal pipe connection is user specified as part of the channel input. The geometry specification is consistent with any pipe component with the added restriction that the cell boundaries in the water rod must match the cell boundaries in the channel. This requirement facilitates the calculation of heat transfer through the water rod clad and direct energy deposition to the water rod fluid. The heat transfer connection between the channel and the water rod is specified using the component-to-component heat transfer logic. The solution of the water rod is handled in the same manner as that used for the secondary branch of the tee component. In the water rod, both end junctions are internal, whereas in the secondary tee branch only one end is an internal junction. This formulation allows for an implicit coupling of the water rod flow.

7.5.8 References

- 7.5-1 A.B. Burgess, *ISCOR07 Technical Description and User's Manual*, NEDE-24762, November 1979.
- 7.5-2 F.D. Shum, et. al., *The GESTR-LOCA and SAFER Models for the Evaluation of the Loss-of-Coolant Accident - Volume II*, NEDC-23785-1-PA, October 1984.
- 7.5-3 B.S. Shiralkar and J.R. Ireland, General Electric Company, Analytical Model for Loss-of-Coolant Analysis in Accordance with 10CFR Appendix K, Amendment No. 5, *Backflow Leakage from the Bypass Region for ECCS Calculations*, NEDE-20566-5P, June 1978.
- 7.5-4 S.O. Akerlund, et. al, *The GESTR-LOCA and SAFER Models for the Evaluation of the Loss-of-Coolant Accident, Vol. 1, GESTR-LOCA - A Model for the Prediction of Fuel Rod Thermal Performance*, NEDE-23785-1-PA, June 1984.
- 7.5-5 Letter, R.H. Buchholz (GE) to L.S. Rubenstein (NRC), *General Electric Fuel Clad Swelling and Rupture Model*, May 15, 1981.

7.5.3 Cladding Perforation

The cladding swelling and rupture model calculates the cladding hoop stress, strain (elastic and plastic) and the conditions of cladding perforation. The cladding hoop stress is calculated from the differential pressure (internal gas pressure – system coolant pressure) across the cladding. This hoop stress is then compared to the stress at which perforation will occur, which decreases as the cladding temperature increases. The transient internal gas pressure is calculated from the perfect gas law, which requires calculation of the transient gas temperature in the fuel rod plenum and in the fuel column.

7.5.4 Thermal Radiation Heat Transfer

In addition to heat transfer options available for other components, the fuel rod and channel wall heat transfer models include detailed radiation heat transfer for each rod group as well as for the inside of the channel wall. Section 6.6.12 describes the thermal radiation model used in TRACG.

7.5.5 Critical Power

The critical power ratio (CPR) is defined as the ratio of the bundle power required to cause a boiling transition to the operating bundle power. At steady state, the channel critical power is determined by holding constant the boundary conditions of flow, inlet enthalpy, and pressure and increasing the channel power until a boiling transition is calculated.

$$\text{CPR}(0) = \frac{\text{Critical Power}}{\text{Initial Power}} = \frac{P_c(0)}{P(0)} \quad (7.5-4)$$

During a transient, the local mass flux, boiling boundary, and coolant quality are calculated at each axial node. The boiling length and nodal mass flux are used to compute the instantaneous critical quality at each node using the GEXL correlation (Section 6.6.6). The thermal margin (TM) for each node is defined as follows:

$$\text{TM} = \frac{x_c + \frac{\Delta h_s}{h_{fg}}}{x_e + \frac{\Delta h_s}{h_{fg}}} \quad (7.5-1)$$

where

- x_c = Node instantaneous critical quality
- Δh_s = Subcooling at channel inlet
- x_e = Node instantaneous equilibrium quality
- = $(h_\ell + x(h_v - h_\ell) - h_f)/h_{fg}$

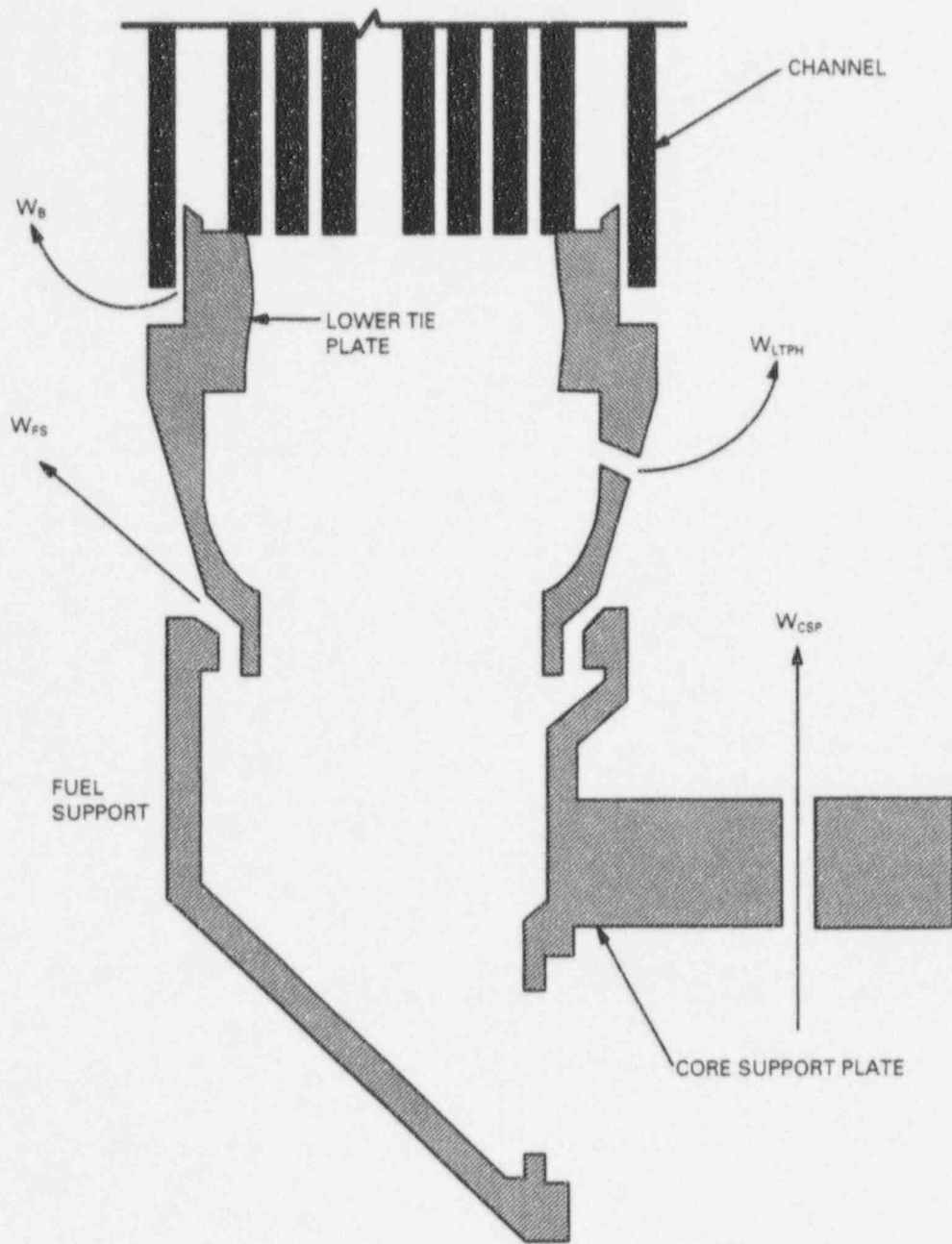


Figure 7.5-3. Leakage Flow Paths

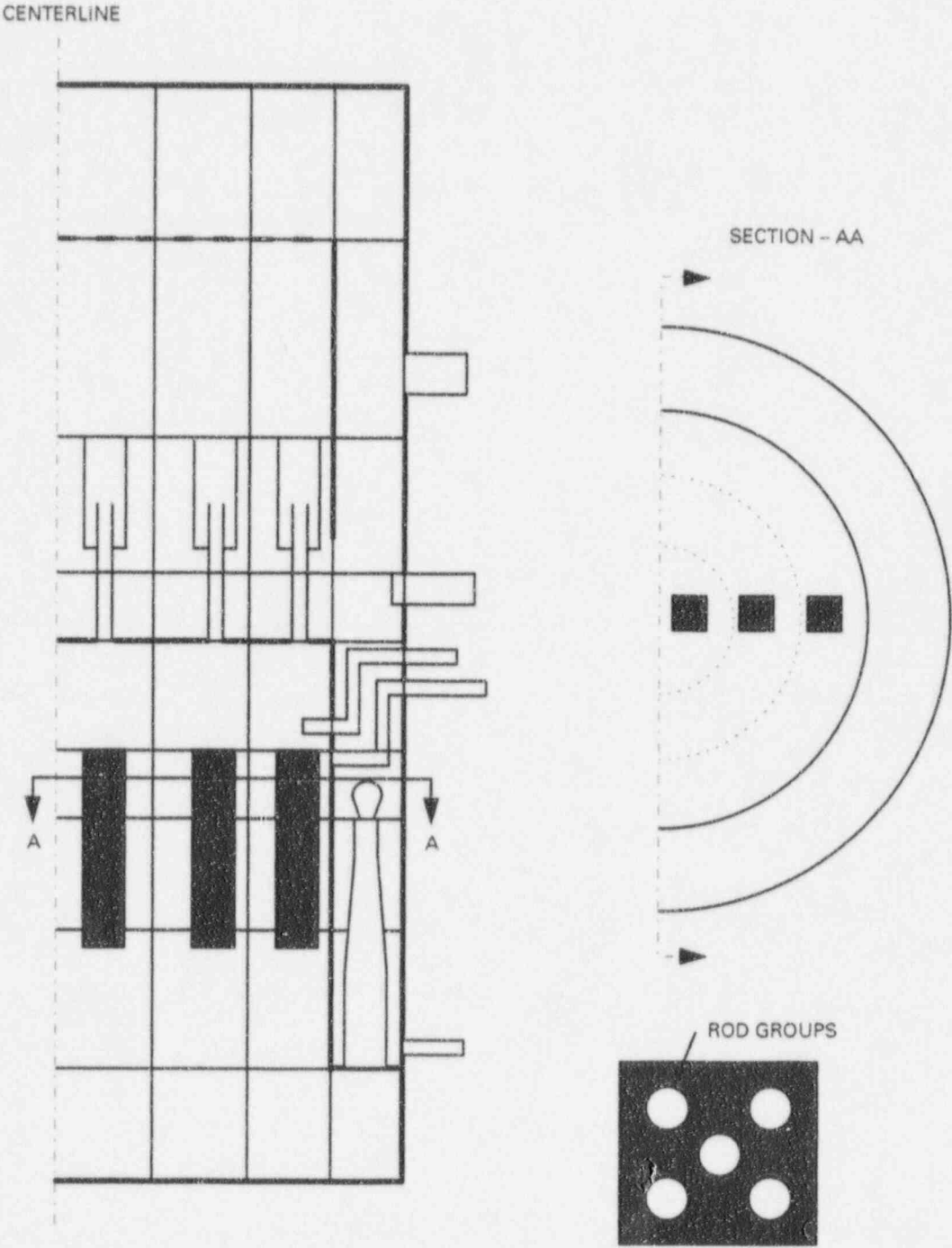


Figure 7.5-2. Simplified Reactor Nodalization Showing CHAN Components

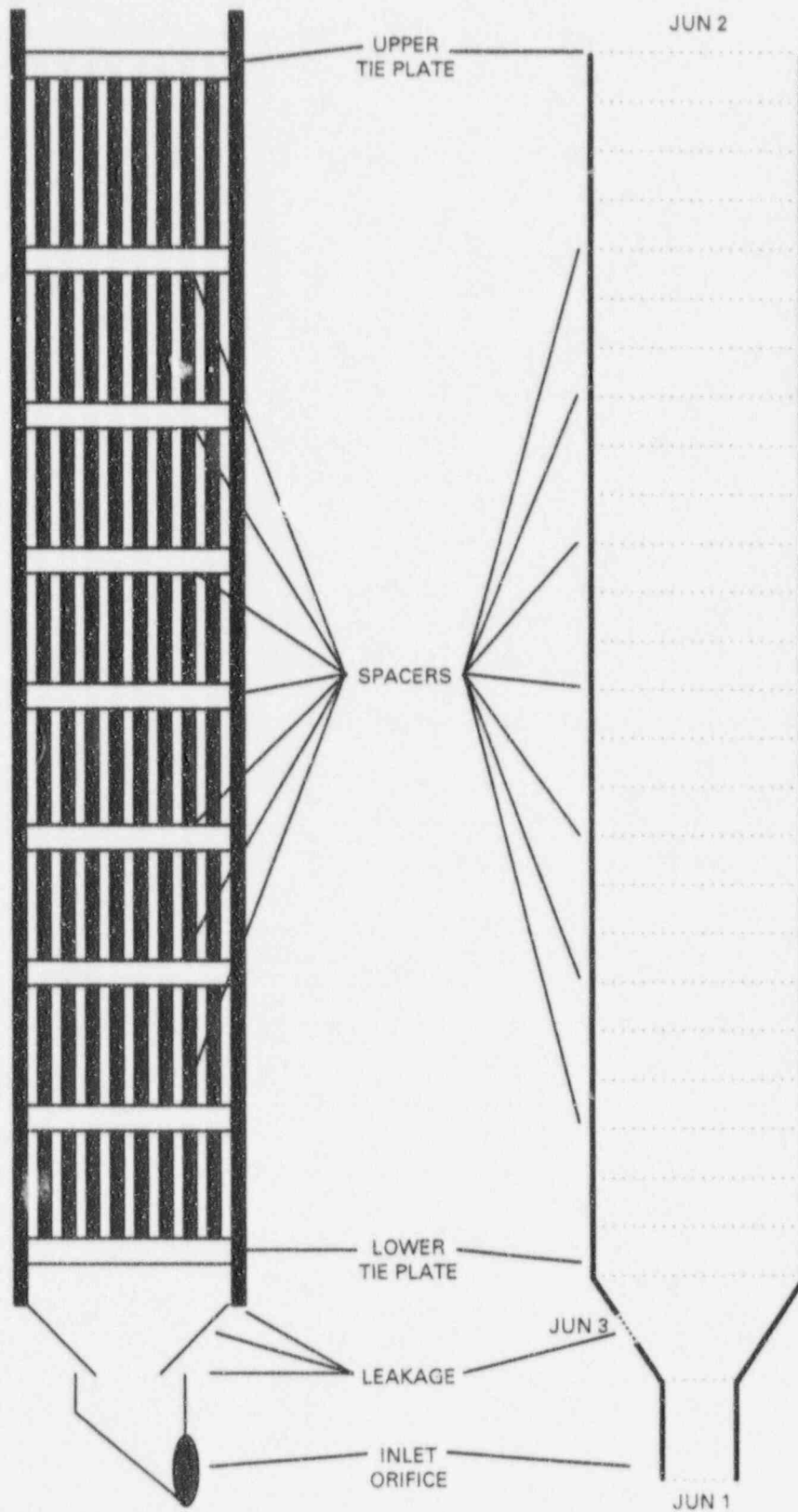


Figure 7.5-1. Channel Noding Diagram

LEAK	leakage
LTPH	lower tie plate hole
o	outer
p	plenum
r	reference
ref	reference
sat	saturated condition
sg	spring/getter
v	vapor
w	wall

Superscript

H	hot rod
---	---------

7.5.1 Leakage Flows

The bypass flow rate is the summation of the leakage flows through several paths. The flow rate across each leakage path is represented as a function of the pressure difference across the path. These leakage flow expressions are correlated from test data [7.5-1,2]. The leakage paths are shown in Figure 7.5-3. There are two basically different types of leakage paths. The first category consists of the paths in which the flow rates are functions of the core support plate pressure difference (ΔP_{csp}). There are seven different paths of this type represented by W_{csp} in Figure 7.5-3. The second type of leakage path depends on the fuel assembly type and is dependent on the pressure distribution in the fuel assembly. There are three leakage paths of this type.

7.5.2 Fuel Pellet Gap Conductance

The gap between the fuel pellet and the surrounding cladding of a fuel rod causes a local thermal resistance which must be included in an accurate model of the fuel cladding radial temperature distribution. The gap contains a mixture of helium fuel rod filler gas and xenon and krypton gaseous fission products released from the fuel. The gap can be characterized by assuming that it has negligible thermal capacitance and a thermal conductance which is calculated from a rather complex model that considers such phenomena as relative fuel cladding thermal expansion, fuel cladding creep and plasticity, fuel relocation, densification, irradiation swelling, and fission gas release.

\bar{T}_c	cladding average temperature at the maximum LHGR axial position
$\bar{T}_{f,max}$	volume weighted fuel temperature at the maximum LGHR axial position
TM	thermal margin
V_f	fuel rod volume
V_p	plenum volume
W	flow
x_c	node instantaneous critical quality
x_e	node instantaneous equilibrium quality
X_i	gm-moles of the i^{th} component

Greek

α_{fi}	thermal expansion coefficient of the i^{th} fuel node
α_c	thermal expansion coefficient of cladding
α	void fraction
ρ	density
ϵ	thermal emissivity
ϵ	cladding strain
ϵ_E	cladding elastic strain
σ_β	Stefan-Boltzman constant
σ_c	cladding hoop stress
σ_Y	cladding yield stress
ν	Poisson's ratio for the cladding

Subscript

csp	core support plate leakage path
B	channel-lower tie plate leakage path
c	cladding
f	fuel pellet
f	saturated liquid
g	gas gap
g	saturated steam
FS	fuel support leakage path
i	inner
i	initial
i	i^{th} component
ℓ	liquid

n_i	empirical constant for the i^{th} component
N	number of radial nodes in the fuel
N_{fgr}	total moles of gaseous fission products released from the fuel
N_{fgf}	total moles of gaseous fission products remaining in the fuel
N_{He}	total moles of filler gas in the rod
N_{Xe}	total moles of Xenon
N_{Kr}	total moles of Krypton
P	system coolant pressure
P	power
P_c	fuel/cladding contact pressure
P_c	critical power
P_g	fuel rod internal gas pressure
P_Y	fuel/cladding contact pressure corresponding to cladding yield
ΔP	pressure difference
q	heat transfer per unit volume
Δr_i	reference (cold) radial dimension of the i^{th} fuel node
r_{fo}	fuel nominal (cold dimension) outer radius
r_{ci}	cladding nominal (cold dimension) inner radius
r_{co}	cladding nominal (cold dimension) outer radius
R	nominal radial gap size
R	universal gas constant
R_1	fuel pellet surface roughness
R_2	cladding surface roughness
R_4	mean roughness
R_{eff}	effective hot radial thermal gap between the fuel pellet and cladding
R_{ci}	hot cladding inner radius
R_{fo}	hot outer fuel radius
ΔR_f	fuel thermal expansion
t	cladding thickness
T	temperature
T_c	cladding average temperature
T_f	gas temperature in the fuel rod volume
T_p	plenum gas temperature
T_{fi}	fuel temperature of the i^{th} fuel node

In addition to the heat transfer options available for other components, the fuel rod and channel wall heat transfer models include detailed radiation heat transfer (Section 6.6.12), and bottom-up and top-down quench fronts (Section 6.6.13) for each rod group as well as for the inside of the channel wall. Heat transfer on the outside of the channel wall is coupled to the vessel hydrodynamics solution.

Nomenclature

A	area
A_o	an empirical constant representing the mean radius of the contact spots
A_{vi}	empirical constant for the i^{th} component
C	coefficient in leakage flow correlation
C	contact pressure constant
C_{g1}	perforated rod gap conductivity equation constant
C_{g2}	perforated rod gap conductivity equation exponent
C_{R1}	=0.2, constant defined by the GESTR-LOCA empirical relocation model
C_{R2}	=0.5, constant defined by the GESTR-LOCA empirical relocation model
CPR	critical power ratio
E	modulus of elasticity
F_r	fraction of additional fission gas released
F_{kx}	the ratio of Krypton to Xenon in the fission gas
$(g_1 + g_2)$	fuel rod gas gap temperature jump distance
h	heat transfer coefficient
h	enthalpy
Δh_s	subcooling at channel inlet
h_g	total gap conductance
h_s	heat transfer coefficient for conduction through fuel/cladding contact spots
h_f	heat transfer coefficient for conduction through the gas layer at fuel/cladding interface
h_r	radiant heat transfer coefficient
H_m	Meyer hardness of the cladding
I	radial pellet/cladding interaction
k_{fg}	thermal conductivity of the fuel rod gas
K	loss coefficient
L	rod heated length
M_i	molecular weight of the i^{th} component
n	total amount of gap gas (gm-mol)

7.5 Fuel Channel

The fuel channel (CHAN) component has been developed to simulate one or more BWR fuel rod bundles and channel walls. The channel is a tee component (Section 7.4) to which fuel rod heat transfer and channel wall heat transfer models have been added. The channel can be used to simulate a single bundle or several bundles in a stand-alone mode in which boundary conditions to the channel are supplied by break and fill components. This capability is quite useful for performing hot bundle analysis or for investigating single bundle experiments. The channel component can also be used to simulate rod bundles in a BWR core region.

Basing the channel component on the tee structure provides an implicit coupling of all flow paths, including the leakage paths. Junction 1 of the channel component represents the channel inlet connection to the lower plenum. The end of the primary section of the channel (JUN2) is the channel exit to the upper plenum. The secondary section of the channel is used to model the leakage path from the channel to core bypass region. The channel utilizes a zero cell secondary pipe as shown in Figure 7.5-1. The secondary function (JUN3) provides a connection from JCELL directly to another component.

The leakage flow calculation makes use of GE design correlations that express leakage flow as functions of pressure drop, fluid conditions, and geometry for all possible leakage paths. The calculated leakage flow is based on an effective loss coefficient applied at the leakage junction (JUN3). A similar process is used in the vessel component to model leakage flow from the lower plenum to the core bypass region. Details of the leakage calculation are provided in Section 7.5.1.

Each channel component is assigned a fraction of the total core power. The axial and rod group distributions of power provide the power deposition in each fuel rod axial node. The radial distribution of power within the fuel rod is also specified. Details of the fuel rod radial conduction solution are provided in Section 4. Direct heating of the channel fluid and structure is also available as described in Section 9.

An option to model water rod flow is available for the channel component. The water rod model (Section 7.5.7) allows the modeling of a flow path between two channel cells. The geometry of this internal pipe connection is user specified. Heat transfer through the water rod and direct energy deposition are modeled.

To model a BWR core, channel components are connected across the usual core region of the vessel component. The connections are made with standard vessel sources (see vessel component in Section 7.8). The 3-D hydrodynamics solution in the core region of the vessel component is used for the flow in the region outside the BWR channels but inside the core barrel. A simplified noding scheme for a BWR vessel is illustrated in Figure 7.5-2. For this nodalization, three channel components are used to simulate all fuel bundles in the BWR core region. Within each channel component, five rod groups are chosen to model radiation heat transfer. This noding scheme allows for fine nodalization in the radial direction of the core without increasing the number of vessel nodes.

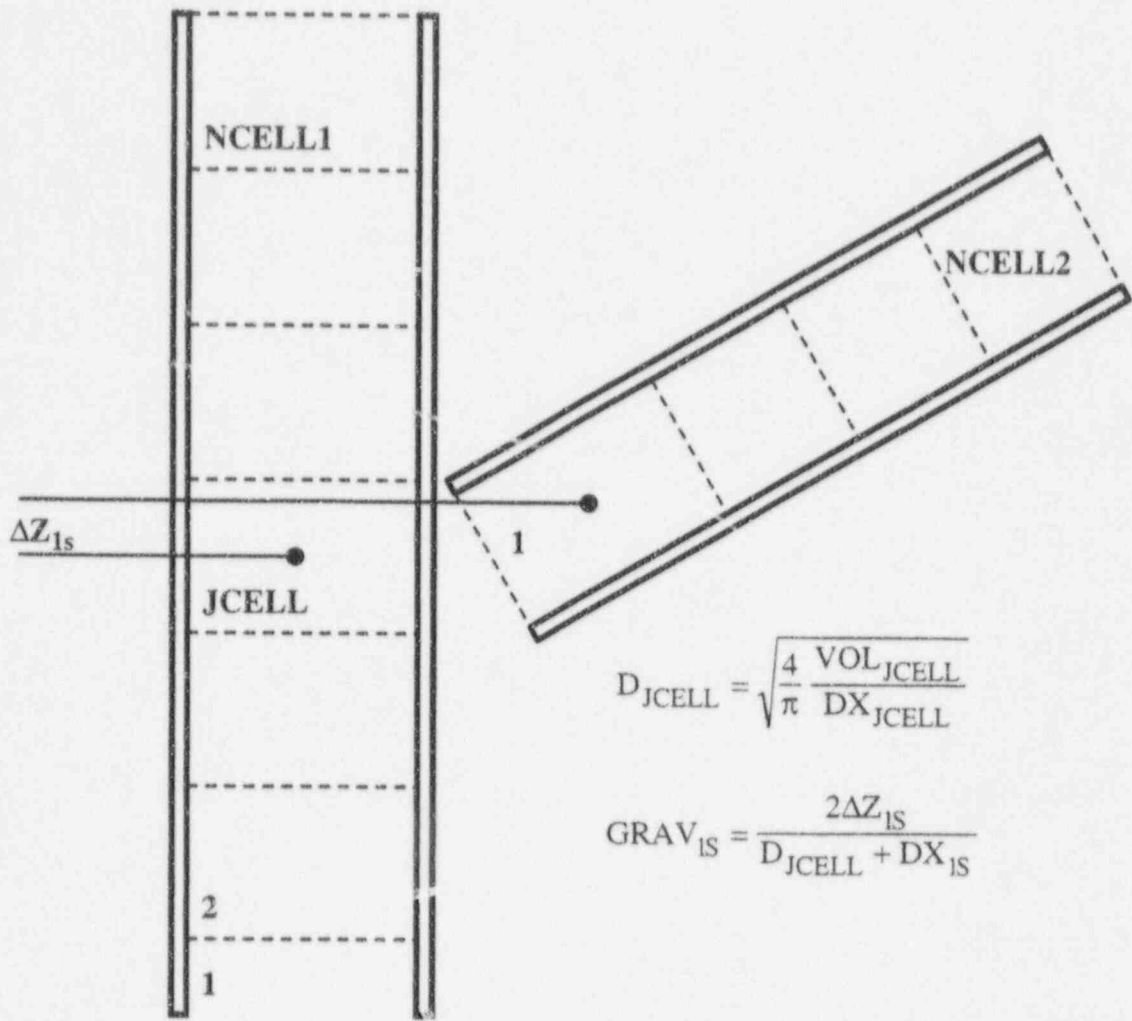


Figure 7.4-1. TEE Noding Diagram

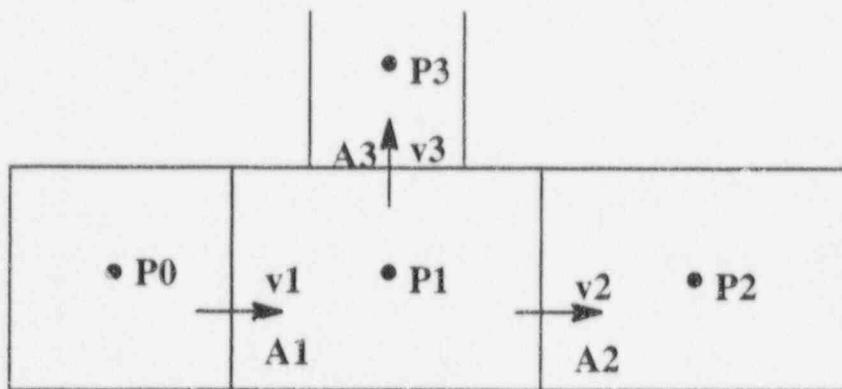


Figure 7.4-2 Sample Noding Scheme for Tee Component

where v' is an estimate for the velocity at the center of Cell 1. Neglecting compressibility effects, this velocity is given by the merging of the two streams:

$$v' = \frac{A_1}{A_2} v_1 - \frac{A_3}{A_2} v_3 \quad (7.4-3)$$

Combining Equations 7.4-1, 7.4-2 and 7.4-3 gives:

$$B_{1-2} = - \frac{A_3}{A_2} v_3 v_2 \quad (7.4-4)$$

This source term is applied in TRACG for both positive and negative source flow. In the case of negative primary flow (v_1), the momentum source term, B_{1-0} , is calculated to be:

$$B_{1-0} = - \frac{A_3}{A_1} v_3 v_1 \quad (7.4-5)$$

In most applications of interest, the error incurred by ignoring the effect of the source momentum is small. In cases where this is not true, however, the user may use the jet pump (JETP) component in place of the tee. This component is a special type of tee in which certain assumptions have been made regarding the normal flow direction and in which the momentum source term in PIPE 1 is not neglected (see JETP description).

Because the tee is modeled as essentially two interconnected pipes, the pipe model description in Section 7.1 should be referenced for additional information.

7.4 Tee

The tee (TEE) component models the thermal-hydraulics of three piping branches, two of which lie along a common line. The third enters at some angle from the main axis of the other two (Figure 7.4-1). In the code, the tee is treated as two pipes, as indicated in Figure 7.4-1. Beta is defined as the angle from the low-numbered end of PIPE1 to PIPE2. The low-numbered end of PIPE2 always connects to PIPE1. The first pipe extends from Cell 1 to Cell NCELL1 and connects to PIPE2 at Cell JCELL. The second pipe begins at Cell 1 and ends at Cell NCELL2.

The connection is effected through mass, momentum, and energy source terms in PIPE1. PIPE2 sees the connection as boundary conditions from Cell JCELL in PIPE1. The time differencing and iteration procedures are such that conservation of the scalar qualities is preserved (within a convergence tolerance) and the level of implicitness at the connection ensures that no additional stability limitations apply at a tee. Phase separation at the junction is not implemented. The void fraction from cell JCELL in PIPE1 is used when donor-celling the boundary conditions of Cell 1 in PIPE2.

The momentum equation in the TRACG solution scheme depends on noding and flow direction. Considering the simple nodalization shown in Figure 7.4-2, the momentum source is derived for the liquid phase momentum equation. The results will also be applicable to the vapor momentum equation. The calculated pressure change for a single-phase steady-state flow with positive velocity and without sources, friction loss, and gravity from Cell 1 to Cell 2 is given by:

$$\frac{P_2 - P_1}{\rho_\ell} = -v_2 \left(v_2 - v_1 \frac{A_1}{A_2} \right) + B_{1-2} \quad (7.4-1)$$

where

$v \frac{\partial v}{\partial x}$ is calculated according to Equation 3.2-2 (for simplicity D and E are set to unity) and B_{1-2} is a source term.

In the derivation of Equation 3.2-2, a side branch was not accounted for. To get the correct pressure drop for two streams mixing (with $D=E=1$) Equation 7.4-1 should read:

$$\frac{P_2 - P_1}{\rho_\ell} = -v_2 (v_2 - v') \quad (7.4-2)$$

Table 7.3-1
Control Options for VLVE

IVTY	Option
-1	Valve area is controlled by a control system.
1	Valve is normally open and is closed instantly on a trip signal.
2	Valve is normally closed and is opened instantly on a trip signal.
3	Valve is normally open and is closed on a trip signal according to a time-dependent valve table.
4	Valve is normally closed and is opened on a trip signal according to a time-dependent valve table.
5	Check valve is controlled by a static pressure gradient. IVPG is the gradient option. IVPS defines the cell face where the valve orifice is located. If IVPG = 1, $DP = P(\text{IVPS} - 1) - P(\text{IVPS})$. If IVPG = 2, $DP = P(\text{IVPS}) - P(\text{IVPS} - 1)$. If $DP + PVC1 \geq 0$, valve opens instantly. If $DP + PVC2 < 0$, valve closes instantly.
6	Power-operated valve that opens or closes at fixed rates based on pressure setpoints.
7	Relief valve with multiple setpoints.

7.3 Valve

The valve (VLVE) component models the flow in a valve. A valve is modeled as a one-dimensional component, as shown in Figure 7.3-1. The heat-transfer and fluid-dynamics models used in a valve calculation are identical to those of a pipe (Section 7.1).

Modeling valve action is achieved by controlling the flow area and associated local loss coefficient between two fluid cells. The expressions used for this purpose are:

$$\text{flow area} = \text{AVLVE} \times \text{FRACT}$$

and

$$K_{\text{LOSS}} = f(\text{FRACT})$$

where

AVLVE = Fully open valve flow area

FRACT = Fraction of the valve that is open

f = A user-defined table of loss coefficient versus valve area fraction

Eight user options are provided for controlling the valve action. Option 1 allows valve area control by a control system. Options 1 to 4 allow trip control, with the valve opening or closing instantly or as a function of time. Option 5 models a check valve; an open or closed condition is determined by a pressure differential between the specified cells and two setpoints. Option 6 is a motor-operated valve, while Option 7 simulates relief valve multiple setpoints. The valve option is specified by the value of the input parameter, IVTY. The possible IVTY values and their corresponding options are given in Table 7.3-1.

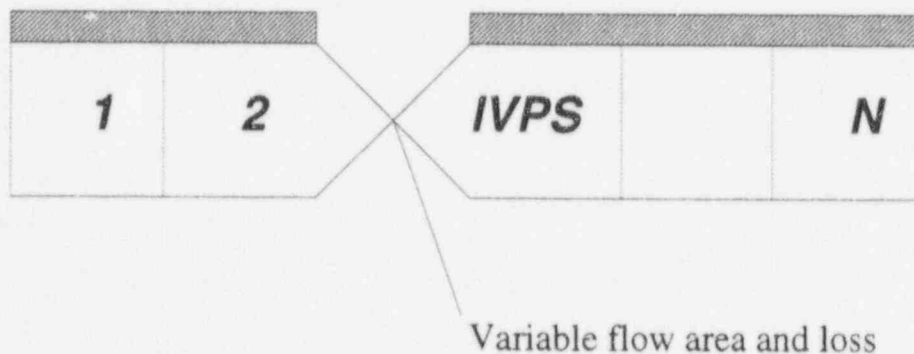


Figure 7.3-1. VLVE Noding Diagram

7.10 Boundary Conditions

The break (BREK) and fill (FILL) components are used to impose boundary conditions at any one-dimensional component terminal junction. Consequently, these components differ from the other components in that they do not model any system component per se or perform hydrodynamic or heat-transfer calculations. However, they are treated like any other component with respect to input, initialization, and identification procedures.

It is recommended that the cell volume and length in these components be identical to those for the neighboring cell of the adjacent component. The void fraction and fluid temperatures specified in the fill and break determine the properties of fluid convected into the adjacent component if an inflow condition should occur. By convention, inflow corresponds to a positive fill velocity and a negative break velocity. The break components may not be connected directly to the vessel component for the purpose of imposing a boundary condition. The connection of the fill directly to the vessel is allowed.

7.10.1 Velocity Specified Boundary Conditions

The fill component imposes a velocity boundary condition at the junction to its adjacent component, as shown in Figure 7.10-1. Fill boundary conditions of velocity, void fraction, and phase temperatures may be constant, user-specified time-dependent, or they may be set by the control system. In addition, the fill velocity condition may be specified as a function of adjacent component pressure. In this case, the pressure functions are imposed in an approximate manner that avoids numerical difficulties caused by instabilities.

7.10.2 Pressure Specified Boundary Conditions

The break component implies a pressure boundary condition one cell away from its adjacent component, as shown in Figure 7.10-2. Like the fill component, this boundary condition may be constant, user-specified time-dependent, or it may be set by the control system. The break component also specifies the boundary conditions of void fraction and phase temperatures at the terminal junctions of one-dimensional components.

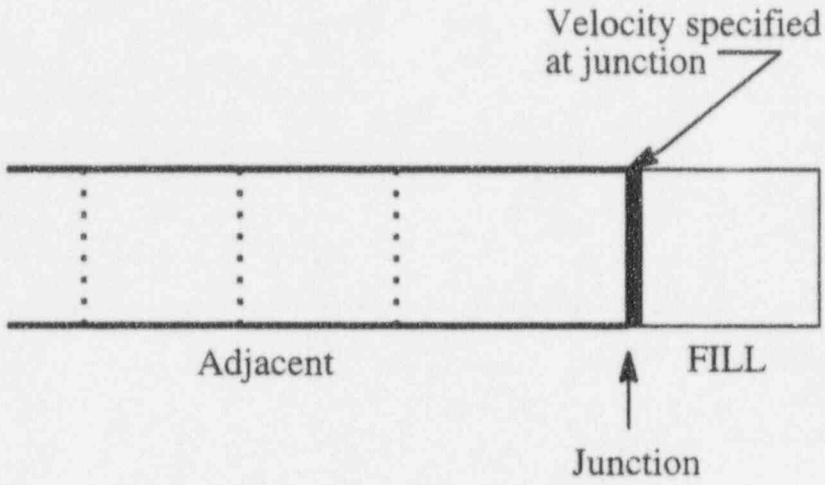


Figure 7.10-1. FILL Noding Diagram

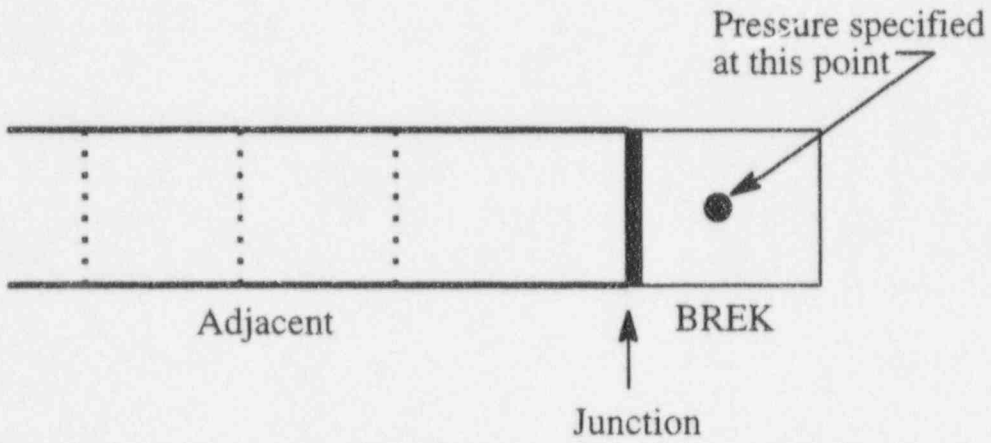


Figure 7.10-2. BREK Noding Diagram

7.11 Containment Components

The containment is modeled with TRACG as a combination of a three-dimensional vessel component in conjunction with one-dimensional components such as pipes, tees and valves. All these components utilize the same conservation equations and constitutive correlations. The set of conservation equations is described in Section 3.1. The correlations for wall heat transfer, interfacial heat transfer, wall shear and interfacial shear are described in Section 6.

BWR containments utilizing the pressure suppression principle have similar components. The specific example referred to in this section is for the Simplified Boiling Water Reactor (SBWR). The SBWR containment is similar in concept to the Mark III and ABWR containments, in that a horizontal vent system is employed to transfer blowdown energy from the drywell to the suppression pool. In addition, the SBWR is equipped with a Passive Containment Cooling System (PCCS) for long-term decay heat removal.

Figure 7.11-1 shows a schematic of the SBWR containment: and reactor pressure vessel (RPV). The three-dimensional vessel (VSSL) component simulates the drywell, wetwell, reactor vessel and the IC and PCC pools.

7.11.1 Drywell

The drywell is composed of an upper drywell, bounded by the drywell head, top slab, containment walls, and the diaphragm floor separating it from the wetwell. The upper drywell (indicated by 1 in Figure 7.11-1) constitutes the largest portion of the drywell volume. A break in the main steam line as well as the opening of the depressurization valves (DPVs) would discharge flow into this region. The annulus region of the drywell (indicated by 2) comprises the region between the RPV and the inner wall of the wetwell horizontal vent duct system. A break in the Gravity-Driven Cooling System (GDCS) line would be expected to discharge flow into this region. The lower drywell (3) is a separate region that is connected to the drywell annulus by 14, 0.8m OD vents. Liquid discharged into the upper drywell or the annulus region 1 (e.g., from a broken GDCS line connected to a GDCS pool) will drain into the lower drywell. A break in the bottom drain line could discharge flow to the lower drywell.

The drywell is modeled as a two-dimensional (axisymmetric) region, with four radial rings in the upper drywell and two radial rings in the annular and lower drywell regions. This allows natural circulation patterns to develop, if calculated, with upflow in one ring and downflow in another. The three-dimensional conservation equations for mass, momentum and energy given in Section 3.1 are applied in this region. Discretization of the equations is shown in Section 3.2.

Specific models are discussed below.

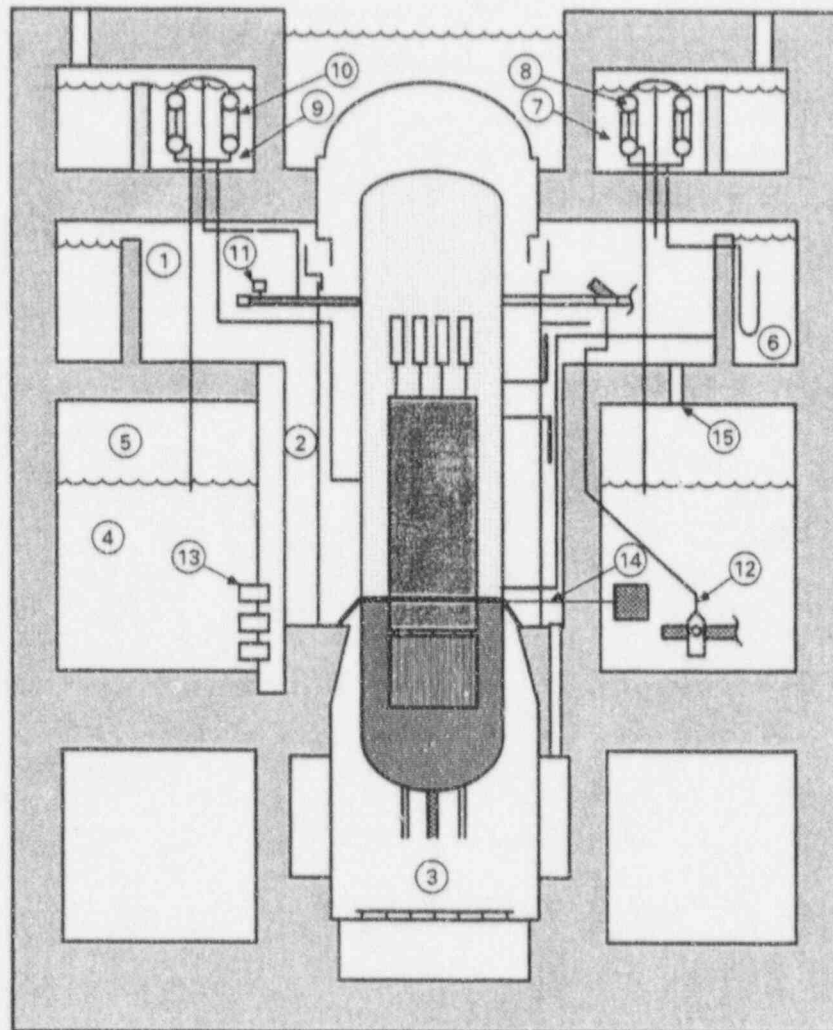


Figure 7.11-1. SBWR Containment

Turbulent Shear Between Cells

The TRACG model for turbulent shear between cells at cell boundaries is not being used. Thus, there is no shear between adjacent cells. All flows in the drywell are driven by buoyancy and wall shear. The nodalization employed ensures the presence of a wall surface in every cell.

Noncondensible Distribution

TRACG has mass continuity equations for multiple species of noncondensibles in addition to steam (Equation 3.1-14). A noncondensible species is treated as a perfect gas and its properties are specified in terms of the gas constant, R and the specific heat c_{pg} (Section 6.6.11). The noncondensible gas (or mixture of gases) has the same temperature and velocity as the steam in a given cell. The partial pressure of the noncondensible gas is calculated based on the temperature and mass of the gas in a cell (Perfect Gas Law). Dalton's law (Equation 3.1-17) relates the partial pressures of steam and noncondensibles to the total pressure. Note that there are no requirements for the steam to be at saturation conditions corresponding to its partial pressure.

The TRACG model for molecular diffusion of noncondensibles driven by concentration gradients is not used. Noncondensibles are transported solely by bulk convection. Diffusion effects will be small for nitrogen and air. Transport by diffusion could be more significant for hydrogen. Buoyancy effects are not treated at a local level (i.e., steam and noncondensibles have the same velocity in a cell). However, buoyancy effects will be accounted for on a global level. For example, if a light noncondensible is injected into a cell, a natural circulation pattern will develop between adjacent rings, and lighter fluid will rise to the upper regions. The distribution of noncondensibles calculated by TRACG is being assessed through comparisons against data from the GIRAFFE and PANDA facilities. Based on these comparisons, a bounding analysis approach will be developed in the SBWR Qualification Report.

Wall Friction Correlations

The flow regime in the drywell is mostly single-phase vapor. In some cells, a dispersed droplet high void fraction regime may exist. This corresponds to cells where liquid from the break or from the GDCS pool with a broken line is falling to the lower regions of the drywell. In some cells, a liquid film can form on the wall because of condensation. The single-phase friction factor is calculated. The Reynolds number is calculated based on the axial velocity in the cell adjacent to the wall and the hydraulic diameter of the cell in the direction of the wall. In case a two-phase flow regime is present, a two-phase multiplier will be applied.

Interfacial Shear Correlations

For the droplet flow regime, the models described in Section 6.1.5 will be employed to calculate the interfacial shear between vapor and droplets. For cells with wall liquid films, the annular flow correlations in Section 6.1.4 are used.

Wall Heat Transfer

The important modes of wall heat transfer in the drywell include forced and free convection to vapor and condensation heat transfer.

For forced convection, TRACG uses the Dittus-Boelter correlation (Equation 6.6-3), based on the cell velocities and properties. The hydraulic diameter of the cell in the direction of the wall is used in the correlation. The vapor properties are calculated at the cell fluid temperature.

For free convection, the McAdams correlation (Equation 6.6-22) is used. Again, the cell temperature is used for the calculation of vapor properties and the cell hydraulic diameter for the calculation of the Grashof number. (The heat transfer coefficient is independent of the hydraulic diameter when correlations of the form $h \sim G_r^{1/3}$ are used.)

These equations and their application are similar to those in other containment codes such as GOTHIC.

TRACG will evaluate both the free and forced convection correlations and use the higher of the two calculated values. The same correlations are used for horizontal surfaces.

The condensation correlations are discussed in Section 6.6.11. A Nusselt condensation correlation is used with multiplicative factors for shear enhancement and degradation by noncondensibles. The Nusselt correlation is expressed in Equations 6.6-66 and 6.6-67. In these equations, the liquid film Reynolds number Re_ℓ is defined as $Re_\ell = 4\Gamma/\mu_\ell$, where Γ is the condensate flow rate per unit perimeter of surface and μ_ℓ is the liquid viscosity. Originally, the Vierow-Schrock correlation was used in TRACG for the shear enhancement and degradation factors. The recommended method currently is to use the Kuhn-Schrock-Peterson (K-S-P) correlation with the shear enhancement factor set to 1. As a lower board, the Uchida correlation is available. For this option, the minimum of the Uchida and K-S-P correlations is used.

Fogging of Drywell Vapor

Heat transfer from the vapor in a cell will result in cooling of the vapor. If the temperature drops below the saturation temperature of the steam corresponding to its partial pressure, condensation will occur. Generally, in this situation a cold wall will be present in the cell. A liquid film will form on the surface because of condensation. This will be typically the dominant form of condensation in the cell. If the temperature drops below saturation in a cell that has no heat transfer surfaces, liquid droplets will form (fogging) by condensation of steam. In this situation, a droplet flow regime will exist. Interfacial heat transfer between droplets and vapor will be calculated as per Section 6.5.5. Interfacial shear between the droplets and steam is calculated using the models in Section 6.1.5.

In general, heat transfer from the vapor is more likely to lead to condensation on the walls. Fogging is more likely to occur as a result of adiabatic expansion of steam from pressures higher than 30 bar.

7.11.2 Wetwell

The wetwell consists of the suppression pool (4) and the wetwell vapor space (5) in Figure 7.11-1. The wetwell is bounded by the diaphragm floor on top, containment outer wall and wetwell inner wall on the sides and the floor of the containment. During blowdown, flow from the safety/relief valves (SRVs) is directed to the suppression pool and quenched via the SRV discharge lines. Flow from the LOCA break and DPVs is directed from the drywell to the suppression pool and quenched via the suppression pool horizontal vent system. Any flow through the Passive Cooling Condenser (PCC) vents is also discharged to the suppression pool.

Wetwell Vapor Space

The wetwell vapor space is also represented by multi-dimensional cells. Typically, two rings and two axial levels are employed in the TRACG model. This would allow for natural circulation in this region. The flow regimes in this region will be the same as in the drywell: single-phase vapor, dispersed droplets resulting from entrainment from the suppression pool, and a condensate film on the walls. The models discussed in the preceding section for the drywell for turbulent shear between cells, noncondensable distribution, wall friction, interfacial friction, wall heat transfer, fogging and interfacial heat transfer apply also in the wetwell vapor space. One other model is important for this region; namely, the heat transfer at the suppression pool interface.

Interfacial Heat Transfer at Pool Interface

The interfacial heat transfer coefficients on the vapor and liquid sides of the interface are defined by Equation 6.5-28. The Sparrow-Uchida correlation shown in Figure 6.5-1 is used to calculate degradation of heat transfer at the pool surface due to noncondensable gases.

Suppression Pool

The suppression pool is represented by multi-dimensional cells. At least two rings are used to represent the pool. The major phenomena of interest for the suppression pool include condensation of vapor bubbles, temperature distribution / thermal stratification and pool two-phase level.

Condensation of Vapor Bubbles

In the presence of noncondensibles, the bubbles will include steam and noncondensibles. The partial pressure of steam and noncondensibles will be calculated as stated earlier. The interfacial heat transfer from the liquid to the vapor is calculated according to Equations 6.5-8 and 6.5-9. There is no degradation in heat transfer due to the presence of noncondensibles. This is based on large-scale data showing complete condensation of steam in the bubbles.

Pool Temperature Distribution

An empirical model is used to force thermal stratification below the lowest thermal source to the pool. This is done by effectively limiting the amount of water that participates in the absorption of energy to that above the lowest discharge location (i.e., lowest active horizontal vent, SRV quencher or PCC vent). Above this elevation, TRACG will calculate circulation velocities which produce a well mixed region. The measured temperature at the top of the pool has been compared with calculations using the empirical model described above. All data are predicted either well or conservatively.

Pool Level

The two-phase level model described in Section 6.4 is used to calculate the pool level. The liquid and vapor side interfacial heat transfer coefficients are calculated with Equation 6.5-28. When the liquid surface is subcooled relative to the partial pressure of steam, the condensation at the surface is reduced by a degradation factor based on the Sparrow-Uchida correlation (Figure 6.5-1).

7.11.3 GDCS Pools

Three GDCS pools (6) are located in the upper drywell (Figure 7.11-1). During the GDCS phase of the post-LOCA transient, the GDCS pools discharge into the RPV downcomer, following the opening of squib valves and check valves in the three divisionally separated GDCS lines. During the intermediate and long-term phases of the post-LOCA transient, the GDCS pools receive condensate from the PCC units. One GDCS pool receives the condensate from two PCC units; one receives condensate from the third PCC unit; and the third is not connected to the PCCS. Each PCC unit condensate return line is designed with a loop seal to prevent reverse flow of steam or noncondensibles in the condensate return line.

The GDCS pools are also modeled as part of the multi-dimensional containment model. In practice, two pools are represented, with one accounting for the volume of two of the three pools. The representation is essentially one-dimensional, with each pool being characterized by one ring. The main phenomenon of interest for the GDCS pool is the pool level and the associated inventory of water in the pool. The two-phase level model referred to earlier is also applicable here. Heat transfer at the pool surface is modeled analogously to that for the suppression pool.

7.11.4 Isolation Condenser (IC)/Passive Containment Condenser (PCC) Pools

The three IC pools (9) are located outside (above) the containment (Figure 7.11-1). Each contains an IC unit. The three pools are interconnected.

The three PCC pools (7) are located outside (above) the containment. Each contains a PCC unit. The three pools are interconnected with each other and with the IC pools.

The pools are represented as part of the 3-D TRACG region, partitioned into the IC and PCC pools. The pools are allowed to communicate with each other at the bottom and the top. Two PCC pools have been combined into one and the third is represented separately. The three IC pools have been combined into one. The pools are modeled with two rings each and with several axial levels. Heat transfer occurs from the PCC and IC headers and tubes to the water in the pools. Pool side heat transfer is calculated by a pool boiling correlation (Forster-Zuber) for boiling heat transfer (Section 6.6.4).

7.11.5 PCC/IC Units

The SBWR has three PCC heat exchanger units (8). Each is comprised of two modules with inlet and outlet headers and 248 tubes in parallel. The PCC units are connected to the top of the upper drywell and discharge condensate into the GDCS pools. Noncondensibles and uncondensed steam are vented to the suppression pool. The vent submergence is 0.9m less than that of the top horizontal LOCA vent. Thus, drywell noncondensibles and uncondensed steam are purged preferentially through the PCC vent line following the early blowdown phase.

The SBWR has three IC heat exchanger units (10) (Figure 7.11-1). Each consists of two modules with inlet and outlet headers and 248 tubes in parallel. The IC units are connected to stub tubes, which are attached to the RPV steam dome. Condensate is discharged into the downcomer of the RPV. Noncondensibles can be vented from the upper and lower IC headers to the suppression pool. This venting processes requires manual action by the operator.

The IC and PCC units are represented by one-dimensional components simulating the inlet piping, headers, condenser tubes, condensate discharge lines and vent lines. One-dimensional forms of the mass, momentum and energy equations in Section 3.1 are applicable. Heat is transferred through the walls of the tubes and headers to the respective pools.

Wall Friction Correlations

The flow regime in the PCC and IC is single-phase vapor at the inlet. Due to condensation, a liquid film forms on the walls. The exit conditions consist of a draining liquid film, and a gas mixture that is rich in noncondensibles. The single-phase friction factor is calculated. The Reynolds number is calculated based on the axial velocity in the cell and the hydraulic diameter of the cell. In the condensing region, a two-phase multiplier will be applied.

Interfacial Shear Correlations

For cells with wall liquid films, the annular flow correlations in Section 6.1.4 are used.

Wall Heat Transfer

The important mode of wall heat transfer in the PCC and IC is condensation heat transfer. Under conditions where condensation heat transfer is severely degraded by a large amount of noncondensibles, forced convection from the vapor to the wall will become the mode of heat transfer.

The condensation correlations are discussed in Section 6.6.11. A Nusselt condensation correlation is used with multiplicative factors for shear enhancement and degradation by noncondensibles. The Nusselt correlation is expressed in Equation 6.6-66. In this equation, the liquid film Reynolds number Re_ℓ is defined as $Re_\ell = 4\Gamma/\mu_\ell$, where Γ is the condensate flow rate per unit perimeter of surface and μ_ℓ is the liquid viscosity. Originally, the Vierow-Schrock correlation was used in TRACG for the shear enhancement and degradation factors. The Kuhn-Schrock-Peterson correlation has also been implemented into TRACG, and is the recommended method. Extensive comparisons have been made against prototypical data from the PANTHERS test facility with excellent results.

For forced convection, TRACG uses the Dittus-Boelter correlation (Equation 6.6-3), based on the cell velocities and properties. The hydraulic diameter of the cell is used in the correlation. The vapor properties are calculated at the cell fluid temperature.

7.11.6 Depressurization Valves

There are 6 DPVs (11) in the SBWR. Four DPVs are on the RPV stub tubes. (The steam supply lines for the three IC units are also connected to three of these stub tubes.) The other two DPVs are on the main steam lines. The DPVs discharge into the upper drywell.

The DPVs are modeled using the VALVE component, which is a one-dimensional component. The TRACG control system will trigger the DPVs to open based on the sensed level in the RPV downcomer. The primary TRACG model associated with the DPV is that of critical flow, which is discussed in Section 7.11.11 in connection with the break.

Critical flow is calculated using the model described in Section 6.3. This model has been extensively qualified. The critical flow is calculated based on the upstream pressure, enthalpy and void fraction. Correlations used in the calculation of interfacial shear in the RPV are given in Section 6.1. The void fraction will depend on the position of the two-phase level in the downcomer. The two-phase level model is described in Section 6.4.

7.11.7 Safety/Relief Valves (SRVs) and Quenchers

Eight SRVs (12) relieve RPV pressure by discharging steam into the suppression pool. Steam is discharged through quenchers to minimize chugging and condensation loads. The quencher submergence is greater than that of the top row of horizontal vents.

The SRVs and associated piping are represented by one-dimensional components. TRACG will trigger the opening of the SRVs based on pressure or downcomer level. The quenchers are not modeled in detail. Condensation and chugging loads will not be calculated with TRACG. Critical flow models used for the SRVs have been discussed for the break and DPVs. Models for the condensation of SRV discharge were referred to in the section on the suppression pool.

7.11.8 Horizontal Vent System

The SBWR has eight sets of horizontal vents between the drywell and the suppression pool. Each set of three vents consists of three horizontal vents (13) attached to a vertical vent pipe (Figure 7.11-1). The top row of horizontal vents is approximately 0.9m below the bottom of the PCC vents. The horizontal vents are represented by one-dimensional TEE components. The vent component is shown in more detail in Figure 7.11-4.

Vent Clearing Model

As the level drops in the pipe to "uncover" the horizontal vent, the vent will be opened to two-phase flow to the suppression pool. This phenomenon is referred to as "vent clearing". Vent clearing terminates the initial pressure rise of the drywell, as the pressure is relieved by the vent discharge to the suppression pool. The top two rows of vents can clear during the early blowdown. As the blowdown flow rate decreases, the water level in the vertical pipes will rise to cover the second row of vents. Eventually, the top row is also covered and only flow through the

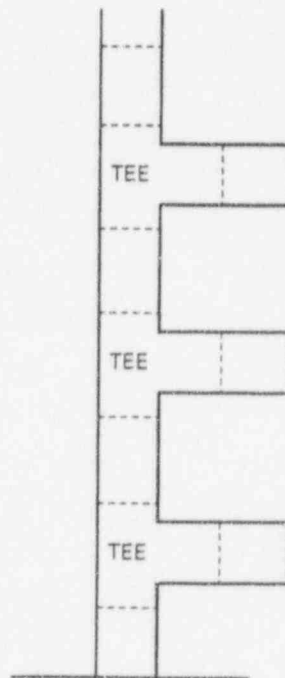


Figure 7.11-4. Horizontal Vent Component

PCC vents, which have a lower submergence, will persist. Following vent clearing, the wetwell gas space pressurizes as the noncondensibles from the drywell are purged into that volume. The drywell pressure is maintained higher than the wetwell by an amount corresponding to the submergence of the open vents.

In the prediction of vent clearing and the associated drywell and wetwell pressure histories, the following phenomena are important:

Level Tracking in the Vertical Vent Pipes

The one dimensional component level tracking model described in Section 6.4 is employed in the vertical pipe that is connected to the three horizontal vents.

Vent Flow Regime

The flow regime in the vents is single-phase liquid, until the vent begins to uncover when it transitions rapidly to bubbly flow. The flow to the vent is "donor celled" at the upstream conditions in the vertical pipe. TRACG calculates a transition from stratified to dispersed flow based on the instability of the interface (Equation 5.1-23).

Pressure Drop Correlations

The single-phase friction factor is calculated. The Reynolds number is calculated based on the axial velocity in the cell and the hydraulic diameter of the cell. The pressure drop in the vent is actually dominated by the inlet and exit form loss coefficients. A two-phase multiplier will be applied for wall friction.

Vent Back Pressure

As the vent discharges vapor into the suppression pool, it will tend to move the liquid in the pool above the vent upwards as it expands. The inertia of this liquid tends to create a back-pressure effect, reducing the discharge flow, and affecting the drywell pressure after vent clearing. This effect is accounted for in the TRACG momentum equation. The liquid mass in the inner ring immediately above the discharge location will have to be accelerated upwards as the vapor expands into the pool.

Model Assessment

The vent clearing model in TRACG has been assessed by comparison against data from the Pressure Suppression Test Facility (PSTF). Figure 7.11-5 shows a schematic of the facility. In the 5703 series tests, the drywell was connected by a set of three full-scale Mark III horizontal vents to an eight degree simulation of the Mark III suppression pool. A rupture disk in the blowdown pipe simulated the break of a main steam line, and a venturi downstream of the rupture disk set the size of the simulated break. The blowdown flow, the vent flow and the drywell and wetwell pressure were monitored.

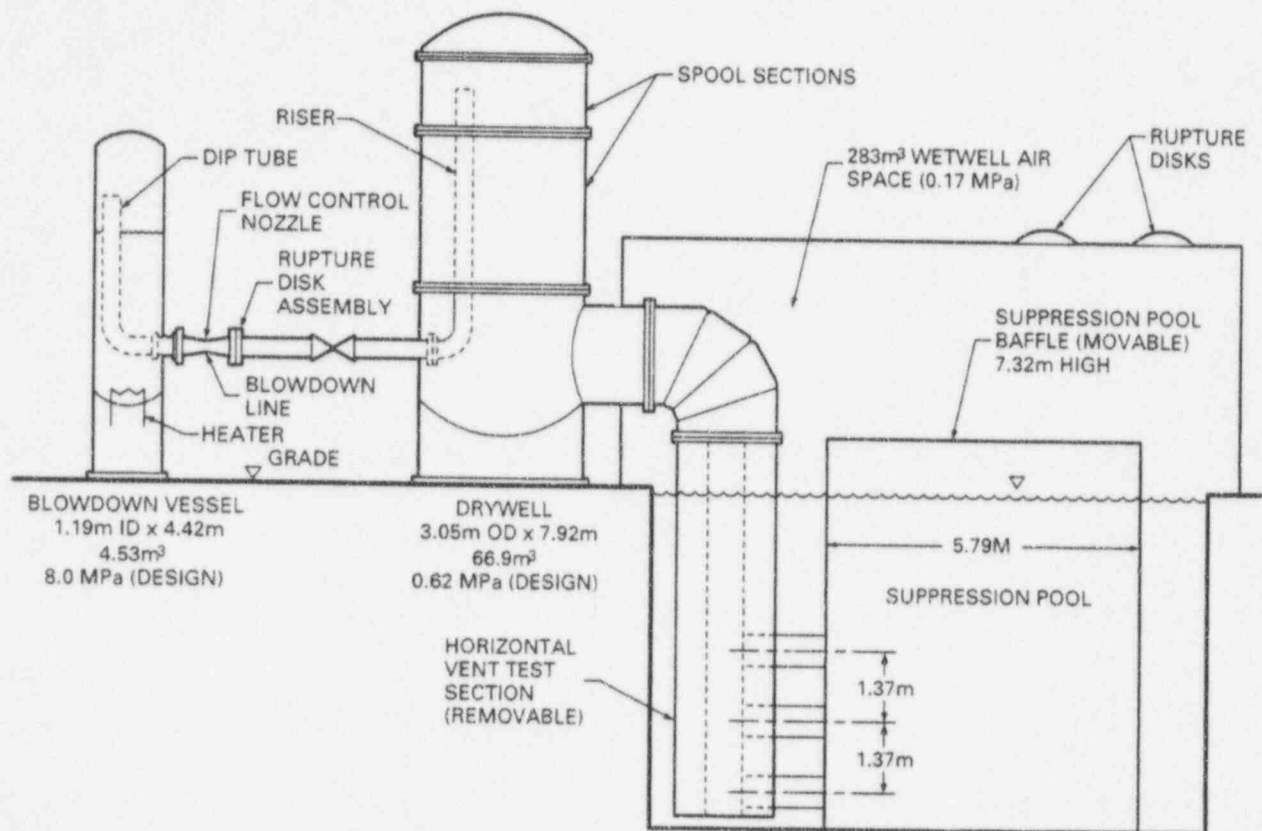


Figure 7.11-5. Pressure Suppression Test Facility

A comparison has been made of the measured and predicted drywell pressures for Test 5703-1. TRACG follows the drywell pressure rate accurately until the time of vent clearing at 0.8 seconds. TRACG also calculates the time of vent clearing correctly. Following the onset of vent clearing, TRACG undercalculates the vent flow, and the drywell pressure increases to a higher value than seen in the data. The discrepancy is due to large vapor bubbles rapidly transiting through the top part of the vent at the inception of vent uncover. This flow regime is not captured by TRACG. A higher calculated two-phase inertial pressure drop in this transient phase delays the increase in the vent flow, and introduces a lag in the calculated transient response. Subsequent to this period, the transient is captured adequately by TRACG. The oscillatory response and slight undershoot in the drywell pressure as well as the final pressure and vent flow are predicted accurately. This indicates that the pressure drop correlation is accurate after the initial vent-clearing transient.

7.11.9 GDCS Equalizing Lines

Three GDCS equalizing lines (14) connect the suppression pool to the RPV downcomer. During the long-term portion of the post-LOCA transient, the squib valves in these lines will open if the level in the downcomer drops to 1m above the top of the active fuel and a time delay of 30 minutes has elapsed.

The equalizing lines are represented by a one-dimensional VALVE component. The correlations used for wall friction and singular losses are the same as described in the previous paragraph for the horizontal vents.

7.11.10 Vacuum Breakers

The SBWR has three vacuum breakers (15) connecting the upper drywell to the wetwell vapor space. The vacuum breakers will open to relieve a negative pressure difference between the drywell and the wetwell.

The vacuum breakers (VB) are represented by one-dimensional VALVE components. Two VBs are lumped together as one component. The VBs are triggered open at a set negative pressure differential between the drywell and wetwell. They will close at a lower value of the pressure differential. The VBs transport flow from the wetwell vapor space to the drywell at conditions corresponding to the cell in the wetwell vapor space to which they are connected. The correlations used for the singular losses are the same as described previously for the horizontal vents.

7.11.11 Break

Critical flow through the break is calculated using the model described in Section 6.3 of this report. This model has been extensively qualified. The critical flow is calculated based on the upstream pressure, enthalpy and void fraction. Correlations used in the calculation of interfacial shear in the RPV are given in Section 6.1 of this report. The void fraction will depend on the position of the two-phase level in the downcomer. The two-phase level model is described in Section 6.4.

In many thermal-hydraulic codes (RELAP, other versions of TRAC), the kinetic energy terms in the energy equation are eliminated by using the momentum equation. This leads to a form of the energy equation which is nonconserving when discretized (i.e., the energy leaving the RPV is not exactly equal to that deposited in the containment). In TRACG, the kinetic energy terms have been retained in the energy equation (Section 3.1), and the discretization is in a conserving form (Section 3.2).

Later in the transient, the flow through the break will no longer be choked. TRACG effectively calculates the minimum of the Bernoulli flow from the momentum equation and critical flow. The flow calculated from the momentum equation cannot exceed the critical flow. At low pressures, the flow will not be limited by critical flow.

8.0 Numerical Method

TRACG uses a fully implicit integration technique for the heat conduction and hydraulic equations. For certain specialized calculations, primarily time domain stability calculations, an optional explicit integration technique can be employed. The fully implicit technique is the default option.

The heat transfer coupling between the structures and the hydraulics is treated implicitly, when the implicit integration technique is used. For this purpose, the heat conduction equation is solved in two steps, and thus integration of the combined equations involves the following steps:

- (1) The heat conduction equation for structures is linearized with respect to fluid temperatures. The result of this step is a system of linear equations for structure temperatures and surface heat flow as functions of the fluid temperatures.
- (2) The hydraulic equations are solved using an iterative technique. This step results in new values for the fluid pressures, void fraction, temperatures and velocities.
- (3) A corrector step is utilized for the hydraulic solution. Due to use of an iterative solution technique, the conservation of the properties is affected by the convergence. The corrector step is employed to correct any lack of conservation due to imperfect convergence.
- (4) Back-substitution into the heat conduction equation is performed to obtain new temperatures for structures.

The linearization of the heat conduction equation and subsequent back-substitution (Steps 1 and 4) are described in Section 8.1. The hydraulic solution (Steps 2 and 3) are described in Section 8.2.

The nomenclature used in Section 8 is given below:

A	flow area between mesh cells
A	surface area
B_s	source term in momentum equation
c	concentration (boron)
c_p	Specific Heat
e	internal energy
E_s	source term in energy equation
F_w	wall shear
f	interfacial shear
g	acceleration of gravity

h	heat transfer coefficient
h	internal enthalpy
h_{fg}	$h_g - h_f$
k	constant in virtual mass term in momentum equation
k	conductivity
M	mass
M_d	interface shear
M_s	source term in mass equation
P	pressure
q	heat transfer rate
r	radial dimension
R	gas constant
r	radial dimension
R	Radial dimension for 3-D components
T	temperature
t	time
V	cell volume
v	velocity
x	dimension for 1-D component
z	axial dimension for 3-D components

Greek Symbols

α	gas volume fraction
Γ_g	interfacial mass transfer rate
ρ	microscopic density
σ	Surface tension
τ	shear tensor
θ	azimuthal dimension for 3-D components
θ	indicator for implicit/explicit integration (hydraulic model)

Subscript

a	all noncondensable gases
b	boron
c	continuous phase
d	dispersed phase
f	saturated liquid

g	saturated steam
i	inner surface
ℓ	liquid phase
n	noncondensable gas
o	outer surface
r	relative (vapor-liquid)
s	steam
sat	saturation
v	gas phase (mixture)
w	wall

Superscript

d	donor celled
n	time step number

8.1 Finite Difference Formulation of Heat Conduction Equation

The heat conduction equation for the fuel rods and heat slabs is solved using either a lumped slab model or a one-dimensional model. The one-dimensional model can be formulated either in cartesian coordinates or in cylindrical coordinates. The lumped slab model is used for heat slabs completely internal to a single cell in the vessel component. The one-dimensional model using cartesian coordinates is used for heat slabs in the vessel component situated between two axial levels. The one-dimensional model using cylindrical coordinates is used for the fuel rods, the walls of a one-dimensional component, and for heat slabs in the vessel component situated between two radial rings.

8.1.1 Lumped Slab Heat Conduction

The lumped slab heat conduction model is given by Equation 4.2.1.

Introducing

$$\Delta T^{n+1} = T^{n+1} - T^n \quad (8.1-1)$$

$$q_{w\ell} = A_w h_{w\ell} (T_w - T_\ell) \quad (8.1-2)$$

and

$$q_{wv} = A_w h_{wv} (T_w - T_v) \quad (8.1-3)$$

Equations 8.1-2 and 8.1-3 can be linearized as:

$$q_{w\ell}^{n+1} = q_{w\ell}^n - \theta \frac{\partial q_{w\ell}}{\partial T_\ell} (\Delta T_w^{n+1} - \Delta T_\ell^{n+1}) \quad (8.1-4)$$

and

$$q_{wv}^{n+1} = q_{wv}^n - \theta \frac{\partial q_{wv}}{\partial T_v} (\Delta T_w^{n+1} - \Delta T_v^{n+1}) \quad (8.1-5)$$

Equation 4.2-1 can be written as:

$$M_w C_{pw}^n \Delta T_w^{n+1} = -\Delta t \left[q_{w\ell}^n - \theta \frac{\partial q_{w\ell}}{\partial T_\ell} (\Delta T_w^{n+1} - \Delta T_\ell^{n+1}) \right] \quad (8.1-6)$$

$$-\Delta t \left[q_{wv}^n - \theta \frac{\partial q_{wv}}{\partial T_v} (\Delta T_w^{n+1} - \Delta T_v^{n+1}) \right]$$

This equation can be rewritten as:

$$\Delta T_w^{n+1} = \Delta \tilde{T}_w^{n+1} + \frac{\partial T_w}{\partial T_\ell} \Delta T_\ell^{n+1} + \frac{\partial T_w}{\partial T_v} \Delta T_v^{n+1} \quad (8.1-7)$$

where

$$\Delta \tilde{T}_w^{n+1} = \frac{-\Delta t (q_{w\ell}^n + q_{wv}^n)}{MC_{pw}^n - \Delta t \theta \left(\frac{\partial q_{w\ell}}{\partial T_\ell} + \frac{\partial q_{wv}}{\partial T_v} \right)}$$

$$\frac{\partial T_w}{\partial T_\ell} = \frac{-\Delta t \theta \frac{\partial q_{w\ell}}{\partial T_\ell}}{MC_{pw}^n - \Delta t \theta \left(\frac{\partial q_{w\ell}}{\partial T_\ell} + \frac{\partial q_{wv}}{\partial T_v} \right)}$$

$$\frac{\partial T_w}{\partial T_v} = \frac{-\Delta t \theta \frac{\partial q_{wv}}{\partial T_v}}{MC_{pw}^n - \Delta t \theta \left(\frac{\partial q_{w\ell}}{\partial T_\ell} + \frac{\partial q_{wv}}{\partial T_v} \right)}$$

Substituting Equation 8.1-7 into Equation 8.1-4, one gets:

$$q_{w\ell}^{n+1} = q_{w\ell}^n - \theta \frac{\partial q_{w\ell}}{\partial T_\ell} \left[\Delta \tilde{T}_w^{n+1} + \left(\frac{\partial T_w}{\partial T_\ell} - 1 \right) \Delta T_\ell^{n+1} + \left(\frac{\partial T_w}{\partial T_v} \right) \Delta T_v^{n+1} \right] \quad (8.1-8)$$

Similar equations can be obtained for the vapor phase:

$$q_{wv}^{n+1} = q_{wv}^n - \theta \frac{\partial q_{wv}}{\partial T_v} \left[\Delta \bar{T}_w^{n+1} + \left(\frac{\partial T_w}{\partial T_\ell} \right) \Delta T_\ell^{n+1} + \left(\frac{\partial T_w}{\partial T_v} - 1 \right) \Delta T_v^{n+1} \right] \quad (8.1-9)$$

At the back-substitution step, after the final fluid temperatures have been obtained, the final wall temperatures are obtained by back-substitution into Equation 8.1-7.

8.1.2 One-Dimensional Heat Conduction in Cartesian Coordinates

The one-dimensional heat conduction equation in cartesian coordinates is given by Equations 4.2-2 – 4.2-4.

These equations represent a system of linear equations, which can be written as:

$$\underline{\underline{A}} \bullet \Delta \bar{T}_w^{n+1} = \bar{B} + \bar{C}_{\ell i} \Delta T_{\ell i}^{n+1} + \bar{C}_{vi} \Delta T_{vi}^{n+1} + \bar{C}_{\ell o} \Delta T_{\ell o}^{n+1} + \bar{C}_{vo} \Delta T_{vo}^{n+1} \quad (8.1-10)$$

8.1.3 One-Dimensional Heat Conduction in Cylindrical Coordinates

The one-dimensional heat conduction equation in cylindrical coordinates is given by Equations 4.2-5 – 4.2-10.

These equations represent a system of linear equations, which can be written as:

$$\underline{\underline{A}} \bullet \Delta \bar{T}_w^{n+1} = \bar{B} + \bar{C}_{\ell i} \Delta T_{\ell i}^{n+1} + \bar{C}_{wi} \Delta T_{wi}^{n+1} + \bar{C}_{\ell o} \Delta T_{\ell o}^{n+1} + \bar{C}_{vo} \Delta T_{vo}^{n+1} \quad (8.1-18)$$

These equations are solved exactly as the system of one-dimensional equations for heat conduction in Cartesian coordinates as described in Section 8.1.2.

8.2 Discretization of Hydraulic Equations

TRACG solves the conservation equations for mass, momentum, and energy for the vapor and liquid phases. The vapor phase can be a mixture of steam and noncondensable gases. Dissolved noncondensable gases in the liquid are not considered.

8.2.1 Predictor Step

The spatial discretization of the 3-D conservation equations was shown in Section 3.2.2. In this section the discretization in time will be developed. The modification to the existing semi-implicit integration technique to generate the predictor step only affects the temporal discretization.

8.2.1.1 Momentum Equations

The spatial discretization of the momentum equations was shown in Section 3.2.2.1. In developing the temporal discretization, let us consider vapor and liquid momentum equations for the axial direction (Equations 3.2-20 and 3.2-23). As mentioned earlier, the main modification affects the convective terms. In the convective terms the diagonal terms will be calculated using a combination of old and new time properties, such that outflow is given by the new time properties and inflow by the old time properties. The off-diagonal terms will be based strictly on old time properties as before. The interfacial shear and wall friction will be based on the new velocities using a Taylor expansion around the old velocities. The fully discretized axial momentum equations then become:

Vapor

$$v_{vz,I+1/2,J,K}^{n+1} - v_{vz,I+1/2,J,K}^n + \Delta t v_{vz,I+1/2,J,K}^n \begin{cases} \frac{v_{vz,I+1/2,J,K}^{n+1} - v_{vz,I-1/2,J,K}^n}{\Delta z_I} & \text{if } v_{vz,I+1/2,J,K}^n \geq 0 \\ \frac{v_{vz,I+3/2,J,K}^n - v_{vz,I+1/2,J,K}^{n+1}}{\Delta z_{I+1}} & \text{if } v_{vz,I+1/2,J,K}^n < 0 \end{cases}$$

$$+ \Delta t \left[v_{vR} \left(\frac{\partial v_{vz}}{\partial R} \right)^d + \frac{v_{v\theta}}{R} \left(\frac{\partial v_{vz}}{\partial \theta} \right)^d \right]_{I+1/2,J,K}^n$$

$$+ \left(\frac{k\rho_c}{\alpha\rho_v} \right)_{I+1/2,J,K}^n \left[v_{rz}^{n+1} - v_{rz}^n + \Delta t v_{dz}^n \begin{cases} \frac{v_{rz,I+1/2,J,K}^{n+1} - v_{rz,I-1/2,J,K}^n}{\Delta z_I} & \text{if } v_{dz}^n \geq 0 \\ \frac{v_{rz,I+3/2,J,K}^n - v_{rz,I+1/2,J,K}^{n+1}}{\Delta z_{I+1}} & \text{if } v_{dz}^n < 0 \end{cases} \right]_{I+1/2,J,K} =$$

$$- \frac{\Delta t}{\rho_{v,I+1/2,J,K}} \frac{P_{I+1,J,K}^{n+1} - P_{I,J,K}^{n+1}}{\Delta z_{I+1/2}} - g\Delta t + B_{vz,I+1/2,J,K}^n \Delta t \tag{8.2-1}$$

$$- \frac{\Delta t}{(\alpha\rho_v)_{I+1/2,J,K}} \left[f_{\ell v}^n + \frac{\partial f_{\ell v}^n}{\partial v_{vz}} (v_{vz}^{n+1} - v_{vz}^n) + \frac{\partial f_{\ell v}^n}{\partial v_{\ell z}} (v_{\ell z}^{n+1} - v_{\ell z}^n) \right]_{z,I+1/2,J,K}$$

$$- \frac{\Delta t}{\rho_{v,I+1/2,J,K}} \left[F_w^n + \frac{\partial F_w^n}{\partial v_{vz}} (v_{vz}^{n+1} - v_{vz}^n) + \frac{\partial F_w^n}{\partial v_{\ell z}} (v_{\ell z}^n - v_{\ell z}^n) \right]_{z,I+1/2,J,K}$$

where B_v include the source and mixing terms.

Liquid:

$$v_{\ell z, I+1/2, J, K}^{n+1} - v_{\ell z, I+1/2, J, K}^n + \Delta t v_{\ell z, I+1/2, J, K}^n \left\{ \begin{array}{l} \frac{v_{\ell z, I+1/2, J, K}^{n+1} - v_{\ell z, I-1/2, J, K}^n}{\Delta z_I} \text{ if } v_{\ell z, I+1/2, J, K}^n \geq 0 \\ \frac{v_{\ell z, I+3/2, J, K}^n - v_{\ell z, I-1/2, J, K}^{n+1}}{\Delta z_{I+1}} \text{ if } v_{\ell z, I+1/2, J, K}^n < 0 \end{array} \right.$$

$$+ \Delta t \left[v_{\ell R} \left(\frac{\partial v_{\ell z}}{\partial R} \right)^d + \frac{v_{\ell \theta}}{R} \left(\frac{\partial v_{\ell z}}{\partial \theta} \right)^d \right]_{I+1/2, J, K}^n$$

$$- \left(\frac{k\rho_c}{(1-\alpha)\rho_\ell} \right)_{I+1/2, J, K}^n \left[v_{rz}^{n+1} - v_{rz}^n + \Delta t v_{dz}^n \left\{ \begin{array}{l} \frac{v_{rz, I+1/2, J, K}^{n+1} - v_{rz, I-1/2, J, K}^n}{\Delta z_I} \text{ if } v_{dz}^n \geq 0 \\ \frac{v_{rz, I+3/2, J, K}^n - v_{rz, I-1/2, J, K}^{n+1}}{\Delta z_{I+1}} \text{ if } v_{dz}^n < 0 \end{array} \right. \right]_{I+1/2, J, K} =$$

$$- \frac{\Delta t}{\rho_{\ell, I+1/2, J, K}} \frac{P_{I+1, J, K}^{n+1} - P_{I, J, K}^{n+1}}{\Delta z_{I+1/2}} - g\Delta t + B_{\ell z, I+1/2, J, K}^n \Delta t \quad (8.2-2)$$

$$+ \frac{\Delta t}{[(1-\alpha)\rho_\ell]_{I+1/2, J, K}} \left[f_{\ell v}^n + \frac{\partial f_{\ell v}^n}{\partial v_{vz}} (v_{vz}^{n+1} - v_{vz}^n) + \frac{\partial f_{\ell v}^n}{\partial v_{\ell z}} (v_{\ell z}^{n+1} - v_{\ell z}^n) \right]_{z, I+1/2, J, K}$$

$$- \frac{\Delta t}{\rho_{\ell, I+1/2, J, K}} \left[F_w^n + \frac{\partial F_w^n}{\partial v_{vz}} (v_{vz}^{n+1} - v_{vz}^n) + \frac{\partial F_w^n}{\partial v_{\ell z}} (v_{\ell z}^{n+1} - v_{\ell z}^n) \right]_{z, I+1/2, J, K}$$

Examination of these equations reveals that they are linear equations in $v_{vz, I+1/2, J, K}^{n+1}$, $v_{\ell z, I+1/2, J, K}^{n+1}$, $P_{I, J, K}^{n+1}$, and $P_{I+1, J, K}^{n+1}$. Consequently, the new velocities can be solved for as a function of the new pressures.

$$v_{vz, I+1/2, J, K}^{n+1} = \tilde{v}_{vz, I+1/2, J, K} + C_{vz, I+1/2, J, K} \left(P_{I, J, K}^{n+1} - P_{I+1, J, K}^{n+1} \right) \quad (8.2-3)$$

$$v_{\ell z, I+1/2, J, K}^{n+1} = \tilde{v}_{\ell z, I+1/2, J, K} + C_{\ell z, I+1/2, J, K} \left(P_{I, J, K}^{n+1} - P_{I+1, J, K}^{n+1} \right) \quad (8.2-4)$$

Similar equations can be generated for the radial and azimuthal directions, and for any source connection to the cell. These equations are used as shown in the next section to eliminate the velocities from the convective terms in the mass and energy equations.

8.2.2 Network Solution

For the sake of completeness, the network solution will be reviewed here.

Multiplying by $(A_{=IJK})^{-1}$ and omitting the superscript, one gets:

$$\begin{Bmatrix} \Delta P \\ \Delta \alpha \\ \Delta T_v \\ \Delta T_\ell \\ \Delta P_a \end{Bmatrix}_{IJK}^{n+1,m} = \bar{B}'_{IJK} + \sum_{j=1}^{N_f} \bar{C}'_{j,IJK} \Delta P_{j,IJK} + \sum_{j=1}^{N_s} \bar{S}c'_{j,IJK} (\Delta P_{IJK} - \Delta P_{s_j,IJK}) \quad (8.2-28)$$

where:

$$\bar{B}'_{IJK} = (A_{=IJK})^{-1} \cdot \bar{B}_{IJK} \quad (8.2-29)$$

$$\bar{C}'_{j,IJK} = (A_{=IJK})^{-1} \cdot \bar{C}_{j,IJK} \quad (8.2-30)$$

$$\bar{S}c'_{j,IJK} = (A_{=IJK})^{-1} \cdot \bar{S}c_{j,IJK} \quad (8.2-31)$$

By examination of this equation, it is obvious that when all ΔP_s are known $\Delta \alpha$, ΔT_v , ΔT_ℓ , and ΔP_a can be obtained through back-substitution. Consequently, the task in the network solution reduces to the calculation of the change in total pressure, ΔP .

The first row in Equation 8.2-28 is:

$$\Delta P_{IJK} = \{B'_{IJK}\}_1 + \sum_{j=1}^{N_f} \{C'_{j,IJK}\}_1 \Delta P_{j,IJK} + \sum_{j=1}^{N_s} \{Sc'_{j,IJK}\}_1 (\Delta P_{IJK} - \Delta P_{s_j,IJK}) \quad (8.2-32)$$

This is the pressure equation that is solved in the network solution.

For a 1-D component, the equivalent equation to Equation 8.2-32 reduces to:

$$\Delta P_i = \{b'_i\}_1 + \sum_{j=1}^{N_f} \{c'_{j,i}\}_1 \Delta P_{j,i} + \sum_{j=1}^{N_s} \{sc'_{j,i}\}_1 (\Delta P_i - \Delta P_{s_j,i}) \quad (8.2-33)$$

where N_n is the number of neighboring cells and N_s is the number of sources to any given cell (in this context a source is a junction to another component)

$$N_n = 2, 3 \quad \text{for an internal cell,} \quad N_n = 1, 2 \quad \text{for an end cell}$$

$$N_s = 0 \quad \text{for an internal cell,} \quad N_s = 1 \quad \text{for an end cell}$$

Rearranging Equation 8.2-33 to:

$$\Delta P_i - \sum_{j=1}^{N_n} \{c'_{j,i}\}_1 (\Delta P_{j,i}) = \{b'_i\}_1 + \sum_{j=1}^{N_s} \{sc'_{j,i}\}_1 (\Delta P_i - \Delta P_{s_j,i}) \quad (8.2-34)$$

and remembering that $\{sc'_{j,i}\}_1$ is only non-zero for an end cell, the system of linear equations can be solved to give:

$$\Delta P_i = d_i + \sum_{s=1}^{N_{st}} e_{i,s} \Delta^2 P_{j_s} \quad (8.2-35)$$

where $\Delta^2 P_{j_s}$ is the change in ΔP across the source junctions:

$$\text{e.g. } \Delta^2 P_{j_{ik}} = \Delta P_{i_1} - \Delta P_{k_m} \quad (8.2-36)$$

and N_{st} is the total number of source junctions.

Let two 1-D components be joined together in a junction as shown in Figure 8.2-1.

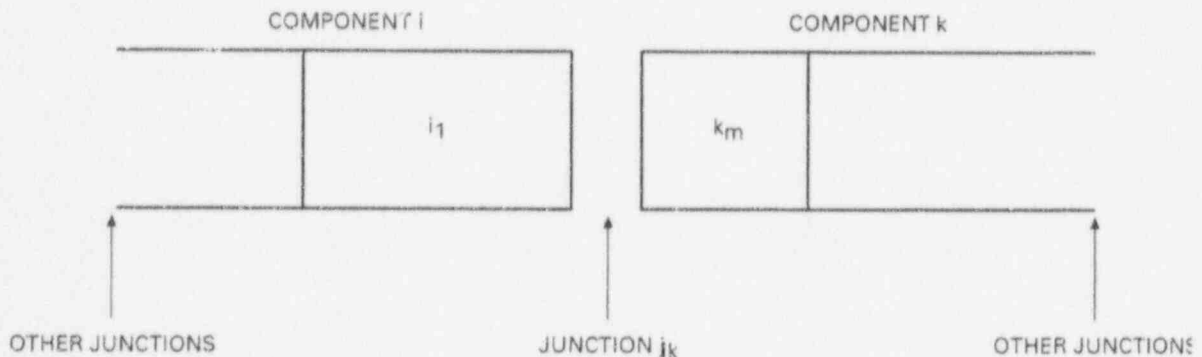


Figure 8.2-1. Junction of 1-D Components

Let $\vec{\Delta^2 P_j}$ be a vector describing the change in ΔP across all junctions in the system including 1D-1D and 1D-3D junctions. For cell i_1 , Equation 8.2-35 can be written as:

$$\Delta P_{i_1} = d_{i_1} + \vec{e}_{i_1} \cdot \vec{\Delta^2 P_j} \quad (8.2-37)$$

Similarly, for cell k_m , Equation 8.2-35 can be written as:

$$\Delta P_{k_m} = d_{k_m} + \vec{e}_{k_m} \cdot \vec{\Delta^2 P_j} \quad (8.2-38)$$

Subtracting Equation 8.2-37 from Equation 8.2-38 and remembering that:

$$\Delta^2 P_{j_{ik}} = \Delta P_{k_m} - \Delta P_{i_1}$$

one gets:

$$\Delta^2 P_{j_{ik}} = d_{k_m} - d_{i_1} + (\vec{e}_{k_m} - \vec{e}_{i_1}) \cdot \vec{\Delta^2 P_j} \quad (8.2-39)$$

A 1-D component is connected to a 3-D component as shown in Figure 8.2-2.

For cell i_1 , Equation 8.2-35 can be written as:

$$\Delta P_{i_1} = d_{i_1} + \vec{e}_{i_1} \cdot \vec{\Delta^2 P_j} \quad (8.2-40)$$

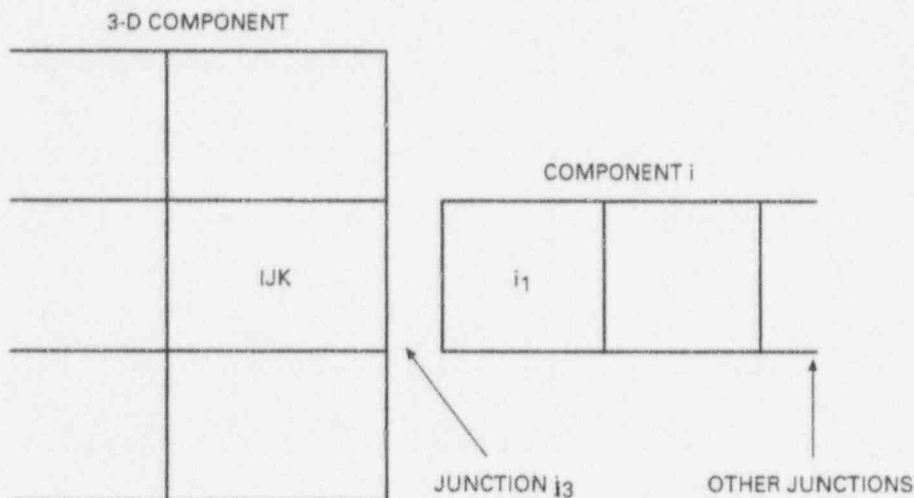


Figure 8.2-2. Junction of 1-D and 3-D Components

Subtracting ΔP_{IJK} from this equation and remembering that:

$$\Delta^2 P_{j_{i3}} = \Delta P_{i_1} - \Delta P_{IJK}$$

one gets:

$$\Delta^2 P_{j_{i3}} = d_{i_1} + e_{i_1} \cdot \vec{\Delta^2 P_j} - \Delta P_{IJK} \quad (8.2-41)$$

For all junctions, Equations 8.2-39 and 8.2-41 will thus form a system of linear equations:

$$\underline{\underline{E}} \cdot \vec{\Delta^2 P_j} = \underline{\underline{D}} + \underline{\underline{F}} \cdot \vec{\Delta P^3} \quad (8.2-42)$$

where $\vec{\Delta P^3}$ is a vector of all the pressure changes for the 3-D component. Equation 8.2-42 can be solved to give:

$$\vec{\Delta^2 P_j} = \underline{\underline{D'}} + \underline{\underline{F'}} \cdot \vec{\Delta P^3} \quad \text{where} \quad (8.2-43)$$

$$\underline{\underline{D'}} = (\underline{\underline{E}})^{-1} \cdot \underline{\underline{D}} \quad (8.2-44)$$

$$\underline{\underline{F'}} = (\underline{\underline{E}})^{-1} \cdot \underline{\underline{F}} \quad (8.2-45)$$

In Equation 8.2-32, $\Delta P_{IJK} - \Delta P_{s_{j,IJK}}$ is ΔP across a junction to a 1-D component. Consequently, Equation 6.3-32 can be written as :

$$\underline{\underline{G}} \cdot \vec{\Delta P^3} = \underline{\underline{B}}_1 + \underline{\underline{S}}_c \cdot \vec{\Delta^2 P_j} \quad (8.2-46)$$

Substituting Equation 8.2-43 into this equation, one gets:

$$\underline{\underline{G}} \cdot \vec{\Delta P^3} = \underline{\underline{B}}_1 + \underline{\underline{S}}_c \cdot [\underline{\underline{D'}} + \underline{\underline{F'}} \cdot \vec{\Delta P^3}] \quad (8.2-47)$$

Equation 8.2-47 is the final equation in the network solution. It is a system of linear equations that can be solved for pressure changes in the 3-D component.

The rest of the solution consists of back-substitution. $\vec{\Delta^2 P_j}$ is obtained from Equation 8.2-43, the changes in individual pressures in the 1D components are obtained from Equation 8.2-35, and finally the changes in α , T_g , $T_{g'}$, and P_a are obtained from Equation 8.2-28 and its equivalent for the 1-D components.

8.2.3 Corrector Step

TRACG uses a fully implicit method for the mass and energy equations in the predictor step. An iterative technique is used for the predictor step. For a fully converged iteration perfect mass and energy conservation is obtained for the predictor step, and the corrector step is not needed. The corrector step is a leftover from the time when TRAC did not have a fully implicit solution. It has been left in since it does assure perfect mass conservation, and for nodes where there is thermal equilibrium conservation of mass is equivalent with conservation of energy for constant pressure.

8.2.3.1 Mixture Mass Conversion

$$\begin{aligned}
 & V_{IJK} \left\{ [(1-\alpha)\rho_\ell + \alpha\rho_v]^{n+1} - [(1-\alpha)\rho_\ell + \alpha\rho_v]^n \right\}_{IJK} = \\
 & - \Delta t A_{I+1/2,J,K} v_{\ell z, I+1/2, J, K}^{n+1} \left\{ \begin{array}{l} [(1-\alpha)\rho_\ell]_{I,J,K}^{n+1} \quad \text{if } v_{\ell z, I+1/2, J, K}^{n+1} \geq 0 \\ [(1-\alpha)\rho_\ell]_{I+1, J, K}^{n+1} \quad \text{if } v_{\ell z, I+1/2, J, K}^{n+1} < 0 \end{array} \right. \\
 & + v_{vz, I+1/2, J, K}^{n+1} \left\{ \begin{array}{l} (\alpha\rho_v)_{I,J,K}^{n+1} \quad \text{if } v_{vz, I+1/2, J, K}^{n+1} \geq 0 \\ (\alpha\rho_v)_{I+1, J, K}^{n+1} \quad \text{if } v_{vz, I+1/2, J, K}^{n+1} < 0 \end{array} \right. \\
 & - \Delta t A_{I-1/2, J, K} v_{\ell z, I-1/2, J, K}^{n+1} \left\{ \begin{array}{l} [(1-\alpha)\rho_\ell]_{I-1, J, K}^{n+1} \quad \text{if } v_{\ell z, I-1/2, J, K}^{n+1} \geq 0 \\ [(1-\alpha)\rho_\ell]_{I, J, K}^{n+1} \quad \text{if } v_{\ell z, I-1/2, J, K}^{n+1} < 0 \end{array} \right. \\
 & + v_{vz, I-1/2, J, K}^{n+1} \left\{ \begin{array}{l} (\alpha\rho_v)_{I-1, J, K}^{n+1} \quad \text{if } v_{vz, I-1/2, J, K}^{n+1} \geq 0 \\ (\alpha\rho_v)_{I, J, K}^{n+1} \quad \text{if } v_{vz, I-1/2, J, K}^{n+1} < 0 \end{array} \right.
 \end{aligned}$$

Similar terms for the J and K directions

$$+ V_{IJK} \left(M_{ms}^{n+1} + M_{mmix}^{n+1} \right)_{IJK} \Delta t + \tag{8.2-49}$$

In this equation, the densities and velocities are those calculated in the predictor for step n+1.

The source term is calculated using a fully implicit technique:

$$\begin{aligned}
 (\mathbf{V} \cdot \mathbf{M}_{ms})_{IJK}^{n+1} = -A_{s,IJK} & \left[v_{\ell s,IJK}^{n+1} \begin{cases} [(1-\alpha)\rho_\ell]_{IJK}^{n+1} & \text{if } v_{\ell s,IJK}^{n+1} \geq 0 \\ [(1-\alpha)\rho_\ell]_{s,IJK}^{n+1} & \text{if } v_{\ell s,IJK}^{n+1} < 0 \end{cases} \right. \\
 & \left. + v_{vs,IJK}^{n+1} \begin{cases} (\alpha\rho_v)_{IJK}^{n+1} & \text{if } v_{vs,IJK}^{n+1} \geq 0 \\ (\alpha\rho_v)_{s,IJK}^{n+1} & \text{if } v_{vs,IJK}^{n+1} < 0 \end{cases} \right] \quad (8.2-50)
 \end{aligned}$$

Again, the densities and velocities are the new values obtained from the predictor step. Substituting Equation 8.2-50 into 8.2-49 gives an equation in only the new void fractions, which can be arranged to be of the form:

$$A_{IJK} \Delta\alpha_{IJK}^{n+1} = B_{IJK} + \sum_{j=1}^{N_f} C_{j,IJK} \Delta\alpha_{j,IJK}^{n+1} + \sum_{j=1}^{N_s} S c_j (\Delta\alpha_{IJK}^{n+1} - \Delta\alpha_{s_j,IJK}^{n+1}) \quad (8.2-51)$$

Dividing this equation with A_{IJK} gives an equation of exactly the same form as the pressure Equation 8.2-32 and the network solver can be used unchanged to obtain the new void fractions. Since Equation 8.2-49 is on a conserving form, the mixture mass is conserved perfectly.

8.2.3.2 Noncondensable Gas Conservation

To determine the amount of total noncondensable gas relative to steam and to get perfect mass conservation, the total noncondensable mass equation is discretized using a fully implicit technique as:

$$\begin{aligned}
 V_{IJK} (m_a^{n+1} - m_a^m)_{IJK} = & \\
 -A_{I+1/2,J,K} & \left[v_{vz,I+1/2,J,K}^{n+1} \begin{cases} (m_a)_{I,J,K}^{n+1} & \text{if } v_{vz,I+1/2,J,K}^{n+1} \geq 0 \\ (m_a)_{I+1,J,K}^{n+1} & \text{if } v_{vz,I+1/2,J,K}^{n+1} < 0 \end{cases} \right] \Delta t \\
 +A_{I-1/2,J,K} & \left[v_{vz,I-1/2,J,K}^{n+1} \begin{cases} (m_a)_{I-1,J,K}^{n+1} & \text{if } v_{vz,I-1/2,J,K}^{n+1} \geq 0 \\ (m_a)_{I,J,K}^{n+1} & \text{if } v_{vz,I-1/2,J,K}^{n+1} < 0 \end{cases} \right] \Delta t \quad (8.2-52)
 \end{aligned}$$

+ Similar terms in J and K directions

$$+ V_{IJK} (M_{as}^{n+1} + M_{arr.ix}^{n+1})_{IJK} \Delta t$$

+ Similar terms in J and K directions

$$+ V_{IJK} \left(M_{as}^{n+1} + M_{amix}^{n+1} \right)_{IJK} \Delta t$$

where $m_a = (\alpha \rho_a)$

The source term is given as:

$$V_{IJK} \bullet M_{as,IJK}^{n+1} = -A_{s,IJK} v_{vs,IJK}^{n+1} \begin{cases} (m_a)_{IJK}^{n+1} & \text{if } v_{vs,IJK}^{n+1} \geq 0 \\ (m_a)_{s,IJK}^{n+1} & \text{if } v_{vs,IJK}^{n+1} < 0 \end{cases} \quad (8.2-53)$$

Substituting Equation 8.2-53 into 8.2-52 gives an equation in only the new total noncondensable mass concentration, which can be rearranged to be of the form:

$$A_{IJK} \Delta m_{a,IJK}^{n+1} = B_{IJK} + \sum_{j=1}^{N_f} C_{j,IJK} \Delta m_{aj,IJK}^{n+1} + \sum_{j=1}^{N_a} Sc_j \left(\Delta m_{a,IJK}^{n+1} - \Delta m_{asj,IJK}^{n+1} \right) \quad (8.2-54)$$

This equation is again of the same form as the pressure equation (8.2-32) and the network solver is used unchanged to get the new total noncondensable gas mass.

8.2.3.3 Liquid Solute Conservation

To determine the amount of boron dissolved in and transported with the liquid, the boron mass equation is discretized and solved using a fully implicit technique similar to the one used for the noncondensable gas.

$$V_{IJK} \left(m_B^{n+1} - m_B^m \right) = -A_{I+1/2,J,K} \left[v_{\ell z,I+1/2,J,K}^{n+1} \begin{cases} (m_B)_{I,J,K}^{n+1} & \text{if } v_{\ell z,I+1/2,J,K}^{n+1} \geq 0 \\ (m_B)_{I+1,J,K}^{n+1} & \text{if } v_{\ell z,I+1/2,J,K}^{n+1} < 0 \end{cases} \right] \Delta t + A_{I-1/2,J,K} \left[v_{\ell z,I-1/2,J,K}^{n+1} \begin{cases} (m_B)_{I-1,J,K}^{n+1} & \text{if } v_{\ell z,I-1/2,J,K}^{n+1} \geq 0 \\ (m_B)_{I,J,K}^{n+1} & \text{if } v_{\ell z,I-1/2,J,K}^{n+1} < 0 \end{cases} \right] \Delta t \quad (8.2-55)$$

+ Similar terms in J and K directions

$$+ V_{IJK} \left(M_{Bs}^{n+1} + M_{Bmix}^{n+1} \right)_{IJK} \Delta t$$

The source term is given as:

$$V_{IJK} \cdot M_{Bs,IJK}^{n+1} = -A_{s,IJK} v_{\ell s,IJK}^{n+1} \begin{cases} (m_B)_{IJK}^{n+1} & \text{if } v_{\ell s,IJK}^{n+1} \geq 0 \\ (m_B)_{sIJK}^{n+1} & \text{if } v_{\ell s,IJK}^{n+1} < 0 \end{cases} \quad (8.2-56)$$

Substituting Equation 8.2-56 into 8.2-55 gives an equation in only the new boron mass concentration, which can be rearranged to be of the form:

$$A_{IJK} \Delta m_{B,IJK}^{n+1} = B_{IJK} + \sum_{j=1}^{N_f} C_{j,IJK} \Delta m_{Bj,IJK}^{n+1} + \sum_{j=1}^{N_s} S c_j (\Delta m_{B,IJK}^{n+1} - \Delta m_{Bs_j,IJK}^{n+1}) \quad (8.2-57)$$

This equation is again of the same form as the pressure equation (6.3-33) and the network solver is used unchanged to get the new boron concentration.

8.2.3.4 Energy Conservation

TRACG solves the fully implicit equations the predictor step and thus automatically conserve energy for the fully converged solution. This, coupled with the mass conservation of the corrector step, produces excellent energy conservation and does not generate the need for an extra corrector step for energy. (It should be noted that the original formulation of the energy equation in TRAC was not on a conserving form due to the elimination of the kinetic energy from the energy equation by substituting the momentum equation into the energy equation. This problem could lead to significant energy balance errors for systems involving critical flow. In TRACG the kinetic energy is treated explicitly in the energy equations, thereby maintaining a conserving form of these equations.)

Table 8.2-1
Energy Error for PSTF Vessel Blowdown 5801-15

	Initial Mass (kg) 1.34398E3		Initial Energy (J) 1.851458E9	
Convergence Criterion		Mass Conservation Error	Final Energy (J)	Relative Energy Error
1.0E-2	1.009360E9	-4.56E-7	1.017515E9	2.9E-2
1.0E-3	1.005698E3	-1.004E-6	0.9970902E9	8.2E-3
1.0E-4	1.004096E3	-1.82E-7	0.9917846E9	2.8E-3
1.0E-5	1.003044E3	-1.82E-7	0.9897846E9	2.9E-4
1.0E-6	1.002951E3	-3.65E-7	0.9890168E9	

To demonstrate the energy conservation in TRACG, a test case using the PSTF vessel blowdown test has been evaluated for various values of the convergence criterion for the predictor step. As the convergence is tightened for the predictor step, the mass and energy balance is improved, and in the limit there is no error. Table 8.2-1 shows the energy error at 20 seconds close to the end of the depressurization of the vessel. The mass conservation is seen to be accurate for all cases. The energy error is evaluated relative to the converged case (the case with the tightest convergence is used). It is seen that there is no significant energy errors for reasonable values of the convergence criterion ($1.0E-3$ - $1.0E-5$).

8.2.4 Time Step Control

TRACG determines the time step size in order to maximize the accuracy of the calculation and minimize the computer time. Two basic criteria are used for this purpose:

- **Convergence.** The iteration to obtain a solution to the thermal-hydraulic equations are required to converge within a prescribed convergence criteria. If convergence is obtained with a low iteration count, the time step size is allowed to increase. On the other hand, if a high iteration count is required, the time step size will be reduced.
- **Rate-of-Change.** TRACG examines the rate of change for the primary dependent variables. If the rate of change is low, a quasi steady-state condition will exist and the time step size is allowed to increase. On the other hand, if the rate-of-change is high, the time step size will be reduced.

In practice the time step size is normally determined by the convergence criteria. If a quasi steady-state condition exists convergence will easily be established within a few iterations, and if a fast transient exist, where the dependent variables are changing fast, a large iteration count will generally be required. The primary purpose of the rate-of-change criteria is to prevent excessive changes in the dependent variables during a time step.

TRACG also allows the time step size to be determined based on the material Courant limit and a user-specified upper and lower limits.

If the time step size is allowed to increase by all of the criteria, the time step size will be increased. However, the time step size will be reduced if a reduction is required by just one of the criteria.

8.2.4.1 Convergence

TRACG checks the convergence of the primary dependent variables using the following criteria:

$$\eta_p = \max \left(\frac{|P_i^m - P_i^{m-1}|}{\max(100, \epsilon P_i^m)} \right)$$

$$\eta_a = \max \left(\frac{\alpha_i^m - \alpha_i^{m-1}}{\max(0.01, 10\epsilon)} \right)$$

$$\eta_{T_v} = \max \left(\frac{|T_{vi}^m - T_{vi}^{m-1}|}{\min(1.0, 10^3 \epsilon)} \right)$$

$$\eta_{T_\ell} = \max \left(\frac{|T_{\ell i}^m - T_{\ell i}^{m-1}|}{\min(1.0, 10^3 \epsilon)} \right)$$

$$\eta_{P_a} = \max \left(\frac{|P_{ai}^m - P_{ai}^{m-1}|}{\max(100, \epsilon P_i^m)} \right)$$

where

P = Pressure

α = Void fraction

T_v = Gas temperature

T_ℓ = Liquid temperature

P_a = Partial noncondensable pressure

i = Node number, and the maximum value is determined by evaluating all nodes

m = Iteration count

ϵ = A user-specified convergence criterion, usually 10^{-3} - 10^{-4} .

Convergence is established when:

$$\eta = \max(\eta_P, \eta_a, \eta_{T_v}, \eta_{T_\ell}, \eta_{P_a}) < 1.0$$

8.2.4.2 Rate-of-Change

TRACG checks the rate-of-change of the primary dependent variables using the following criteria:

$$\zeta_P = \max \left(\frac{|P_i^n - P_i^{n-1}|}{\max(5.0 \cdot 10^4, 0.05 \cdot P_i^n)} \right)$$

$$\zeta_\alpha = \max \left(\frac{\alpha_i^n - \alpha_i^{n-1}}{0.1} \right)$$

$$\eta_{Tv} = \max \left(\frac{|T_{vi}^n - T_{vi}^{n-1}|}{20.0} \right)$$

$$\eta_{T\ell} = \max \left(\frac{|T_{\ell i}^k - T_{\ell i}^{k-1}|}{20.0} \right)$$

$$\eta_{Pa} = \max \left(\frac{|P_{ai}^n - P_{ai}^{n-1}|}{\max(5.0 \cdot 10^4, 0.05 \cdot P_i^n)} \right)$$

where n is the time step number.

The rate-of-change criterion is satisfied when:

$$\zeta = \max(\zeta_P, \zeta_\alpha, \zeta_{Tv}, \zeta_{T\ell}, \zeta_{Pa}) < 1.0$$

8.2.4.3 Other Criteria

TRACG also allows the time step size to be controlled by the material Courant number:

$$\Delta t < C \cdot \min \left(\frac{\Delta x_i}{\max(|v_v|, |v_\ell|)} \right)$$

where

Δ_x = Node size

v_v = Gas velocity

v_ℓ = Liquid velocity

C = User-specified multiplier

Usually a large value for the multiplier C is used, such that this is not a limiting criterion.

Finally, the user has the option to specify upper and lower bounds on the time step size:

$$\Delta t_{\min} < \Delta t < \Delta t_{\max}$$

If TRACG cannot satisfy the other criteria within these bounds, the calculations will abort.

8.3 References

- 8-1 J.G.M. Andersen, K.H. Chu, J.C. Shaug, *BWR Refill-Reflood Program Task 4.7 Model Development Basic Models for the BWR Version of TRAC*, NUREG/CR-2573, ERPI NP-2375, GEAP-22051, September 1983.

9.0 Three-Dimensional Neutron Kinetics Model

TRACG solves the three-dimensional (3-D) transient neutron diffusion equations using one neutron energy group and up to six delayed neutron precursors groups. The basic formulation and assumptions are consistent with the GE 3-D BWR Core Simulator Reference 9-1. This same one-group formulation collapsed radially to one axial dimension is the basis for the NRC-approved ODYN computer code [9-2]. The formulation described fully in [9-2] is used in ODYN for BWR transient simulations. The simplifying assumptions made in ODYN to yield a one-dimensional (1-D) transient kinetics model are not used in the TRACG three-dimensional (3-D) model. Instead, neutron flux and delayed neutron precursor concentrations at every (i,j,k) node are integrated in time in response to moderator density, fuel temperature, boron concentration or control rod changes. Exposure and Xenon concentration distributions are assumed to be constant during the transient.

The mesh points are distributed within (the order of) one fast neutron mean free path, with each mesh point representing approximately a 6-inch cube. The mesh spacing is assumed to be constant. The cross sections and k_{∞} s used within the physics model are derived from three-group cross sections obtained from a lattice physics code.

The core is described in X-Y-Z geometry with the restriction that there is equal mesh spacing in the X-Y directions. The x, y, z mesh is described by i,j,k nomenclature, respectively. In the horizontal planes, each fuel assembly or flow channel is described by one mesh line at the center of the fuel assembly. Mesh line (1,1,k) is in the upper left corner of the horizontal planes (Figure 9.0-1).

Vertically, the first point (k=1) is ($\Delta z/2$) away from the bottom and the last point (k=KMAX) is ($\Delta z/2$) from the top (Figure 9.0-2). The cross sections associated with the point (x,y,z) are defined to be the homogenized cross sections for the fuel, cladding, channel, interior water, exterior water, and (if applicable) control rods and/or burnable poison.

Nomenclature

A	=	amplitude function
B	=	boron concentration
B^2	=	geometric buckling
C	=	delayed neutron precursor concentration
D	=	diffusion coefficient
f	=	decay heat fraction, $f = \sum_{k=1}^5 f_k$
K	=	multiplication constant
M^2	=	migration area (D/Σ)
N	=	total number of delayed neutron precursor groups
N_x	=	xenon concentration
P	=	fission power
q	=	volumetric heat generation rate
r	=	spatial dimension
S	=	shape function
t	=	time
T	=	fuel temperature
U	=	relative water density
v	=	average neutron speed
v^*	=	effective neutron velocity
V	=	volume
w	=	spatial weighting function
x,y	=	coordinates in the horizontal plane
z	=	axial coordinate

Greek

β	=	delayed neutron precursor fraction, $\beta = \sum_{n=1}^N \beta_n$
ϕ	=	neutron flux
$\gamma\Sigma_f$	=	fission cross-section
λ	=	decay constant
μ	=	initial effective multiplication factor
ρ	=	moderator density

Σ	=	total removal cross-section, $\Sigma = \Sigma_a + \Sigma_{sl}$
Σ_a	=	absorption cross-section
Σ_{sl}	=	slowing cross-section
τ	=	neutron flux logarithmic time constant

Subscripts

1	=	neutron energy group 1
2	=	neutron energy group 2
3	=	neutron energy group 3
d	=	decay
g	=	neutron energy group
i	=	generic 3-D node
j	=	generic node j adjoining node i
ij	=	between nodes i and j
k	=	decay heat group
kij	=	specific 3-D node
kn	=	channel component n, axial cell k
n	=	delayed neutron precursor group
o	=	reference value
p	=	prompt
s	=	surface
∞	=	infinite lattice
-	=	vector

Superscripts

n	=	time step index
r	=	rated power

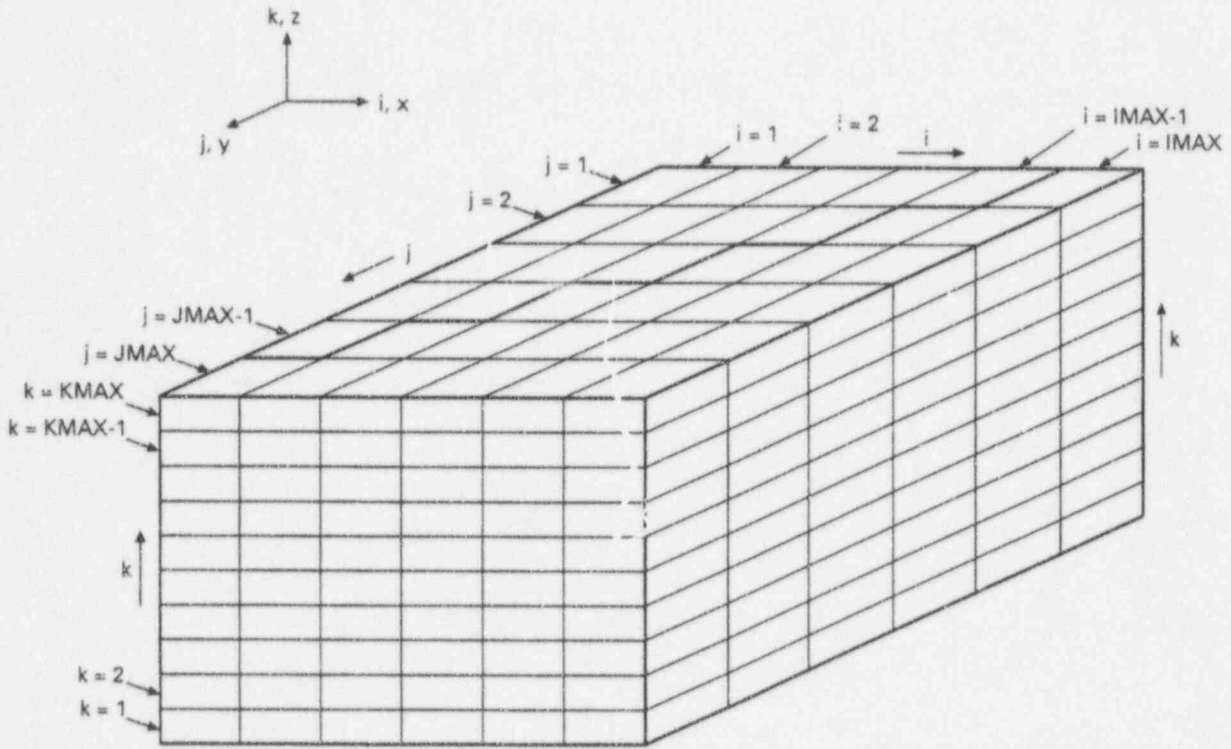


Figure 9.0-1. X-Y-Z View of the Core

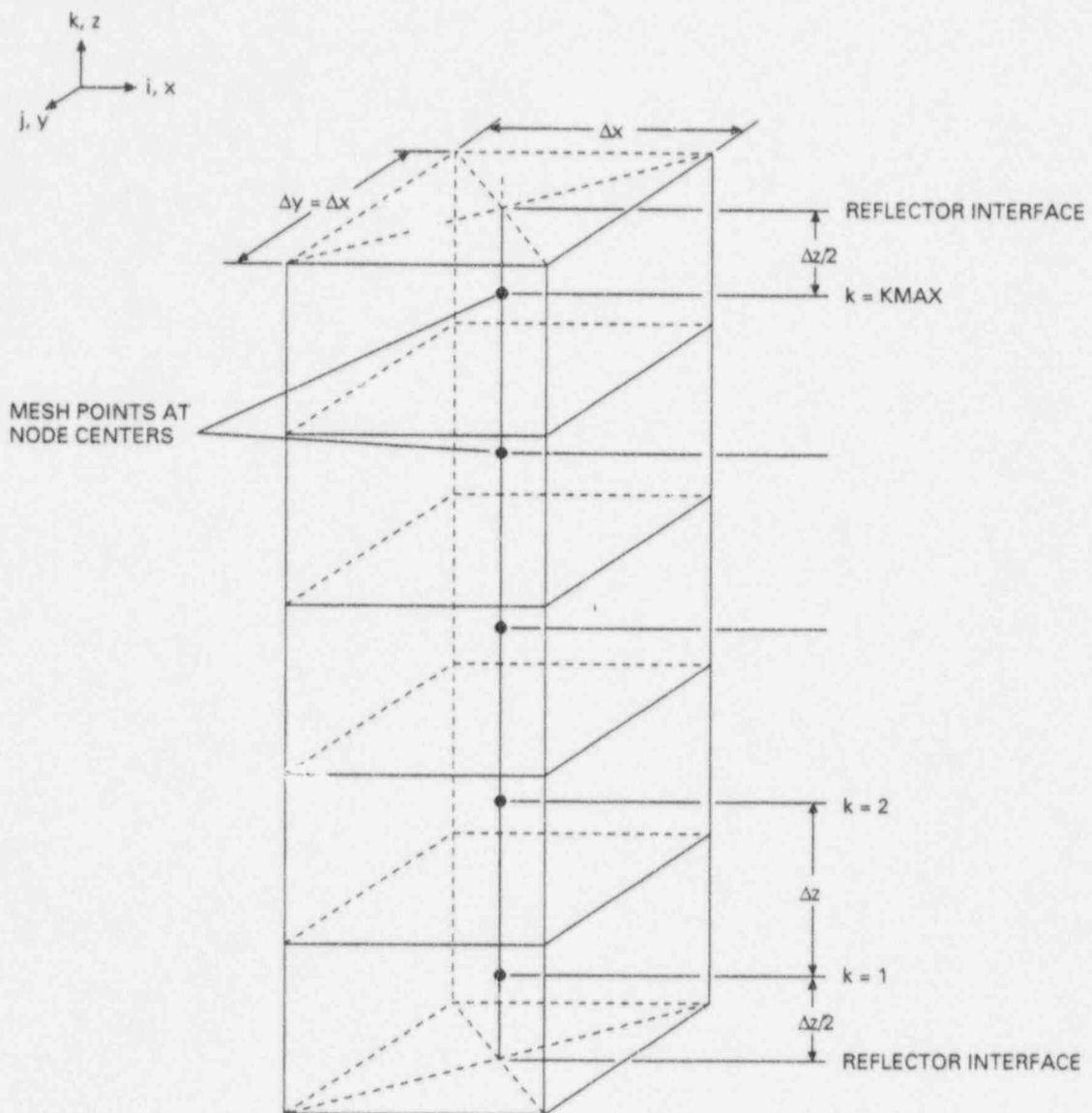


Figure 9.0-2. Node and Mesh Arrangement for a Given Bundle

9.1 Model Formulation and Assumptions

The derivation for the TRACG model begins with the assumption that the three-group transient diffusion equations with N delayed neutron precursor groups are valid:

$$\frac{1}{v_1} \frac{\partial \phi_1}{\partial t} = \nabla \cdot D_1 \nabla \phi_1 - \Sigma_1 \phi_1 + \frac{(1 - \beta)}{\mu_0} \sum_{g=1}^3 v \Sigma_{fg} \phi_g + \sum_{n=1}^N \lambda_n C_n \quad (9.1-1)$$

$$\frac{1}{v_2} \frac{\partial \phi_2}{\partial t} = \nabla \cdot D_2 \nabla \phi_2 - \Sigma_2 \phi_2 + \Sigma_{s\ell 1} \phi_1$$

$$\frac{1}{v_3} \frac{\partial \phi_3}{\partial t} = \nabla \cdot D_3 \nabla \phi_3 - \Sigma_3 \phi_3 + \Sigma_{s\ell 2} \phi_2$$

$$\frac{\partial C_n}{\partial t} = -\lambda_n C_n + \frac{\beta_n}{\mu_0} \sum_{g=1}^3 v \Sigma_{fg} \phi_g \text{ for precursor groups } \{n = 1, \dots, N\}$$

In order to collapse these equations to a single energy group, the assumptions are made that the geometric bucklings of all groups are the same:

$$\frac{\nabla \cdot D_3 \nabla \phi_3}{D_3 \phi_3} \sim \frac{\nabla \cdot D_2 \nabla \phi_2}{D_2 \phi_2} \sim \frac{\nabla \cdot D_1 \nabla \phi_1}{D_1 \phi_1} = -B^2 \quad (9.1-2)$$

and that the logarithmic time derivatives of all groups are the same:

$$\frac{1}{\phi_3} \frac{\partial \phi_3}{\partial t} \sim \frac{1}{\phi_2} \frac{\partial \phi_2}{\partial t} \sim \frac{1}{\phi_1} \frac{\partial \phi_1}{\partial t} = \tau \quad (9.1-3)$$

This latter assumption is equivalent to assuming that the neutron spectrum does not vary in time (unless the neutron cross sections change, in which case the spectrum is assumed to vary instantaneously).

For convenience, the following definitions are made:

$$K = \sum_{g=1}^3 v \Sigma_{fg} \phi_g / \Sigma_1 \phi_1 \quad (9.1-4)$$

$$\dot{C}_n = \frac{\partial C_n}{\partial t}$$

Dividing each energy group equation in Equation 9.1-1 by the group removal rate for that energy group and making use of the assumptions and definitions:

$$\frac{\tau}{\Sigma_1 v_1} = -M_1^2 B^2 - 1 + \frac{(1-\beta)}{\mu_0} K + \frac{\sum_{n=1}^N \lambda_n C_n}{\Sigma_1 \phi_1} \quad (9.1-5)$$

$$= -M_1^2 B^2 - 1 + \frac{K}{\mu_0} - \frac{\sum_{n=1}^N \dot{C}_n}{\Sigma_1 \phi_1}$$

$$\frac{\tau}{\Sigma_2 v_2} = -M_2^2 B^2 - 1 + \frac{\Sigma_{s\ell 1}}{\Sigma_2} \frac{\phi_1}{\phi_2}$$

$$\frac{\tau}{\Sigma_3 v_3} = -M_3^2 B^2 - 1 + \frac{\Sigma_{s\ell 2}}{\Sigma_3} \frac{\phi_2}{\phi_3}$$

$$\dot{C}_n = -\lambda_n C_n + \frac{\beta_n \Sigma_1 \phi_1}{\mu_0} K$$

The flux ratios can now be eliminated from the group flux equations. Using the definition of K and eliminating the second and third group flux ratios from the fast group:

$$1 + M_1^2 B^2 + \frac{\tau}{\Sigma_1 v_1} = \frac{1}{\mu_0 \Sigma_1} [v \Sigma_{f1} \quad (9.1-6)$$

$$+ v \Sigma_{f2} \frac{\Sigma_{s\ell 1} / \Sigma_2}{1 + M_2^2 B^2 + \frac{\tau}{\Sigma_2 v_2}}$$

$$+ v \Sigma_{f3} \frac{\Sigma_{s\ell 2} / \Sigma_3}{1 + M_3^2 B^2 + \frac{\tau}{\Sigma_3 v_3}} \cdot \frac{\Sigma_{s\ell 1} / \Sigma_2}{1 + M_2^2 B^2 + \frac{\tau}{\Sigma_2 v_2}}]$$

$$- \frac{1}{\Sigma_1 \phi_1} \sum_{n=1}^N \dot{C}_n$$

Multiplying through by the denominators of the terms in brackets [...] results in an equation which is impractical to solve, since it involves powers and cross products of B^2 , τ , and \dot{C}_n . The equation must therefore be linearized by assuming that the terms involving these powers and cross products are small and may be neglected:

9.2 Nuclear Parameters

The nuclear parameters (M^2 , D_1 , k_∞ , Σ_1 , and A_∞) are obtained from the detailed X-Y physics calculations performed for lattice cells (fuel types) normally consisting of one fuel bundle and its surrounding water. These multi-group calculations produce three-group cross sections homogenized over the lattice cell. The data are represented by polynomial fits and by Lagrangian interpolation of tabulated values for each fuel type.

In the solution of the coarse mesh nodal approximation of the one-group diffusion theory model, void, exposure, and fuel type conditions of a node in three-dimensional space are used in the fits and tables to determine nuclear properties for that node. In this way, void feedback, burnup effects, and heterogeneous fuel loading are taken into account.

Void dependence is represented by the ratio of cell average water density relative to the reference water density used in the lattice cell calculation. This ratio is given by:

$$U = \frac{\rho}{\rho_0} \quad (9.2-1)$$

Every node in three-dimensional space has a value of U at a given operating point during burnup of the core, where U is an instantaneous relative moderator density. By averaging U with respect to exposure of the node E , history-dependent relative moderator density is defined as:

$$UH = \frac{\int U dE}{\int dE} \quad (9.2-2)$$

Local U , UH , and E conditions determine nuclear properties of a node according to correlations of the lattice cell physics calculations. For each fuel type, k_∞ is dependent upon U , UH , and E , while M^2 , D_1 , Σ_1 , and A_∞ are expressed in terms of U only.

The detailed lattice cell calculations are performed with the control rod in or out. Therefore, nuclear parameters are obtained for each fuel type at several void and exposure conditions, for both controlled and uncontrolled conditions. In the three-dimensional diffusion theory solution, the control rod configuration is accounted for by using controlled or uncontrolled data for each node. If a control rod is only partially inserted into a node, linear averaged nuclear data are used. For each fuel type, k_∞ , D_1 , and M^2 are control dependent. A_∞ , which is a small correction to the migration area for fast and resonance fission, is not strongly dependent on the presence of a control blade and therefore uncontrolled data are used.

Fuel temperature (T) affects resonance absorption in uranium and plutonium (the Doppler effect). This is accounted for by making a Doppler reactivity of k_∞ at each node in the form:

$$k_\infty(T) = k_\infty(T_0) \left[1 + \frac{\Delta k}{k}(T) \right] \quad (9.2-3)$$

where T_0 represents base fuel temperature, and

$$\frac{\Delta k}{k}(T) = C_T [\sqrt{T} - \sqrt{T_0}]$$

The Doppler coefficient C_T is dependent upon exposure and U for each fuel type. It is determined by lattice cell physics calculations performed parametrically as a function of fuel temperature.

Xenon is a fission product which acts as a strong absorber of thermal neutrons. It is produced directly from fission and indirectly by decay of iodine. The xenon poisoning effect is accounted for by making a xenon reactivity correction to k_∞ at each node in the form:

$$k_\infty(N_x) = k_\infty(N_x = 0) \left[1 + \frac{\Delta k}{k}(N_x) \right] \quad (9.2-4)$$

where N_x represents xenon concentration and xenon reactivity is expressed by:

$$\frac{\Delta k}{k}(N_x) = C_x \frac{N_x}{N_x^r}$$

where N_x^r represents xenon concentration at rated power density. The xenon coefficient C_x is evaluated at rated power density and represented as a function of exposure for each fuel type.

The effect of introducing liquid boron is accounted for by making a boron reactivity correction to k_∞ at each node in the form:

$$k_\infty(B) = k_\infty(B = 0) \left[1 + \frac{\Delta k}{k}(B) \right] \quad (9.2-5)$$

where B represents boron concentration in parts per million and boron reactivity is expressed by:

$$\frac{\Delta k}{k}(B) = C_{B1}(B) + C_{B2}(B \cdot U) + C_{B3}(B \cdot U)^2$$

where C_{B1} , C_{B2} , C_{B3} are boron reactivity coefficients determined by lattice cell physics calculations.

The conversion of neutron flux to power at each node requires the evaluation of the average number of neutrons produced by fission, $\bar{\gamma}_i$, and the spectral mismatch correction. $\bar{\gamma}_i$ is a function of exposure for each fuel type. The spectral index used to evaluate the spectral mismatch is a function of exposure and relative water density.

9.3 Decay Heat Model

The decay heat model calculates the delayed component of the volumetric heat generation rate in the fuel. A time integral relation links the fission rate to the decay heat. Nodal power history is accounted for in TRACG. In TRACG, up to five exponential terms can be input to fit the decay power curve. The decay heat model described in this section is used with the 3-D neutron kinetics model for transient simulation. For LOCA applications, the power is input in tabular form as a function of time.

9.4 Thermal-Hydraulic Interface and Implementation

Power distribution in the core is calculated in the orthogonal 3-D (x-y-z) geometry in the kinetics model, which takes into account feedback due to changes in fuel temperature and coolant density, and control rod movement. In the channel thermal-hydraulics and fuel heat transfer models, the core is simulated with multiple parallel channels, each having one or more fuel bundles associated with it. Their properties are solved for each axial node for each channel. Hydraulic boundary conditions for these channels are determined in the external core model in the code. Each component is coupled by such data, as shown in Figure 9.4-1.

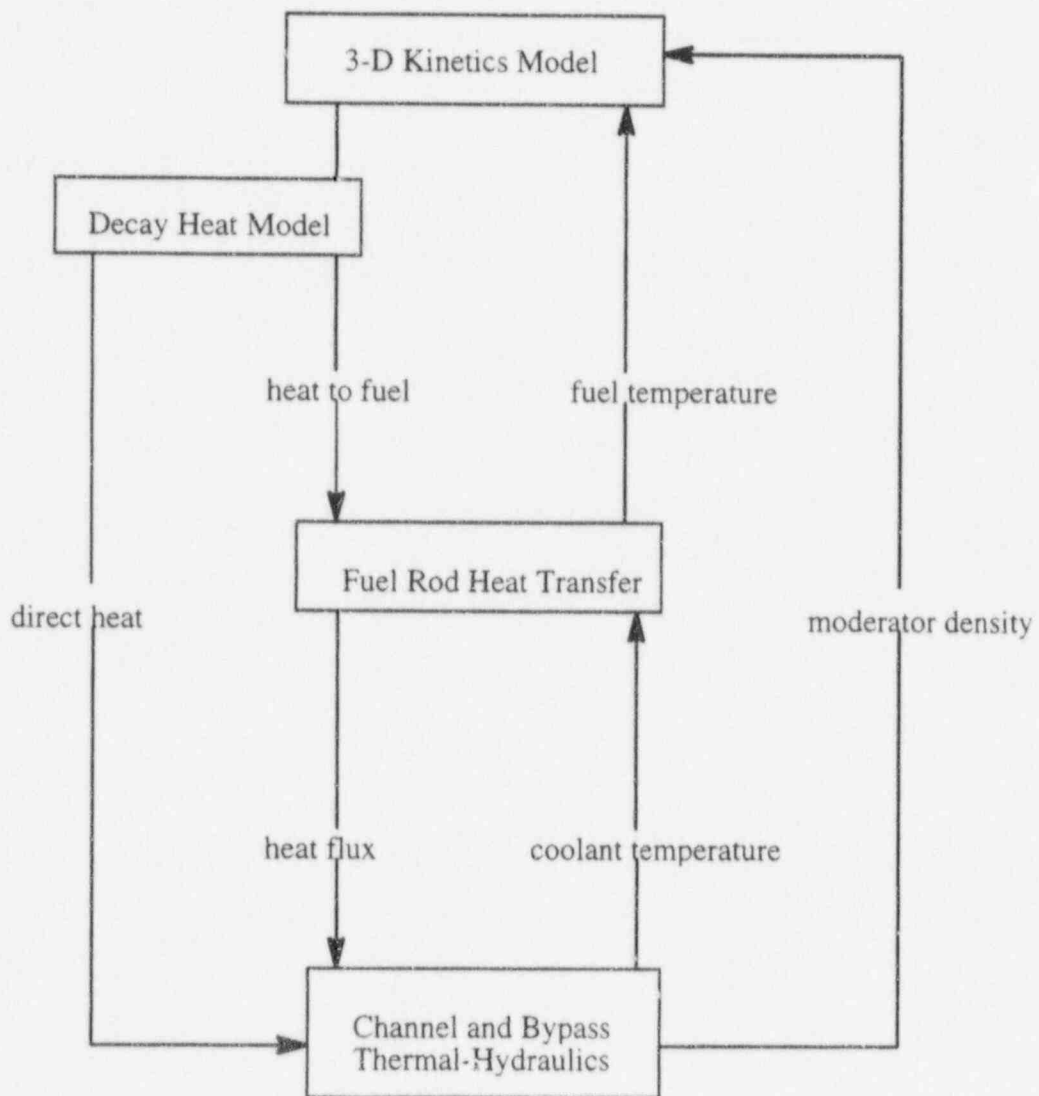


Figure 9.4-1. Data Transfer Between TRACG Models

$$\begin{aligned}
 & \left| \begin{aligned}
 & 1 + (M_1^2 + M_2^2 + M_3^2) B^2 + \left(\frac{1}{\Sigma_1 v_1} + \frac{1}{\Sigma_2 v_2} + \frac{1}{\Sigma_3 v_3} \right) \tau \\
 & = \frac{1}{\mu_0 \Sigma_1} \left(v \Sigma_{f1} + v \Sigma_{f2} \frac{\Sigma_{s\ell 1}}{\Sigma_2} + v \Sigma_{f3} \frac{\Sigma_{s\ell 2}}{\Sigma_3} \frac{\Sigma_{s\ell 1}}{\Sigma_2} \right. \\
 & \quad \left. + v \Sigma_{f1} \left[(M_2^2 + M_3^2) B^2 + \left(\frac{1}{\Sigma_2 v_2} + \frac{1}{\Sigma_3 v_3} \right) \tau \right] \right. \\
 & \quad \left. + v \Sigma_{f2} \frac{\Sigma_{s\ell 1}}{\Sigma_2} \left[M_3^2 B^2 + \frac{1}{\Sigma_3 v_3} \tau \right] \right) - \frac{\sum_{n=1}^N \dot{C}_n}{\Sigma_1 \phi_1}
 \end{aligned} \right. \tag{9.1-7}
 \end{aligned}$$

Making the following definitions:

$$M^2 = M_1^2 + M_2^2 + M_3^2 \tag{9.1-8}$$

$$K_\infty = \left[v \Sigma_{f1} + v \Sigma_{f2} \frac{\Sigma_{s\ell 1}}{\Sigma_2} + v \Sigma_{f3} \frac{\Sigma_{s\ell 2}}{\Sigma_3} \frac{\Sigma_{s\ell 1}}{\Sigma_2} \right] / \Sigma_1$$

$$A_\infty = \frac{v \Sigma_{f1}}{\Sigma_1} (M_2^2 + M_3^2) + \frac{v \Sigma_{f2}}{\Sigma_1} \frac{\Sigma_{s\ell 1}}{\Sigma_2} M_3^2$$

$$\bar{v} = \left[\frac{1}{v_1} + \frac{\Sigma_1}{\Sigma_2 v_2} + \frac{\Sigma_1}{\Sigma_3 v_3} \right]^{-1}$$

$$\bar{c} = \left[v \Sigma_{f1} \left(\frac{1}{\Sigma_2 v_2} + \frac{1}{\Sigma_3 v_3} \right) + v \Sigma_{f2} \frac{\Sigma_{s\ell 1}}{\Sigma_2} \frac{1}{\Sigma_3 v_3} \right]^{-1}$$

results in the collapsed one-group, transient diffusion equation:

$$1 + (M^2 - A_\infty / \mu_0) B^2 + \frac{1}{\Sigma_1} \left(\frac{1}{\bar{v}} - \frac{1}{\bar{c} \mu_0} \right) \tau \tag{9.1-9}$$

$$= \frac{K_\infty}{\mu_0} - \frac{\sum_{n=1}^N \dot{C}_n}{\Sigma_1 \phi_1}$$

In order to obtain an expression for K , the last term of this equation is eliminated using the original first group Equation 9.1-5:

$$K = K_{\infty} + (A_{\infty} + \mu_0 (M_1^2 - M^2)) B^2 \quad (9.1-10)$$

$$+ \frac{1}{\Sigma_1} \left(\frac{1}{\bar{c}} + \mu_0 \left(\frac{1}{v_1} - \frac{1}{\bar{v}} \right) \right) \tau$$

Then the neutron precursor equations can be written as:

$$\dot{C}_n = -\lambda_n C_n + \frac{\beta_n \Sigma_1 \phi_1}{\mu_0} [K_{\infty} + (A_{\infty} + \mu_0 (M_1^2 - M^2)) B^2] \quad (9.1-11)$$

$$+ \frac{1}{\Sigma_1} \left(\frac{1}{\bar{c}} + \mu_0 \left(\frac{1}{v_1} - \frac{1}{\bar{v}} \right) \right) \tau$$

Further simplification of Equations 9.1-9 and 9.1-11 can be accomplished by noting that average neutron velocities are very large. Since these velocities are so large and since $\bar{c} \gg \bar{v}$, an effective velocity v^* can be defined for use in Equation 9.1-9 by setting $\mu_0 \sim 1$:

$$v^* = \left[\frac{1}{\bar{v}} - \frac{1}{\bar{c}\mu_0} \right]^{-1}$$

In addition, the term involving τ in the neutron precursor Equation 9.1-11 can be eliminated entirely.

These assumptions lead to the final equation for the neutron flux and the precursor densities.

$$\frac{1}{\Sigma_1 v^*} \tau = - (M^2 - A_{\infty} / \mu_0) B^2 - 1 + \frac{K_{\infty}}{\mu_0} - \frac{\sum_{n=1}^N \dot{C}_n}{\Sigma_1 \phi_1} \quad (9.1-12)$$

$$\dot{C}_n = -\lambda_n C_n + \frac{\beta_n \Sigma_1 \phi_1}{\mu_0} [K_{\infty} + (A_{\infty} + \mu_0 (M_1^2 - M^2)) B^2]$$

or returning to the differential notation

$$\left| \begin{aligned} \frac{1}{v^*} \frac{\partial \phi_1}{\partial t} &= \Sigma_1 (M^2 - A_\infty / \mu_o) \frac{1}{D_1} \nabla \cdot D_1 \nabla \phi_1 \\ &+ \Sigma_1 \left(\frac{K_\infty}{\mu_o} - 1 \right) \phi_1 - \sum_{n=1}^N \frac{\partial C_n}{\partial t} \end{aligned} \right. \quad (9.1-13)$$

$$\frac{\partial C_n}{\partial t} = -\lambda_n C_n + \frac{\beta_n \Sigma_1 \phi_1}{\mu_o} \cdot \text{FTRM}$$

where

$$\text{FTRM} = K_\infty + (A_\infty + \mu_o (M_1^2 - M^2)) \cdot \left(-\frac{1}{D_1 \phi_1} \nabla \cdot D_1 \nabla \phi_1 \right)$$

The TRACG physics model employs boundary conditions of the "mixed" type at the interface between the core and the reflector:

$$D \hat{n} \cdot \nabla \phi_1(\underline{r}_s) + \Gamma \phi_1(\underline{r}_s) = 0$$

or

$$\Gamma = -\frac{D \hat{n} \cdot \nabla \phi_1}{\phi_1} \Big|_{\underline{r}=\underline{r}_s} \quad (9.1-14)$$

where \underline{r}_s is the vector that defines the boundary surface.

The value of Γ used in this model varies according to the reflector location and the surrounding nodes. The bottom axial reflector is represented by a Γ which varies linearly with the relative water density of the bottom fuel node. The top axial reflector is represented by a Γ which varies linearly with the relative water density of the top fuel node. For nodes adjacent to the radial reflector, a base value of Γ is used, along with multiplicative correction factors according to the type and number of neighboring bypass nodes.

To obtain the transient solution, TRACG uses the "Improved Quasi-static Method" [9-3]. The procedure used in the quasi-static method is based on the factorization of the space-time dependent neutron flux $\phi_1(r,t)$ into a scalar amplitude function $A(t)$ which determines primary time dependence and a shape function $S(r,t)$, which determines primary spatial dependence of the solution.

The factorization is defined as follows:

$$\phi_1(r,t) = A(t) S(r,t) \quad (9.1-15)$$

The quasi-static method defines the amplitude function in the following way using an arbitrary weighting function that is independent of time:

$$A(t) = \int w(r) \frac{1}{v^*} \phi_1(r,t) dr \quad (9.1-16)$$

Then, the shape function is defined:

$$S(r,t) = \phi_1(r,t) / A(t) \quad (9.1-17)$$

Application of the same weighting function to $S(r,t)$ and subsequent integration over space leads to the constraint:

$$\int w(r) \frac{1}{v^*} S(r,t) dr = 1 \quad (9.1-18)$$

The weighting function is chosen to be the adjoint flux which for one energy group is the same as the neutron flux.

9.5 Solution Procedure

In the solution for the factorized neutron flux, a separate reactivity time step and a shape time step are used. In the TRACG code, the thermal-hydraulic time step and the reactivity time step are equal. For transient calculations, the thermal-hydraulic time step size is in the range of 1-30 msec. The time step will vary to reflect the rate-of-change of the thermal-hydraulic parameters. Time steps of this magnitude are sufficient to provide the change in reactivity parameters resulting from changes in the thermal-hydraulic conditions in the core. In the calculation of the amplitude function, the integration time step is reduced to assure convergence. The shape function is recalculated every other amplitude/reactivity step. As the reactivity step size varies, there will be a corresponding variation in shape function time step size. The fundamental advantage of this method is based on reducing the frequency with which the computer-intensive shape function calculation module is called.

Considering the possibility for the rapid change of $A(t)$, the reactivity step should be reasonably fine while the shape step can be relatively coarse.

The calculational sequence for the reactivity step consists of the following five steps:

1. Perform thermal-hydraulic calculations.
2. Calculate nodal cross sections.
3. Calculate the point kinetics parameters.
4. Obtain the amplitude function.
5. Obtain the delayed neutron precursor density by solving Equation 9.1-13.

For the thermal-hydraulics calculation, it is necessary to estimate the amplitude function $[A(t)]$ and the shape function $[S(r,t)]$. The shape function is estimated by the extrapolation of the linear equation fit to the shape functions of the former two shape steps. The amplitude function is obtained by extrapolating quadratically the values from previous reactivity steps. The decay heat calculation is evaluated to determine the power input to each channel.

The nodal cross sections described in Section 9.2 are updated using the latest calculated values of moderator density and fuel temperature. Any change in control rod position is also taken into account. The point kinetics parameters are calculated with the nodal cross sections and the extrapolated shape function.

9.6 References

- 9-1 *Steady State Nuclear Methods*, NEDE-30130PA, April 1985.
- 9-2 *Qualification of the One-Dimensional Core Transient Model for Boiling Water Reactors*, NEDE-24154PA, August 1988.
- 9-3 S. Tsunoyama, et. al., *3-D Neutronics Model Implementation Into TRAC-BD1*, Transactions of the Fourteenth Water Reactor Safety Information Meeting, NUREG/CP-0081, 1986.
- 9-4 J.J. Kaganove, *Numerical Solution of the One-Group Space-Independent Reactor Kinetics Equations for Neutron Density Given by Excess Reactivity*, ANL-6132, 1960.

10.0 Control System

The TRACG control system model is designed to serve two primary purposes. First, it allows the user to model an actual BWR plant control system at any desired level of detail. Accurate modeling of the plant control system can play an important role in the successful analysis of many transients, including ATWS and operational transient analyses. Secondly, the control system may be used to assist in the initialization of any plant deck by allowing the user to automatically control the value of certain plant parameters during the initialization process.

In practice, the control system model permits the user to take data from the thermal-hydraulic (T/H) database, perform a wide variety of user-specified operations on these data in an external control system, then use the results of these operations to adjust geometric or dynamic variables in the database. For example, pressure in a BWR main steamline may be used as input to the control system that generates an output signal to adjust the area of the steamline pressure control valve (PCV). A large number of control loops of a similar nature may be utilized to simulate an entire BWR plant control system.

The control system solution scheme is sequential based on the order in which the control blocks are specified on input. The input to a block is the current value which may be the new time value if the input is the output of a block already calculated or the old time value if the input is the output of a block that has yet to be updated. This potentially explicit scheme can lead to instabilities if care is not taken to organize the control system in a manner to increase the implicitness as much as possible. The existence of feedback loops makes organizing the computation in an implicit manner impossible given the sequential solution scheme used in TRACG. To guarantee that the control system will be stable, a sufficiently small time step size must be used to evaluate the control system. The specification of time step size is discussed in Section 10.3.

10.1 Control Blocks

A TRACG control system model is built up from basic functional elements called control blocks. Each control block performs a simple operation on input data to generate an output value. A complete list of the types of control blocks and a description of their operations is found in Table 10.1-1. The various control block types require from zero to three input values, and each generates a single output value. Input and output values may be logical (0 or 1) or continuously varying, depending upon the type of control block. Associated with each control block are the following user-specified parameters:

- A control block number from 1 to 9999, uniquely identifying each block. Block numbers need not be consecutive.
- The type of operation to be performed upon the input data.

- The constants C1 and C2. [NOTE: The various control block constants (C1, C2, XMAX, and XMIN) may not be required, depending on the control block type. See Table 10.1-1 for specific requirements.]
- The gain factor G.
- The maximum and minimum limits XMAX and XMIN of the block output.
- The initial value (XIV or LIV) of the block output.
- An optional 12-character name.

A control block may be represented schematically by a control block diagram, as shown in Figure 10.1-1.

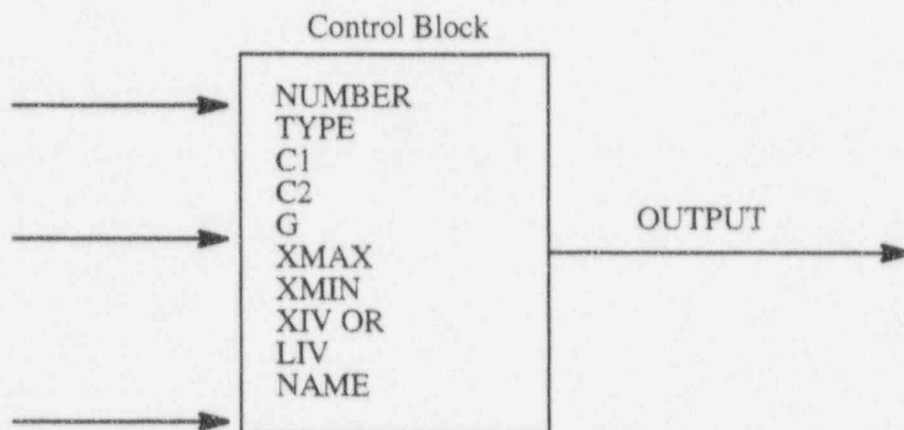


Figure 10.1-1. Schematic Control Block Diagram

The majority of the available control blocks perform simple algebraic or logic operations as indicated in the rightmost column of Table 10.1-1 and require no further explanation. Seven of the control blocks are state variable blocks which involve an integration with respect to time. The evaluation of the state variable blocks is described below.

The state variable control block types are DINL, INT, INTM, LAG, LINT, LLAG, and SOTF. The method of integration with respect to time used in all of these blocks is implicit; that is, the input (derivative) value to be integrated is taken to be the value at the end of the control system time step. When the control system subdivides the hydraulic time step, the input parameter is interpolated between the old and new hydraulic timestep values.

A pass is taken through the control system calculation at time zero (before the TRACG thermal-hydraulic equations have been advanced) to load initial input values for use as old time

inputs by the state variable blocks in the next pass through the control system. The user-supplied initial control block output values are used for determining these initial inputs and for initializing the output values of state variable blocks.

The computational method used for each of the state variable block types is illustrated in the following section. In each case, Y is the block output value, $X1$ is the block input value, $X2$ is the intermediate integral value for double integrations, Δt is the control system time step size, and G is the control block gain.

DINL (double integrator with output limiting)

$$Y^{n+1} = Y^n + X2^n \Delta t \quad (10.1-1)$$

$$X2^{n+1} = X2^n + X1^{n+1} G \Delta t \quad (10.1-2)$$

Equations 10.1-1 and 10.1-2 are evaluated in sequence. $X2^n = 0$ at time zero. If $Y^{n+1} > XMAX$ or $Y^{n+1} < XMIN$, then the output of the block supplying input $X1$ is set to zero if its output sign is such as to hold the DINL output locked at its limit.

INT (simple integrator)

$$Y^{n+1} = Y^n + X1^{n+1} G \Delta t \quad (10.1-3)$$

INTM (integrator with mode control)

If $(L2 + L3) = 0$ (reset mode),

$$Y^{n+1} = XIV. \quad (10.1-4)$$

If $(L2 + L3) = 2$ (integrate mode),

$$Y^{n+1} = Y^n + X1^{n+1} G \Delta t \quad (10.1-5)$$

If $(L2 + L3) = 1$ (hold mode),

$$Y^{n+1} = Y^n. \quad (10.1-6)$$

$L2$ and $L3$ are logic input variables (1 or 0) to block inputs 2 and 3.

LAG (first order lag)

$$Y^{n+1} = Y^n + \frac{[G X1^{n+1} - Y^{n+1}] \Delta t}{C1} \quad (10.1-7)$$

$C1$ is the lag time constant. This equation is rearranged algebraically and solved for Y_{n+1} .

LINT (limited integrator)

$$Y^{n+1} = Y^n + X1^{n+1} G \Delta t \quad (10.1-8)$$

If $(Y^{n+1} > XMAX$ or $Y^{n+1} < XMIN$, then the output of the block supplying input X1 is set to zero if its output sign is such as to hold the LINT output locked at its limit.

LLAG (lead-lag transfer function)

$$\frac{Y^{n+1}}{X2^{n+1}} = \frac{(GX1^{n+1} - X2^{n+1})}{C2} \quad (10.1-9)$$

$$X2^{n+1} = X2^n + \overline{X2^{n+1}} \Delta t \quad (10.1-10)$$

$$Y^{n+1} = X2^{n+1} + C1 \overline{X2^{n+1}} \quad (10.1-11)$$

X2 is the intermediate state derivative, and C1 and C2 are the lead and lag time constants. Equations 10.1-9, 10.1-10 and 10.1-11 are rearranged algebraically and solved to obtain values for Y^{n+1} and $X2^{n+1}$. $X2^n$ is initialized to the same value as $X1^n$.

SOTF (second order transfer function)

$$\frac{Y^{n+1}}{X2^{n+1}} = \frac{(GX1^{n+1} - Y^{n+1} - C1X2^{n+1})}{C2} \quad (10.1-12)$$

$$X2^{n+1} = X2^n + \overline{X2^{n+1}} \Delta t \quad (10.1-13)$$

$$Y^{n+1} = Y^n + X2^{n+1} \Delta t \quad (10.1-14)$$

C1 and C2 are the transform coefficients in the Laplace transform:

$$Y = \frac{X1}{1.0 + C1S + C2S^2} \quad (10.1-15)$$

where S is the Laplace transform operator. Equations 10.1-12, 10.1-13 and 10.1-14 are rearranged algebraically and solved to obtain values for Y^{n+1} and $X2^{n+1}$. $X2^n$ is initialized to the same value as $X1^n$.

Table 10.1-1
Description of Control Block Operations

Number	Block Type	Block Input 1 (a)	Block Input 2 (b)	Block Input 3	Block Const 1	Block Const 2	Gain Factor (c)	Upper Limit (c)	Lower Limit (c)	Initial Value (d)	Name	Mathematical Operation (e)
1	ABSV	X1	N/A	N/A	N/A	N/A	G	XMAX	XMIN	XIV	Absolute Value	$XOUT = G * ABS(X1)$
2	ACOS	X1	N/A	N/A	N/A	N/A	G	XMAX	XMIN	XIV	Arcosine	$XOUT = G * ACOS(X1)$, XOUT in Radians
3	ADD	X1	X2	N/A	N/A	N/A	G	XMAX	XMIN	XIV	Add	$XOUT = G * (X1 + X2)$
4	AINT	X1	N/A	N/A	N/A	N/A	G	XMAX	XMIN	XIV	Integerizer	$XOUT = G * FLOAT(IFIX(X1))$
5	AND	L1	L2	N/A	N/A	N/A	N/A	N/A	N/A	LIV	Logical "And"	$LOUT = 1.0 \text{ IF}((L1.EQ.1).AND.L2.EQ.1)$ $= 0.0 \text{ Otherwise}$
6	ASIN	X1	N/A	N/A	N/A	N/A	G	XMAX	XMIN	XIV	Arcsine	$XOUT = G * ASIN(X1)$, XOUT in Radians
7	ATAN	X1	N/A	N/A	N/A	N/A	G	XMAX	XMIN	XIV	Arctangent	$XOUT = G * ATAN(X1)$, XOUT in Radians
8	ATN2	X1	X2	N/A	N/A	N/A	G	XMAX	XMIN	XIV	Arctangent	$XOUT = G * ATAN(X1/X2)$, XOUT in Radians
9	CONS	N/A	N/A	N/A	N/A	N/A	N/A	N/A	N/A	XIV	Constant	$XOUT = C1$
10	COS	X1	N/A	N/A	N/A	N/A	G	XMAX	XMIN	XIV	Cosine	$XOUT = G * COS(X1)$, XOUT in Radians
11	DEAD	X1	N/A	N/A	C1	C2	G	XMAX	XMIN	XIV	Dead Band, Dead Zone, or Dead Space	$XOUT = G * (X1 - C2) \text{ IF}(X1.GT.C2)$ $= G * (X1 - C1) \text{ IF}(X1.LT.C1)$ $= 0.0 \text{ Otherwise}$
12	DER	X1	(X2)	N/A	N/A	N/A	G	XMAX	XMIN	XIV	Derivative	$XOUT = G * (dX1/dT)$
13	DINL	X1	(X2)	N/A	N/A	N/A	G	XMAX	XMIN	XIV	Double Integrator With XOUT Limited	$XOUT = G * \int \{ \int (X1 * dt) dt \} + XIV$ X1 and (X2) are reset to 0.0 if XOUT is against a limit and the sign of X1 does not change
14	DIV	L1	X2	N/A	N/A	N/A	G	XMAX	XMIN	LIV	Divide	$XOUT = G * X1/X2$
15	EOR	L1	X2	N/A	N/A	N/A	G	XMAX	XMIN	LIV	Logical "Exclusive OR"	$LOUT = 1.0 \text{ IF}((L1+L2).EQ.1.0)$ $= 0.0 \text{ otherwise}$
16	EQL	L1	L2	N/A	N/A	N/A	N/A	N/A	N/A	LIV	Logical "Equivalent"	$LOUT = 1.0 \text{ IF}(L1.EQ.L2)$ $= 0.0 \text{ otherwise}$

Table 10.1-1 (Continued)
Description of Control Block Operations

Number	Block Type	Block Input 1 (a)	Block Input 2 (b)	Block Input 3	Block Const 1	Block Const 2	Gain Factor (c)	Upper Limit (c)	Lower Limit (c)	Initial Value (d)	Name	Mathematical Operation (e)
17	EXP	X1	L2	N/A	N/A	N/A	G	XMAX	XMIN	XIV	Exponential	$XOUT = G * EXP(X1)$
18	FLFP	L1	(L2)	L3	N/A	N/A	N/A	N/A	N/A	XIV	Logical "Flip Flop"	LOUT = Flip-flop Output Which Changes State Whenever L1 Changes State (only if L3=1.0)
19	GATE	X1	L2	N/A	N/A	N/A	N/A	N/A	N/A	XIV	Gate	$XOUT = X1 \text{ IF}(L2.EQ.1.0)$ $= 0.0 \text{ IF}(L2.EQ.0.0)$
20	GREQ	X1	X2	N/A	N/A	N/A	N/A	N/A	N/A	XIV	Greater Than or Equal to	$XOUT = 1.0 \text{ IF}(X1.GE.X2)$ $= 0.0 \text{ otherwise}$
21	GRTH	X1	X2	N/A	N/A	N/A	N/A	N/A	N/A	LIV	Greater Than	$LOUT = 1.0 \text{ IF}(X1.GT.X2)$ $= 0.0 \text{ otherwise}$
22	INSW	X1	X2	L3	N/A	N/A	N/A	N/A	N/A	LIV	Input Switch	$LOUT = X1 \text{ IF}(L3.EQ.1.0)$ $= X2 \text{ IF}(L3.EQ.0.0)$
23	INT	X1	N/A	N/A	N/A	N/A	G	XMAX	XMIN	XIV	Integrate	$XOUT = G * \text{Int}(X1 * dt) + XIV$
24	INTM	X1	L2	L3	N/A	N/A	G	XMAX	XMIN	XIV	Intergrate with Mode Control	$XOUT = XIV, \text{ IF}((L2+L3).EQ.0.0)$ Reset or IC Mode $= G * \text{Int}(X1 * dt) + XIV$ IF((L2+L3).EQ.2.0), Intergrate Mode $= XOUT \text{ IF}((L2+L3).EQ.1.0)$ Hold Mode
25	IOR	L1	L2	N/A	N/A	N/A	N/A	N/A	N/A	LIV	Logical "Inclusive OR"	$LOUT = 0.0 \text{ IF}((L1+L2).EQ.0.0)$ $= 1.0 \text{ otherwise}$
26	LAG	X1	N/A	N/A	C1	N/A	G	XMAX	XMIN	XIV	First Order Lag	$XOUT = G * X1 / (1.0 + C1 * s)$ s is Laplace Operator
27	LDLY	L1	(L2)	N/A	C1	(C2)	N/A	N/A	N/A	LIV	Logic Delay	$LOUT = 0.0$ IF((L1.EQ.0.0).OR. (TIMET.LT.(C1+C2))) $= 1.0$ IF((L1.EQ.1.0).AND. (TIMET.GE.(C1+C2))) Where (C2) is the TIMET When L1 Switches from 0.0 to 1.0

Table 10.1-1 (Continued)
Description of Control Block Operations

Number	Block Type	Block Input 1 (a)	Block Input 2 (b)	Block Input 3	Block Const 1	Block Const 2	Gain Factor (c)	Upper Limit (c)	Lower Limit (c)	Initial Value (d)	Name	Mathematical Operation (e)
28	LGPC	L1	(L2)	L3	N/A	N/A	N/A	N/A	N/A	LIV	Logic General Purpose Counter	L _{OUT} = 0.0 If (L3.EQ.0.0), Reset Mode = Number of Times L1 Has Changed State Since Enabled (When L3 = 1.0), Count Mode
29	LISW	L1	L2	L3	N/A	N/A	N/A	N/A	N/A	LIV	Logic Input Switch	L _{OUT} = L1 IF(L3.EQ.1.0) = L2 IF(L3.EQ.0.0)
30	LLAG	X1	(X2)	(X3)	C1	C2	G	XMAX	XMIN	XIV	Lead-Lag Transfer Function	X _{OUT} = $G \cdot X1 / (1.0 + C1 \cdot s) / (1.0 + C2 \cdot s)$ s is Laplace Transform Operator
31	LINT	X1	N/A	N/A	N/A	N/A	G	XMAX	XMIN	XIV	Limited Integrator	X _{OUT} = $G \cdot \int (X1 \cdot dt) + XIV$, X1 is set to 0.0 if X _{out} is against a limit and the sign of X1 does not change
32	LOGN	X1	N/A	N/A	N/A	N/A	G	XMAX	XMIN	XIV	Natural Logarithm	X _{OUT} = $G \cdot \text{ALOG}(X1)$
33	LSEQ	X1	X2	N/A	N/A	N/A	N/A	N/A	N/A	LIV	Less Than or Equal to	L _{OUT} = 1.0 IF (X1.LE.X2) = 0.0 otherwise
34	LSTN	X1	X2	N/A	N/A	N/A	N/A	N/A	N/A	LIV	Less Than	L _{OUT} = 1.0 IF(X1.LT.X2) = 0.0 otherwise
35	MAXS	X1	X2	N/A	N/A	N/A	N/A	N/A	N/A	XIV	Maximum of 2 Signals	X _{OUT} = $\text{AMAX1}(X1, X2)$
36	MAXT	X1	N/A	N/A	N/A	N/A	N/A	N/A	N/A	XIV	Maximum During Transient	X _{OUT} = $\text{AMAX1}(X1, X_{OUT})$
37	MINS	X1	X2	N/A	N/A	N/A	N/A	N/A	N/A	XIV	Minimum of 2 Signals	X _{OUT} = $\text{AMIN1}(X1, X2)$
38	MINT	X1	N/A	N/A	N/A	N/A	N/A	N/A	N/A	XIV	Minimum During Transient	X _{OUT} = $\text{AMIN1}(X1, X_{OUT})$
39	MULT	X1	X2	N/A	N/A	N/A	G	XMAX	XMIN	XIV	Multiply	X _{OUT} = $G \cdot X1 \cdot X2$
40	NAND	L1	L2	N/A	N/A	N/A	N/A	N/A	N/A	LIV	Logical "Not And"	L _{OUT} = 0.0 IF ((L1+L2).EQ.2.0) = 1.0 otherwise
41	NEQ	L1	L2	N/A	N/A	N/A	N/A	N/A	N/A	LIV	Logical "Not Equal"	L _{OUT} = 1.0 IF ((L1.NE.L2) = 0.0 otherwise

Table 10.1-1 (Continued)
Description of Control Block Operations

Number	Block Type	Block Input 1 (a)	Block Input 2 (b)	Block Input 3	Block Const 1	Block Const 2	Gain Factor (c)	Upper Limit (c)	Lower Limit (c)	Initial Value (d)	Name	Mathematical Operation (e)
42	NOR	L1	L2	N/A	N/A	N/A	N/A	N/A	N/A	LIV	Logical "Not Inclusive OR"	$L_{OUT} = 1.0 \text{ IF}((L1+L2.EQ.0.0) = 0.0 \text{ otherwise}$
43	NOT	L1	N/A	N/A	N/A	N/A	N/A	N/A	N/A	LIV	Logical "Not" or Negation	$L_{OUT} = 1.0 \text{ IF}(L1.EQ.0.0) = 0.0 \text{ IF}(L1.EQ.1.0)$
44	PDIF	X1	X2	N/A	N/A	N/A	G	XMAX	XMIN	XIV	Positive Difference	$X_{OUT} = G((X1-X2) \text{ IF}(X1.GT.X2) = 0.0 \text{ otherwise}$
45	QUAN	X1	N/A	N/A	N/A	N/A	G	XMAX	XMIN	XIV	Quantizer	$L_{OUT} = G*(X1-X2) \text{ IF}(X1.GT.X2)$
46	RAMP	N/A	N/A	N/A	C1	N/A	G	XMAX	XMIN	XIV	Ramp	$X_{OUT} = G*(TIMET-C1) \text{ IF}(TIMET.GT.C1) = 0.0 \text{ otherwise}$
47	RAND	N/A	N/A	N/A	C1	N/A	G	XMAX	XMIN	XIV	Random Number Generator	$X_{OUT} = G*RAND(DUMY) \text{ IF}(TIMET.GE.C1) = 0.0 \text{ otherwise}$
48	SIGN	X1	X2	N/A	N/A	N/A	N/A	N/A	N/A	XIV	Sign Function	$X_{OUT} = X1 \text{ IF}(X2.GE.0.0) = - X1 \text{ IF}(X2.LT.0.0)$
49	SIN	X1	X2	N/A	N/A	N/A	G	XMAX	XMIN	XIV	Sine	$X_{OUT} = G*SIN(X1), X1 \text{ in Radians}$
50	SINV	X1	X2	N/A	N/A	N/A	G	XMAX	XMIN	XIV	Sign Inversion	$X_{OUT} = -G*SIN(X1), X1 \text{ in Radians}$
51	SOTF	X1	(X2)	(X3)	C1	C2	G	XMAX	XMIN	XIV	Second Order Transfer Function	$X_{OUT} = G*X1/(1.0 + C1*S+C2*S*S)$ s is Laplace Transform Operator
52	SQRT	X1	N/A	N/A	N/A	N/A	G	XMAX	XMIN	XIV	Square Root	$X_{OUT} = G*SQRT(X1)$
53	STEP	N/A	N/A	N/A	C1	N/A	G	XMAX	XMIN	XIV	Step	$X_{OUT} = G \text{ IF}(TIMET.GT.C1) = 0.0 \text{ otherwise}$
54	SUBT	X1	X2	N/A	C1	N/A	G	XMAX	XMIN	XIV	Subtract	$X_{OUT} = G*(X1-X2)$
55	TAN	X1	N/A	N/A	C1	N/A	G	XMAX	XMIN	XIV	Tangent	$X_{OUT} = G*TAN(X1), X1 \text{ in Radians}$
56	TIME	N/A	N/A	N/A	C1	N/A	N/A	N/A	N/A	XIV	Time	$X_{OUT} = TIMET$
57	TRIP	L1	N/A	N/A	C1	N/A	N/A	N/A	N/A	LIV	Trip Status	$L_{OUT} = L1=1.0 \text{ If Trip + Delay Time Has Elapsed} = L1=0.0 \text{ otherwise}$

Table 10.1-1 (Continued)
Description of Control Block Operations

Number	Block Type	Block Input 1 (a)	Block Input 2 (b)	Block Input 3	Block Const 1	Block Const 2	Gain Factor (c)	Upper Limit (c)	Lower Limit (c)	Initial Value (d)	Name	Mathematical Operation (e)
58	VLIM	X1	X2	X3	C1	N/A	N/A	N/A	N/A	XIV	Variable Limiter	$XOUT = X2 \text{ IF } ((G \cdot X1) \text{ GT } X2)$ at Upper Limit $= X3 \text{ IF } ((G \cdot X1) \text{ LT } X3)$ at Lower Limit $= G \cdot X1 \text{ Otherwise, Between Limits}$
59	WSUM	X1	X2	N/A	C1	C2	G	XMAX	XMIN	XIV	Weighted Sumer	$XOUT = G \cdot (C1 \cdot X1 + C2 \cdot X2)$
60	XPO	X1	X2	N/A	N/A	N/A	G	XMAX	XMIN	XIV	Exponentiate	$XOUT = G \cdot (X1^{**}X2)$
61	ZOH	X1	L2	N/A	N/A	N/A	N/A	N/A	N/A	XIV	Zero Order Hold	$XOUT = X1 \text{ IF } (L2 \text{ EQ } 1.0)$ $= XOUT \text{ otherwise}$
100	DLAY	X1	n	N/A	C1	N/A	G	XMAX	XMIN	XIV	Time Delay	$XOUT = XIV \text{ IF } (TIMET \text{ LE } C1)$ $= G \cdot X1 \text{ (TIMET - C1) Otherwise}$ Where n is number of Delay Table(f) Intervals
101	FNG1	X1	n	N/A	C1	N/A	G	XMAX	XMIN	XIV	Function of One Independent Variable	$XOUT = G \cdot fn(X1)$, Where n is Function Table Number

Note:

- (a) An "X" parameter indicates a continuous variable; an "L" parameter indicates a logical (or discrete) parameter having a value of 0.0 or 1.0 only.
- (b) Variables enclosed in () are not input variables but are used internally by the control block for data storage.
- (c) If G, XMAX, and XMIN are required for a control block, a constant gain factor and constant upper and lower limits will be applied at the values given. Default values for the limits are +1.0E+50 and -1.0E+50. If $XOUT \text{ GT } XMAX$, XOUT is set equal to XMAX. If $XOUT \text{ LT } XMIN$, XOUT is set equal to XMIN.
- (d) An initial value (XIV or LIV) is loaded into a control block output (XOUT or LOUT) at $TIMET = 0.0$ seconds.
- (e) XOUT appearing on the right-hand side of a defining equation indicates a previous time step value.
- (f) Delay Table is internal to TRAC, i.e., not a Function Table, n entries determine accuracy of delay, resolution of table.

10.2 Control System Interfaces

The input values to control blocks may be obtained from the TRACG thermal-hydraulic data base (pressure, liquid level, and flow rate) or from the output of other control blocks. Thus, an extensive network of control blocks can be assembled to perform very complex operations. Control block outputs may be used as input values for other control blocks, or may be used to control (redefine) the values of variables in the component data base (VALVE areas, PUMP torques, and FILL velocities). Table 10.2-1 contains a list of variables from the TRACG data base that may be used as control block inputs or may be adjusted by control block outputs.

Figure 10.2-1 illustrates a system comprised of seven control blocks, representing a basic BWR pressure control system, designed to control the steamline inlet pressure by varying the pressure control valve area. This system obtains one of its inputs (steamline pressure) from the component database and uses one of its outputs (new valve area) to alter the VALVE component database. The remaining inputs and outputs are internal to the control system simulation.

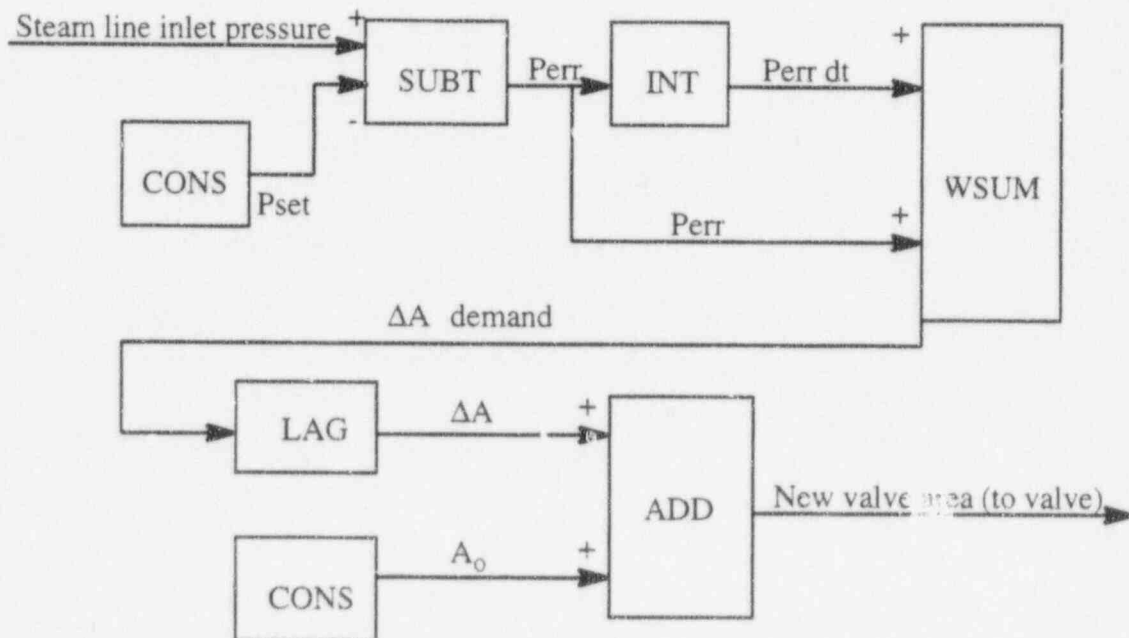


Figure 10.2-1 Simplified BWR Pressure Control System

**Table 10.2-1
Control System Input/Output Variables**

Variable Symbolic Name	Description	Input Components (Variable may be input to control system from these components)	Output Components (Variable may be adjusted by control system output for these components)	Comments
TIME	Reactor Time (s)	TIME	- None -	
POWR	Total Reactor power (W)	KINETICS	KINETICS	
TRIP	Trip Condition	TRIP	TRIP	Input variable IOCEL is Trip number
ALFA	Vapor Fraction	CHAN, FILL, PIPE, PUMP, TEE, VLVE, VSSL	FILL	
PRES	Pressure (Pa)	BREK, CHAN, FILL, PIPE, PUMP, TEE, VLVE, VSSL	BREK	
TLIQ	Liquid Temperature (K)	CHAN, FILL, PIPE, PUMP, TEE, VLVE, VSSL	FILL	
TVAP	Vapor Temperature (K)	CHAN, FILL, PIPE, PUMP, TEE, VLVE, VSSL	FILL	
MDOT	Mass Flow Rate (kg/s)	CHAN, FILL, PIPE, PUMP, TEE, VLVE	FILL	For MDOT and ENTH: IOCEL=1 gives inlet quantity IOCEL=2 gives outlet quantity IOCEL=3 gives TEE side arm quantity
ENTH	Mixture Enthalpy (J/kg)	CHAN, PIPE, PUMP, TEE, VLVE	- None -	IOCEL=2 gives outlet quantity IOCEL=3 gives Tee side arm quantity

Table 10.2-1 (Continued)
Control System Input/Output Variables

Variable Symbolic Name	Description	Input Components (Variable may be input to control system from these components)	Output Components (Variable may be adjusted by control system output for these components)	Comments
ENTH	Liquid Enthalpy (J/kg)	FILL	FILL	
TORQ	Motor Torque (Fraction of rated torque)	PUMP	PUMP	
DTOM	Derivative of pump motor with respect to speed	- None -	PUMP	
OMEG	Pump Speed (rad/s)	PUMP	- None -	
AREA	Valve Area (Fraction of fully open area)	VLVE	VLVE	
LLEV	Downcomer Liquid Level (m)	VSSL	- None -	IOCEL is VESSEL theta zone number
RHOC	Control Rod Reactivity	KINETICS	- None -	
RHOA	Additive Control Reactivity ($\Delta k/k$)	- None -	KINETICS	
BORC	Core Average Boron Concentration (ppm)	KINETICS	- None -	
ROLN	Liquid Density	VESSEL	- None -	
PW3D	3-D kinetics nodal power distribution	KINETICS	- None -	ICOMP, IOLEV, IOCELL are taken as I,J,K respectively of the node

Table 10.2-1 (Continued)
Control System Input/Output Variables

Variable Symbolic Name	Description	Input Components (Variable may be input to control system from these components)	Output Components (Variable may be adjusted by control system output for these components)	Comments
LPRM	Simulated LPRM reading	KINETICS	- None -	ICOMP, IOLEV, IOCELL are taken as I,J,k respectively of the node. LPRM location is in lower right hand corner of the node. LPRM is the average of 8 surrounding nodes
VDOT	Velocity (m/sec)		FILL	
DISP	Control block output	- None -	File code 101	Binary output for interactive display, max 100 variables
KEYB	Control block input	File code 102	- None -	Binary input for interactive control, max 100 variables
CROD	Control Rod position change (kinetics nodes)		KINETICS	ICOMP is the Control Rod Group

10.3 Control System Solution Procedure

The TRACG control system calculation may be executed with a smaller time step size than the thermal-hydraulic calculation. This feature allows the control system model to be calculated accurately, independent of the thermal-hydraulic time step size. Selection of the maximum allowable control system time step size should be based on the following criteria:

- **Accuracy in Calculating State Variable Control Blocks**

This criterion is satisfied by limiting the control system time step size smaller than the shortest time constant occurring in any of state variable control blocks.

- **Detection and Resolution of Discontinuous Transient Events**

This criterion is satisfied by limiting the control system time step size smaller than the shortest delay time occurring in any LDLY control block.

If the control system time step logic determines that the maximum allowable control system time step size is greater than or equal to the thermal-hydraulic time step size, then the thermal-hydraulic time step size will be used for the control system time step size. If the maximum allowable control system time step size is less than the thermal-hydraulic time step size, then the thermal-hydraulic time step size will be divided into the smallest number of equal intervals such that the interval size is less than or equal to the maximum control system time step size. This interval is then used as the control system time step size. In this manner, the control system calculation may be taken in several steps while it catches up with the thermal-hydraulic calculation. At the end of this series of steps, the control system calculation will be at the same time level as the thermal-hydraulic calculation. If the control system takes smaller time steps, the thermal-hydraulic block inputs are linearly interpolated between the old and new hydraulic time step values to provide consistency over the hydraulic time step.

Appendix A

Differences Between TRACG and TRAC-BF1

TRACG development has continued at General Electric after the completion of joint development programs with INEL. This appendix summarizes the major models in TRACG, which are different from the models in TRACB-BF1/MOD1 [A-1].

A.1 Modular Structure

The differences in the modular structure affect how a given facility is simulated using the thermal hydraulic components. The differences fall into two categories: (1) increased flexibility in the nodalization, and (2) restrictions on the nodalization through input and consistency checks.

A.1.1 Component Nodalization and Interaction

Zero-Cell Tee: The side branch of the tee component can have zero cells, in which case the side branch is reduced to a simple flow path.

Tee Based Channel: The channel component is based on a tee component with a zero-cell side branch representing the channel leakage path. This allows the inclusion of the leakage flow into the implicit network solution.

Flexible Valve Nodalization: TRACG allows the valve model to operate on any cell boundary in the component, including the first and the last boundary.

Horizontal Vessel Heat Slabs: The vessel component can include horizontal double-sided heat slabs, which are placed on a cell boundary between two axial levels in the vessel component. A horizontal heat slab can also be placed at the bottom or top of the vessel component.

One-Dimensional Heat Slab Properties: The properties for a one-dimensional heat slab can be specified separately for each node.

Fill to Vessel Junction: TRACG allows a fill component to be connected directly to a vessel component cell.

A.1.1 Nodalization and Consistency Checks

Nodalization and Loss Coefficient Checks: TRACG evaluates the nodalization for each component and determines when a flow restriction, contraction or expansion exists. An irreversible form loss is expected at these locations, and TRACG will produce a warning if no loss coefficients are specified in the input.

Junction Elevations: TRACG calculates the elevation of all junctions between components. Whenever a loop exists (e.g., the recirculation loop for a BWR or the simple loops composed of

the channel and the vessel components for a BWR), TRACG evaluates the consistency of the input by requiring that:

$$\oint_{\text{Around loop}} \bar{g} \cdot d\bar{x} = 0 \quad (\text{A-1})$$

Junction Consistency: At a junction between two components, a number of parameters (e.g., loss coefficients, hydraulic diameter, gravity vector) are specified for each component. TRACG requires that identical inputs are specified for each component at a junction.

A.2 Basic Models

There are very few differences in the basic thermal-hydraulic models between TRACG and TRAC-BF1/MOD1, since these models were jointly developed by GE and INEL. A number of additional model features, however, have been included in TRACG.

Multiple Noncondensable Gas Species: The equations for the noncondensable gas component have been upgraded to simulate a mixture of several noncondensable gases.

Kinetic Energy: Previous TRAC versions eliminated the kinetic energy term from the energy equations through algebraic manipulations involving the momentum equation. In that form, the flow work in the energy equation was on a nonconserving form, and energy balance errors could occur. TRACG avoids this problem by retaining the kinetic energy term in the energy equations (Section 3.1.2).

Stratified Flow: A stratified flow model is added to the flow regime map (Section 5.1.3).

Friction: TRACG uses the GE design correlation for the wall friction (Section 6.2).

Turbulent Mixing: A simple model for turbulent mixing between two cells is included in TRACG (Section 6.7).

Condensation Heat Transfer: The correlations for condensation heat transfer in TRACG are upgraded to include shear enhancement and degradation due to presence of noncondensable gases (Sections 6.6.11 and 6.5).

Quenching: The original model for quenching heat transfer from TRAC-P1A [A-3] has been retained in TRACG (Section 6.6.13).

Boiling Transition: The GEXL-correlation is included in TRACG for calculation of boiling transition in the channel component (Section 6.6.6).

Pump Work: The pump work is included in the energy equations (Section 7.2.1).

A.3 Component Models

There are a number of differences for the component models. They all involve additional features, which have been added to TRACG.

Pump: A fully implicit integration scheme has been implemented for the calculation of the pump speed. This includes a coupled solution for the pump fluid momentum equations (Section 7.2.1).

Jet Pump: TRACG allows a more realistic simulation of the flare at the suction inlet to the jet pump (Section 7.6.1).

Channel: There are a number of differences for the channel component: (1) the channel component is based on the tee component, allowing a fully implicit calculation of the leakage flow (Section 7.5); (2) calculation of the channel to bypass leakage flow has been upgraded to include all flow paths consistent with existing GE design methods (Section 7.5.1); (3) simulation of the hydraulics inside the water rod has been included (Section 7.5.7); (4) dynamic gap conductance and cladding perforation models have been included consistent with existing GE design methods (Section 7.5.2); (5) a hot rod model for bounding temperature calculations is included in TRACG (Section 7.5.6); and (6) critical power ratio is calculated (Section 7.5.5).

Vessel Upper Plenum: A model for the interaction between the ECC injected from the core spray spargers and the ambient fluid in the upper plenum of a BWR is included. The model considers submerged jet and spray injection (Section 7.8.2).

Vessel Bypass Heating: When the kinetics option is applied, direct moderator heating of the bypass fluid is included (Section 9.4).

Vessel Horizontal Heat Slabs: In TRACG, one-dimensional heat slabs can be placed at a cell boundary between two vessel levels (Section 7.8).

A.4 Kinetics

TRACG utilizes a three-dimensional kinetics model consistent with the GE three-dimensional core simulator PANAC [A-4] (Section 9). It is a modified one-group model and includes six delayed neutron precursor groups. Feedback from the thermal hydraulic model includes moderator density, fuel temperature, control rod and boron reactivity. A five-group decay heat model is applied, and the energy can be deposited in the fuel and in the coolant.

A.5 Control System

Additional interfaces have been added to the control system model in TRACG, allowing more realistic simulation of the BWR (Section 10):

BWR Instrumentation: Additional inputs have been added to the control system to allow simulation of BWR instruments such as level sensors and LPRM's.

Reactivity Control: Additional outputs have been added to the control system, allowing movement of the control rods.

Numerics: TRACG has retained the original explicit integration scheme for the control system [A-2], but TRACG allows the use of a smaller time step size for the control system than for the hydraulics.

A.6 Numerics

Several refinements have been made to the numerical integration scheme in TRACG. These refinements generally only affect the computer time and have only a small effect on the calculated results. The following changes have been made (Section 8):

Implicit Integration: TRACG utilizes an optional semi-implicit or fully implicit integration of the hydraulic conservation equations for mass, momentum and energy for both one-dimensional and three-dimensional components. In the semi-implicit integration scheme, only properties convected with the speed of sound are treated implicitly, whereas properties convected with the fluid speed are treated explicitly. For the fully implicit integration, all convective terms are treated implicitly.

Implicit Heat Transfer Coupling: For the implicit integration scheme, a fully implicit heat transfer coupling between the heat conduction equation and the hydraulic equations is applied in TRACG.

A.7 References

- A-1 J.A. Borkowski, et. al., *TRAC-BF1/MOD1: An Advanced Best Estimate Program for BWR Accident Analysis*, NUREG/CR-4356, Idaho National Engineering Laboratory, August 1992.
- A-2 D.D. Taylor, et. al., *TRAC-BD1/MOD1: An Advanced Best Estimate Computer Program for Boiling Water Reactor Transient Analysis, Volume 1: Model Description*, NUREG/CR-3633, EGG-2294, April 1984.
- A-3 R.J. Pryor, et. al., *TRAC-PIA, An Advanced Best Estimate Computer Program for PWR LOCA Analysis*, Los Alamos Scientific Laboratory, NUREG/CRA-0665, May 1979.
- A-4 *Steady-State Nuclear Methods*, NEDE-30130PA, April 1985.

Appendix B

Thermodynamic and Transport Fluid Properties

B.1 Introduction

Thermodynamic and transport property subroutines used in TRACG are based on polynomial fits to steam table data for water and ideal gas behavior for the noncondensable gas. Transport property fits were obtained from Reference B-1 and thermodynamic property fits were obtained from Reference B-2. Both the thermodynamic and transport property routines are used by all TRACG component modules. Tables B-1 through B-6 list the values of the constants. The nomenclature used in this Appendix is consistent with the terminology defined in Section 3.

Table B-1

Polynomial Constants for Thermodynamic Properties of Water and Air

C_1	= 117.8	C_{24}	= 1.3
C_2	= 0.223	C_{26}	= 0.3
C_3	= 255.2	C_{28}	= 1.0×10^5
C_4	= 958.75	C_{40}	= 273.0
C_5	= -0.856 6	C_{41}	= 239.36
C_6	= $2.619\ 410\ 618 \times 10^6$	C_{42}	= 2.786 7
C_7	= -4.995×10^{10}	C_{43}	= -5.776 26
C_8	= 3.403×10^5	C_{44}	= 3.938
C_9	= 1.066 554 48	C_{45}	= 1.0×10^{-6}
C_{10}	= 1.02×10^{-8}	C_{47}	= 1.0×10^3
C_{11}	= -2.548×10^{-15}	C_{48}	= -0.15×10^3
C_{12}	= $2.589\ 600 \times 10^6$	C_{49}	= -20.0
C_{13}	= 6.350×10^{-3}	C_{51}	= 0.657×10^{-6}
C_{14}	= $-1.058\ 2 \times 10^{-9}$	C_{52}	= $2.996\ 018\ 036 \times 10^3$
C_{15}	= 1.076 4	C_{53}	= $9.700\ 016\ 602 \times 10^3$
C_{16}	= 3.625×10^{-10}	C_{54}	= $-8.448\ 077\ 393 \times 10^3$
C_{17}	= -9.063×10^{-17}	C_{55}	= 8.349 824
C_{20}	= 461.7	C_{56}	= $3.495\ 194\ 44 \times 10^2$
C_{21}	= 2.0×10^6	C_{k0}	= $-8.335\ 44 \times 10^{-4}$
C_{23}	= 647.3	C_{k2}	= $-2.247\ 45 \times 10^{-17}$
ELC0	= $1.758\ 80 \times 10^4$	ELE0	= $2.283\ 789\ 029 \times 10^9$
ELC1	= $3.740\ 2 \times 10^3$	ELE1	= $-2.622\ 156\ 77 \times 10^7$
ELC2	= 4.024 35	ELE2	= $1.129\ 486\ 67 \times 10^5$
ELC3	= -0.015 729 4	ELE3	= $-2.162\ 339\ 85 \times 10^2$
ELC4	= $3.130\ 1 \times 10^{-5}$	ELE4	= 0.155 283 438
ELD0	= $6.185\ 27 \times 10^6$	C_{vg}	= 714.9
ELD1	= $-8.145\ 47 \times 10^4$	R	= 287.12
ELD2	= $4.465\ 98 \times 10^2$		
ELD3	= -1.041 16		
ELD4	= $9.260\ 22 \times 10^{-4}$		

Table B-1
Polynomial Constants for Thermodynamic Properties of Water and Air
(Continued)

CVL1	=	1.002 136 23	CVH1	=	2.252 62
CVL2	=	-5.632 785 x 10 ⁻⁵	CVH2	=	0.014 859 4
CVL3	=	-8.971 304 77 x 10 ⁻⁹	CVH3	=	-7.154 88 x 10 ⁻⁵
CVL4	=	-2.282 874 59 x 10 ⁻⁵	CVH4	=	-0.010 458 8
CVL5	=	4.765 967 87 x 10 ⁻⁷	CVH5	=	-1.029 62 x 10 ⁻⁴
CVL6	=	5.021 318 x 10 ⁻¹⁰	CVH6	=	5.091 35 x 10 ⁻⁷
CVL7	=	4.101 156 58 x 10 ⁻⁶	CVH7	=	2.592 66 x 10 ⁻⁵
CVL8	=	-3.803 989 08 x 10 ⁻⁹	CVH8	=	1.724 1 x 10 ⁻⁷
CVL9	=	-1.421 997 52 x 10 ⁻¹²	CVH9	=	-8.984 19 x 10 ⁻¹⁰

Table B-2
Derived Constants for Thermodynamic Properties of Water and Air

A ₁	=	C ₁ • C ₂ /C ₂₈	A ₁₁	=	2 • C ₂₆ /(C ₂₄ • C ₂₀)
A ₂	=	C ₂ - 1.0	A ₁₃	=	A ₁₁ • (1.0 + C ₂₆)
A ₃	=	-C ₄ • C ₅ /C ₂₃	A ₁₂	=	1.0/A ₁₃
A ₄	=	C ₅ - 1.0	A ₁₄	=	1.0/C ₂₈
A ₅	=	C ₄₅ • C ₄₉	A ₁₅	=	1.0/C ₂₃
A ₆	=	2 • C ₄₅ • C ₄₈	A ₁₆	=	2 • C ₁₁
A ₇	=	4 • C ₄₄ • C ₄₅	A ₁₇	=	2 • C ₁₄
A ₈	=	3 • C ₄₃ • C ₄₅	A ₁₈	=	2 • C ₁₇
A ₉	=	2 • C ₄₂ • C ₄₅	A ₁₉	=	2 • C ₄₈ • C ₄₅
A ₁₀	=	C ₄₁ • C ₄₅	A ₂₀	=	C ₄₅ • C ₄₉
DELC0	=	ELC1	DELDO	=	ELD1
DELC1	=	2 • ELC2	DELD1	=	2 • ELD2
DELC2	=	3 • ELC3	DELD2	=	3 • ELD3
DELC3	=	4 • ELC4	DELD3	=	4 • ELD4
DELE0	=	ELE1			
DELE1	=	2 • ELE2			
DELE2	=	3 • ELE3			
DELE3	=	4 • ELE4			

Table B-3
Basic Constants for Transport Properties of Water and Air

B_{0l}	=	$2.394\ 907 \times 10^{-4}$	B_{1l}	=	$-5.196\ 250 \times 10^{-13}$
C_{0l}	=	$1.193\ 203 \times 10^{-11}$	C_{1l}	=	$2.412\ 704 \times 10^{-18}$
D_{0l}	=	$-3.944\ 067 \times 10^{-17}$	D_{1l}	=	$-1.680\ 771 \times 10^{-24}$
		C_{1g}	=	$1.688\ 359\ 68 \times 10^3$	
		C_{2g}	=	$0.602\ 985\ 6$	
		C_{3g}	=	$4.820\ 979\ 623 \times 10^2$	
		C_{4g}	=	$2.953\ 179\ 05 \times 10^7$	
		C_{5g}	=	1.8	
		C_{6g}	=	4.60×10^2	

Table B-4
Liquid Viscosity Constants

A_{0l}	=	$1.299\ 470\ 229 \times 10^{-3}$	B_{0l}	=	$-6.595\ 9 \times 10^{-12}$
A_{1l}	=	$-9.264\ 032\ 108 \times 10^{-4}$	B_{1l}	=	6.763×10^{-12}
A_{2l}	=	$3.810\ 470\ 61 \times 10^{-4}$	B_{2l}	=	$2.888\ 25 \times 10^{-12}$
A_{3l}	=	$-8.219\ 444\ 458 \times 10^{-5}$	B_{3l}	=	$4.452\ 5 \times 10^{-13}$
A_{4l}	=	$7.022\ 437\ 984 \times 10^{-6}$			
D_{0l}	=	$3.026\ 032\ 306 \times 10^{-4}$	E_{0l}	=	$1.452\ 605\ 261\ 2 \times 10^{-3}$
D_{1l}	=	$-1.836\ 606\ 896 \times 10^{-4}$	E_{1l}	=	$-6.988\ 008\ 498\ 5 \times 10^{-9}$
D_{2l}	=	$7.567\ 075\ 775 \times 10^{-5}$	E_{2l}	=	$1.521\ 023\ 033\ 4 \times 10^{-14}$
D_{3l}	=	$-1.647\ 878\ 879 \times 10^{-5}$	E_{3l}	=	$1.230\ 319\ 494\ 6 \times 10^{-20}$
D_{4l}	=	$1.416\ 457\ 633 \times 10^{-6}$			
F_{0l}	=	$-3.806\ 350\ 753\ 3 \times 10^{-11}$	h_0	=	$8.581\ 289\ 699 \times 10^{-6}$
F_{1l}	=	$3.928\ 520\ 767\ 7 \times 10^{-16}$	c_{0n}	=	$4.265\ 884 \times 10^4$
F_{2l}	=	$-1.258\ 579\ 929\ 2 \times 10^{-21}$	P_i	=	$6.894\ 575\ 293 \times 10^5$
F_{3l}	=	$1.286\ 018\ 078\ 8 \times 10^{-27}$			
h_{00}	=	$3.892\ 077\ 365 \times 10^{-6}$	e_{h0}	=	$6.484\ 503\ 981 \times 10^{-6}$
e_{c0n}	=	$5.535\ 88 \times 10^4$	c_n	=	$4.014\ 676 \times 10^5$
h_1	=	2.76×10^5	h_2	=	3.94×10^5

Table B-5
Vapor Viscosity Constants

A_{0g}	= 3.53×10^{-8}	B_{1g}	= 0.407×10^{-7}
A_{1g}	= 6.765×10^{-11}	C_{1g}	= 8.04×10^{-6}
A_{2g}	= 1.021×10^{-14}	D_{1g}	= 1.858×10^{-7}
		E_{1g}	= 5.9×10^{-10}
F_{1g}	= -0.2885×10^{-5}	G_{1g}	= 176.0
F_{2g}	= 0.2427×10^{-7}	G_{2g}	= -1.6
F_{3g}	= $-0.6789333 \times 10^{-10}$	G_{3g}	= 0.0048
F_{4g}	= $0.6317037037 \times 10^{-13}$	G_{4g}	= $-0.474074074 \times 10^{-5}$
$H_{\ell 1}$	= 1.708×10^{-5}	H_{u1}	= 1.735×10^{-5}
$H_{\ell 2}$	= 5.927×10^{-8}	H_{u2}	= 4.193×10^{-8}
$H_{\ell 3}$	= 8.14×10^{-11}	H_{u3}	= 1.09×10^{-11}
T_1	= 573.15		
T_2	= 648.15		

Table B-6
Thermal Conductivity Constants

h_0	= 5.815×10^5
$A_{\ell 0}$	= 0.573738622
$A_{\ell 1}$	= 0.2536103551
$A_{\ell 2}$	= -0.145468269
$A_{\ell 3}$	= 0.01387472485
C	= 2.1482×10^5
A_{g0}	= 1.76×10^{-2}
A_{g1}	= 5.87×10^{-5}
A_{g2}	= 1.04×10^{-7}
A_{g3}	= -4.51×10^{-11}
B_{g0}	= 1.0351×10^{-4}
B_{g1}	= 0.4198×10^{-6}
B_{g2}	= -2.771×10^{-11}

B.2 Thermodynamic Properties

Subroutine THERMO supplies thermodynamic properties for TRACG. The input variables are pressure, liquid, and vapor temperatures. The output variables include (a) saturation temperature, (b) the derivative of T_{sat} with respect to pressure, (c) internal energy, (d) density, (e) the derivatives of internal energy and density with respect to pressure for each phase, and (f) the derivatives of internal energy and density with respect to temperature for each phase. Subroutine THERMO also includes an ideal gas option to calculate the density, internal energy, and their associated derivatives with respect to pressure and temperature for the noncondensable.

The ranges of validity for the thermodynamic properties supplied by THERMO are $280.0 \text{ K} \leq T_\ell \leq 647.0 \text{ K}$, $280.0 \text{ K} \leq T_v \leq 3000.0 \text{ K}$, and $1.0 \times 10^3 \text{ Pa} \leq P \leq 190.0 \times 10^5 \text{ Pa}$. If THERMO is provided with data outside this range, it adjusts the data to the corresponding limit and issues a warning message.

Polynomial equations for the various properties used in THERMO are given below. Values of the constants are given in Tables B-1 and B-2.

B.2.1 Saturation Properties

B.2.1.1 Temperature

For $T_{\text{sat}} \leq C_{23}$ (higher saturation temperatures cause THERMO to abort):

$$T_{\text{sat}} = C_1 (A_{14}P)^{C_2} + C_3 \quad (\text{B-1a})$$

and

$$\frac{\partial T_{\text{sat}}}{\partial P} = A_1 (A_{14}P)^{A_2} \quad (\text{B-1b})$$

B.2.1.2 Internal Energy

For $P \leq C_{21}$

$$e_{\text{sat}} = C_6 + C_7 \left(\frac{1.0}{C_8 + P} \right) \quad (\text{B-2a})$$

For $P > C_{21}$

$$e_{\text{sat}} = C_{12} + (C_{14}P + C_{13})P \quad (\text{B-2b})$$

For $P \leq C_{21}$

$$\frac{\partial e_{\text{sat}}}{\partial P} = -C_7 \left(\frac{1.0}{C_8 + P} \right)^2 \quad (\text{B-2c})$$

and for $P > C_{21}$

$$\frac{\partial e_{\text{sat}}}{\partial P} = C_{13} + A_{17}P. \quad (\text{B-2d})$$

B.2.1.3 Heat Capacity

$$C_{\text{ps}} = C_{52} + T_1(C_{53} T_1 + C_{54}) + \left(\frac{C_{55} + C_{56}}{T_1} \right) \quad (\text{B-3a})$$

and

$$\frac{\partial C_{\text{ps}}}{\partial P} = -A_{15} \frac{\partial T_{\text{sat}}}{\partial P} \left[C_{54} + 2C_{53} T_1 - \frac{\left(\frac{2C_{55}}{T_1} + C_{56} \right)}{T_1^2} \right] \quad (\text{B-3b})$$

where

$$T_1 = 1.0 - A_{15} T_{\text{sat}}.$$

B.2.1.4 Enthalpy

$$hg = e_{\text{sat}} \gamma_s \quad (\text{B-4a})$$

and

$$\frac{\partial h_g}{\partial P} = \frac{\partial e_{\text{sat}}}{\partial P} \gamma_s \quad (\text{B-4b})$$

where

$$\begin{aligned} \gamma_s &= C_9 + (C_{11}P + C_{10})P \text{ for } P \leq C_{21} \\ &= C_{15} + (C_{17}P + C_{16})P \text{ for } P > C_{21} \end{aligned}$$

$$h_f = e_\ell(T_{\text{sat}}) + \frac{P}{\rho_\ell(T_{\text{sat}})}$$

$$\frac{\partial h_f}{\partial P} = \left. \frac{\partial e_\ell}{\partial T} \right|_{T_{\text{sat}}} + \frac{1}{\rho_\ell(T_{\text{sat}})} - \frac{P}{\rho_\ell^2(T_{\text{sat}})} \left. \frac{\partial \rho_\ell}{\partial T} \right|_{T_{\text{sat}}} \left(\frac{\partial T_{\text{sat}}}{\partial P} + \frac{\partial P}{\partial P} \right)$$

and e_ℓ , ρ_ℓ , and their derivatives are evaluated using the liquid equations given below.

B.2.2 Liquid Properties

B.2.2.1 Internal Energy

$$\text{TLC} = T_\ell - 273.15$$

$$\text{PSL} = \frac{\left[\frac{(T_\ell - C_3)^{1/2}}{C_1} \right]}{A_{14}}$$

$$\text{ELP} = (P - \text{PSL})(C_{k0} + C_{k2} \text{PSL}^2)$$

and

$$\text{ERT} = \frac{-C_{k0} + C_{k2}(2 \cdot \text{PSL} \cdot p - 3 \cdot \text{PSL}^2)}{A_1 (A_{14} \cdot \text{PSL})^2}$$

There are three temperature domains used in evaluating the liquid internal energy:

- (1) $T_\ell < 548.15$
- (2) $548.15 \leq T_\ell \leq 611.15$
- (3) $T_\ell > 611.15$

For $T_\ell < 548.15$:

$$e_\ell = \text{ELC0} + \text{ELC1} \cdot \text{TLC} + \text{ELC2} \cdot \text{TLC}^2 + \text{ELC3} \cdot \text{TLC}^3 + \text{ELC4} \cdot \text{TLC}^4 + \text{ELP}. \quad (\text{B-5a})$$

$$\frac{\partial e_\ell}{\partial T} = \text{DELCO} + \text{DELCO} \cdot \text{TLC} + \text{DELCO} \cdot \text{TLC}^2 + \text{DELCO} \cdot \text{TLC}^3 + \text{ERT}. \quad (\text{B-5b})$$

For $548.15 \leq T_\ell \leq 611.15$:

$$e_\ell = \text{ELD0} + \text{ELD1} \cdot \text{TLC} + \text{ELD2} \cdot \text{TLC}^2 + \text{ELD3} \cdot \text{TLC}^3 + \text{ELD4} \cdot \text{TLC}^4 + \text{ELP}. \quad (\text{B-6a})$$

$$\frac{\alpha e_\ell}{\partial T} = \text{DELD0} + \text{DELD1} \cdot \text{TLC} + \text{DELD2} \cdot \text{TLC}^2 + \text{DELD3} \cdot \text{TLC}^3 + \text{ERT}. \quad (\text{B-6b})$$

For $T_\ell > 611.15$:

$$e_\ell = \text{ELE0} + \text{ELE1} \cdot \text{TLC} + \text{ELE2} \cdot \text{TLC}^2 + \text{ELE3} \cdot \text{TLC}^3 + \text{ELE4} \cdot \text{TLC}^4 + \text{ELP}. \quad (\text{B-7a})$$

$$\frac{\alpha e_\ell}{\partial T} = \text{DELE0} + \text{DELE1} \cdot \text{TLC} + \text{DELE2} \cdot \text{TLC}^2 + \text{DELE3} \cdot \text{TLC}^3 + \text{ERT}. \quad (\text{B-7b})$$

For all three temperature domains:

$$\frac{\partial e_\ell}{\partial P} = C_{k0} + C_{k2} \cdot \text{PSL}^2. \quad (\text{B-8})$$

B.2.2.2 Density

Define $\text{PBAR} = 1.0 \times 10^{-5} P$ and $\text{TLC} = T_\ell - 273.15$. There are three temperature domains:

- (1) $T_\ell > 525.15$
- (2) $T_\ell < 521.15$
- (3) $521.15 \leq T_\ell \leq 525.15$

For $T_\ell > 525.15$:

$$\rho_\ell = 1.43 + \frac{1000}{(CVH1 + CVH2 \cdot PBAR + CVH3 \cdot PBAR^2 + \beta_1 \cdot TLC + \gamma_1 \cdot TLC^2)} \quad (B-9a)$$

$$\frac{\partial \rho_\ell}{\partial P} = -(\rho_\ell - 1.43)^2 \cdot 1.0 \times 10^{-8} [CVH2 + 2 \cdot CVH3 \cdot PBAR + TLC(CVH5 + 2 \cdot CVH6 \cdot PBAR) + TLC^2 (CVH8 + 2 \cdot CVH9 \cdot PBAR)] \quad (B-9b)$$

$$\frac{\partial \rho_\ell}{\partial T_\ell} = -(\rho_\ell - 1.43)^2 \cdot 1.0 \times 10^{-3} (\beta_1 + 2 \cdot \gamma_1 \cdot TLC) \quad (B-9c)$$

where

$$\beta_1 = CVH4 + CVH5 \cdot PBAR + CVH6 \cdot PBAR^2$$

and

$$\gamma_1 = CVH7 + CVH8 \cdot PBAR + CVH9 \cdot PBAR^2.$$

For $T_\ell < 521.15$:

$$\rho_\ell = \frac{1000}{(CVL1 + CVL2 \cdot PBAR + CVL3 \cdot PBAR)^2 + \beta_1 \cdot TLC + \gamma_1 \cdot TLC^2} - 2.01 \quad (B-10a)$$

$$\frac{\partial \rho_\ell}{\partial P} = -(\rho_\ell + 2.01)^2 \cdot 1.0 \times 10^{-8} [CVL2 + 2 \cdot CVL3 \cdot PBAR + TLC(CVL5 + 2 \cdot CVL6 \cdot PBAR) + TLC^2 (CVL8 + 2 \cdot CVL9 \cdot PBAR)] \quad (B-10b)$$

$$\frac{\partial \rho_\ell}{\partial T_\ell} = -(\rho_\ell + 2.01)^2 \cdot 1.0 \times 10^{-3} (\beta_1 + 2 \cdot \gamma_1 \cdot TLC) \quad (B-10c)$$

where

$$\beta_1 = CVL4 + CVL5 \cdot PBAR + CVL6 \cdot PBAR^2$$

$$\gamma_1 = CVL7 + CVL8 \cdot PBAR + CVL9 \cdot PBAR^2.$$

For $521.15 \leq T_\ell \leq 525.15$, an average of the functions in Equations B-9 and B-10 is used in this range. Call the two values $\rho_{\ell a}$ and $\rho_{\ell b}$, then:

$$\rho_\ell = \left(\frac{525.15 - T_\ell}{4.0} \right) \rho_{\ell b} + \left(\frac{T_\ell - 521.15}{4.0} \right) \rho_{\ell a} \quad (\text{B-11a})$$

$$\frac{\partial \rho_\ell}{\partial P} = \left(\frac{525.15 - T_\ell}{4.0} \right) \frac{\partial \rho_{\ell b}}{\partial P} + \left(\frac{T_\ell - 521.15}{4.0} \right) \frac{\partial \rho_{\ell a}}{\partial P} \quad (\text{B-11b})$$

$$\frac{\partial \rho_\ell}{\partial T_\ell} = \left(\frac{525.15 - T_\ell}{4.0} \right) \frac{\partial \rho_{\ell b}}{\partial T_\ell} + \left(\frac{T_\ell - 521.15}{4.0} \right) \frac{\partial \rho_{\ell a}}{\partial T_\ell} + \frac{\rho_{\ell a} - \rho_{\ell b}}{4.0} \quad (\text{B-11c})$$

After evaluation above, a pressure correction is applied to ρ_ℓ and its derivatives. In the following, the values calculated in Equations B-9a through B-11c are denoted by a tilde (~).

(a) $P \geq 4.0 \times 10^5 \text{ Pa}$

$$\left(\frac{\partial \rho_\ell}{\partial T_\ell} \right)_P = \left(1 - \frac{1000}{P} \right) \left(\frac{\partial \tilde{\rho}_\ell}{\partial T_\ell} \right)_P$$

$$\left(\frac{\partial \rho_\ell}{\partial P} \right)_{T_\ell} = \left(1 - \frac{1000}{P} \right) \left(\frac{\partial \tilde{\rho}_\ell}{\partial P} \right)_{T_\ell} + \frac{1000 \tilde{\rho}_\ell}{P^2}$$

$$\rho_\ell = \left(1 - \frac{1000}{P} \right) \tilde{\rho}_\ell$$

(b) $P \leq 4.0 \times 10^5 \text{ Pa}$

$$\left(\frac{\partial \rho_\ell}{\partial T_\ell} \right)_P = (0.995 + 6.25 \times 10^{-9} P) \left(\frac{\partial \tilde{\rho}_\ell}{\partial T_\ell} \right)_P$$

$$\left(\frac{\partial \rho_\ell}{\partial P} \right)_{T_\ell} = (0.995 + 6.25 \times 10^{-9} P) \left(\frac{\partial \tilde{\rho}_\ell}{\partial P} \right)_{T_\ell} + 6.25 \times 10^{-9} \tilde{\rho}_\ell$$

$$\rho_\ell = (0.995 + 6.25 \times 10^{-9} P) \tilde{\rho}_\ell$$

B.2.2.4 Enthalpy

Enthalpy is not evaluated by the water property routines, but may be evaluated easily through:

$$h_\ell = e_\ell + \frac{P}{\rho_\ell} \quad (\text{B-12})$$

B.2.3 Vapor Properties

B.2.3.1 Superheated Vapor

$$(T_v - T_{\text{sat}}) > 0.$$

B.2.3.1.1 Internal Energy

$$e_s = e_{\text{sat}} + A_{12} \left[(T_v - T_{\text{sat}}) + (T_v^2 - \beta) \right]^{1/2} - \frac{T_{\text{sat}}}{(A_{11} C_{ps} - 1.0)} \quad (\text{B-13})$$

where

$$\beta = T_{\text{sat}}^2 \left[1.0 - \frac{1.0}{(A_{11} C_{ps} - 1.0)^2} \right]$$

$$\frac{\partial e_s}{\partial T_v} = \left[\frac{A_{12}}{2} \left(1.0 - \frac{\beta}{k^2} \right) \right]^{-1.0}$$

$$k = A_{13} (e_s - e_{\text{sat}}) + T_{\text{sat}} \left[1.0 + \frac{1.0}{(A_{11} C_{ps} - 1.0)} \right]$$

$$\frac{\partial e_s}{\partial P} = -\frac{1}{2} \left(\frac{\partial e_s}{\partial T_v} \right) \left[\left(1.0 - \frac{\beta}{k^2} \right) \frac{\partial k}{\partial P} + \frac{1}{k} \frac{\partial \beta}{\partial P} \right]$$

$$\frac{\partial k}{\partial P} = -A_{13} \frac{\partial e_{\text{sat}}}{\partial P} + \left[1.0 + \frac{1.0}{(A_{11} C_{ps} - 1.0)} \right] \frac{\partial T_{\text{sat}}}{\partial P}$$

$$-T_{\text{sat}} A_{11} \left[\frac{1.0}{(A_{11} C_{ps} - 1.0)^2} \right] \frac{\partial C_{ps}}{\partial P}$$

and

$$\frac{\partial \beta}{\partial P} = \frac{2.0}{T_{\text{sat}}} \left[\beta \left(\frac{\partial T_{\text{sat}}}{\partial P} \right) + \frac{T_{\text{sat}}^3 A_{11}}{(A_{11} C_{\text{ps}} - 1.0)^3} \right] \left(\frac{\partial C_{\text{ps}}}{\partial P} \right)$$

B.2.3.1.2 Density

$$\rho_s = \frac{P}{[(\gamma_s - 1.0)e_{\text{sat}} + C_{26}(e_s - e_{\text{sat}})]} \quad (\text{B-14a})$$

$$\frac{\partial \rho_s}{\partial T_v} = - \left(\frac{\partial e_s}{\partial T_v} \right) \left[\frac{C_{26} \rho_s}{(\gamma_s - 1.0)e_{\text{sat}} + C_{26}(e_s - e_{\text{sat}})} \right] \quad (\text{B-14b})$$

and

$$\frac{\partial \rho_s}{\partial P} = \rho_s \left\{ \left[\frac{1.0}{P} - e_{\text{sat}} \left(\frac{\partial \gamma_s}{\partial P} \right) + (\gamma_s - 1.0 - C_{26}) \frac{\partial e_{\text{sat}}}{\partial P} \right] \right. \quad (\text{B-14c})$$

$$\left. \left[\frac{1.0}{(\gamma_s - 1.0)e_{\text{sat}} + C_{26}(e_s - e_{\text{sat}})} \right] \right\} + \left(\frac{\partial \rho_s}{\partial e_s} \right) \left(\frac{\partial e_s}{\partial P} \right)$$

where

$$\frac{\partial \gamma_s}{\partial P} = C_{10} + A_{16} P \text{ for } P \leq C_{21}$$

$$\frac{\partial \gamma_s}{\partial P} = C_{16} + A_{18} P \text{ for } P > C_{21}$$

and

$$\frac{\partial \rho_s}{\partial e_s} = \frac{-C_{26} \rho_s}{[(\gamma_s - 1.0)e_{\text{sat}} + C_{26}(e_s - e_{\text{sat}})]}$$

If ρ_s exceeds $0.9\rho_\ell$ or is < 0 , Equation B-14 is superseded by

$$\rho_s = 0.9\rho_\ell \quad (\text{B-15a})$$

$$\frac{\partial \rho_s}{\partial T_v} = 0.9 \left(\frac{\partial \rho_\ell}{\partial T_\ell} \right) \quad (\text{B-15b})$$

and

$$\frac{\partial \rho_s}{\partial P} = 0.9 \left(\frac{\partial \rho_\ell}{\partial P} \right) \quad (\text{B-15c})$$

B.2.3.1.3 Enthalpy

Enthalpy is not evaluated by the water property routines, but may be calculated easily through:

$$h_s = e_s + \frac{P}{\rho_s} \quad (\text{B-16})$$

B.2.3.2 Subcooled Vapor

$$(T_v - T_{\text{sat}}) \leq 0.$$

B.2.3.2.1 Internal Energy

$$e_s = e_{\text{sat}} + (T_v - T_{\text{sat}}) \frac{C_{\text{ps}}}{C_{24}} \quad (\text{B-17a})$$

$$\frac{\partial e_s}{\partial T_v} = \frac{C_{\text{ps}}}{C_{24}} \quad (\text{B-17b})$$

$$\frac{\partial e_s}{\partial P} = - \left(\frac{\partial e_s}{\partial T_v} \right) \left\{ \frac{\partial T_{\text{sat}}}{\partial P} - \left(\frac{C_{24}}{C_{\text{ps}}} \right) \left[\frac{\partial e_{\text{sat}}}{\partial P} + \frac{(e_s - e_{\text{sat}})}{C_{\text{ps}}} \left(\frac{\partial C_{\text{ps}}}{\partial P} \right) \right] \right\} \quad (\text{B-17c})$$

B.2.3.2.2 Density

The formulas are identical to the superheated vapor case above, but the subcooled vapor energy is used in this case.

B.2.3.2.3 Enthalpy

Enthalpy is not evaluated by the water property routines, but may be calculated easily through:

$$h_s = e_s + \frac{P}{\rho_s} \quad (\text{B-18})$$

B.2.3.3 Noncondensable Gas (Air)

The density and internal energy of the noncondensable gas are computed from the perfect gas law. The default noncondensable gas is air. The option to overlay the gas constant (R) and specific heat (C_{vg}) to model other gas(es) is available.

B.2.3.3.1 Internal Energy

$$e_a = C_{vg} T_g \quad (\text{B-19a})$$

$$\frac{\partial e_a}{\partial T_v} = C_{vg} \quad (\text{B-19b})$$

$$\frac{\partial e_a}{\partial P} = 0.0. \quad (\text{B-19c})$$

B.2.3.3.2 Density

$$\rho_a = \frac{P}{RT_v} \quad (\text{B-20a})$$

$$\frac{\partial \rho_a}{\partial P} = \frac{1.0}{RT_v} \quad (\text{B-20b})$$

$$\frac{\partial \rho_a}{\partial T_v} = -R\rho_a \left(\frac{\partial \rho_a}{\partial P} \right) \quad (\text{B-20c})$$

where R is the universal gas constant divided by the molecular weight for the noncondensable.

B.2.3.4 Properties of Water Mixtures

The internal energy of a mixture of steam and noncondensable gas is given by the density-weighted average of the internal energies of the two species. The density of a mixture of steam and noncondensable gas is the sum of the densities of the two species.

B.3 Transport Properties

Subroutine FPROP is used to obtain transport water properties for TRACG. The input variables for this routine are (a) the saturation temperature, (b) pressure, (c) enthalpies of each phase, (d) vapor density, and (e) the vapor temperature. The output transport variables include (a) the latent heat of vaporization, (b) surface tension, (c) constant pressure specific heat, (d) viscosity, and (e) thermal conductivity of each phase. The transport property calls are function calls within Subroutine FPROP. The polynomial equation fits for the transport properties used in FPROP are described below. Values of the constants are given in Tables B-3 through B-6.

B.3.1 Latent Heat of Vaporization

$$h_{fg} = h_g - h_f \quad (\text{B-21})$$

where h_g is calculated using Equation B-4a and

$$h_f = e_\ell + \frac{P}{\rho_\ell}$$

where e_ℓ and ρ_ℓ are calculated at saturation conditions according to Section B.2.2.

B.3.2 Constant Pressure Specific Heats

Constants used in this section are given in Table B-3.

$$c_{p\ell} = \left\{ h_\ell \left[(D_{0\ell} + D_{1\ell}P) + (C_{0\ell} + C_{1\ell}P) \right] + B_{0\ell} + B_{1\ell}P \right\}^{-1} \quad (\text{B-22})$$

$$c_{pg} = c_{1g} + C_{2g}T_v + \frac{C_{3g}P}{(C_{5g}T_v - C_{6g})^{2.4}} + \frac{C_{4g}P^3}{(C_{5g}T_v - C_{6g})^9} \quad (\text{B-23})$$

Specific heat of the noncondensable gas is 1037.0.

B.3.3 Fluid Viscosities

B.3.3.1 Liquid

Constants used in this section are given in Table B-4. The evaluation of liquid viscosity is divided into three different enthalpy ranges:

$$(1) \quad h_\ell \leq h_1$$

$$(2) \quad h_1 < h \leq h_2$$

$$(3) \quad h_\ell > h_2$$

For $h_\ell \leq h_1$:

$$\begin{aligned} \mu_\ell = & (A_{0\ell} + A_{1\ell}x + A_{2\ell}x^2 + A_{3\ell}x^3 + A_{4\ell}x^4) \\ & - (B_{0\ell} + B_{1\ell}\eta + B_{2\ell}\eta^2 + B_{3\ell}\eta^3)(P - P_1) \end{aligned} \quad (\text{B-24a})$$

where

$$x = (h_\ell - c_{0n})h_0$$

and

$$\eta = (h_\ell - e_{c0n})e_{h0}$$

In the range $h_1 < h \leq h_2$

$$\begin{aligned} \mu_\ell = & (E_{0\ell} + E_{1\ell}h_\ell + E_{2\ell}h_\ell^2 + E_{3\ell}h_\ell^3) \\ & + (F_{0\ell} + F_{1\ell}h_\ell + F_{2\ell}h_\ell^2 + F_{3\ell}h_\ell^3)(P - P_1). \end{aligned} \quad (\text{B-24b})$$

For $h_\ell > h_2$

$$\mu_\ell = (D_{0\ell} + D_{1\ell}z + D_{2\ell}z^2 + D_{3\ell}z^3 + D_{4\ell}z^4) \quad (\text{B-24c})$$

where

$$z = (h_\ell - c_n)h_{00}$$

B.3.3.2 Vapor

Constants used in this section are given in Table B-5. Three vapor temperature ranges are used to represent the data:

- (1) $T_v \leq T_1$
- (2) $T_1 < T_v < T_2$
- (3) $T_v \geq T_2$

For $T_v \leq T_1$:

$$\mu_s = [B_{1g}(T_v - 273.15) + C_{1g}] - \rho_s [D_{1g} - E_{1g}(T_v - 273.15)]. \quad (\text{B-25a})$$

If $\mu_s < 10^{-7}$, it is set to that value.

For $T_1 < T_v < T_2$:

$$\begin{aligned} \mu_s = & B_{1g}(T_v - 273.15) + C_{1g} - \rho_s [F_{1g} + F_{2g}(T_v - 273.15) \\ & + F_{3g}(T_v - 273.15)^2 + F_{4g}(T_v - 273.15)^2] \\ & + \rho_s [G_{1g} + G_{2g}(T_v - 273.15) + G_{3g}(T_v - 273.15)^2 \\ & + G_{4g}(T_v - 273.15)^3] (A_{0g} + A_{1g}\rho_s + A_{2g}\rho_s^2). \end{aligned} \quad (\text{B-25b})$$

For $T_v \geq T_2$:

$$\mu_s = B_{1g}(T_v - 273.15) + C_{1g} - \rho_s (A_{0g} + A_{1g}\rho_s + A_{2g}\rho_s^2). \quad (\text{B-25c})$$

B.3.3.3 Noncondensable Gas

For the ideal gas, two ranges of T_v are used:

- (1) $T_v \leq 502.15$
- (2) $T_v > 502.15$

For $T_v \leq 502.15$:

$$\mu_a = H_{\ell 1} + H_{\ell 2}(T_v - 273.15) + H_{\ell 3}(T_v - 273.15)^2. \quad (\text{B-26a})$$

For $T_a > 502.15$:

$$\mu_a = H_{u1} + H_{u2}(T_v - 273.15) + H_{u3}(T_v - 273.15)^2. \quad (\text{B-26b})$$

B.3.4 Fluid Thermal Conductivities

B.3.4.1 Liquid

The liquid thermal conductivity is given by:

$$k_\ell = A_{\ell 0} + A_{\ell 1}x_k + A_{\ell 2}x_k^2 + A_{\ell 3}x_k^3 \quad (\text{B-27})$$

where

$$x_k = \frac{h_f}{h_0}$$

and the constants are given in Table B-6.

B.3.4.2 Vapor

For the vapor, thermal conductivity is given by:

$$k_s = x_1 + \rho_s \left[x_2 + \frac{Cp_s}{(T_v - 273.15)^{4.2}} \right] \quad (\text{B-28})$$

where

$$x_1 = A_{g0} + A_{g1}(T_v - 273.15) + A_{g2}(T_v - 273.15)^2 + A_{g3}(T_v - 273.15)^3$$

and

$$x_2 = B_{g0} + B_{g1}(T_v - 273.15) + B_{g2}(T_v - 273.15)^2.$$

The constants are given in Table B-6. The thermal conductivity of the noncondensable gas is 0.0228.

B.3.5 Surface Tension

For $T_{\text{sat}} < 374.15^\circ\text{C}$:

$$\sigma = S_{21}TR^2 + S_3TR^3 + S_4TR^4 + S_5TR^5$$

$$S_{21} = S_2 + \left(\frac{S_1}{1 + S_0TR} \right) \quad (\text{B-29})$$

where

$$TR = 647.3 - T_{\text{sat}}$$

$$S_0 = 0.83$$

$$S_1 = 1.160936807 \times 10^{-4}$$

$$S_2 = 1.12140468 \times 10^{-6}$$

$$S_3 = -5.752805180 \times 10^{-9}$$

$$S_4 = 1.286274650 \times 10^{-11}$$

$$S_5 = -1.149719290 \times 10^{-14}$$

For $T_{\text{sat}} \geq 374.15^\circ\text{C}$:

$$\sigma = 0. \quad (\text{B-30})$$

This completes the description of the functional fits to the water transport properties.

B.4 Verification

The TRACG thermodynamic and transport fluid properties are consistent with the properties used in TRAC-BD1. These properties have been compared to steam table data over a wide range of conditions in Reference B-3. This assessment found good agreement for both thermodynamic and transport properties throughout the saturation and nonequilibrium regions. Additional assessment to confirm this conclusion was performed by comparing the TRACG values to ASME steam table values. A summary of these comparisons is provided in Tables B-7 through B-9.

Table B-7
Comparison of Saturation Properties
(14.7 < P < 1500 psia)

Property	RMS Error* (%)		
		Liquid	Vapor
Saturation Temperature	0.17		
Enthalpy		0.16	0.07
Specific Volume		0.23	0.49
Specific Heat		2.94	5.13
Thermal Conductivity		2.28	0.17
Viscosity		2.27	0.14
Surface Tension	0.21		

*Error = (ASME-TRACG)/ASME

Table B-8
RMS Error* (%) of Subcooled Liquid Properties (100°F < T < T_{sat})

Property	Pressure (psia)						
	14.7	250	500	750	1000	1250	1500
Enthalpy	1.78	0.84	0.56	0.43	0.48	0.63	0.82
Specific Volume	0.20	0.20	0.18	0.19	0.22	0.23	0.24
Specific Heat	0.38	0.27	0.23	0.30	0.42	0.60	0.89
Thermal Conductivity	0.72	1.07	1.09	1.10	0.98	0.84	0.68
Viscosity	2.16	2.95	2.71	2.47	2.18	1.91	1.70

*Error = (ASME-TRACG)/ASME

Table B-9
RMS Error* (%) of Superheated Steam Properties ($1500^{\circ}\text{F} > T > T_{\text{sat}}$)

Property	Pressure (psia)						
	14.7	250	500	750	1000	1250	1500
Enthalpy	0.74	0.52	0.33	0.30	0.55	0.96	1.59
Specific Volume	0.40	2.35	1.86	1.30	0.55	0.74	2.16
Specific Heat	1.16	1.25	1.38	1.21	1.10	0.67	0.87
Thermal Conductivity	< 0.01	0.05	0.07	0.07	0.05	0.13	0.38
Viscosity	< 0.01	0.03	0.06	0.10	0.15	0.21	0.31

*Error = (ASME-TRACG)/ASME

B.5 References

- B-1 W.A. Coffman and L.L. Lynn, *WATER: A Large Range Thermodynamic and Transport Water Property FORTRAN-IV Computer Program*, Bettis Atomic Power Laboratory, WAPD-TM-568, December 1966.
- B-2 W.C. Rivard and M.D. Torrey, *Numerical Calculations of Flashing from Long Pipes Using a Two-Fluid Model*, Los Alamos National Laboratory, LA-6104-MS, 1975.
- B-3 J.W. Spore, et. al., *TRAC-BD1: An Advanced Best Estimate Computer Program for Boiling Water Reactor Loss-of-Coolant Accident Analysis*, NUREG/CR-2178, EGG-2109, October 1981.

Appendix C Material Properties

An extensive library of temperature-dependent material properties is incorporated in the TRACG code. There are 10 sets of materials properties that comprise the library, each set supplying values for thermal conductivity, specific heat, density, and spectral emissivity for use in heat transfer calculations. The first five sets contain properties for nuclear heated or electrically heated fuel rod simulation. Included are nuclear fuel, zircaloy cladding, and electrical heater rod insulating material. The last five sets are for structural materials, including stainless steels, carbon steel, Inconel and concrete. The material indices used in the library are:

- Mixed oxide fuel
- Zircaloy
- Zirconium oxide
- ATLAS heater rod insulator
- Boron nitride insulation
- Stainless steel, Type 304
- Stainless steel, Type 316
- Carbon steel, Type A508
- Inconel, Type 718
- Concrete

The material properties in TRACG are verified and controlled and must be used for all design applications. The application of these material properties in TRACG is consistent with all other licensed GE computer codes. In addition to the library of built-in material properties, the code provides for user-supplied tables of material properties. When tables versus temperature are provided, linear interpolation is used for property evaluation.

Atlas Heater Rod Insulator

The properties of the Atlas test facility heater rod insulator material are used.

Boron Nitride Insulator

The properties of BN Insulator material are provided in the following paragraphs.

Density

$$\rho = 2002 \text{ kg/m}^3 \text{ [C-2].}$$

Specific Heat

$$C_p = 760.59 + 1.7955 * T_F - 8.6704E-4 * T_F^2 + 1.5896E-7 * T_F^3$$

where T_F = temperature ($^{\circ}\text{F}$) [C-3].

Thermal Conductivity

$$k = 25.27 - 1.365E-3 * T_F$$

where T_F = temperature ($^{\circ}F$) [C-4]

Spectral Emissivity

$$\epsilon = 1.0$$

Concrete

The properties of concrete are provided in the following paragraphs.

Density

$$\rho = 2322.6767 \text{ kg/m}^3$$

Specific Heat

$$C_p = 879.228 \text{ J/kg-K}$$

Thermal Conductivity

$$k = 1.3845872 \text{ W/m-K}$$

Spectral Emissivity

$$\epsilon = 0.0$$

C.11 References

Y.S. Touloukian, Ed., *Thermophysical Properties of High Temperature Solid Materials*, MacMillan Co., New York, 1967.

Electric Power Research Institute, *A Prediction of the Semiscale Blowdown Heat Transfer Test S-02-8 (NRC Standard Problem Five)*, EPRI NP-212, October 1976.

W.L. Kirchner, *Reflood Heat Transfer in a Light Water Reactor*, Volumes I and II, NUREG-0106, August 1976.

Appendix D

Derivation of the Isentropic Sound Speed as a Function of Pressure and Temperature for a Single-Component, Single-Phase Substance

To begin, let us consider the following expressions for the differential change in entropy:

$$ds = C_v \frac{dT}{T} - \frac{1}{\rho^2} \left(\frac{\partial P}{\partial T} \right)_\rho d\rho \quad (D-1)$$

and

$$ds = C_p \frac{dT}{T} + \frac{1}{\rho^2} \left(\frac{\partial \rho}{\partial T} \right)_P dP. \quad (D-2)$$

For isentropic systems, $ds = 0$, so

$$C_v = \frac{T}{\rho^2} \left(\frac{\partial P}{\partial T} \right)_\rho \left(\frac{\partial \rho}{\partial T} \right)_S \quad (D-3)$$

and

$$C_p = \frac{-T}{\rho^2} \left(\frac{\partial \rho}{\partial T} \right)_P \left(\frac{\partial P}{\partial T} \right)_S \quad (D-4)$$

Thus,

$$\frac{C_v}{C_p} = - \frac{\left(\frac{\partial P}{\partial T} \right)_\rho \left(\frac{\partial \rho}{\partial T} \right)_S}{\left(\frac{\partial \rho}{\partial T} \right)_P \left(\frac{\partial P}{\partial T} \right)_S} \quad (D-5)$$

Multiply Equation D-5 by the unity ratio:

$$1 = \frac{\left(\frac{\partial T}{\partial P} \right)_\rho \left(\frac{\partial T}{\partial P} \right)_S}{\left(\frac{\partial T}{\partial P} \right)_P \left(\frac{\partial T}{\partial P} \right)_S} \quad (D-6)$$

and rearrange terms to get,

$$\frac{C_v}{C_p} = - \frac{\left[\left(\frac{\partial P}{\partial T} \right)_p \left(\frac{\partial T}{\partial P} \right)_p \right] \left[\left(\frac{\partial \rho}{\partial T} \right)_s \left(\frac{\partial T}{\partial P} \right)_s \right]}{\left[\left(\frac{\partial \rho}{\partial T} \right)_p \left(\frac{\partial T}{\partial P} \right)_p \right] \left[\left(\frac{\partial P}{\partial T} \right)_s \left(\frac{\partial T}{\partial P} \right)_s \right]} \quad (D-7)$$

Next apply the following relationships

$$\begin{aligned} \left(\frac{\partial P}{\partial T} \right)_p \left(\frac{\partial T}{\partial P} \right)_p &= 1 \\ \left(\frac{\partial P}{\partial T} \right)_s \left(\frac{\partial T}{\partial P} \right)_s &= 1 \\ \left(\frac{\partial \rho}{\partial T} \right)_s \left(\frac{\partial T}{\partial P} \right)_s &= \left(\frac{\partial \rho}{\partial P} \right)_s \\ \left(\frac{\partial \rho}{\partial T} \right)_p \left(\frac{\partial T}{\partial P} \right)_p &= - \left(\frac{\partial \rho}{\partial P} \right)_T \end{aligned} \quad (D-8)$$

and simply Equation D-7 to get

$$\frac{C_v}{C_p} = \frac{\left(\frac{\partial \rho}{\partial P} \right)_s}{\left(\frac{\partial \rho}{\partial P} \right)_T} \quad (D-9)$$

This means that $\left(\frac{\partial \rho}{\partial P} \right)_s$ can be calculated from

$$\left(\frac{\partial \rho}{\partial P} \right)_s = \left(\frac{\partial \rho}{\partial P} \right)_T \frac{C_v}{C_p} \quad (D-10)$$

Now, for any gaseous substance,

$$C_p - C_v = - \frac{T \left(\frac{\partial \rho}{\partial T} \right)_p^2}{\rho^2 \left(\frac{\partial \rho}{\partial P} \right)_T} \quad (D-11)$$

Rearrange Equation D-11 to produce:

$$\frac{C_v}{C_p} = 1 - \frac{T \left(\frac{\partial \rho}{\partial T} \right)_P^2}{\rho^2 \left(\frac{\partial \rho}{\partial P} \right)_T C_p} \quad (D-12)$$

Apply the definition for C_p

$$C_p = \left(\frac{\partial h}{\partial T} \right)_P \quad (D-13)$$

and the definition for specific enthalpy

$$h = e(\rho, T) + \frac{P}{\rho} \quad (D-14)$$

in order to expand C_p to

$$C_p = \left[\left(\frac{\partial e}{\partial T} \right)_P - \frac{P}{\rho^2} \left(\frac{\partial \rho}{\partial T} \right)_P \right] \quad (D-15)$$

The value for the specific energy $e(\rho, T)$ and its derivatives are obtained from the thermodynamic properties.

Substitute the expression for C_p from Equation D-15 into Equation D-12 and expand the result to:

$$\frac{C_v}{C_p} = 1 - \frac{T \left(\frac{\partial \rho}{\partial T} \right)_P^2}{\rho^2 \left(\frac{\partial \rho}{\partial P} \right)_T \left[\left(\frac{\partial e}{\partial T} \right)_P - \frac{P}{\rho^2} \left(\frac{\partial \rho}{\partial T} \right)_P \right]} \quad (D-16)$$

Substitute the expression from Equation D-16 into Equation D-10 to get an expression for $\left(\frac{\partial \rho}{\partial P} \right)_S$. It follows from the definition for the isentropic sound speed for homogeneous equilibrium that

$$a_{HE} := \left(\frac{\partial P}{\partial \rho} \right)_S^{1/2} = \left(\frac{\partial \rho}{\partial P} \right)_S^{-1/2} \quad (D-17)$$

The final expanded expression for the isentropic sound speed is then

$$a_{HE} = \left(\frac{\partial P}{\partial \rho} \right)_S^{1/2} = \left\{ \left(\frac{\partial P}{\partial P} \right)_T - \frac{T \left(\frac{\partial \rho}{\partial T} \right)_P^2}{\rho^2 \left[\left(\frac{\partial e}{\partial T} \right)_P - \frac{P}{\rho^2} \left(\frac{\partial \rho}{\partial T} \right)_P \right]} \right\}^{-1/2} \quad (D-18)$$

Appendix E

Derivation of the Two-Phase, Two-Component HEM Sonic Velocity

Following the analysis of Ransom [6.3-5, 6] which has been derived in more detail in Appendix D, the sonic velocity for a homogeneous equilibrium mixture is given as:

$$a = \left(\frac{\partial P}{\partial \rho} \right)_S^{1/2} \quad (\text{E-1})$$

Assuming that one component is a steam-liquid mixture and the other is an immiscible component such that the gaseous phase is a Gibbs-Dalton mixture, the density of the mixture may be expressed as:

$$\rho = \alpha (\rho_s + \rho_a) + (1 - \alpha) \rho_\ell \quad (\text{E-2})$$

Taking the derivative of this mixture density with respect to pressure at constant entropy gives:

$$\left(\frac{\partial \rho}{\partial P} \right)_S = \alpha \left(\frac{\partial \rho_s}{\partial P} \right)_S + \alpha \left(\frac{\partial \rho_a}{\partial P} \right)_S + (1 - \alpha) \left(\frac{\partial \rho_\ell}{\partial P} \right)_S + (\rho_s + \rho_a - \rho_\ell) \left(\frac{\partial \alpha}{\partial P} \right)_S \quad (\text{E-3})$$

To evaluate $\left(\frac{\partial \alpha}{\partial P} \right)_S$, consider the mixture specific entropy,

$$S = X_s S_s + X_a S_a + (1 - X_s - X_a) S_\ell \quad (\text{E-4})$$

where

$$X_s = \frac{\alpha \rho_s}{\rho} \quad (\text{E-5})$$

$$X_a = \frac{\alpha \rho_a}{\rho} \quad (\text{E-6})$$

In an isentropic system,

$$\left(\frac{\partial S}{\partial P}\right)_S = 0 = X_a \left(\frac{\partial S_a}{\partial P}\right)_S + X_s \left(\frac{\partial S_s}{\partial P}\right)_S + (1 - X_a - X_s) \left(\frac{\partial S_\ell}{\partial P}\right)_S + (S_s - S_\ell) \left(\frac{\partial X_s}{\partial P}\right)_S + (S_a - S_\ell) \left(\frac{\partial X_a}{\partial P}\right)_S \quad (\text{E-7})$$

Since the noncondensable is assumed to be immiscible in the liquid-vapor mixture,

$$\left(\frac{\partial X_a}{\partial P}\right)_S = 0 \quad (\text{E-8})$$

From Equation E-5,

$$\left(\frac{\partial X_s}{\partial P}\right)_S = \frac{\alpha}{\rho} \left(\frac{\partial \rho_s}{\partial P}\right)_S + \frac{\rho_s}{\rho} \left(\frac{\partial \alpha}{\partial P}\right)_S - \frac{\alpha \rho_s}{\rho^2} \left(\frac{\partial \rho}{\partial P}\right)_S \quad (\text{E-9})$$

If we substitute Equation E-9 into Equation E-7 and rearrange terms, we get:

$$\left(\frac{\partial \alpha}{\partial P}\right)_S = \frac{\sum_1}{\rho_s (S_s - S_\ell)} - \frac{\alpha}{\rho_s} \left(\frac{\partial \rho_s}{\partial P}\right)_S + \frac{\alpha}{\rho} \left(\frac{\partial \rho}{\partial P}\right)_S \quad (\text{E-10})$$

where

$$\sum_1 = - \left[\alpha \rho_a \left(\frac{\partial S_a}{\partial P}\right)_S + \alpha \rho_s \left(\frac{\partial S_s}{\partial P}\right)_S + (1 - \alpha) \rho_\ell \left(\frac{\partial S_\ell}{\partial P}\right)_S \right] \quad (\text{E-11})$$

Substitute Equation E-10 into Equation E-3 and rearrange terms to get:

$$\left[1 - \alpha \left(\frac{\rho_a + \rho_s - \rho_\ell}{\rho} \right) \right] \left(\frac{\partial \rho}{\partial P}\right)_S = \alpha \left[1 - \left(\frac{\rho_s + \rho_a - \rho_\ell}{\rho_s} \right) \right] \left(\frac{\partial \rho_s}{\partial P}\right)_S + \alpha \left(\frac{\partial \rho_a}{\partial P}\right)_S + (1 - \alpha) \left(\frac{\partial \rho_\ell}{\partial P}\right)_S + \sum_2 \quad (\text{E-12})$$

where

$$\sum_2 = \frac{(\rho_s + \rho_a - \rho_\ell) \sum_1}{\rho_s (S_s - S_\ell)} \quad (\text{E-13})$$

so that

$$\left(\frac{\partial \rho}{\partial P}\right)_S = \frac{\rho}{\rho_s \rho_\ell} \left[\alpha \rho_s \left(\frac{\partial \rho_a}{\partial P}\right)_S + \alpha (\rho_\ell - \rho_a) \left(\frac{\partial \rho_s}{\partial P}\right)_S + (1 - \alpha) \rho_s \left(\frac{\partial \rho_\ell}{\partial P}\right)_S + \rho_s \sum_2 \right]. \quad (\text{E-14})$$

Having defined an expression for $\left(\frac{\partial \rho}{\partial P}\right)_S$, the next step is to define the property derivatives. Recall that the thermodynamic variables are defined as:

$$f_a = f_a(P_a, T) \quad (\text{E-15})$$

$$f_s = f_s(P_s, T) \quad (\text{E-16})$$

and

$$f_\ell = f_\ell(P_\ell, T) \quad (\text{E-17})$$

where

$$P = P_a + P_s \quad (\text{E-18})$$

since we are dealing with a Gibbs-Dalton mixture. The result of this is that:

$$\left(\frac{\partial P_a}{\partial P}\right)_S = 1 - \left(\frac{\partial P_s}{\partial T}\right)_S \left(\frac{\partial T}{\partial P}\right)_S \quad (\text{E-19})$$

and

$$\left(\frac{\partial P_s}{\partial P}\right)_S = \left(\frac{\partial P_s}{\partial T}\right)_S \left(\frac{\partial T}{\partial P}\right)_S \quad (\text{E-20})$$

Here, the assumption has been made that the equilibrium partial steam pressure is that which corresponds to the equilibrium temperature. Thus,

$$P_s = P_s(T) \quad (\text{E-21})$$

From this knowledge, the basic derivative properties may be defined as from the chain rule as:

$$\left(\frac{\partial \rho_a}{\partial P}\right)_S = \left(\frac{\partial \rho_a}{\partial P_a}\right)_T + \left[\left(\frac{\partial \rho_a}{\partial T}\right)_{P_a} - \left(\frac{\partial \rho_a}{\partial P_a}\right)_T \left(\frac{\partial P_s}{\partial T}\right)_S \right] \left(\frac{\partial T}{\partial P}\right)_S \quad (E-22)$$

$$\left(\frac{\partial \rho_s}{\partial P}\right)_S = \left[\left(\frac{\partial \rho_s}{\partial P_s}\right)_T \left(\frac{\partial P_s}{\partial T}\right)_S + \left(\frac{\partial \rho_s}{\partial T}\right)_{P_s} \right] \left(\frac{\partial T}{\partial P}\right)_S \quad (E-23)$$

$$\left(\frac{\partial \rho_\ell}{\partial P}\right)_S = \left(\frac{\partial \rho_\ell}{\partial P_\ell}\right)_T + \left(\frac{\partial \rho_\ell}{\partial T}\right)_{P_\ell} \left(\frac{\partial T}{\partial P}\right)_S \quad (E-24)$$

$$\left(\frac{\partial S_a}{\partial P}\right)_S = \frac{1}{\rho_a^2} \left(\frac{\partial \rho_a}{\partial T}\right)_{P_a} + \left[\left(\frac{C_{P_a}}{T}\right) - \frac{1}{\rho_a^2} \left(\frac{\partial \rho_a}{\partial T}\right)_{P_a} \left(\frac{\partial P_s}{\partial T}\right)_S \right] \left(\frac{\partial T}{\partial P}\right)_S \quad (E-25)$$

$$\left(\frac{\partial S_s}{\partial P}\right)_S = \left[\frac{C_{P_s}}{T} + \frac{1}{\rho_s^2} \left(\frac{\partial \rho_s}{\partial T}\right)_{P_s} \left(\frac{\partial P_s}{\partial T}\right)_S \right] \left(\frac{\partial T}{\partial P}\right)_S \quad (E-26)$$

$$\left(\frac{\partial S_\ell}{\partial P}\right)_S = \frac{1}{\rho_\ell^2} \left(\frac{\partial \rho_\ell}{\partial T}\right)_{P_\ell} + \frac{C_{P_\ell}}{T} \left(\frac{\partial T}{\partial P}\right)_S \quad (E-27)$$

where

$$C_{P_a} = \left(\frac{\partial e_a}{\partial T}\right)_{P_a} - \frac{P_a}{\rho_a^2} \left(\frac{\partial \rho_a}{\partial T}\right)_{P_a} \quad (E-28)$$

$$C_{P_s} = \left(\frac{\partial e_s}{\partial T}\right)_{P_s} - \frac{P_s}{\rho_s^2} \left(\frac{\partial \rho_s}{\partial T}\right)_{P_s} \quad (E-29)$$

$$C_{P_\ell} = \left(\frac{\partial e_\ell}{\partial T}\right)_{P_\ell} - \frac{P_\ell}{\rho_\ell^2} \left(\frac{\partial \rho_\ell}{\partial T}\right)_{P_\ell} \quad (E-30)$$

This leaves the specification of $\left(\frac{\partial T}{\partial P}\right)_S$. To this, consider the identity

$$X_a \rho_s = X_s \rho_a \quad (E-31)$$

Differentiating with respect to pressure gives

$$X_a \left(\frac{\partial \rho_s}{\partial P} \right)_S = X_s \left(\frac{\partial \rho_a}{\partial P} \right)_S + \rho_a \left(\frac{\partial X_s}{\partial P} \right)_S \quad (E-32)$$

Using the result from Equation E-9 and simplifying gives:

$$X_a \left(\frac{\partial \rho_s}{\partial P} \right)_S = X_s \left(\frac{\partial \rho_s}{\partial P} \right)_S - \left[\frac{\rho_a}{S_s - S_\ell} \right]^* \quad (E-33)$$

$$\left[X_a \left(\frac{\partial S_a}{\partial P} \right)_S + X_s \left(\frac{\partial S_s}{\partial P} \right)_S + (1 - X_a - X_s) \left(\frac{\partial S_\ell}{\partial P} \right)_S \right]$$

Substituting the relations defined above,

$$\begin{aligned} \alpha \rho_a \left(\frac{-\partial \rho_s}{\partial T} + \frac{\partial \rho_s}{\partial P_s} \frac{\partial P_g}{\partial T} \right) \left(\frac{\partial T}{\partial P} \right)_S &= \alpha \rho_s \left[\frac{\partial \rho_a}{\partial P_a} + \left(\frac{\partial \rho_a}{\partial T} - \frac{\partial \rho_a}{\partial P_a} \frac{\partial P_g}{\partial T} \right) \left(\frac{\partial T}{\partial P} \right)_S \right] \\ &- \frac{\rho_a}{S_s - S_\ell} \left\{ \alpha \rho_a \left[\frac{1}{\rho_a^2} \frac{\partial \rho_a}{\partial T} + \left(\frac{C_{P_a}}{T} - \frac{1}{\rho_a^2} \frac{\partial \rho_a}{\partial T} \frac{\partial P_g}{\partial T} \right) \left(\frac{\partial T}{\partial P} \right)_S \right] \right. \\ &\left. + \alpha \rho_s \left[\frac{C_{P_s}}{T} + \frac{1}{\rho_s^2} \frac{\partial \rho_s}{\partial T} \frac{\partial P_g}{\partial T} \right] \left(\frac{\partial T}{\partial P} \right)_S + (1 - \alpha) \rho_\ell \left[\frac{1}{\rho_s^2} \frac{\partial \rho_\ell}{\partial T} + \frac{C_{P_\ell}}{T} \left(\frac{\partial T}{\partial P} \right)_S \right] \right\} \quad (E-34) \end{aligned}$$

Solving for $\left(\frac{\partial T}{\partial P}\right)_S$ then gives the result

$$\begin{aligned} \left(\frac{\partial T}{\partial P}\right)_S &= \left[\alpha \rho_s \frac{\partial \rho_a}{\partial P_a} - \frac{1}{S_s - S_\ell} \left(\alpha \frac{\partial \rho_a}{\partial T} + \frac{(1-\alpha) \rho_a}{\rho_\ell} \frac{\partial \rho_\ell}{\partial T} \right) \right] / \\ &\quad \left\{ \alpha \rho_a \left(\frac{\partial \rho_s}{\partial P_s} \frac{\partial P_g}{\partial T} - \frac{\partial \rho_g}{\partial T} \right) + \alpha \rho_s \left(\frac{\partial \rho_a}{\partial P_a} \frac{\partial P_g}{\partial T} - \frac{\partial \rho_a}{\partial T} \right) \right. \\ &\quad \left. + \frac{1}{S_s - S_\ell} \left[\alpha \left(\frac{\rho_a^2 C_{P_a}}{T} - \frac{\partial \rho_a}{\partial T} \frac{\partial P_g}{\partial T} \right) \right. \right. \\ &\quad \left. \left. + \alpha \left(\rho_a \rho_s \frac{C_{P_s}}{T} + \frac{\rho_a^2}{\rho_s} \frac{\partial \rho_s}{\partial T} \frac{\partial P_g}{\partial T} \right) + (1-\alpha) \rho_a \rho_\ell \frac{C_{P_\ell}}{T} \right] \right\}. \end{aligned} \tag{E-35}$$

Finally, at saturation conditions, this Clasius-Clayron equation gives:

$$\frac{\partial P_s}{\partial T} = \left(\frac{S_s(P_s, T) - S_\ell(P_s, T)}{\rho_\ell(P_s, T) - \rho_s(P_s, T)} \right) \rho_\ell(P_s, T) \rho_s(P_s, T). \tag{E-36}$$

Assuming that the following approximation is valid in the presence of a noncondensable gas,

$$\left(\frac{S_s(P_s, T) - S_\ell(P_s, T)}{\rho_\ell(P_s, T) - \rho_s(P_s, T)} \right) \rho_\ell(P, T) = \left(\frac{S_s(P_s, T) - S_\ell(P_s, T)}{\rho_\ell(P_s, T) - \rho_s(P_s, T)} \right) \rho_\ell(P_s, T) \tag{E-37}$$

allows for $(S_s - S_\ell)$ to be expressed as

$$S_s - S_\ell = \frac{\partial P_s}{\partial T} \left(\frac{\rho_\ell - \rho_s}{\rho_\ell \rho_s} \right). \tag{E-38}$$

where ρ_ℓ is evaluated at the total pressure and ρ_s is evaluated at the partial pressure due to steam.

Equations E-14, E-35, and E-38 thus provide complete closure for the two-phase, two-component HEM sonic velocity. It is interesting to examine the limit for no noncondensable as $\rho_a \rightarrow 0$. In this case,

$$\lim_{\rho_a \rightarrow 0} \left[\left(\frac{\partial T}{\partial P} \right)_S \right] = \left(\frac{\partial P_g}{\partial T} \right)^{-1} \quad (\text{E-39})$$

and

$$\lim_{\rho_a \rightarrow 0} \left[\left(\frac{\partial \rho}{\partial P} \right)_S \right] = \frac{\rho}{\rho_\ell \rho_s} \left\{ \alpha \rho_\ell \left(\frac{\partial \rho_s}{\partial P} \right)_S + (1 - \alpha) \rho_s \left(\frac{\partial \rho_\ell}{\partial P} \right)_S \right. \\ \left. - \frac{\rho_s - \rho_\ell}{S_s - S_\ell} \left[\alpha \rho_s \left(\frac{\partial S_s}{\partial P} \right)_S + (1 - \alpha) \rho_\ell \left(\frac{\partial S_\ell}{\partial P} \right)_S \right] \right\}. \quad (\text{E-40})$$

This result is in agreement with that prescribed by Free and Spore [6.3-1, 2] in the original choking model.